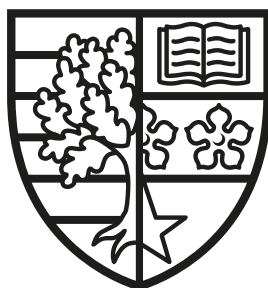


# **Novel systems and tools for quantum spintronics**

MUHAMMAD JUNAID ARSHAD  
H00337794

Submitted for the degree of  
Doctor of Philosophy

Heriot-Watt University



Institute of Photonics and Quantum Sciences (IPAQS)  
School of Engineering and Physical Sciences

SEPTEMBER 2023

The copyright in this thesis is owned by the author. Any quotation from the thesis or use of any of the information contained in it must acknowledge this thesis as the source of the quotation or information.

---

---



## ABSTRACT

**F**or quantum technologies to develop in the future, we need to create and manipulate systems of increasing complexity. Consequently, a number of challenges must be overcome when it comes to controlling, calibrating, and validating quantum states and their dynamics. There is no doubt that a quantum computer will be the only way to simulate large-scale quantum systems fully; however, classical characterisation and optimisation methods will continue to play a critical role in the process. In this thesis, we look at one such adaptive method of characterising the dynamics of a quantum system. We provide theoretical and experimental results on the study of  $\{T_1, T_2^*, T_2\}$  for a single qubit. We also provide results for the case of multiparameter estimation and finish the discussion on adaptive estimation with an experiment on frequency estimation via Ramsey measurement.

Spin-based quantum emitters have shown great promise to be the ideal platforms for quantum applications, particularly quantum networking. However, most of these suffer from large inhomogeneous broadening and emit outside the telecom band. In the second part of this thesis, we look at optical, electronic and charge state properties of vanadium (V) defect in SiC with the goal of its use in quantum networking applications owing to O-band emission and ultra-narrow inhomogeneous broadening.



## DEDICATION

*To my parents, sisters and nieces Haniya, Rimsha, Irha and newborn nephew Azhaan.*



## ACKNOWLEDGEMENTS

First of all, I would like to thank Almighty Allah. Who has given me the strength to complete this journey.

My PhD journey has been a challenging ride. Hence few people deserve my utmost gratitude for their support during this time. None more so than my PhD supervisor, Cristian Bonato, for his unwavering support throughout my PhD. For sharing his knowledge and expertise and creating a well-organised environment to learn new things. He was always there to support me in all possible capacities. Not only was he a source of light for guidance academically, but he was there for me during the most challenging period of my life when I was diagnosed and subsequently treated for a brain haemorrhage last year. A big THANK YOU for everything!

I also thank Brian Gerardot for his helpful discussion and suggestion during our meetings. I would also like to thank Margherita Mazzera for her support that helped me settle into the team and navigate around a few initial hiccups. To my colleagues at Quantum Photonics Laboratory, Dr Mauro Brotons-Gisbert, Dr Christiaan Bekker, Dr Pasquale Cilibrizzi, Dr Daniel White, Dr Ben Haylock, and other team members, thank you all for the invaluable support you have provided along this journey.

I would like to acknowledge the support given by Tam and Michelle (late). Michelle was one of a kind person, a pure soul.


Lastly, the assistance offered through the Rank Prize Return to Research grant was also beneficial.


## Inclusion of Published Works Form

Please note you are only required to complete this form if your thesis contains published works. If this is the case, please include this form within your thesis before submission.


### Declaration

This thesis contains one or more multi-author published works. I hereby declare that the contributions of each author to these publications is as follows:

Citation details	<b>Arshad, M. J.</b> , Bekker, C., Haylock, B., Skrzypczak, K., White, D., Griffiths, B., ... & Bonato, C. (2022). Online adaptive estimation of decoherence timescales for a single qubit. arXiv preprint arXiv:2210.06103.
<b>Arshad, M. J.</b> , Bekker, C., White, D. Bonato, C.	Designed the experiment.
<b>Arshad, M. J.</b> , Haylock, B., Bekker, C.	Performed the experiment and collected data.
<b>Arshad, M. J.</b> , Haylock, B., Bonato, C.	Analysed the data.
Skrzypczak, K., <b>Arshad, M. J.</b> , Haylock, B., Bonato, C.	Performed the simulations.
Griffiths, B., Gore, J., Morley, G.W., Salter, P., Smith, J.,	Laser wrote the sample.
Zohar, I., Finkler, A., Altmann, Y., Gauger, E. M.	Supported with theory.
<b>Arshad, M. J.</b> , Bekker, C., Haylock, B., Altmann, Y., Gauger, E. M., Bonato, C.	Wrote the manuscript.
Bonato, C.	Conceived and supervised the project.
Signature:	
Date:	20/04/2023

Citation details	Zohar, I., Haylock, B., Romach, Y., <b>Arshad, M. J.</b> , Halay, N., Drucker, N., ... & Finkler, A. (2023). Real-time frequency estimation of a qubit without single-shot-readout. Quantum Science and Technology, 8(3), 035017.
Zohar, I., Haylock, B., <b>Arshad, M. J.</b> ,	Performed the simulations and the experiments.
Romach, Y., Halay, N., Drucker, N., Stöhr, R., Denisenko, A., Cohen, Y.,	Developed the algorithm and theory support.
Zohar, I., Haylock, B., <b>Arshad, M. J.</b> , Bonato, C. and Finkler, A.,	Analysed the data.
Zohar, I., Haylock, B., Bonato, C. and Finkler, A.,	Wrote the manuscript.
Bonato, C. and Finkler, A.,	Conceived and supervised the project.
Signature:	
Date:	20/04/2023



Citation details	Cilibrizzi, P., <b>Arshad, M. J.</b> , Tissot, B., Son, N. T., Ivanov, I. G., Astner, T., ... & Bonato, C. (2023). Ultra-narrow inhomogeneous spectral distribution of telecom-wavelength vanadium centres in isotopically-enriched silicon carbide. arXiv preprint arXiv:2305.01757.
Cilibrizzi, P., <b>Arshad, M.J.</b> , White, D., Bekker, C., Bonato, C.	Constructed the experimental setup.
Cilibrizzi, P., <b>Arshad, M.J.</b> ,	Performed the experimental measurements.
Ul-Hassan, J.,	Designed and performed epitaxial growth.
Ghezellou, M., Ul-Hassan, J.,	Performed annealing.
Tissot, B., Burkard, G.	Simulated the expected vanadium spectra and provided general theoretical input relevant for data analysis.
Cilibrizzi, P., <b>Arshad, M.J.</b> , Tissot, B., Son, N.T., Ivanov, I.G., Astner, T., Koller, P., Trupke, M., Bonato, C.	Analysed the data with input from all co-authors.
Cilibrizzi, P., <b>Arshad, M.J.</b> , Tissot, B., Son, N.T, Trupke, M., Bonato, C.	Prepared the manuscript with input from all co-authors.
Bonato, C. and Trupke, M.	Conceived and supervised the project.
Signature:	
Date:	20/04/2023

Please include additional citations as required.



## OTHER PUBLICATIONS

The following work has been published in Applied Physics Letters but has not been included in this thesis.

Bekker, C., **Arshad, M. J.**, Cilibrizzi, P., Nikolatos, C., Lomax, P., Wood, G. S., ... Bonato, C. (2023). Scalable fabrication of hemispherical solid immersion lenses in silicon carbide through grayscale hard-mask lithography. Applied Physics Letters, 122(17).

## TABLE OF CONTENTS

	<b>Page</b>
<b>List of Figures</b>	<b>xiv</b>
<b>1 Introduction</b>	<b>1</b>
1.1 Towards quantum-enhanced technologies . . . . .	1
1.1.1 Quantum networks . . . . .	2
1.1.2 Quantum sensing . . . . .	8
1.2 Characterising quantum systems . . . . .	11
1.2.1 Decoherence timescales . . . . .	12
1.3 The nitrogen-vacancy (NV) centre in diamond . . . . .	15
1.3.1 Electronic structure of an NV centre . . . . .	15
1.3.2 DC sensing: NV centres . . . . .	16
1.3.3 AC sensing: NV centres . . . . .	17
1.4 Spin-based quantum technology in Silicon carbide (SiC) . . . . .	18
1.4.1 Key quantum emitters in SiC . . . . .	20
1.4.2 Why vanadium? . . . . .	21
1.5 PhD thesis outline . . . . .	24
1.5.1 My contribution . . . . .	25
1.5.2 Impact of COVID19 . . . . .	26
<b>2 Bayesian Inference</b>	<b>29</b>
2.1 Introduction . . . . .	29
2.1.1 Bayesian inference . . . . .	29
2.2 Introduction to estimation theory . . . . .	31
2.2.1 Fisher information $F$ . . . . .	31
2.3 Bayesian experimental design . . . . .	33
2.4 Sequential Monte Carlo (SMC) algorithm . . . . .	35
2.5 Bayesian estimation for quantum technology . . . . .	38
<b>3 Experimental Setup for Adaptive Quantum Sensing</b>	<b>41</b>
3.1 Confocal microscopy setup . . . . .	41

3.1.1	Characterisation of the confocal microscope . . . . .	44
3.2	Optical pulsing system . . . . .	48
3.2.1	Working principles of an AOM . . . . .	48
3.2.2	Double-pass AOM configuration . . . . .	49
3.2.3	Design and performance of the AOM system . . . . .	49
3.3	Microwave (MW) chain . . . . .	50
3.3.1	Design of coplanar waveguide . . . . .	51
3.3.2	Single-sideband Modulation . . . . .	51
3.3.3	Microwave chain . . . . .	54
3.4	Nuclear spin assisted optical readout . . . . .	55
3.5	Characterisation of an NV centre . . . . .	56
3.5.1	Basic electron spin measurement and control . . . . .	59
3.5.2	Optically detected magnetic resonance (ODMR) . . . . .	60
3.5.3	Rabi oscillations . . . . .	61
3.5.4	Ramsey interferometry . . . . .	62
3.5.5	Longitudinal relaxation time $T_1$ . . . . .	63
3.5.6	Hahn echo . . . . .	63
3.6	Nuclear spin polarisation . . . . .	64
3.6.1	Magnetic field alignment . . . . .	66
3.7	Temperature stability of the setup and magnet . . . . .	67
3.7.1	Temperature stability of the magnet . . . . .	68
3.8	Adaptive electronics . . . . .	70
3.8.1	Microcontroller - ADwin-Pro II . . . . .	71
3.8.2	High definition arbitrary waveform generator (HDAWG) . . . . .	73
3.8.3	Photon pulse routing . . . . .	74
3.8.4	Adaptive experiment at a glance . . . . .	76
3.9	Real-time Sequential Montecarlo implementation . . . . .	76
3.9.1	HDWAG Programming . . . . .	77
3.9.2	ADwin flow-chart . . . . .	79
3.10	Cryogenic setup for vanadium in SiC experiments . . . . .	80
<b>4</b>	<b>Adaptive decoherence estimation</b> . . . . .	<b>85</b>
4.1	Introduction . . . . .	85
4.2	Fisher information of a qubit . . . . .	86
4.2.1	Decay factor N . . . . .	87
4.2.2	Maximisation of Fisher information . . . . .	87
4.2.3	Optimising sensitivity . . . . .	89
4.3	Adaptive estimation protocol . . . . .	90
4.4	Simulation results . . . . .	91

TABLE OF CONTENTS

---

4.4.1	Non-single shot readout . . . . .	91
4.5	Experimental results . . . . .	95
4.6	Multiparameter estimation . . . . .	101
<b>5</b>	<b>Adaptive frequency estimation experiment</b>	<b>105</b>
5.1	Introduction . . . . .	105
5.2	Adaptive frequency estimation algorithm (FEA) . . . . .	106
5.2.1	Rundown of the adaptive FEA experiment . . . . .	108
5.3	Majority voting vs Binomial distribution . . . . .	109
5.4	Adaptive frequency estimation algorithm result . . . . .	111
5.5	Simulations: Performance of adaptive protocols for different experimental settings	115
<b>6</b>	<b>Single vanadium centres in SiC</b>	<b>119</b>
6.1	Introduction . . . . .	119
6.1.1	Sample . . . . .	120
6.1.2	Optical measurements . . . . .	123
6.2	Optical spectroscopy of a single vanadium centre . . . . .	123
6.2.1	Theoretical study of electronic structure . . . . .	125
6.2.2	Experimental results for PLE . . . . .	126
6.3	Ultra-narrow inhomogeneous distribution . . . . .	129
6.3.1	Narrowest linewidth . . . . .	132
6.4	Charge state stability $V^{(4+)}$ . . . . .	133
6.5	Summary . . . . .	136
<b>7</b>	<b>Conclusion/Outlook</b>	<b>137</b>
7.1	Conclusion . . . . .	137
7.2	Outlook . . . . .	138
7.2.1	Adaptive learning prospects . . . . .	138
7.2.2	SiC-based quantum technologies . . . . .	140
<b>A</b>	<b>Appendix</b>	<b>143</b>
A.1	Smallest incremental step size calculation . . . . .	143
A.2	Code for ADwin . . . . .	144
A.3	Code for High definition arbitrary waveform generator (HDAWG) . . . . .	147
A.4	Use of HDAWG and ADwin for adaptive experiments . . . . .	151
A.5	Fisher information calculation for single parameter estimation . . . . .	151
A.6	FIM matrix calculations . . . . .	154
A.6.1	FIM entries for two consecutive sensing times . . . . .	156
A.7	Optimal phase calculation . . . . .	157
A.8	Inhomogeneous distribution calculation . . . . .	160

**Bibliography**

**165**

## LIST OF FIGURES

<b>FIGURE</b>	<b>Page</b>
1.1 Quantum networks architecture . . . . .	2
1.2 Essential elements of quantum network . . . . .	4
1.3 Quantum repeater working . . . . .	4
1.4 Quantum sensing setups . . . . .	9
1.5 Types of quantum sensors . . . . .	10
1.6 Online adaptive scheme for quantum system learning . . . . .	11
1.7 $T_1$ measurement sequence. . . . .	13
1.8 $T_2^*$ measurement pulse sequence for a qubit . . . . .	13
1.9 Spin echo pulse sequence to measure $T_2$ timescale for a qubit . . . . .	14
1.10 NV centre in diamond with energy level structure . . . . .	16
1.11 Energy levels of defects in SiC . . . . .	23
1.12 Emission spectrum of defects in SiC . . . . .	23
1.13 Emission spectrum of vanadium and coherent spin dynamics of vanadium ensemble . . . . .	25
2.1 Bayes inference for parameter estimation . . . . .	30
3.1 Confocal microscopy principle . . . . .	42
3.2 Schematic design of confocal microscope setup . . . . .	43
3.3 Issues with underfilling of the objective . . . . .	44
3.4 Scanning confocal configure . . . . .	45
3.5 Confocal scan of a checkerboard . . . . .	46
3.6 Spot size calculation from line profile . . . . .	46
3.7 Scan range of the designed optical setup . . . . .	47
3.8 Characterisation of vibrations in the setup . . . . .	47
3.9 Schematic of the AOM . . . . .	48
3.10 Retro-reflected light . . . . .	49
3.11 AOM setup schematic . . . . .	50
3.12 Coplanar waveguide for MW delivery . . . . .	50
3.13 Microwave (MW) PCB . . . . .	51
3.14 MW transmission across sample . . . . .	52



3.15 IQ modulation of input signal . . . . .	52
3.16 Local oscillator phase mismatch . . . . .	54
3.17 Microwave circuit diagram . . . . .	54
3.18 Nuclear spin assisted optical readout . . . . .	56
3.19 Photoluminescence (PL) map of a single NV centre . . . . .	57
3.20 NV centre photoluminescence (PL) spectrum . . . . .	57
3.21 Autocorrelation measurement . . . . .	58
3.22 Power saturation measurement of NV centre . . . . .	58
3.23 Photoluminescence (PL) map of laser written NVs . . . . .	59
3.24 Optically detected magnetic resonance (ODMR) . . . . .	60
3.25 Rabi oscillation of ensemble of NV centre . . . . .	62
3.26 Ramsey decay of NV centre . . . . .	63
3.27 $T_1$ measurement of a single NV centre . . . . .	64
3.28 Spin echo $T_2$ measurement of a single NV centre . . . . .	64
3.29 Nuclear spin polarisation . . . . .	65
3.30 Ramsey with and without nitrogen contribution . . . . .	66
3.31 Magnetic field alignment . . . . .	67
3.32 Counts fluctuations . . . . .	68
3.33 Slow drift of XYZ stage . . . . .	69
3.34 Styrofoam box to cover the optical setup . . . . .	69
3.35 Temperature reading of the sample stage . . . . .	70
3.36 Counts stability after TEC installation . . . . .	70
3.37 Frequency drift due to temperature change of magnets . . . . .	71
3.38 Connection of electronics . . . . .	71
3.39 Micro-controller ADwin pro II . . . . .	72
3.40 DIO and Counter port of ADwin . . . . .	72
3.41 HDAWG Zurich instrument . . . . .	73
3.42 HDAWG interface connector. . . . .	74
3.43 Time resolved fluorescence signal from an NV centre . . . . .	74
3.44 Schematic of RF switch box. . . . .	75
3.45 Experimental schematic for adaptive experiment . . . . .	76
3.46 HDAWG programming for wave padding . . . . .	77
3.47 HDAWG code to receive input from ADwin . . . . .	77
3.48 HDAWG code get the value from ADwin . . . . .	78
3.49 Command table for HDAWG . . . . .	78
3.50 Flowchart illustrating the control sequence of the adaptive experiments . . . . .	79
3.51 ADwin speed to update probability distribution of N points . . . . .	80
3.52 Schematic of the optical setup used for vanadium study . . . . .	81

LIST OF FIGURES

---

3.53	Design of the cryostat used for vanadium study . . . . .	82
4.1	Fisher information $F$ in terms of $t/T_\chi$ . . . . .	88
4.2	Rescaled Fisher information $F_T$ as a function of $t/T_\chi$ . . . . .	90
4.3	Numerical simulations for estimation of $T_2^*$ . . . . .	94
4.4	Online adaptive feedback . . . . .	96
4.5	Comparing adaptive and non-adaptive experimental estimation of dephasing time $T_2^*$ . . . . .	97
4.6	Comparing adaptive and non-adaptive experimental estimation of $T_1$ time . . . . .	98
4.7	Comparing adaptive and non-adaptive experimental estimation of $T_2$ time . . . . .	99
4.8	Experimental comparison between maximizing $F$ and $F_T$ . . . . .	100
4.9	Simulations for simultaneous estimation of $T_2^*$ and $N$ . . . . .	103
4.10	Concurrent experimental estimation of $T_2^*$ and $N$ . . . . .	104
5.1	Adaptive phase estimation algorithm (PEA) and histograms of state ‘0’ and ‘1’ . . . . .	107
5.2	DC magnetometry for non-SSR case . . . . .	109
5.3	Majority voting vs Binomial distribution . . . . .	110
5.4	Phase values for frequency estimation via Ramsey measurement . . . . .	112
5.5	Simulations and experimental results for frequency estimation with $R = 10000$ . . . . .	112
5.6	Simulations and experimental results for frequency estimation with $R = 4000$ . . . . .	113
5.7	Simulations and experimental results for frequency estimation with $R = 100000$ . . . . .	114
5.8	Simulations and experimental results for frequency estimation for different protocols with $R = 2000$ . . . . .	114
5.9	Simulations and experimental results for frequency estimation for different protocols with $R = 20000$ . . . . .	115
5.10	Simulations comparing different protocols for frequency estimation with $R = 2500$ and $25000$ . . . . .	116
5.11	Simulations comparing different protocols performance against contrast . . . . .	117
6.1	empty . . . . .	121
6.2	Optical spectroscopy of a single vanadium $V^{4+}$ centre in 4H-SiC . . . . .	124
6.3	Magnetic field-dependent PLE spectroscopy . . . . .	128
6.4	Inhomogeneous distribution study of Vanadium emitter for two samples . . . . .	130
6.5	PLE spectrum of a single vanadium impurity . . . . .	132
6.6	Charge state stability study of vanadium $V^{4+}$ in SiC . . . . .	134
A.1	Minimum incremental step size . . . . .	143
A.2	ADwin programming case 0 . . . . .	144
A.3	ADwin programming case 1 . . . . .	144
A.4	ADwin programming case 2 . . . . .	145
A.5	ADwin programming case 3 . . . . .	145

---

A.6 ADwin programming case 4 . . . . .	145
A.7 ADwin programming case 5 . . . . .	146
A.8 ADwin programming case 6 . . . . .	146
A.9 ADwin programming case 7 . . . . .	147
A.10 ADwin programming case 100 . . . . .	147
A.11 Python script to initialise HDAWG . . . . .	151
A.12 Python script to initialise ADwin . . . . .	151
A.13 Python script to upload file to ADwin and HDAWG . . . . .	152
A.14 Series of PLE maps in region A of sample A . . . . .	160
A.15 Series of PLE spectra in region A of sample A . . . . .	161
A.16 Series of PLE maps in sample B with a natural abundance of isotopes . . . . .	162
A.17 Series of PLE spectra in sample B with a natural abundance of isotopes . . . . .	163



## INTRODUCTION

## 1.1 Towards quantum-enhanced technologies

As computing systems are nearing the limits of Moore's law [1], with smaller and smaller components, it is becoming more and more important to think about the quantum limits of computation and information processing. This limit opens the possibility to explore how quantum effects could be used to develop completely new information processing protocols that exploit purely non-classical effects such as quantum coherence and entanglement for enhanced performance. Examples are the development of quantum computing platforms that reduce algorithm complexity (e.g. in factoring numbers [2] compared to their classical counterparts) or protocols to enhance the security of communication channels [3]. Quantum systems can also be harnessed as sensors of physical quantities, exploiting either the improved spatial resolution resulting from the use of single particles, atoms [4] or miniaturised circuits [5] or the enhanced sensitivity enabled by quantum entanglement in multi-particle systems [6, 7].

This thesis will focus on quantum technology implementations based on individual electronic and nuclear spins. In Chap. 4 and Chap. 5 of this thesis, we describe the work done on the use of Bayesian learning techniques to achieve a faster and more robust estimation of decoherence timescales and frequency for a single qubit, leading to enhancement in the sensitivity of a quantum sensor. In Chap. 6 We discuss optical, electronic and charge state studies of a telecom-ready emitter in SiC with potential use as quantum nodes for quantum networking applications.

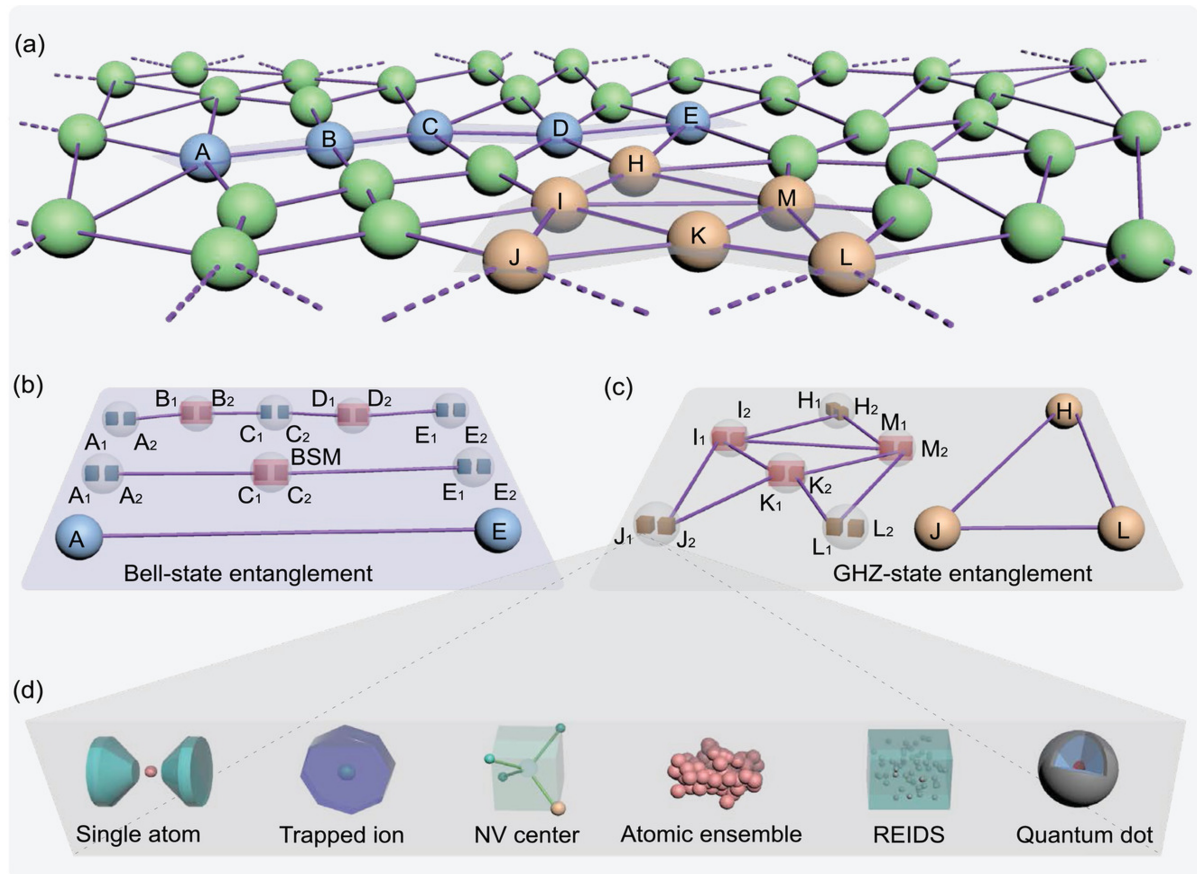


FIGURE 1.1. An example of a real-world quantum network structure. (a) Sketch showing a potential future quantum network that will have entangled quantum nodes. (b) A quantum network with a one-dimensional structure. (c) A two-dimensional quantum network. (d) Examples of several types of physical platforms that can be used to create quantum memories. These quantum memories, represented by cubes, can be placed in the nodes represented by balls in (a), (b), and (c). Figure adapted from [8].

### 1.1.1 Quantum networks

We may see a revolution in how we think about communication security in the near future if we can demonstrate a wide-range quantum network [9, 10]. Quantum networks comprise several quantum systems interconnected by single-photon links [9, 10]. The quantum network distributes quantum states between users by means of those single optical photons. Quantum processing systems in such a network are used to generate, process and store quantum information locally. In comparison, the quantum channels connecting these quantum systems can distribute entanglement across the network and transport the quantum state from site to site with high fidelity. This architecture is promising for developing distributed quantum computing, where the interfacing of smaller, higher-performance quantum processing units through lossy/noisy links enables the

scaling up of a larger platform [11].

Quantum networks are also important for sharing quantum entanglement and secret encryption keys over long distances. Underpinning these technologies is the transition from classical to quantum bits, where states can simultaneously be in a superposition of 0 and 1. Crucial to tasks such as QKD, where any unauthorized attempt to copy the quantum states being sent disrupts their unique properties, and hence it will unavoidably alter them. This disruption acts as a built-in alarm system allowing eavesdropping attempts to be detected. This safeguards the communication against unauthorized interception. Unlike quantum computing which requires many interconnected qubits to offer a computation advantage over classical computers, quantum networks can be achieved with interconnected single qubit modules, a much more feasible task in the short term.

Other applications of quantum networks include clock synchronisation [12], and sensor networks [13]. Fig. 1.1a depicts a schematic representation of a potential quantum network comprising several entangled quantum nodes. Such a quantum network can be constructed in two ways: Fig. 1.1b shows a linear quantum network scheme composed of Bell-state entanglement, and Fig. 1.1c depicts a 2D-quantum network scheme with GHZ-state entanglement [14]. Fig. 1.1d shows various quantum memories that can implement quantum nodes.

#### 1.1.1.1 Basic components of a quantum network

A quantum network comprises the following main components. Each of the below-mentioned component has a specific task and associated challenges.

1. end nodes
2. quantum channels
3. quantum repeaters

End nodes (quantum processors) are used for the manipulation of quantum information. These can be used to perform quantum operations on qubits, such as preparing and measuring a qubit. Nodes in solid state systems such as NV centres in diamond, a point defect with unique optical and spin properties (see Sec. 1.3 for more details) have been explored for applications such as quantum error correction [15], the entanglement of two [16] or three [17] quantum processors, as well as unconditional quantum teleportation [18]. Other platforms, such as trapped-ions, have also been used for end-node processors [19, 20].

In a network, such nodes are connected by quantum states transmitted over a physical channel, such as a telecom fibre network. These channels, however, suffer from being inherently lossy, leading to a loss of quantum information over a large distance as the transmissivity of the fibre changes. Hence to counter this issue and reach longer distances, quantum repeaters are usually required [21, 22].

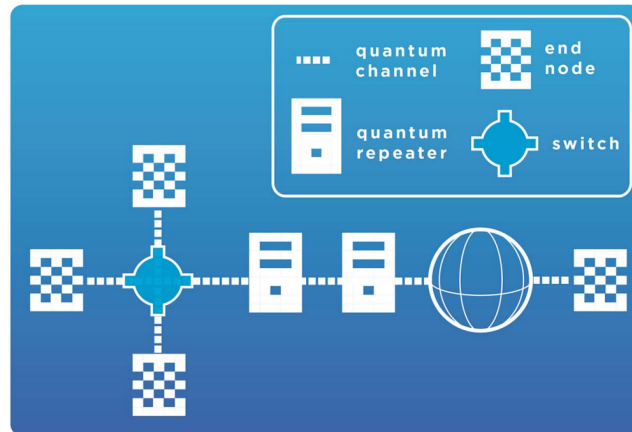


FIGURE 1.2. **Essential elements of a quantum network.** A quantum network is composed of three essential elements, quantum channel, end node and quantum repeater. Quantum channels allow the transmission of information between end nodes (quantum processors) across the network. Such channels are inherently lossy; hence to counter this, quantum repeaters are implemented to increase the transmission over long distances. Figure adapted from [10].

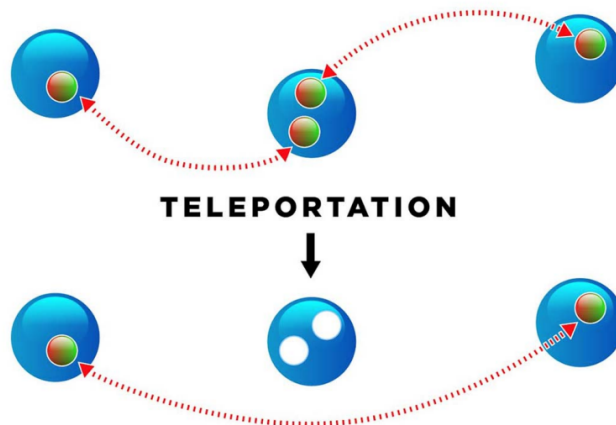


FIGURE 1.3. In a quantum repeater, entanglement (dashed lines) between the nodes (left and right balls) and the repeater (middle) is generated individually. One of the qubits entangled with node 1 is then teleported onto node 2, which subsequently allows the data qubit to be transmitted via quantum teleportation. Figure adapted from [10].

Quantum repeaters are a key technology that can help scale up quantum networks. Quantum signals, which transmit quantum information, are fragile and easily disrupted by noise and interference. As a result, the range of quantum communication is currently limited to a few hundred kilometres over optical fibres [23, 24]. Quantum repeaters can overcome this limitation through a series of entanglement-based protocols and quantum techniques, including entanglement swapping, entanglement purification, and quantum teleportation. By creating and maintaining entangled pairs of particles at intermediate nodes, quantum repeaters extend



the reach of quantum communication. This allows quantum information to be transmitted over much longer distances without losing fidelity or being disrupted by noise. Quantum repeaters are analogues of amplifiers used in classical communication to overcome signal loss during transmission. Such amplifiers, however, can not be used for quantum bits since they cannot be copied (non-cloning theorem) [25]. Additionally, manipulating them will result in a change of information the qubit carries.

The basic idea behind a quantum repeater is to break up a long-distance transmission into shorter segments, each of which can be corrected for errors, leading to more robust and reliable transmission over long distances. A schematic of a quantum repeater working is shown in Fig. 1.3, where the process of entanglement swapping allows the teleportation of data qubits between two nodes via the help of a quantum repeater.

### Requirements for spin-based quantum networking

One of the leading architectures to implement a quantum network node consists of a single quantum emitter (point defect, impurity, quantum dot) interfacing optical photons to spins. The key requirements of an ideal quantum emitter for this application are:

1. **Spin coherence:** The electron spin coherence time should be long, with the ability to initialise, manipulate and readout with high fidelity. The ability to address nearby nuclear spins for entanglement purification, quantum error correction etc., is also highly desirable [26, 27].
2. **Spin-photon interfacing:** The spin should be interfaceable to optical photons through a coherent spin-photon interface based on spectrally stable, spin-selective optical transitions. Optical networks employing fibres demand access to O, C and L telecom bands. Hence a system directly emitting in these bands is beneficial.
3. **Brightness:** which is the number of photons extracted from a single emitter per second, is important since it determines the efficiency of spin readout schemes and entanglement-generation protocols. Brightness depends on intrinsic properties and practical matters such as collection efficiency. In many of the systems currently, under study, emitter brightness is severely affected by total internal reflection, which greatly reduces the photon collection efficiency [28, 29].
4. **Photon purity and indistinguishability:** For measurement-based entanglement protocols, where remotely located spins are projected into entangled states by measurements performed on photons they are interfaced to, generated photons quality is very important. In particular, the requirements are that the photon states are pure with a negligible contribution of multi-photon states and indistinguishable, i.e. perfectly overlapping in all degrees

of freedom (spatial, spectral, polarisation) [30]. This is crucial to achieving high-visibility quantum interference, which then translates into high-quality quantum entanglement.

5. **Spectral stability:** The spin-photon interface should be stable over time. In practice, fluctuations in the electric environment due to trapped charges and dangling bonds induce spectral shifts. These shifts result in decoherence of the spin-photon interface and reduce the success rate of measurement-based entanglement [31, 32].
6. **Device integration and scalability:** The system should be easy to integrate and offer possibilities to enhance light-matter interaction. Additionally, integration with electronic functionalities can stabilise the quantum emitter charge state and its electric environment. For scalability, the platform must be compatible with standard photonics circuitry and industrial-scale nanofabrication standards [27].

### 1.1.1.2 State of the art experiments

Many groups worldwide have taken up the challenge to develop a large-scale quantum network, with many different approaches being developed in parallel. While no single approach can claim a long-distance quantum network, several systems are progressing in the right direction. It is important to note that several physical systems, for instance, trapped ions, NV centres, cold atomic ensembles, and single neutral atoms, are not only capable of absorbing and storing incident photons directly but are also useful for generating quantum correlations between photons and matter directly. Here we will discuss some of the critical experiments conducted over the past few years and the recent progress made towards building large-scale quantum networks.

Implementing a quantum node requires local matter qubits that can be interfaced to the single photon states used for long-distance quantum information sharing between the nodes. The local qubit should operate as a long-term quantum memory, and additional qubits could be used to achieve fault tolerance through quantum error correction. One of the possibilities for implementing local qubits in a quantum network is given by electronic and nuclear spins in a solid-state matrix. Due to the localised nature of the magnetic dipolar interaction, single spins interact very weakly with other spins in the environment if the host material is sufficiently pure. This results in very long coherence times, which is crucial for quantum memory applications. Solid-state implementations, particularly in semiconductors, are appealing for applications since one can potentially fabricate devices at an industrial scale [33]. A point defect in diamond, the nitrogen-vacancy (NV) centre (see Sec. 1.3 for more details), is among the leading solid-state platforms to implement these quantum nodes, with several groundbreaking studies, particularly by Ronald Hanson’s group at TU Delft. In 2013 remote entanglement between two NV centre electron spins separated by 3m distance [34] was demonstrated, later extended to the current record ( $\sim 1.3$  km) for the production of heralded entanglement between distant locations [16]. More recently, entanglement purification via dark electron-nuclear spin has also been achieved

[35]. To facilitate entanglement distribution through commercial telecom fibres, conversion of coherent NV emission from 637 nm to the telecom region (1550 nm) while preserving the coherence of the spin-photon interface [36] was implemented. To establish a long-distance quantum network between elementary links, it is typically necessary to use higher-level entanglement swapping operations of matter-matter entanglement as part of the quantum repeater scheme. A new quantum repeater scheme has been proposed to solve this long-distance problem without relying on linear optics-based entanglement swapping [37]. A fibre-based city-scale quantum communication network prototype without trusted nodes has also been shown [38]. A similar demonstration of entanglement within an urban environment over a distance of 12.5 km was also shown recently [39]. More recently, quantum memory in a trapped-ion network node has been demonstrated where they combine the capabilities of strontium and calcium ions to achieve robust, high-quality entanglement and store it for a longer time period [40]. Additionally, studies using an ensemble of Rb atoms have been used to quantum-enable millimetre wave to optical transduction for efficient entanglement generation and transfer of quantum information between different quantum technologies [41]. A study demonstrating the transmission of entangled telecom photons with rare earth-based solid-state quantum memory over deployed optical fibre has showcased highly non-classical correlations up to 50 km fibre separation and shown potential for long-distance quantum communication networks [42]. An additional study on rare earth-based quantum memory demonstrates long-distance quantum teleportation of a photonic telecom qubit into a solid-state qubit using active feed-forward and a temporally-multiplexed protocol, resulting in increased teleportation attempts and higher repetition rates for practical quantum communication setups [43]. A study done by Dario et. al. in 2021 [44] presents a successful demonstration of heralded entanglement between spatially separated quantum nodes using multimode solid-state quantum memories, enabling telecom-compatible and temporally-multiplexed operation for future quantum networks. However, perhaps the most significant step taken in recent times in the realisation of a quantum internet is the study done last year by the team of physicists at Delft, where they have shown the use of quantum teleportation to send data over three distinct locations [45], which was only limited to two locations previously. This work is significant in that before this, quantum teleportation between stationary qubits was only possible when they were connected via direct quantum channels due to requirements of efficient light-matter interfacing and high-fidelity entanglement. This work will allow information sharing between two nodes in the absence of a direct connection. A notable advancement in achieving a quantum internet.

Additionally, some commercially available devices can perform QKD at short distances (~100km in telecom fibre) [23, 24]. There have also been laboratory demonstrations on using coiled fibre for long-distance communication [46–48] or through free space communication [49]. Using a fibre-based framework, a study demonstrated the entanglement over 22 km for field-deployed fibres and 50 km using coiled fibres [50]. Various QKD devices have been implemented in field tests and short-distance networks [51, 52]. Using satellite technology, entanglements

between distant sites have been produced involving distances of more than 1200 kilometres [53]. Laboratory experiments have also demonstrated the feasibility of more complex applications, such as quantum sensing [54] via an entangled quantum network.

Considerations concerning the design of quantum networks that come from technological rather than just fundamental limitations are a crucial part of the development of quantum networks and an issue that needs to be addressed when considering realistic deployments of quantum networks. These are enormous technological challenges, which include - for instance, storing qubits for an extended period of time and manipulating a large number of qubits simultaneously. A possible vision for a quantum network, which inspires the work in this thesis, is a set of quantum nodes connected by optical links. Quantum states are shared between the nodes by single optical photons in the telecom range to reduce losses. Local nodes, implemented by atomic or solid-state qubits, provide mechanisms to store the quantum states and basic processing capabilities, such as quantum error correction.

### **1.1.2 Quantum sensing**

A branch of quantum science and technology that has been gaining prominence in recent times is quantum sensing. It constitutes a separate and swiftly expanding domain within quantum science and technology, with the prevalent platforms encompassing trapped ions, spin and superconducting qubits. As the term implies, quantum sensing refers to the process of measuring physical quantities, for example, magnetic and electric fields, rotation, temperature, and pressure, using a quantum system, quantum phenomena, or quantum properties. Several quantum sensors have been developed over the years, including magnetometers based on superconducting quantum interference devices (SQUIDs), atomic vapours and clocks.

In addition to providing new opportunities in applied physics and other scientific fields, the field is expected to offer novel opportunities in areas such as high sensitivity and precision measurements. The hope is also to improve the performance of classic sensor systems [4] by reducing the noise compared to what is known as a “shot noise limit” [55]. Quantum sensing applications take advantage of the fact that the quantum states of particles can be susceptible to changes in their environment. According to the literature [4, 56], a few critical criteria must be met in order to construct a working quantum sensor:

1. It is essential that the quantum system has resolvable, discrete energy levels with finite energy transitions.
2. Quantum sensors should be able to be initialised into well-known states and read out.
3. It is possible to manipulate the quantum sensor coherently.

The idea behind having these preset conditions to classify a quantum sensor is important in order to allow the system to be in a well-defined quantum state, which helps to calibrate the sensor and gives a known starting point along with giving the option of controlling and manipulating in a way that is consistent and predictable. Generally, measuring any physical quantity with the help of quantum sensors takes the steps described in Fig. 1.4. To begin using the quantum sensor, the basis state of the quantum sensor must be determined first, which is then transformed into the initial state that is desired by the user based on the particular measurement of interest. After which, it is left under the influence of external perturbations. Then a superposition of observable readout states is created, followed by the readout of the final state of the sensor. These first five steps represent one measurement cycle, which is repeated several times before a final average estimate is yielded for the unknown quantity of interest.

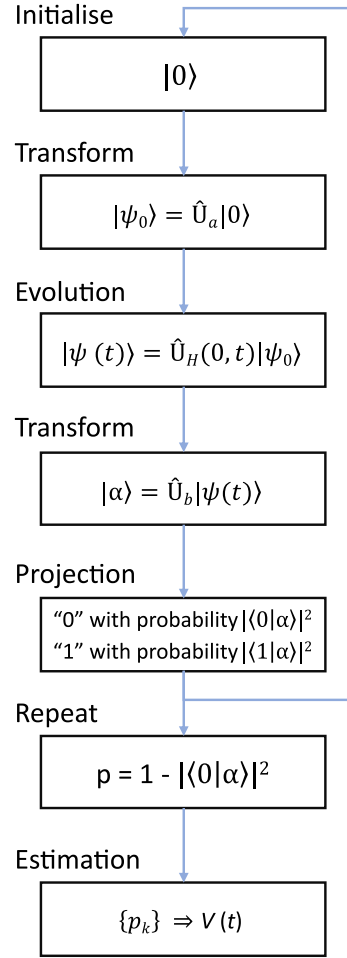


FIGURE 1.4. Generalised steps of a quantum sensing protocol.

Some examples of different types of quantum sensors and their properties are given in Fig. 1.5. Where the types I, II, and III (in the last column of Fig. 1.5) refer to the three different definitions of Quantum sensing:

1. Measuring a physical quantity with the help of a quantum object (type I).
2. Measurement of a physical quantity using quantum coherence (type II).
3. The use of quantum entanglement to enhance a measurement's precision and sensitivity (type III).

Significant progress has been made over the years with the use of solid-state spin sensors in quantum sensing. In 2019, a study showed the mapping of 27 individual nuclear spins and demonstrated the 3D structure of spin cluster with atomic-scale resolution [57]. A number of studies followed, including one published last year showing the mapping of over 20 C-13 nuclear spins at room temperature with a 2.4 nm distance from the spin sensor [58].

## CHAPTER 1. INTRODUCTION

Implementation	Qubit(s)	Measured quantity(ies)	Typical frequency	Initialization	Readout	Type <sup>a</sup>
Neutral atoms						
Atomic vapor	Atomic spin	Magnetic field, Rotation, Time/Frequency	DC–10 GHz	Optical	Optical	II–III
Cold clouds	Atomic spin	Magnetic field, Acceleration, Time/Frequency	DC–10 GHz	Optical	Optical	II–III
Trapped ion(s)						
	Long-lived electronic state	Time/Frequency Rotation	THz	Optical	Optical	II–III
	Vibrational mode	Electric field, Force	MHz	Optical	Optical	II
Rydberg atoms						
	Rydberg states	Electric field	DC, GHz	Optical	Optical	II–III
Solid state spins (ensembles)						
NMR sensors	Nuclear spins	Magnetic field	DC	Thermal	Pick-up coil	II
NV <sup>b</sup> center ensembles	Electron spins	Magnetic field, Electric field, Temperature, Pressure, Rotation	DC–GHz	Optical	Optical	II
Solid state spins (single spins)						
P donor in Si	Electron spin	Magnetic field	DC–GHz	Thermal	Electrical	II
Semiconductor quantum dots	Electron spin	Magnetic field, Electric field	DC–GHz	Electrical, Optical	Electrical, Optical	I–II
Single NV <sup>b</sup> center	Electron spin	Magnetic field, Electric field, Temperature, Pressure, Rotation	DC–GHz	Optical	Optical	II
Superconducting circuits						
SQUID <sup>c</sup>	Supercurrent	Magnetic field	DC–10 GHz	Thermal	Electrical	I–II
Flux qubit	Circulating currents	Magnetic field	DC–10 GHz	Thermal	Electrical	II
Charge qubit	Charge eigenstates	Electric field	DC–10 GHz	Thermal	Electrical	II
Elementary particles						
Muon	Muonic spin	Magnetic field	DC	Radioactive decay	Radioactive decay	II
Neutron	Nuclear spin	Magnetic field, Phonon density, Gravity	DC	Bragg scattering	Bragg scattering	II
Other sensors						
SET <sup>d</sup>	Charge eigenstates	Electric field	DC–100 MHz	Thermal	Electrical	I
Optomechanics	Phonons	Force, Acceleration, Mass, Magnetic field, Voltage	kHz–GHz	Thermal	Optical	I
Interferometer	Photons, (Atoms, Molecules)	Displacement, Refractive Index	–			II–III

FIGURE 1.5. Quantum sensors for estimation of various quantities. Figure adapted from [4].

Based on the spectral properties of the fields to be sensed, we can categorize quantum sensing into DC sensing and AC sensing. DC sensing is used for static, slowly varying signals. While AC sensing is used for time-varying signals up to a frequency of 10 MHz [59–61], with some experiments using quantum mixers, have shown sensing signals of  $\sim 150$  MHz [62] (more on this

in Sec. 1.3.2 and 1.3.3).

## 1.2 Characterising quantum systems

As quantum technological platforms are being scaled up to larger and larger quantum systems, the need for efficient characterisation, verification, and validation protocols becomes more and more compelling. In this context, it is essential to understand that the dynamics of a quantum system become exponentially complex with increasing size, making a description of the system a challenging task. A recent review [63] gives a quite complete introduction overview of methods that have been used to learn the state, dynamics and measurements of a quantum system.

Even in the case of small-size quantum systems, characterising and optimising quantum systems is crucial to develop fast, high-fidelity processing. For example, in quantum metrology, optimising measurement strategies and probe states are essential to maximising the sensitivity and precision of a quantum sensor. In many cases, it is crucial to minimise the total sensing time for an experiment, for example, to track processes with fast timescales or fast lifetimes (for example, bio-molecules that might only be stable for a short time). A possible way to do this is to employ "smart" adaptive approaches that optimise sensing settings in real-time. In an adaptive measurement, the protocol uses the newly acquired information to compute the optimal settings for the next experimental run. Moreover, for the case where the optimal settings depend on the unknown parameter, the adaptive strategies outperform the standard measurement schemes. A general example of such a Bayesian-informed adaptive measurement cycle is depicted in Fig. 1.6. In this protocol, the Bayes rule is used to update our current knowledge about the probability distribution for the quantity of interest. The updated probability distribution can then be used to optimise the settings for the next measurements in the series.

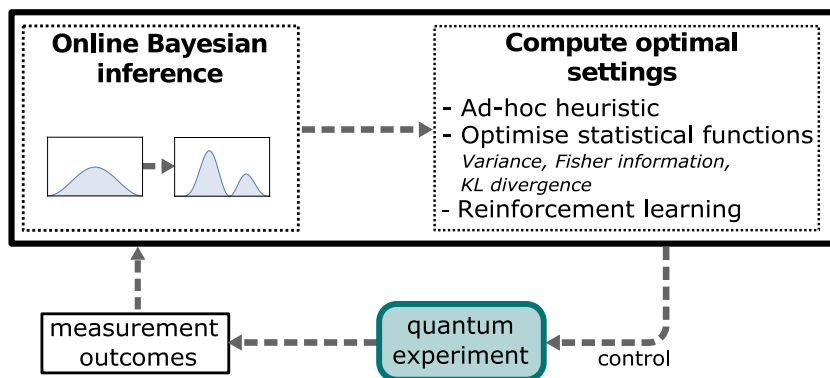


FIGURE 1.6. **Online adaptive scheme employing Bayesian inference.** Using the Bayesian inference after each measurement outcome, the optimal parameters/settings for the next cycle can be calculated by using different statistical functions. Figure adapted from [63].

A key consideration for applying these adaptive schemes is the time constraints. Hence a

near-optimal scheme which is time efficient, might perform better than the optimal scheme, which is computationally intensive. For the scope of this thesis, we will focus on a few such examples of a learning protocol to adaptively estimate the decoherence properties of a single spin qubit via the application of Bayesian inference (see Chap. 4). We will also discuss the case of multiparameter estimation (see Sec. 4.6) as well as frequency estimation (see Chap. 5) via these adaptive techniques. The subsection below briefly introduces the decoherence timescales associated with a qubit.

### 1.2.1 Decoherence timescales

Coherent manipulation of spin qubits is important in various applications [64], ranging from quantum sensing to quantum computing. Coherent operations are limited by the loss of coherence of the qubit, resulting from unwanted interaction with the environment. Decoherence is typically characterised by  $T_1$ ,  $T_2^*$  and  $T_2$  timescales [65]. The section below will briefly describe the main factors contributing to the decoherence of a quantum system and the protocol used to measure the timescales ( $T_1$ ,  $T_2$ , and  $T_2^*$ ) associated with these interactions.

#### 1.2.1.1 Longitudinal spin-lattice relaxation time $T_1$

The relaxation time  $T_1$  describes the timescale over which a polarised spin reaches the thermal equilibrium configuration. Relaxation can be driven, for example, by interactions with phonons in the crystal lattice or charge noise enabled by the spin-orbit interaction.  $T_1$  relaxation timescales are not only an important parameter of quantum information processing but can also be used as a sensing tool to infer quantities such as the concentration of paramagnetic species from the noise they create on the quantum system [66]. This has been used, for example, in medical imaging to create images with high contrast between different tissue types by selectively suppressing the signals from specific tissues based on their  $T_1$  relaxation times [67].

$T_1$  his time can be measured by polarising the spin into an eigenstate and detecting the probability of being left in the initial state as a function of time. The pulse sequence used for  $T_1$  measurement is shown in Fig. 1.7. Using an initialisation pulse, the system is initialised into the initial state, for example,  $|\psi_0\rangle$ . After a certain delay time  $\tau$ , the remaining spin population is read out with a readout pulse. A spin-relaxation curve is obtained by varying the delay time  $\tau$  between initialisation and readout pulses. Such a curve can be fitted to extract the characteristic decay time  $T_1$ .

#### 1.2.1.2 Dephasing time ( $T_2^*$ )

The dephasing ( $T_2^*$ ) time describes the loss of coherence of a quantum superposition induced by inhomogeneities in the surrounding environment. Such inhomogeneities lead to qubit precession occurring at different rates causing the wave function to lose coherence and resulting in dephasing.



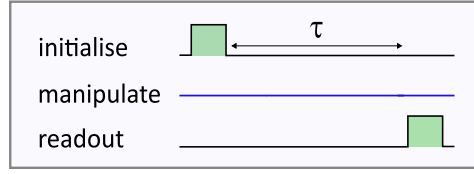


FIGURE 1.7.  $T_1$  measurement pulse sequence to estimate the spin-lattice relaxation time. In this case, no manipulation pulse is applied between initialisation and readout.

These inhomogeneities include magnetic field fluctuations, coupling to other spins, thermal effects and imperfections in control pulses [68, 69]. The standard approach to measure  $T_2^*$  is based on Ramsey interferometry through the sequence depicted in Fig. 1.8. The quantum system is initially prepared in a well-defined state, such as the ground  $|\Psi_0\rangle$  or excited state  $|\Psi_1\rangle$  via an initialisation pulse. The first  $\pi/2$  pulse is then applied to the quantum system, which causes a rotation of the states into a superposition of  $|\Psi_0\rangle$  and  $|\Psi_1\rangle$ . The quantum system is allowed to precess freely for a variable sensing time  $\tau$  in such a superposition state. A second  $\pi/2$  pulse is applied to project the system back into the  $|\Psi_0\rangle$ ,  $|\Psi_1\rangle$  basis. Finally, the system is measured to determine the probability of finding it in a particular eigenstate. The Ramsey pulse sequence can measure the spin precession frequency by varying the sensing interval  $\tau$  between the two  $\pi/2$  pulses. The resulting Ramsey decay curve can be used to extract the  $T_2^*$  time.

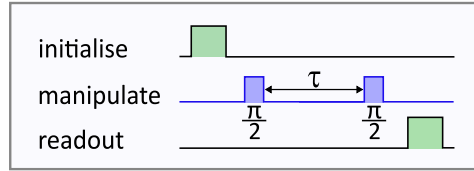


FIGURE 1.8. Ramsey interferometry pulse sequence to measure the  $T_2^*$  time of a qubit. Here two  $\pi/2$  pulses are used to manipulate the state of the quantum system.

The characterisation of dephasing time is important in quantum sensing, spectroscopy and quantum computation. Dephasing [70, 71] limits the storage time for a quantum memory and the sensitivity for a quantum sensor (by limiting the coherent signal accumulation time). The optimal sensitivity is achieved for  $\tau \sim T_2^*$  as [72]:

$$(1.1) \quad \eta_{DC} \approx \frac{\hbar}{g\mu_B C \sqrt{T_2^*}}$$

here  $C$  is the contrast.

The  $T_2^*$  value for a single spin measures how the spin's phase accumulation over time is distributed due to repeated measurements on that spin [73, 74]. In contrast, for the ensemble,  $T_2^*$  gives the relative dephasing of each spin in the ensemble. Within the same sample, different spins

can have varying values of  $T_2^{*single}$  due to the non-uniform distribution of the surrounding spin baths [75, 76]. While for an ensemble of spins,  $T_2^{*ensemble}$  is not only affected by the fluctuations in the spin bath but also limited due to noise sources like inhomogeneous distribution, strain, and the g factors [74].

### 1.2.1.3 Decoherence time ( $T_2$ )

Decoherence time  $T_2$ , also known as transverse relaxation time, is a measure of the duration for which a quantum system can maintain its coherence before it becomes randomised due to interactions with environmental noise, such as fluctuations in the magnetic field, coupling to the nearby nuclear spins and surface interactions.  $T_2$  is more sensitive to temporal fluctuations in the environment as it removes the contribution from the environment's slowly varying and static inhomogeneities.

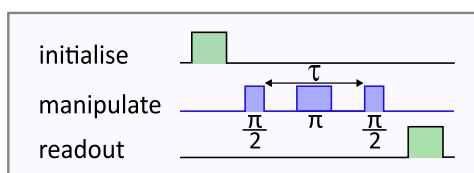


FIGURE 1.9. Spin echo sequence to measure  $T_2$  timescale for a qubit. Here qubit is manipulated via the application of two  $\pi/2$  pulses and one  $\pi$  pulse to cancel the effect of the static, slowly varying field.

The Hahn echo sequence is most commonly employed to measure the  $T_2$  decoherence time [77, 78]. As depicted in Fig. 1.9, The system is initialised, and a  $\pi/2$  creates a superposition state of  $|\Psi_0\rangle$  and  $|\Psi_1\rangle$ . The spins evolve freely under the influence of the local magnetic fields for a precession time  $\tau/2$ . During this time, spins will accumulate different phases due to the differences in precession frequencies. After this free precession time, a  $\pi$  pulse is applied, which rotates the spins by 180 degrees. The system is then allowed to precess for another  $\tau/2$  to refocus the spin. After this, the second  $\pi/2$  MW pulse projects the spin back to  $|\Psi_0\rangle$  and  $|\Psi_1\rangle$  basis. Finally, a laser is applied to read out the system's state. The detected signal contains information about the properties of the system, including its  $T_2$  relaxation time and the local magnetic field distribution. Additionally, such a coherent control can help increase the sensitivity (by  $\sim \sqrt{T_2^*/T_2}$ ) at the cost of reduced bandwidth, given as [72]:

$$(1.2) \quad \eta_{AC} \approx \frac{\pi \hbar}{2g\mu_B C \sqrt{T_2}}$$

with optimal sensitivity achieved for fields with frequency  $\sim 1/T_2$ .

## 1.3 The nitrogen-vacancy (NV) centre in diamond

The adaptive protocols described in Chap. 4 and 5 of this thesis are general and can be applied to any qubit system. We demonstrate the working of these protocols on an  $e^-$  spin associated with a nitrogen-vacancy (NV) centre in diamond as it is one of the most studied optical defects, and room temperature spin manipulation is possible.

More than 100 luminescent defects have been studied in diamond [79, 80]. Many of these have been characterised as optically active [81]. At the same time, some of these defects allow optical detection of magnetic resonance (ODMR) [82, 83]. The nitrogen-vacancy (NV) centre is among the most extensively researched defects. As shown in Fig. 1.10 (left), an NV centre comprises a substitutional nitrogen atom adjacent to a missing carbon atom (vacancy) in the diamond lattice. NV (nitrogen-vacancy) centres can be formed naturally in some diamonds or artificially created using implantation and annealing [84–86]. For an NV centre, most of its features are attributed to the two unpaired electrons exhibiting a trigonal  $C_{3v}$  symmetry [87]. The paramagnetic ground state of the NV centres strongly interacts with optical and microwave fields. NV centres have unique optical and spin properties with long spin coherence times. They can operate at room temperature, making them attractive for various applications in quantum technology, including quantum computing, quantum cryptography, and quantum sensing. The host material, diamond, is biocompatible, which means that NV centres in diamond could be used for biomedical applications such as bioimaging and biosensing.

### 1.3.1 Electronic structure of an NV centre

The electronic structure of an NV (nitrogen-vacancy) centre in a diamond is characterised by two unpaired electrons in the defect's electronic configuration; for a detailed review, see [87, 89]. NV centre has a spin-triplet ground state ( $^3A_2$ ) and excited ( $^3E$ ), as shown in Fig. 1.10 (right). The ground state has a zero-field splitting, which arises from the interaction of the unpaired electron's spin with the crystal lattice. This splitting results in three energy levels with different spin projections, separated by approximately 2.87 GHz at room temperature. The ground state is directly coupled with the excited state via an optical transition of 637 nm (red fluorescence). In comparison, the transition between the two intermediate states ( $^1A_1$ ) and ( $^1E$ ) is a weak transition in the infra-red regime. These transitions are spin-conserving due to the weak spin-orbit coupling [90, 91]. In the presence of these intermediate states, there are two more non-radiative and non-spin conserving transitions between ( $^3E$ ) and ( $^1A_1$ ) as well as between ( $^1E$ ) and ( $^3A_2$ ). These transitions are brought about by the mechanism of phonon-assisted intersystem crossing (ISC). The lifetime of these ISC transitions is about  $\sim 150$  ns as opposed to 12 ns for the radiative transition between the ground and excited state. This difference in lifetime is the reason behind the spin polarisation and optical contrast of an NV centre. Looking at this in more detail, we find that when an NV is optically pumped into the excited state, it takes either a radiative path from

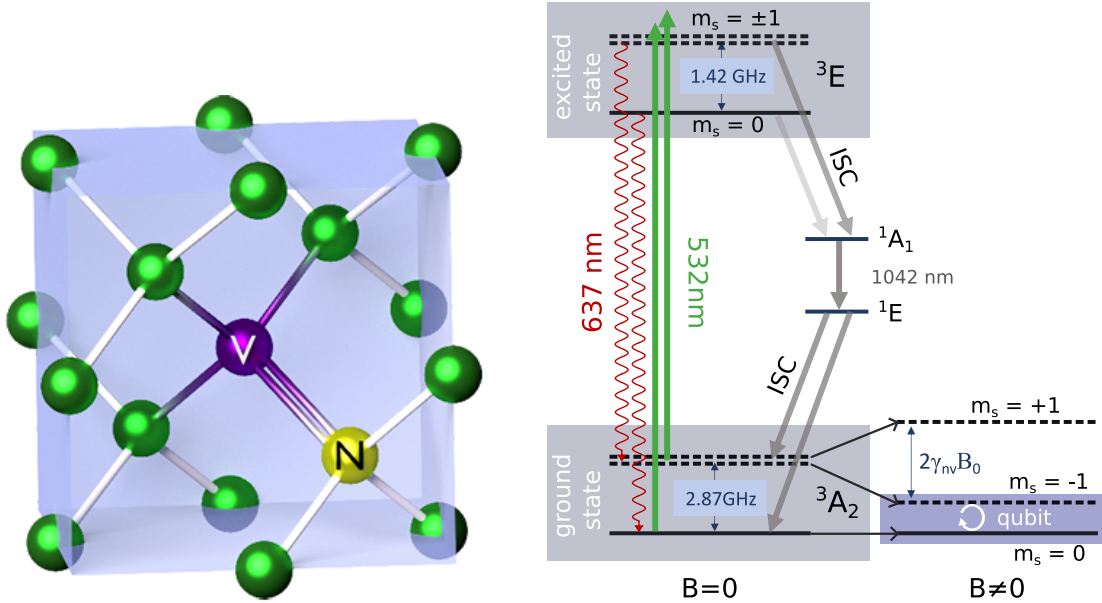


Figure 1.10: **NV centre in diamond with energy level structure.** **Left:** NV centre in the diamond. Here carbon atoms are represented by green balls, nitrogen with yellow, while a purple ball represents a vacancy. Figure adapted from [88]. **Right:** Schematic of energy level structure of an NV centre. Green and red arrows represent the most common excitation and relaxation optical transitions. While the grey arrow represents the intersystem crossing leading to polarisation and fluorescence contrast of the NV defect.

${}^3E$  to  ${}^3A_2$ , giving a fluorescence signal in visible light, or a non-radiative path accompanied by the inter-system crossing (ISC),  ${}^3E \rightarrow {}^1A_1 \rightarrow {}^1E \rightarrow {}^3A_2$ . The probability of following this ISC path is high when the system is optically pumped from  $m_s = \pm 1$  [92]. This state-dependent ISC transition probability selectivity polarises the NV centre into the  $m_s = 0$  spin state after a few initialisation cycles. Moreover, since the radiative lifetime of the two paths is an order of magnitude different, this means that fewer optical photons will be detected when the system starts in  $m_s = \pm 1$  spin state. The value for this difference in fluorescence contrast between the two spin states can be as high as  $\sim 20\%$  [93, 94]. Using these two properties of the NV centres is the primary mechanism behind many applications.

### 1.3.2 DC sensing: NV centres

In DC quantum sensing with NV centres, a diamond sample containing NV centres is placed in an external magnetic field. The presence of the magnetic field lifts the degeneracy of the  $|\pm 1\rangle$  and leads to field-dependent splitting of the levels. To measure such a change in the energy levels of the NV centres, a Ramsey sequence, as depicted in Fig. 1.8, is used. Where an NV centre is optically addressed, and their fluorescence is measured to determine the strength and direction of the magnetic field with high precision and sensitivity. An NV centre accumulates a phase  $\phi = 2\pi\gamma B\tau$  during this measurement. From this, the value of the unknown applied field can be

estimated with the gyromagnetic ratio  $\gamma = g\mu_B/h \approx 28.024$  GHz/T [95]. One advantage of NV centres for DC quantum sensing is that they are highly sensitive even at room temperature, making them suitable for a wide range of applications. Additionally, NV centres can be fabricated in diamond samples with controlled positioning and density, enabling high-resolution magnetic field maps to be created. Potential applications of DC quantum sensing with NV centres include monitoring the current flow in electronic devices [96], detecting magnetic fields produced by biological processes [97, 98], and studying the magnetic properties of materials at the nanoscale [99, 100].

### Sensitivity

The sensitivity of a given quantum sensor depends on many factors, including readout noise, decoherence time, and overhead time. The final expression for optimal sensitivity taking all these factors into account, can be given as [70]:

$$(1.3) \quad \eta_{ramsey}^{opt} = \frac{1}{\gamma_e e^{-(\tau/T_2^*)^2}} \frac{\sqrt{\tau + t_O}}{\tau} \sqrt{1 + \frac{1}{C^2 n_{avg}}}$$

here  $\gamma_e$  is the gyromagnetic ratio of the NV  $e^-$  spin,  $t_O$  gives the experimental overhead time,  $\tau$  is the sensing time,  $C$  is the contrast and  $n_{avg}$  is the averaged collected photons per readout. And as the measurement sensitivity is dependent on the NV spin dephasing time  $T_2^*$ , it limits the maximum possible sensitivity for any quantum sensor. Several studies have been done to extend this timescale and increase the sensitivity of the sensor, with studies showing the value of  $T_2^*$  reaching hundreds of microseconds at room temperature [101].

### Initial demonstrations

C degen et al. demonstrated the magnetometry scheme [102] in 2008. While some other studies were also done during the same time analysing the sensitivity and usability of DC sensing for various applications [72, 103–105].

#### 1.3.3 AC sensing: NV centres

In addition to DC sensing, NV centres in diamonds can also be utilised for AC sensing. AC sensing with NV centres involves detecting and measuring high-frequency oscillating magnetic fields, typically in the MHz range. With applications ranging from fundamental studies to material science [106] to biology [95]. Usually, an AC sensing measurement is performed via the spin echo protocol, as depicted in Fig. 1.9, where the use of an additional  $\pi$  pulse cancels out the phase accumulation due to slow varying and static inhomogeneities in the environment, which

leads to sensitive detection of the oscillating signals. The advantage of using spin echo for AC sensing with NV centres is that it can reduce the effect of decoherence by using the  $\pi$  pulse to cancel the effect of the surrounding environment leading to longer coherence time  $T_2$  and more precise measurements of the AC magnetic field. Like the Ramsey interferometry, we can use the accumulated phase during the free precession time to find the unknown field  $B_{ac}$ . Additionally, for NVs with the presence of nearby carbon-13 isotope, collapses and revivals of NV spin coherence can be observed in the spin echo signal [107, 108] for an AC field of frequency given as:

$$(1.4) \quad f_{ac} = \frac{1}{\tau} = \frac{\gamma_{^{13}\text{C}} B_o}{2l}$$

here nuclear gyromagnetic ratio is represented by  $\gamma_{^{13}\text{C}}$ , ac field magnitude by  $B_{ac}$ . While  $l$  is an integer.

### Sensitivity

Similar to the case of Ramsey measurement, the sensitivity of an AC quantum sensor is dependent on the decoherence time  $T_2$ , with the optimum sensitivity achieved for  $\tau \sim T_2$  [72]:

$$(1.5) \quad \eta_{echo} \sim \frac{\pi \hbar}{2g\mu_B} e^{(\tau/T_2)^N} \frac{\sqrt{\tau + t_0}}{C\tau}$$

here the decay factor  $N$  can vary from  $N = 1$  to 4 [109] (see Sec. 4.2.1 for more details).

### Initial demonstration

Experimentally, Maze et al. used a spin echo-based NV magnetometer for the first time to demonstrate the feasibility and operation of such a device [110]. Since then, it has been applied to many applications in the field of physics and biology. With a huge amount of work focused on improving the sensitivity by improving the photon collection efficiency [111–114], improving coherence time via material engineering [103], getting better measurement contrast [115], and by using more complex measurement sequences [116, 117]. For a high-purity sample,  $T_2$  coherence time is usually around  $\sim 500 \mu\text{s}$ ; a value of  $\sim 2 \text{ ms}$  is reported for a high-purity isotropically purified sample [103].

## 1.4 Spin-based quantum technology in Silicon carbide (SiC)

Diamond is an excellent material for spin-based quantum technology due to its wide bandgap, diluted nuclear-spin bath and weak spin-orbit coupling. The ability to grow highly purified

samples, combined with isotope engineering, can further enhance already long spin coherence times [118]. The NV centre in diamond is currently the platform of choice for optical spin qubits, both for quantum sensing [98] and quantum networking applications [119]. In parallel, many groups are exploring other colour centres in diamond, such as silicon-vacancy (SiV) [120] or Germanium vacancy (GeV) [121], whose spin-photon interface exhibits superior robustness due to insensitivity to the electric field given by their symmetry structure [122].

Despite its excellent properties, the diamond remains a difficult material to scale, integrate and fabricate on a large scale. The NV centre, in particular, presents several challenges for further advances towards quantum networks:

1. only 3-4% of the optical emission goes to the zero phonon line (ZPL) [123]. Only this emission is coherent and hence can be used for photon-based entanglement-swapping as the phonon involvement in non-ZPL emission leads to dephasing very quickly [124]. This drastically reduces the success rate for measurement-based entanglement protocols. This problem could be addressed by embedding the NV centre in a cavity and exploiting a strong Purcell effect to transfer most of the emission into the ZPL [124, 125].
2. ZPL emission at 637 nm is very lossy when propagated through an optical fibre. Though conversion to the telecom range is possible [36, 126], it adds noise. Hence direct emission in the telecom range would be preferable [127].
3. the spin-selective atomic-like optical transitions employed for interfacing spin with photons are strongly affected by electric noise, resulting in random spectral jumps [128]. This effect is even more pronounced when the NV centre is close to a surface or the nanofabricated regions [129], for example, in optical cavities, due to the higher concentration of defects, impurities and dangling bonds that induce electric noise. This has made the demonstration of a cavity-enhanced spin-photon interface very challenging, and no group has been able to demonstrate this for an NV centre, despite a couple of decades of work in this field.
4. diamond is notoriously hard to grow, dope and fabricate, hindering its applicability for scalable quantum devices compatible with industrial production processes [130].

Silicon carbide (SiC) is an alternative platform which has been in use for various applications. There are more than 200 polytypes of SiC available in nature, and all of them have band gaps of around 2-3 eV [131]. It is typically grown by the chemical vapour deposition (CVD) process. Our collaborators at the University of Linköping in Sweden have pushed material purity down to the impurity concentration level of  $\sim 10^{13} \text{ cm}^{-3}$ , resulting in excellent spectral stability of the spin-photon interface [132]. Improving material purity and quality has led to fewer surface and morphological defects and fewer carbon vacancies. This means that the point defects within the deep bandgap (also referred to as colour centres), which were previously investigated as ensembles, can now be studied individually. SiC also boasts the advantage of mature production

protocols that are available for silicon on a large scale and excellent nanofabrication quality [133]. However, certain challenges still remain in fabricating materials for integrated photonics and in the control and generation of colour centres [134]. According to a study [135], SiC can have many optically active colour centres with quantum properties. These defects mainly originate from vacancies of either C or Si and are typically associated with substitutional impurities like transition metals (TM), transition metal oxides (V, Cr, Ti, Er, Mo, etc.), and the most common nitrogen impurities.

SiC is an established material for electronics, with heavy investments by the semiconductor industry over the last 20 years [136], which have resulted in high-quality single-crystal wafers [137, 138]. SiC is currently one of the leading power electronics platforms, particularly for harsh environments [139]. SiC is also a good candidate for high-temperature electronic applications [140]. In addition to high-power electronics [141], it is also a promising material due to its 10-fold higher breakdown voltage and three-fold higher thermal conductivity than Si [131, 140]. SiC has also been exploited in the field of microelectromechanical systems (MEMS) [142] and in metal-oxide-semiconductor field-effect transistors (MOSFETs) [143].

While not yet extensively developed for photonics applications, SiC exhibits quite good linear and nonlinear optical properties. Apart from its second-order nonlinear dielectric properties and optical transparency, it has extensive application in photonic devices, serving as waveguides and components in photonic circuits such as photonic crystals and micro-ring resonators [144] since the early 1990s, and in optoelectronics, [145]. Applications for SiC have been found in the field of optical sensors [146] such as for ultraviolet light, x-rays, and gas sensors.

In the past decade, silicon carbide (SiC) has been attracting more and more interest as an alternative platform for spin-based quantum technology. The implementation of quantum technology depends heavily on reliable manufacturing and optical and spin stability at a single defect level, which is why SiC is among the leading light-matter quantum interfaces available, competing well with atomically thin semiconductors and diamond for this position. A lot of attention is currently focused on single-photon emitters in SiC with proven spin-photon interface capability for quantum photonic applications [147]. SiC is a very exciting material for quantum devices [148], since it is possible to envisage electrically controlled quantum devices to detect spin signals and the excitation of single-photons [132, 149–151]. As a result of its optical transparency, low two-photon absorption, and second-order nonlinearity, SiC offers a good platform for integrated quantum photonics [138]; however, its integration with optically controlled devices is at a very early stage of development.

### 1.4.1 Key quantum emitters in SiC

SiC hosts a number of point defects potentially useful for quantum technology (see, for example, S. Castelletto et al. [152] and Table. 1.1 for a review).

The silicon vacancy ( $V_{Si}^-$ ) [153], formed at the site of a missing silicon atom, is one of the most



widely studied and well-known defects in silicon carbide (SiC).  $V_{Si}^-$  features zero-phonon lines (ZPLs) at 861.6 nm and 916.5 nm for V1 and V2 centres and a spin  $S = 3/2$ . In 4H-SiC  $V_{Si}^-$ , the V1 centre has about 8% of the emission in ZPL at 4K [154] with spin coherence times reaching milliseconds [155, 156]. The spectral stability of the silicon vacancy ( $V_{Si}^-$ ) in SiC is quite high [157]. This is a desirable property for many applications, as it ensures that the defect's emission wavelength remains stable and predictable. Studies have shown that silicon-vacancy ( $V_{Si}^-$ ) in SiC can be controlled with high fidelity and does not suffer from rapid spin dephasing and strong electron-phonon interaction [157–159]. In order to achieve system scalability for large-scale quantum networks, it is necessary to integrate efficient spin-photon interfaces into nanophotonic structures. Unfortunately, the majority of colour centre platforms have not yet reached their potential due to the degradation of spin-optical coherence that typically occurs after integration in these structures. A study has been done exhibiting the successful implantation of silicon vacancy centres ( $V_{Si}$ ) in SiC while preserving their inherent spin-optical properties [160]. The study reveals that single defects implanted both in bulk material and in nanophotonic waveguides made via reactive ion etching exhibit long spin-coherence times and nearly lifetime-limited photon emission. See Table 1.3 for details on magneto-optical properties of  $V_{Si}$ .

The divacancy ( $V_{Si}V_C^0$ ) is another more commonly known defect [161] with ZPLs in the region from 1078-1132 nm in 4H-SiC [162]. The divacancy ( $V_{Si}V_C^0$ ) consists of a pair of silicon and carbon neighbouring vacancies. Its electronic structure ( $C3v$  symmetry and spin  $S = 1$ ) is identical to the NV centre in diamond [163], facilitating the extension of protocols originally developed for the NV centre. Important results demonstrated on the divacancy include spin coherence time of up to 5 s [164, 165] and the integration in microelectronic devices to reduce electrical noise and stabilise the spin-photon interface [166, 167]. See Table 1.2 for details on magneto-optical properties of  $V_{Si}V_C^0$ .

A promising yet less explored group of defects correspond to transition metal impurities in SiC, e.g. chromium (Cr<sup>4+</sup>), molybdenum (Mo<sup>5+</sup>), tungsten (W<sup>5+</sup>), erbium (Er<sup>3+</sup>) as well as vanadium (V<sup>4+</sup>). This thesis (Chap. 6) focuses on the optical and electronic study of vanadium due to its direct emission at telecom wavelengths, as discussed below.

### 1.4.2 Why vanadium?

Recent studies have indicated the potential of transition metals in SiC, such as chromium (Cr), molybdenum (Mo), and vanadium (V), for spin-based quantum technology [162, 172, 173]. Vanadium dopants in SiC have been studied quite extensively as compensation impurities due to their amphoteric nature [174]. The first optical study conducted at temperatures of  $\geq 77$  K in an ensemble showed strong luminescence lines with narrow ESR features having a linewidth less than 2 G [175]. Based on the linewidth, the spin coherence lifetime corresponds to several tens of nanoseconds, thus allowing coherent manipulation of spins. Moreover, it has been shown that the defect contains multiple charge states [176], a property that is of interest for spin-to-

Colour centres	ZPLs (pm)	Spin	ZFS (GHz)	DWF(%)	Single photon saturation counts (kcps)	Optical transition lifetime (ns)	Electron spin coherence time (ms)
$V_{Si}$ (4H-SiC)	0.862 (V1), 0.858 (V1'), 0.917 (V2)	3/2	0.070 (V2), 0.004(V1 )	40 (V1)	8-10 (V2), 12 (V1), 4 (V1')	6.2 (V2), 5.5 (V1), 5.6 (V1')	0.6 (V1), 20 (V2)
DV (4H-SiC)	1.078, 1.108, 1.131, 1.132	1	1.334, 1.224, 1.305, 1.336	5	27	14	
DV(3C-SiC)	1.127	1	1.3	7	26	18.7	0.9
3 C unknown	1085-1225	unknown			900	0.81	
$CAV^{(+)}$ (4H-SiC)	0.6487, 0.6518, 0.6651, 0.6685, 0.6717, 0.673, 0.6752, 0.6765	1/2			2000	1.8	
DI (4H-SiC)	0.540-0.689	1/2			900	2-5	
Oxidation annealing related	0.564-0.69			33	2000	2.0-2.2	
$N_C V_{Si}$ (4H-SiC)	1.180, 1.223, 1.241, 1.242	1	1.193, 1.282, 1.328, 1.331		17.4	2.7	0.001 ( $T_2^*$ )
Ti	0.433, 0.435, 0.44, 0.45	1	10-11				
$Cr^{2+}$	1.033-1.127	2	39				
$Cr^{3+}$	Unknown	3/2	>40				
$Cr^{4+}$	1.142-1.181	1	1-6.7	75		135 000	0.000 0370
$V^{3+}$	2	1	7-11				
$V^{4+}$ (SiC-4H)	1.279, 1.335	1/2	529-43	<25, <50		167, 45	0.0002- 0.0012
$V^{4+}$ (SiC-6H)	1.309, 1352, 1389	1/2	524, 25, 16	<45, <40, <40		108, 11, 31	
Mo (SiC-4H)	1.076, 1.121	1/2	3.3			60	0.0003( $T_2^*$ )

Table 1.1: A summary of colour centres in SiC based on their Zero Phonon Line (ZPL), spin, Zero Field Splitting (ZFS), Debye-Waller factor (DWF), saturation count rate, lifetime, and spin coherence time. Table adapted from [159].

charge conversion and protection of nuclear spin memory [177–179]. Vanadium is particularly appealing given its optical emission in the telecom O-band (1278 to 1388 nm) [175, 179–181] (see the spectrum of vanadium in Fig. 1.13(a)), making it a perfect match for the SMF-28 fibres commercially used for telecommunications applications [182]. While fibre propagation at 1300nm is only slightly more lossy than at 1550nm ( $\sim 0.1$  dB/km more), standard SMF-28 telecom fibres are single mode for both wavelength regions. This opens the possibility to utilise the O-band for the quantum channel and the C-band for the classical channel, avoiding problems of over-crowding and cross-talk. The O-band is quite popular in quantum key distribution implementations, for example, in quantum devices by Toshiba [179, 183].

Additionally, studies on vanadium ensembles at cryogenic temperatures have shown that spin-relaxation times ( $T_1$ ) can reach up to 25 s [185]. The coherent spin dynamics of an ensemble of vanadium defects have also been investigated in relation to clock transition, both in isolation and in conjunction with adjacent nuclear spins [184] (see Fig. 1.13(b)). The findings indicate spin

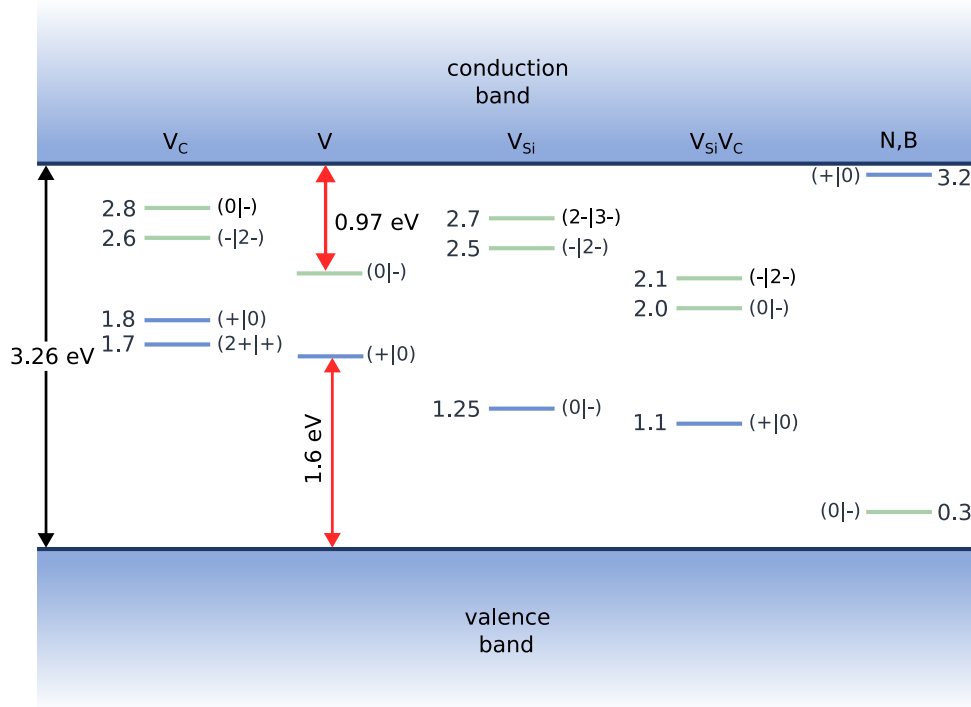


FIGURE 1.11. **Energy levels of defects in SiC.** Energy levels corresponding to various charge states of  $V_C$ ,  $V$ ,  $V_{Si}$ , and  $V_{Si}V_C$  in 4H-SiC are presented. All energy values are given in electronvolts (eV) and are referenced to the valence band unless otherwise specified. The bandgap of 4H-SiC is taken as 3.26 eV. N and B are for nitrogen and boron shallow dopants [168].

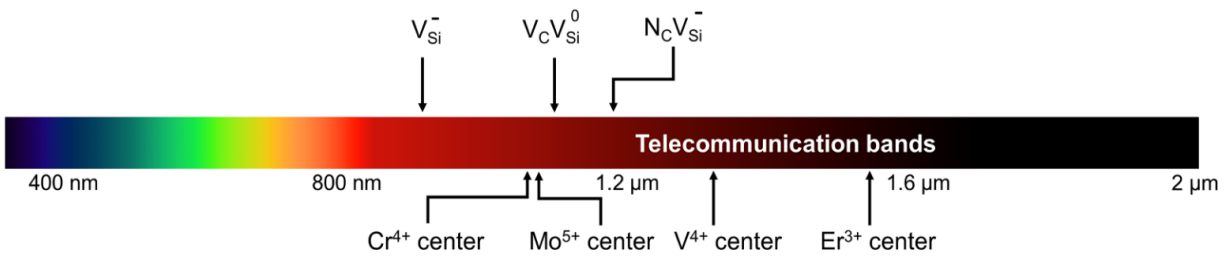


FIGURE 1.12. Emission wavelength of various colour centres in 4H-SiC. Figure adapted from [158].

dephasing times that extend up to  $7.2 \mu\text{s}$  and coherence lifetimes exceeding tens of microseconds. By identifying operational points where the coupling to neighbouring nuclear spins does not impair the coherence of the central vanadium spin, the potential for vanadium as a reliable, coherent spin register has been demonstrated.

Hence combined with SiC's properties as a well-established material for industrial-scale growth, doping and fabrication, along with equally promising linear and nonlinear parameters

	PL line	ID	Orientation	ZPL (eV)	ZPL (nm)	ODMR1 (GHz)	ODMR2 (GHz)	D (GHz)	E (MHz)	room T?
4H	PL1	(hh) divacancy	c-axis	1.095	1132.3	1.336		1.336	<1	
	PL2	(kk) divacancy	c-axis	1.096	1131.2	1.305		1.305	<1	no
	PL3	basal divacancy	basal	1.119	1108.0	1.140	1.304	1.222	82	yes
	PL4	basal divacancy (kh)	basal	1.150	1078.1	1.316	1.353	1.334	18.7	no
	PL5	?	c-axis	1.189	1042.8	1.356	1.389	1.373	16.5	yes
	PL6	?	basal	1.194	1038.4	1.365		1.365	<1	yes
	PL7	?	basal			1.333				yes
6H	QL1	?	c-axis	1.088	1139.6	1.300		1.300	<2	no
	QL2	?	c-axis	1.092	1135.4	1.334		1.334	<2	yes
	QL3	?	basal	1.103	1124.1	1.228	1.243	1.236	7.5	yes
	QL4	?	basal	1.119	1108	1.208	1.425	1.317	109	no
	QL5	?	basal	1.134	1093.3	1.340				yes
	QL6	?	c-axis	1.134	1093.3	1.347		1.347	<5	no
	QL7	?	c-axis			1.345		1.345	<5	yes
	QL8	?	c-axis			1.371		1.371	<5	yes
	QL9	?	basal			1.332	1.365	1.349	17	yes

Table 1.2: **Data on the magneto-optical properties of divacancy configurations in 4H and 6H-SiC.** The optical energies of the observed defects with their ODMR lines and orientations. Although the association is not definitively established, the transition energies of QL1-QL6 in 6H-SiC, as measured by photoluminescence (PL) and optically-detected magnetic resonance (ODMR), appear to be comparable to those of the neutral divacancies (PL1-PL4) in 4H-SiC, indicating a potential connection. Table adapted from [169].

	PL line	ID	Orientation	ZPL (eV)	ZPL (nm)	ZFS (MHz)
4H	V1	Si vacancy (h)	c-axis	1.44	861.0	2.6
	V1'	Si vacancy (h)	c-axis	1.445	858.0	2.6
	V2	Si vacancy (k)	c-axis	1.352	917.0	35
6H	V1	Si vacancy	c-axis	1.433	862.5	28
	V1'	Si vacancy	c-axis	1.434	864.6	28
	V2	Si vacancy	c-axis	1.398	886.9	128
	V3	Si vacancy	c-axis	1.368	906.3	28

Table 1.3: Data on the magneto-optical properties and configuration of Si vacancy configurations in 4H and 6H-SiC. Data adapted from [170, 171].

for photonics applications [159, 186] having a defect with good optical and charge state properties in SiC is highly desirable. Which is the topic of research in Chap. 6 of this thesis.

## 1.5 PhD thesis outline

This thesis presents original work on quantum spintronics, with the development of characterisation tools for quantum systems and the investigation of a novel spin system in SiC.

After this introductory Chap., I will review in Chap. 2 some elements of statistical learning, such as Fisher information, Bayesian experimental design and sequential Montecarlo methods, required to understand the experiments on the adaptive characterisation of quantum systems in Chap. 4 and 5. In Chap. 3, I will discuss in detail the experimental setup that I designed and constructed during the course of my PhD. I chose to give a very detailed overview of the setup, as I hope it will be helpful as an introduction for future group members willing to use it for their research.

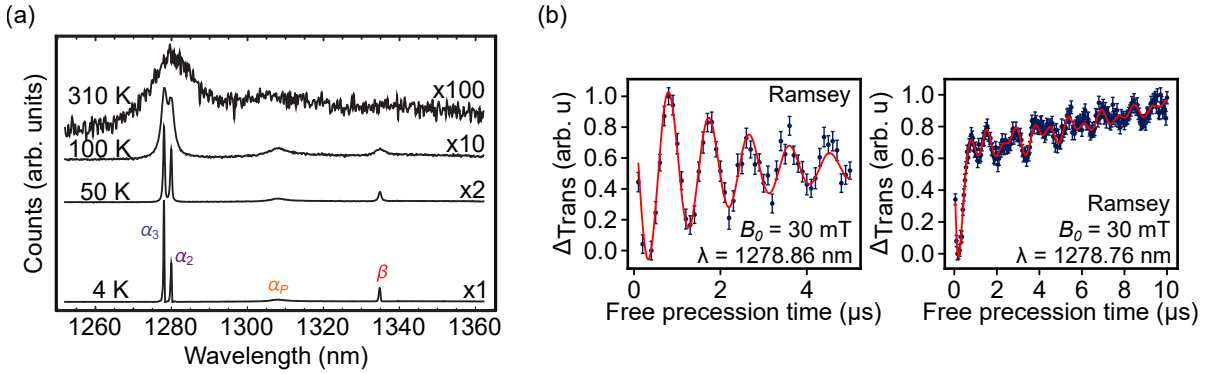


**FIGURE 1.13. Emission spectra of vanadium and coherent spin dynamics of vanadium ensemble.** (a) The fluorescence spectral analysis revealed three distinct lines for  $V^{4+}$  at low temperatures. Specifically, a doublet at the wavelengths of 1278.0 and 1279.9 nm (referred to as  $\alpha_3$  and  $\alpha_2$ , respectively) and a smaller feature at 1334 nm (referred to as  $\beta$ ). The doublet was associated with the hexagonal site, while the single line was linked to the quasi-cubic site located in 4H-SiC. Figure adapted from [173]. (b) Display the outcomes of the Ramsey interferometry conducted at the clock transition (30 mT) probed with optical wavelengths ( $\lambda = 1278.86$  nm and  $\lambda = 1278.76$  nm). At short wavelength ( $\lambda = 1278.76$  nm), strong 9.7 MHz coupling between the vanadium spin system and adjacent  $^{29}\text{Si}$  nuclear spin is present. Figure adapted from [184].

Chap. 4 presents experimental results related to the adaptive estimation of decoherence timescales (single and multiparameter estimation), showing how a self-optimised approach can give a quite large measurement speed up even in the case of simple sequences. In Chap. 5, I describe an adaptive frequency estimation scheme designed to optimally measure static magnetic fields using a quantum sensor. Further, Chap. 6 presents an experimental study of the optical and charge state properties of a novel quantum system in SiC related to single vanadium impurities, appealing for its emission in the telecom O-band. Finally, I will present an outlook on future steps in this research field (Chap. 7).

### 1.5.1 My contribution

My contribution to the work presented in this thesis can be summarised as follows. I have designed, built and tested a confocal microscope setup (discussed in Chap 3) for experiments on adaptive quantum sensing. This setup includes a unique adaptive control system comprising a microcontroller and a real-time programmable arbitrary waveform generator (AWG). This system can update the probability distribution for the physical quantity being estimated and compute optimal experimental settings in about 100  $\mu\text{s}$ : to the best of my knowledge, this is the fastest adaptive Bayesian estimation system in the literature. Dr Christiaan Bekker has further contributed to designing and testing adaptive electronics.

Using this unique setup, I have performed measurements about the adaptive estimation of

decoherence and static magnetic fields in collaboration with Dr Ben Haylock (a post-doc in our group).

The cryogenic setup utilised for the studies on single vanadium impurities in SiC has been constructed by Dr Daniel White (former PhD in our group), with some help from myself and Dr Pasquale Cilibrizzi (post-doc). My main technical contribution has been designing and implementing optical pulsing by an acousto-optic modulator and the microwave chain for spin control. The results discussed in Chap. 6 were taken in collaboration with Dr Pasquale Cilibrizzi. The main highlight of this work was the demonstration of an extremely narrow inhomogeneous distribution ( $\sim 100$  MHz) of optical emission for vanadium impurities in isotopically-purified SiC. To the best of our knowledge, this is the smallest value reported in the literature for a single emitter: a very important result, as photon indistinguishability is a crucial prerequisite to demonstrate remote entanglement.

Both projects have been carried out within the Quantum Photonics Laboratory at Heriot-Watt University (Edinburgh, UK) under the supervision of Prof. Cristian Bonato. We have enjoyed several international collaborations for both works on adaptive sensing and SiC quantum spintronics. We have collaborated with the Quantum-Enhanced Sensing Techniques group headed by Dr Amit Finkler at Weizmann Institute of Science, Israel, on adaptive sensing, carrying out parallel work in the two labs. Our work on SiC has been funded by the European project QuanTELCO, enabling a fruitful collaboration with Michael Trupke (Vienna), Nguyen Tien Son and Ivan Ivanov (Linköping), and Benedikt Tissot and Guido Burkard (Konstanz).

### **1.5.2 Impact of COVID19**

The COVID-19 pandemic has had a significant impact on my PhD work. I started my PhD in October 2019 with the goal of setting up a completely new experimental setup from scratch. The university was completely shut down for 5 months starting in March 2020, just when the first components had arrived and I was starting to assemble the setup. With input from my supervisor, I adapted to new ways of working and started doing research from home. My laboratory work was replaced with computer simulations and data analysis. While this was useful for planning future experiments, it caused more serious delays for me than for other students as I could not run any measurements remotely or analyse data previously taken. I also missed the excitement of building experiments and discovering new things in the lab.

Eventually, the university reopened its research labs, but this came with new challenges, such as strict safety protocols, including wearing personal protective equipment (PPE) at all times, maintaining social distancing, and sanitising the lab equipment. Another challenge was related to the availability of resources. Due to the pandemic, the supply chain was disrupted, and there was a struggle to get the necessary equipment in a timely manner. This was particularly severe for researchers like myself, who were building a lab from scratch. This led to delays in experiments and hindered the progress of my research. Finally, the pandemic had a toll on my mental health

as I struggled to cope with the fear of contracting the virus and subsequent isolation. Despite these challenges, I managed stress and maintained motivation to continue my research. With perseverance, I made progress in research, even if at a slower pace than before the pandemic.





## BAYESIAN INFERENCE

## 2.1 Introduction

Here I will describe the basics of statistical learning and Bayesian inference, which form a prerequisite for the work in chapters 4 and 5.

Bayesian inference is an approach to data processing based on Bayes' theorem. In this framework, parameter estimation is based on the information contained within observed data, and the available data is used to update the parameters in the statistical model. The prior distribution encapsulates the background knowledge and is combined with observed data through a likelihood function based on a statistical model to determine the posterior distribution.

### 2.1.1 Bayesian inference

Bayesian inference is one of the most frequently used statistical methods to update the degree of belief in a hypothesis based on new evidence. This idea is based on Bayes' theorem, given as:

$$(2.1) \quad P(\theta|x) = \frac{P(x|\theta)P(\theta)}{P(x)}$$

Or, in some cases, simplified to:

$$(2.2) \quad P(\theta|x) \propto P(x|\theta)P(\theta)$$

here  $\theta$  is the unknown parameter, while  $x$  is a new observation (e.g. a series of measurement outcomes  $x = \{x_1, x_2, \dots, x_n\}$ ). The term  $P(\theta|x)$  shows the conditional probability of estimating the unknown  $\theta$  based on the observation  $x$ , also commonly known as **posterior distribution**.  $P(x|\theta)$  gives the conditional probability of getting observation  $x$  for the model parameter  $\theta$ , this is known

as **likelihood function**. While the term  $P(\theta)$  highlights the probability of unknown parameter  $\theta$  existing in the search range, hence termed as **prior distribution**. The last term,  $P(x)$ , is the normalisation factor.

For a sequence of independent measurement results ( $x$ ), the Bayes rule can also be applied recursively, as illustrated in Fig. 2.1. At each instant, the current knowledge about the unknown parameter  $\theta$  can be utilised to choose the optimal parameters for the next measurement. And for the case where the optimal settings depend on the unknown parameter  $\theta$ , the adaptive techniques, such as those discussed in Chap. 4 and Chap. 5 can significantly improve performance and enhance the estimation protocol's sensitivity. Another advantage of using the Bayesian inference is the ability to integrate optimisation techniques [187, 188].

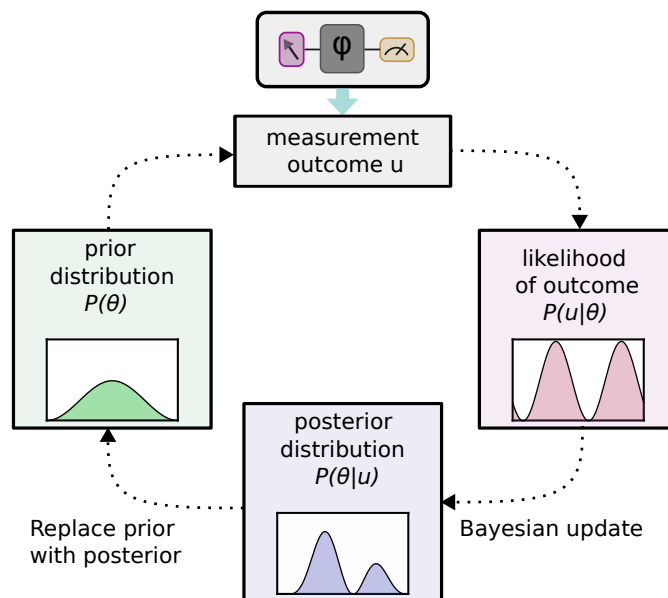


FIGURE 2.1. **Bayes inference for parameter estimation.** The learning process involved in Bayes' inference. Where after each measurement event prior is updated using the likelihood function to result in an updated posterior. This posterior probability distribution is then used to extract the optimal settings and serves as a new prior for the next measurement, and the cycle continues until the final estimate of the unknown parameter.

Though this theorem is pretty straightforward to apply, caution must be taken when deciding the prior of each problem as results highly depend on how one parametrises the problem. Usually, uniform prior distribution may seem reasonable to start off when no information is available. However, it is not always an informative prior and may lead to the wrong posterior (for more information, see discussion in Sec. 3.2 of [189]). As an alternative, Jeffreys et al. proposed a prior based on Fisher information which is parameterisation-invariant [190], meaning it leads to the same posterior regardless of how one models the problem.

## 2.2 Introduction to estimation theory

Typically, the parameter estimation problem entails determining the best estimate of a parameter based on a sample of data obtained according to its probability distribution. One natural question to ask is how much information can be obtained about an unknown parameter from a sample of data. We can use this information measure to determine the bounds on the variance of the estimation. If the sample size is sufficiently large, this method can obtain an approximate confidence interval.

### 2.2.1 Fisher information $F$

In statistics, Fisher information refers to the amount of information a random variable  $X$  conveys about one or more unknown distribution parameters modelled by that variable  $X$ . Formally the Fisher information ( $F_X(\theta)$ ) contained in a variable  $X$  for an unknown parameter  $\theta$  is defined as [189]:

$$(2.3) \quad F_X(\theta) = \begin{cases} \sum_{x \in X} \left( \frac{\partial}{\partial \theta} \log f(x|\theta) \right)^2 f(x|\theta) & \text{if } X \text{ is discrete,} \\ \int_X \left( \frac{\partial}{\partial \theta} \log f(x|\theta) \right)^2 f(x|\theta) dx & \text{if } X \text{ is continuous.} \end{cases}$$

here the term  $\frac{\partial}{\partial \theta} \log f(x|\theta)$ , describes how sensitive is  $f$  (model function) to any variations in  $\theta$  for any particular value of  $\theta$ . So in a mathematical sense, the Fisher information ( $F_X(\theta)$ ) describes how sensitive the functional relationship between  $f$  and  $\theta$  is. It does that by weighing the sensitivity at each potential outcome  $x$  in relation to the probability  $f(x|\theta)$ , which implies that the Fisher information ( $F_X(\theta)$ ) is an expectation about the unknown  $\theta$ .

Suppose there is more than one parameter, namely  $N$  parameters corresponding to parameter vector  $\theta = [\theta_1, \theta_2, \dots, \theta_N]$ . In that case, we can generalise the Fisher information ( $F_X(\theta)$ ) in the form of a positive semi-definite matrix with  $N \times N$  dimensions with  $i^{th}$  row and  $j^{th}$  column as [189]:

$$(2.4) \quad F_X(\theta)_{i,j} = \begin{cases} \sum_{x \in X} \left( \frac{\partial}{\partial \theta_i} \log f(x|\theta), \frac{\partial}{\partial \theta_j} \log f(x|\theta) \right) f(x|\theta) & \text{if } X \text{ is discrete,} \\ \int_{x \in X} \left( \frac{\partial}{\partial \theta_i} \log f(x|\theta), \frac{\partial}{\partial \theta_j} \log f(x|\theta) \right) f(x|\theta) dx & \text{if } X \text{ is continuous.} \end{cases}$$

where under mild regularity condition the Fisher information matrix can also be written as:

$$(2.5) \quad F_X(\theta)_{i,j} = \begin{cases} -\sum_{x \in X} \left( \frac{\partial}{\partial \theta_i} \frac{\partial}{\partial \theta_j} \log f(x|\theta) \right) f(x|\theta) & \text{if } X \text{ is discrete,} \\ -\int_{x \in X} \left( \frac{\partial}{\partial \theta_i} \frac{\partial}{\partial \theta_j} \log f(x|\theta) \right) f(x|\theta) dx & \text{if } X \text{ is continuous.} \end{cases}$$

In this case of multiparameter estimation, the  $N \times N$  dimension covariance matrix of the estimator is bounded by the inverse of the Fisher information matrix (FIM) [191, 192]. While in the case of multi-parameter estimation, due to the non-commutativity of the optimal measurements [191, 192], no optimal observable can saturate the quantum Cramér-Rao bound. Hence in such a case, a more involved Holevo-Cramér-Rao bound should be used [193].

### 2.2.1.1 Quantum Fisher information $\mathcal{F}$

Following from Eqn. 2.3, a quantum analogue of the Fisher information ( $F$ ) can be found. Which is a measure of the maximum possible sensitivity of a quantum system to a parameter of interest and bounds the ultimate precision of estimation [194]. It can be written as [195]:

$$(2.6) \quad \mathcal{F}(\theta) = \text{Tr}(\rho_\theta L_\theta^2) = \text{Tr}\left[\left(\frac{\partial}{\partial \theta} \rho_\theta\right) L_\theta\right]$$

here  $L_\theta$  is the symmetric logarithmic derivative (SLD) operator. And by diagonalising the density matrix as  $\rho_\theta = \sum \lambda |\psi_i\rangle \langle \psi_i|$  with  $\lambda_i \geq 0$  and  $\sum_i \lambda_i = 1$ , Eqn. 2.6 can be rewritten as [195]:

$$(2.7) \quad \mathcal{F} = \sum_{i'} \frac{1}{\lambda_{i'}} \left(\frac{\partial \lambda_{i'}}{\partial \theta}\right)^2 + 2 \sum_{i \neq j} \frac{(\lambda_i - \lambda_j)^2}{\lambda_i + \lambda_j} |\langle \psi_i | \partial_\theta \psi_j \rangle|^2$$

here  $\partial_\theta \equiv \frac{\partial}{\partial \theta}$ , with the first term representing the classical Fisher information  $F(\theta)$ , while the second term is the quantum Fisher information  $\mathcal{F}(\theta)$ . Meanwhile, for the case of 2-dimensional density matrices, the formula for quantum Fisher information is given as [196]:

$$(2.8) \quad \mathcal{F}_\theta = \text{Tr}(\partial_\theta \rho)^2 + \frac{1}{\det \rho} \text{Tr}(\rho \partial_\theta \rho)^2$$

For a case where the  $F(\theta) = \mathcal{F}(\theta)$ , the measurement is said to be optimal.

### 2.2.1.2 Fisher information $F$ and Cramér-Rao bound

As stated above, the Fisher information's role is to measure the "intrinsic accuracy" of an estimation protocol. Considering a family of quantum states  $\rho_\theta$  as a function of the unknown parameter  $\theta$ . For the adaptive studies discussed in this thesis, the goal is to estimate this unknown parameter  $\theta$ . For this, as will be mentioned in more detail in upcoming chapters, our strategy is to do repeated estimations on the system to generate a sample of results leading to an estimator  $\hat{\theta} = \hat{\theta}(x_1, x_2, \dots, x_n)$ , here  $x_i$  is a measurement result. Where the corresponding mean-squared error (MSE) can be given as  $V(\hat{\theta})$ . We know from the basic understanding of statistics that an estimator is more accurate if the  $V(\hat{\theta})$  is smaller since the  $V(\hat{\theta})$  is the measure of the estimate's accuracy.

In reality, however, any unbiased estimator is bounded by the lowest achievable limit to accuracy; such a lower bound is known as Cramér-Rao lower bound (CRLB), given in Eqn. 2.9. Where an unbiased estimator is the one for which the expected value is the true value (see Eqn. 2.10).

$$(2.9) \quad V(\hat{\theta}) \geq \frac{1}{NF(\theta)}$$

here total number of measurements and Fisher information is represented by  $N$ , and  $F(\theta)$  respectively. This relationship specifies that the minimum variance of an unbiased estimator is determined by the reciprocal of the Fisher information. An unbiased estimator  $\hat{\theta}(X)$  mathematically means that:

$$(2.10) \quad E[\hat{\theta}(X) - \theta | \theta] = \int (\hat{\theta}(x) - \theta) f(x|\theta) dx = 0$$

regardless of  $\theta$  value. Since this expression is 0 and independent of  $\theta$ . The partial derivative of it with respect to  $\theta$  must also be 0. Hence by taking the partial derivative of Eqn. 2.10 with respect to  $\theta$ , we get:

$$(2.11) \quad \frac{\partial}{\partial \theta} \int (\hat{\theta}(x) - \theta) f(x|\theta) dx = \int (\hat{\theta}(x) - \theta) \frac{\partial f}{\partial \theta} dx - \int f dx = 0$$

where  $\int f dx = 1$  since the likelihood function is a probability density function for each  $\theta$ . Taking a partial derivative of  $\log f$  combined with the chain rule, one can get that:

$$(2.12) \quad \frac{\partial f}{\partial \theta} = f \frac{\partial \log f}{\partial \theta}$$

substituting this in Eqn. 2.11 we get:

$$(2.13) \quad \int (\hat{\theta}(x) - \theta) f \frac{\partial \log f}{\partial \theta} dx = 0$$

Factoring the equation above and squaring it via the Cauchy-Schwarz inequality gives:

$$(2.14) \quad 1 = \left( \int [(\hat{\theta}(x) - \theta) \sqrt{f}] \cdot \left[ \sqrt{f} \frac{\partial \log f}{\partial \theta} \right] dx \right)^2 \leq \left[ \int (\hat{\theta}(x) - \theta)^2 f dx \right] \cdot \left[ \int \left( \frac{\partial \log f}{\partial \theta} \right)^2 f dx \right]$$

$$(2.15) \quad 1 \leq \left[ \int (\hat{\theta}(x) - \theta)^2 f dx \right] \cdot \left[ \int \left( \frac{\partial \log f}{\partial \theta} \right)^2 f dx \right]$$

here the first term in brackets is the mean-squared error (MSE) of the estimator  $\hat{\theta}$ , while the second term is the Fisher information  $F(\theta)$ . By rearranging the terms, we get the relation mentioned in Eqn. 2.9.

## 2.3 Bayesian experimental design

In this section, I will describe the sequential Bayesian experimental design scheme, which is usually employed in parameter estimation to adaptively optimise the control settings with

respect to some statistical criterion related to the variance matrix of the estimator, such that each measurement run gives the maximum information about the unknown parameter. Suppose we performed a measurement with some control settings  $C = \{c_1, c_2, \dots, c_n\}$  and obtained the outcomes  $x = \{x_1, x_2, \dots, x_n\}$ . The corresponding likelihood function is given by:

$$(2.16) \quad P(x|\theta; C) = \prod_{k=1}^n P(x_k|\theta; c_k)$$

An idea for sequential Bayesian estimation is to adaptively select the control parameters  $c$  for the next estimation cycle from the last one. Hence we write the probability of obtaining future outcome  $x_{n+1}$  with the experimental control settings  $c_{n+1}$  by marginalizing the current probability over the model parameters as:

$$(2.17) \quad P(x_{n+1}|\theta; c_{n+1}, C) = \int P(x_{n+1}|\theta; c_{n+1})P(\theta|x; C)dx = \mathbb{E}_{\theta|x; C}[P(x_{n+1}|\theta; c_{n+1})]$$

where  $\mathbb{E}$  is the expectation taken over the mentioned variable. This expectation value can inform the algorithm about the choice of settings more useful than others; this usefulness is quantified via a utility function which, as described previously, is the information gain or Fisher information. Each successive iteration finds the settings which will give the most information about the unknown estimator.

In the case of multiparameter estimation, the variance of the parameter-estimator vector is a matrix (see Sec. 2.2.1). Therefore, it is unclear how it can be “maximised” to minimise variance. Statisticians devised a set of “information criteria”, based on the information matrix, that can be minimised or maximised; for example, [197]:

1. **A-optimality:** A common approach for experimental design is to use A-optimality. This criterion aims to minimise the trace of the inverse of the information matrix. Minimising this criterion can reduce the average variance of the estimated regression coefficients.
2. **C-optimality:** In this criterion, the variance of an unbiased linear best estimator of a given linear combination of model parameters is minimised.
3. **D-optimality:** D-optimality is a commonly used criterion in experimental design that aims to maximise the determinant of the information matrix  $X'X$ , or equivalently, minimize  $|(X'X)^{-1}|$ . By doing so, the D-optimality criterion seeks to maximise the differential Shannon information content of the estimated parameters, which can be useful for obtaining precise estimates across a wide range of possible values. Differential Shannon information measures the change in the uncertainty or entropy of the parameter estimates as a result of observing additional data. The term “differential” refers to the fact that the Shannon information is calculated based on the difference between the model parameters’ prior and

posterior probability distributions. The more the posterior distribution is concentrated around a specific value, the lower the uncertainty or entropy and the higher the differential Shannon information. In the context of experimental design, maximising the differential Shannon information is desirable, as it indicates that the additional data obtained from the experiment contains more information about the parameters of interest.

4. **E-optimality:** maximise the minimum eigenvalue of the information matrix.
5. **V-optimality:** V-optimality criterion seeks to identify the experimental design that produces the most precise predictions at specific points of interest. This can be particularly useful in situations where the goal is to optimize the performance of a system at specific operating conditions or to obtain precise predictions for a small number of key variables.

There is no general proven optimality for any of the criteria above: the choice of which to use must be made on a case-to-case basis, often by simulating their performance in the specific problem under study. In general, sequential optimal design helps to reduce the cost of experimentation by choosing the settings which lead to the estimation of the unknown quantity in fewer measurement runs.

## 2.4 Sequential Monte Carlo (SMC) algorithm

As we have seen from Eqn. 2.2, for each measurement outcome  $x$  we have:

$$(2.18) \quad P(\theta|x_1) \propto P(x_1|\theta)P(\theta)$$

such that each successive iteration can be processed sequentially as:

$$(2.19) \quad \begin{aligned} P(\theta|x_2, x_1) &\propto P(x_2|\theta)P(\theta|x_1), \\ P(\theta|x_3, x_2, x_1) &\propto P(x_3|\theta)P(\theta|x_2, x_1), \\ &\vdots \\ &\vdots \\ &\vdots \end{aligned}$$

In the simplest approach, one can implement this algorithm numerically by discretising  $P(\theta)$  over a uniform grid for  $\theta$ . This can be computationally expensive to perform since it requires evaluation of posterior distribution over large parameter space. Sequential Monte Carlo (SMC) methods have been proposed to address this issue [198–200] The idea is to approximate a distribution over a finite number of support points, known as particles, sampled from the distribution; each particle is assigned a weight  $w_i$  (with  $\sum_i w_i = 1$ ). At each iteration, the weight  $w_i$  of each particle

$\theta_i$  is updated according to the Bayes rule. The probability distribution can be written in terms of these particles as:

$$(2.20) \quad P(\theta|x) \approx \sum_{k=1}^n w_k(x) \delta(\theta - \theta_k)$$

the new weight at each subsequent iteration is calculated from the previous iteration as:

$$(2.21) \quad w_k(x_{j+1} \cup x) = \sum_{k=1}^n P(x_{j+1}|\theta_k) w_k(x_j)$$

The SMC method ensures a finite number of particles in each iteration, leading to better, faster algorithm performance, with the freedom of increasing the number of particles to make a more accurate approximation. Since both support points and the weight of the particles contain information regarding the distribution of the model parameter  $\theta$ , we can choose initial weights to  $w_k = 1/n$  without any loss of generality and support points can be drawn from the initial prior  $P(\theta)$ . We can calculate the mean expectation and covariance values using the particle approximation (algorithm 1) and perform a Bayesian update (algorithm 2) [201].

---

**Algorithm 1** SMC for mean and covariance

---

**Input:**Particle weights:  $w_i, i \in \{1, 2, \dots, n\}$ .Particle position:  $\theta_i, i \in \{1, 2, \dots, n\}$ .**Output:** Approximation  $\mu$  and  $\sigma$  for  $E[\theta]$  and  $\text{Cov}(\theta)$ .1: **function** MEAN( $\{\theta_i\}, \{w_i\}$ )2:    $\mu \leftarrow \sum_i \theta_i \cdot w_i$ 3: **return**  $\mu$ 4: **function** COV( $\{\theta_i\}, \{w_i\}$ )5:    $\mu \leftarrow \sum_i \theta_i \cdot w_i$ 6:    $\sigma^2 \leftarrow \sum_i \theta_i^2 \cdot w_i - \mu^2$ 7: **return**  $\sigma$ 

---



**Algorithm 2** SMC for Bayes update**Input:**Particle weights:  $w_i, i \in \{1, 2, \dots, n\}$ .Particle position:  $\theta_i, i \in \{1, 2, \dots, n\}$ .New measurement  $x$ : measurement outcome  $x$  from an experiment with control settings  $C$ .**Output:** Update weights  $w'_i$ .

```

1: function BAYES UPDATE( $\{\theta_i\}, \{i\}, x, C$ )
2:   for  $i \in 1..N$  do
3:      $\tilde{w}_i \leftarrow w_i P(x|\theta_i, C) \Rightarrow$  unnormalised updated weights  $\tilde{w}_i$ .
4:    $w'_j \leftarrow \tilde{w}_j / \sum_i \tilde{w}_i \Rightarrow$  normalisation of the updated weights.
5: return  $\{w'_j\}$ 

```

The strength of the SMC method resides in the possibility of resampling the particles to improve the way they describe the posterior distribution. This is normally done by sampling new particles based on the current weights, such that regions in the distribution with small weights are less represented in the particles than regions with stronger support (such as peaks in the posterior). Resampling removes the issue of numerical errors given by limited numerical precision when the weights approach zero, as particles with small weights have a small probability of being picked up in re-sampling. This is notably challenging because we operate effectively with the reduced number of particles while utilizing the same computational resources. As the support for our approximate distribution constitutes a measure-zero set, all weights will eventually be zero; it is impossible to completely evade this issue, but it can be delayed by employing **resampling**. Summarising, the purpose of resampling is to adjust the particle locations to those that are most likely to occur. A simple resampling algorithm (importance sampling) selects the original number of particles ( $n$ ), replaces them with new ones based on the distribution of weights, and then resets their weights to  $1/n$ . As a result, particles with zero weight are pushed to those with higher weight locations. A threshold known as “resampling\_threshold”, which is the effective ratio of the original number of particles  $n$ , will determine when to initiate the resampling process based on the effective sample size  $n = 1 / \sum_i w_i^2$ .

In our experiments in Chap. 4 and 5, we employ a technique known as Liu-West resampling [202], described in algorithm 3. This algorithm draws particles distributed as Gaussian, with the same covariance matrix as the current posterior distribution, and a mean which is the linear combination of the current particle location and the mean of the distribution (with weights to be determined by the user). In this approach, one balances the drive to simplify the procedure by approximating it to a Gaussian, with the opposite drive to avoid errors by oversimplification [201]:

$$(2.22) \quad p(\theta') = \sum_i w_i \frac{1}{\sqrt{(2\pi)^k |\sigma|}} \exp\left(-\frac{1}{2}(\theta' - \mu_i)\sigma^{-1}(\theta' - \mu_i)\right)$$

**Algorithm 3** SMC for resampling algorithm**Input:**Particle weights:  $w_i, i \in \{1, 2, \dots, n\}$ .Particle position:  $\theta_i, i \in \{1, 2, \dots, n\}$ .Resampling parameter  $a$ :  $a \in [0, 1]$ .**Output:** Update weights  $w'_i$  and locations  $\theta'_i$ .

---

```

1: function RESAMPLE( $\{\theta_i\}, \{i\}, a$ )
2:    $\mu \leftarrow \text{MEAN}(\{\theta_i\}, \{i\})$ 
3:    $h \leftarrow \sqrt{1 - a^2}$ 
4:    $\sigma \leftarrow h^2 \text{Cov}(\{w_i\}, \{\theta_i\})$ 
5:   for  $i \in 1..N$  do
6:     draw  $j$  with probability  $w_j \Rightarrow$  particle to perturb.
7:      $\mu_i \leftarrow a\theta_j + (1 - a)\mu \Rightarrow$  mean of new particle location.
8:     draw  $\theta'_i$  from normal distribution.  $\Rightarrow$  location of perturbed particles.
9:      $w_i \leftarrow 1/n \Rightarrow$  resetting of weights.
return  $\{w'_i\}, \{\theta'_i\}$ 

```

---

here  $k$  is the number of model parameters. A mixture distribution of this type can be efficiently sampled by selecting a particle first, followed by a perturbation vector. The mean  $\mu_i$  for each component in the resampling mixture distribution is selected using a convex combination of the expected model  $\mu = \mathbb{E}[x]$  and the original particle location  $\theta_i$ .

$$(2.23) \quad \mu_i = a\theta_i + (1 - a)\mu,$$

here  $a$  is the adjustable parameter of the model. While the covariance of the perturbation is given as:

$$(2.24) \quad \sigma = (1 - a^2)\text{Cov}(\theta)$$

Every time we resample, we draw  $n$  new particles from Eqn. 2.22 and set their weights to  $1/n$ .

## 2.5 Bayesian estimation for quantum technology

In the past few years, several research groups have started applying sequential Bayesian estimation to optimise quantum sensing.

Seminal theoretical and experimental work in the field has examined the scaling of variance for phase estimation, in terms of the number of measurements, in the application of Kitaev's quantum phase estimation protocol [203]. In the year 2000, Berry et al. introduced the concept of adaptive phase measurements using Bayesian analysis [188]. Their study revealed that an

innovative approach of choosing a feedback phase that minimizes the expected phase uncertainty after the next detection resulted in obtaining minimal phase uncertainty. Based on that work, adaptive phase estimation schemes have been shown to achieve Heisenberg-limited scaling (i.e. sensitivity scaling as  $1/N$ , where  $N$  represents the number of measurements) [187].

These ideas have been more recently extended to the estimation of Larmor frequencies in quantum magnetometry [204, 205]. The basic principle here is that an electron spin in a magnetic field  $B$  precesses at the Larmor frequency given by  $\omega_B = 2\pi\gamma Bt$ , where  $t$  is the sensing time. By adjusting the sensing time, the phase estimation algorithm can then be used to estimate frequencies.

In a repeated Ramsey experiment with a constant sensing time  $t$ , the uncertainty diminishes as the total sensing time  $T$  increases, following the pattern  $1/(2\pi\sqrt{t \cdot T})$ , also known as the standard measurement sensitivity (SMS). Nonetheless, as time  $t$  progresses, the field range also decreases due to the periodic nature of the signal, resulting in uncertainties whenever  $\|2\pi f_B t\| > \pi$ . As a consequence, this imposes a limitation on the dynamic range:

$$(2.25) \quad \frac{f_{B,max}}{\sigma_{f_B}} < \pi \sqrt{\frac{T}{\tau_{min}}}$$

here  $\tau_{min}$  is the shortest sensing time in the sequence. More recently, it was found that for an estimation sequence, having multiple sensing times can result in a scaling that is directly proportional to  $1/T$ , which significantly enhances the dynamic range:

$$(2.26) \quad \frac{f_{B,max}}{\sigma_{f_B}} < \pi \frac{T}{\tau_{min}}$$

We name a scaling linear in  $T/\tau_{min}$  as **Heisenberg-limited scaling**.

The first experimental demonstration of real-time adaptive frequency estimation in quantum magnetometry, and comparison with the best non-adaptive protocol, was given by C. Bonato et al. [206]. This paper shows an improvement in measurement bandwidth of factor 3, and a record sensitivity of  $32 \text{ nT Hz}^{1/2}$ , achieved with single-shot spin readout at cryogenic temperature and isotopically-purified diamond with  $T_2^* \sim 100\mu\text{s}$ . In this work, the sensing times are deterministic (exponentially increasing as  $2^k \cdot \tau_{min}$ ), while the readout phase is optimised adaptively based on the combination of an analytical formula in [207] and a further optimisation based on particle swarm techniques [208].

Further work in this field has targeted the extension of this technique to room-temperature magnetometry and its improvement by the adoption of better Bayesian inference techniques such as Sequential Monte Carlo (see Chap. 2). R. Santagati et al. [209, 210] have applied theoretical proposals by Chris Granade, Nathan Wiebe and Chris Ferrie on Hamiltonian learning to NV quantum sensing. The algorithm implements a more efficient Bayesian inference scheme (sequential Monte Carlo) and uses an adaptive heuristic that optimises the sensing time based

on the standard deviation  $\sigma_f$  of the current probability distribution  $P(f)$  for the Larmor frequency, as  $\tau \sim 1/(2\pi\sigma_f)$ . This heuristic can be computed fast also in the case of multi-dimensional distribution using the so-called *particle guess heuristic*,  $\tau \sim 1/(2\pi\|f_2 - f_1\|)$  where  $f_{1,2}$  are two values of frequency sampled from the current  $P(f)$ . The algorithm was first demonstrated offline, in pre-acquired data [211], and then in real-time to estimate the Larmor frequency of a single strongly coupled nuclear spin [212].

The utilization of the quantum phase estimation algorithm is based on binary outcomes. As we will see in Chap. 4 and 5, the single-shot projective readout is not available for NV centre experiments at room temperature, and experiments typically make use of the number of detected photons over  $R$  repetitions, distributed as a Poissonian. Santagati et al. [211], and Joas et al. [212] circumvent this issue by comparing the number of detected photons to a threshold and converting to a binary outcome (“majority voting”). This is not the most effective approach as some information is lost in the thresholding process: as shown numerically by H. Dinani et al. [213] and experimentally in Chap. 5. One can still use Bayesian phase estimation with the number of detected photons.

Online learning approaches have been utilised to predict and suppress decoherence by compensating in real-time the semi-classical noise associated with the nuclear-spin bath fluctuations in GaAs quantum dots [214] and to external fields in ion traps [215]. A theoretical proposal by our group [216] has investigated how a sequence of adaptive measurements can be used to deterministically narrow the distribution of magnetic fields associated with different configurations of the bath: this can be used as a tool to extend the dephasing time  $T_2^*$  up to the  $T_2$  limit (when nuclear-nuclear interactions will change the bath configuration).

As discussed previously, the standard Bayesian approach can be problematic since it is based on updating a probability distribution which can be computationally intensive for certain complex problems or may involve regions with little information. Hence, Sequential Monte Carlo (SMC) methods combined with Bayesian estimation, as discussed in Sec. 2.3, come in handy. The adaptive schemes discussed in chap. 4 and 5 of this thesis are, to the best of our knowledge, one of the first experimental demonstrations of the use of SMC and Bayesian experimental design to estimate the decoherence ( $T_1, T_2, T_2^*$ ) and frequency estimation via adaptive phase estimation of a single qubit. Applications of these protocols range from quantum information to quantum sensing to biological and chemical estimations.

## EXPERIMENTAL SETUP FOR ADAPTIVE QUANTUM SENSING

This chapter will discuss the design, construction and characterisation of the experimental setups used in my PhD work. In the majority of this chapter, I will discuss the room-temperature confocal microscope setup I designed and built from scratch for the adaptive measurements mentioned in Chap. 4 and 5. In the last section of this chapter, I will describe the setup, mostly built by my colleagues Dr Daniel White and Dr Pasquale Cilibrizzi, which I used to perform optical spectroscopy of single vanadium centres in SiC (see Chap. 6).

The description of the room temperature setup is quite didactic, as it is written to provide a tutorial for new group members planning to use it in the future for their own research,

### 3.1 Confocal microscopy setup

I have designed and constructed a room-temperature scanning laser confocal microscope setup equipped with microwave excitation capabilities to precisely control and manipulate a single NV centre in diamond. This requires illuminating with a green laser and detecting the fluorescence emitted by the single NV centre while minimising the background.

Confocal microscopes work according to the conjugate plane principle [217]. In the case of point source imaging, the image plane and the source plane are referred to as conjugate planes [218]. A source (image) plane comprises the source (image) points. A patent filed by M. Minsky et al. in 1961 outlines the concept of this type of microscope [219]; it was demonstrated that this microscope could only image the point source of interest and rejects other light components. According to Fig. 3.1, the image point of interest is intersected by a pinhole at the image plane. The main idea of this microscope is to image the source plane via a pinhole. In this configuration, the image plane of the off-axis source points is formed off-axis of the pinhole entrance; therefore,

the pinhole blocks these points. In comparison, the source points not within the same plane but on-axis are imaged before or after the pinhole, decreasing the collected signal's intensity.

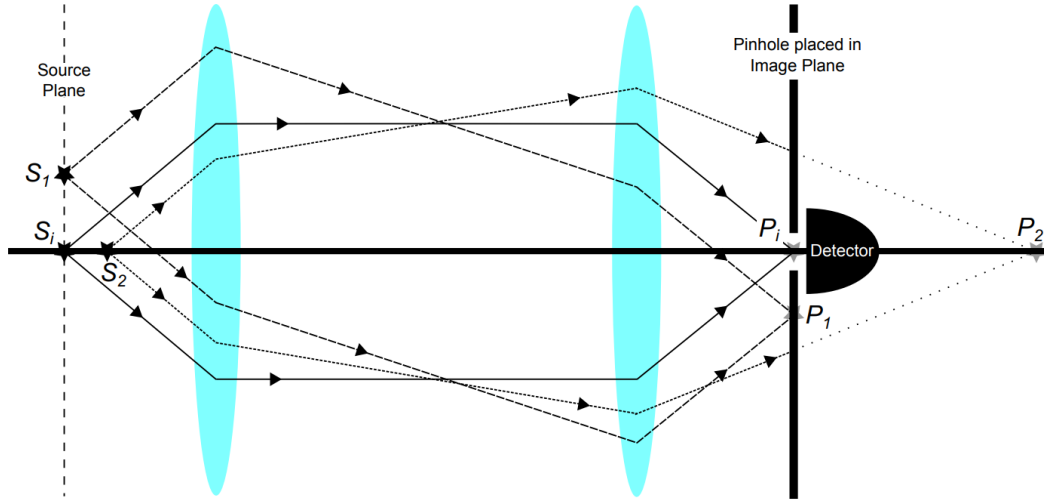
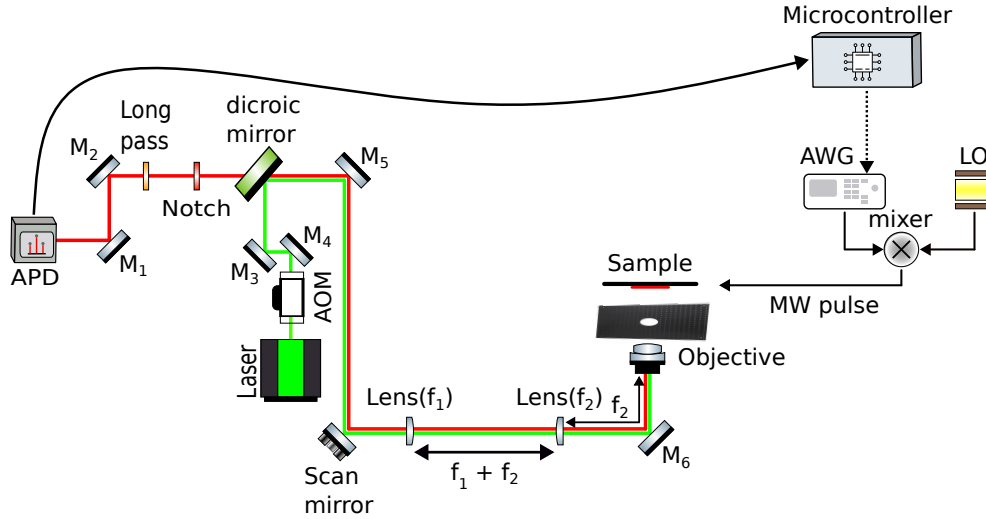


FIGURE 3.1. An illustration of the confocal microscope system. Where pinholes block all light except that coming from the point source  $S_i$ . Figure adapted from [220].

Typically, two ways can be used to scan the entire sample surface to locate point sources. One solution is to move the sample stage across the excitation laser spot to image the sample. An alternative method is to use a pair of scanning mirrors to scan the entire sample for laser excitation and detection points (Epi-illumination) [221]. In our setup, we will take the latter approach.

As shown in Fig. 3.2, the excitation green laser goes into the acousto-optic modulator (AOM) to produce microsecond pulses with nanosecond resolution, which are used for initializing and reading out the NV centre  $e^-$  spin (refer to Sec. 3.2 for more information regarding the AOM). The AOM output is then reflected off of a dichroic mirror and fed into scanning optics. The dichroic mirror (Di02-R532-25x36) reflects the green laser while allowing the fluorescent signal to be transmitted through. Using the scanning mirrors (Thorlabs GVS012/M), the beam can be steered with about  $14\mu\text{rad}$  repeatability, and the laser light can be scanned across the sample at a maximum scanning angle of  $\pm 20^\circ$ . A Labjack DAQ (U3-HV) controls this scanning mirror, with the smallest incremental step size of  $\approx 15\text{ nm}$  (refer to Appx. A.1 for more details).

If the objective is underfilled, it will lead to a reduction of effective numerical aperture (NA), resulting in reduced resolution (see Fig. 3.3). Hence to achieve the full numerical aperture of the objective for excitation, we need to overfill the back pupil of the objective slightly to ensure it is not underfilled at any time. This is accomplished through the utilization of a 4f telescope system (with  $f_1 = 50\text{ mm}$  and  $f_2 = 175\text{ mm}$ ) to enlarge the input beam, expanding it from its initial waist size of approximately  $1.5\text{ mm}$  to  $5.25\text{ mm}$ . We slightly overfill the back pupil of the objective since the laser beams have Gaussian intensity distribution; hence to achieve the maximum NA,



**FIGURE 3.2. Design of the room temperature confocal microscope.** Microsecond pulses are created by passing the excitation laser 532 through an acousto-optic modulator (AOM) (refer to Sec. 3.2 for more information regarding the AOM). Those pulses are then subjected to scanning mirrors (galvos) by reflecting off of the dichroic mirrors, which help perform the raster scanning of the sample. A telescope is built between the galvos and the objective. This ensures the beam remains fixed at the back pupil of the objective and only changes in angle, resulting in no vignetting. The fluorescence signal follows the same path back and is collected via an APD. The AWG (refer to Sec. 3.8.2 for more information on AWG), combined with an RF source (LO), is used to create microwaves (MWs) (refer to Sec. 3.3 for more information on MWs) pulses for spin manipulation. The microcontroller uses counts from the APD to generate optimal MW pulse sequences to perform adaptive experiments (refer to Sec. 3.8.4 for more information on the adaptive experiments design). The microscope objective is mounted on a digital piezo controller (E-709 from Physik Instrumente) to achieve displacement in the  $z$ -direction.

the objective should capture only the  $1/e^2$  core of the beam. We also ensure that the output from this telescope is well-collimated, as it is a requirement of an infinity-corrected objective. In our confocal microscope, the role of the scanning mirrors is to perform a raster scan. Since the scanning mirrors are positioned at a plane conjugate to the back pupil of the objective, as these mirrors rotate in the  $xy$ -axis, the incident light will enter the objective at various angles, which will be transformed into light moving across the entire focal plane (see Fig. 3.4(c)). Moving the objective relative to the sample (movement in the  $z$ -direction) can accomplish a full 3-dimensional scan of the sample.

Specific optics criteria must be met to ensure the light entering the objective is properly collimated. We must ensure that the two lenses are separated by  $f_1 + f_2$  (see Fig. 3.2). Additionally, the distance ( $d_1$ ) between the galvos and the scan lens can be related to the distance ( $d_3$ ) between the tube lens and the objective by the following equation.

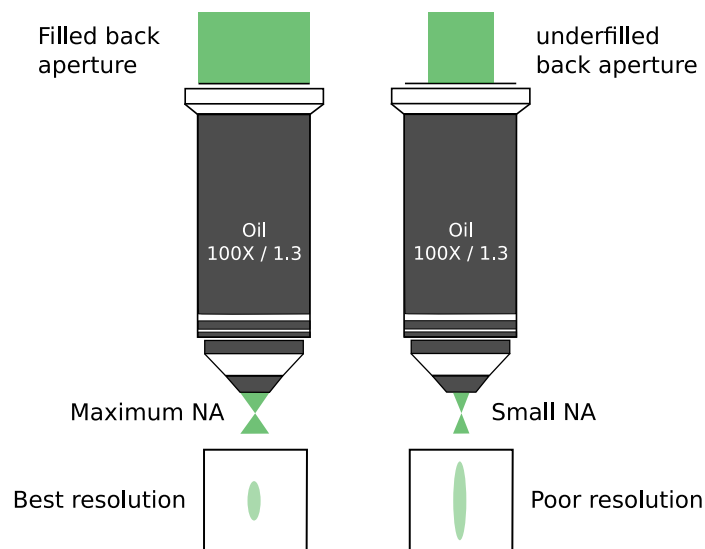


FIGURE 3.3. **Filling of back aperture of objective.** Left: (over)Filled back aperture of the objective leading to full effective NA and a resultant best possible resolution. Right: Underfilled back aperture of the objective results in a smaller effective NA and a lower resolution.

$$(3.1) \quad d_1 = \frac{f_1^2}{f_2} + f_1 - d_3 \left( \frac{f_1}{f_2} \right)^2$$

A red diode laser is sent backwards through the collection optics to check the alignment of the setup. The path of both green and red lasers overlap in the scanning apparatus, so the green and red lasers will be co-axial and concentric. We use Excelitas Technologies single photon detectors (SPCM-AQRH-15-FC) to detect the fluorescence signal from the sample. The scattered excitation laser is filtered out by a notch filter (Thorlabs NF533-17). In addition, we use a longpass filter (Semrock LP02-633RU-25) and a shortpass filter (Thorlabs FESH0800) to filter fluorescence in the expected emission range for the NV centre (633 to 800 nm).

### 3.1.1 Characterisation of the confocal microscope

Two types of 100x objectives are used for initial characterisation, an air objective with a numerical aperture (NA) of 0.9 and an oil-immersed objective with an NA of 1.3. We will ultimately use the oil-immersive objective in the experiments described in later chapters since it provides greater resolving power and better counts than the air objective. The performance of our designed setup was tested against the following four parameters.

- Confocal resolution
- Smallest incremental step size



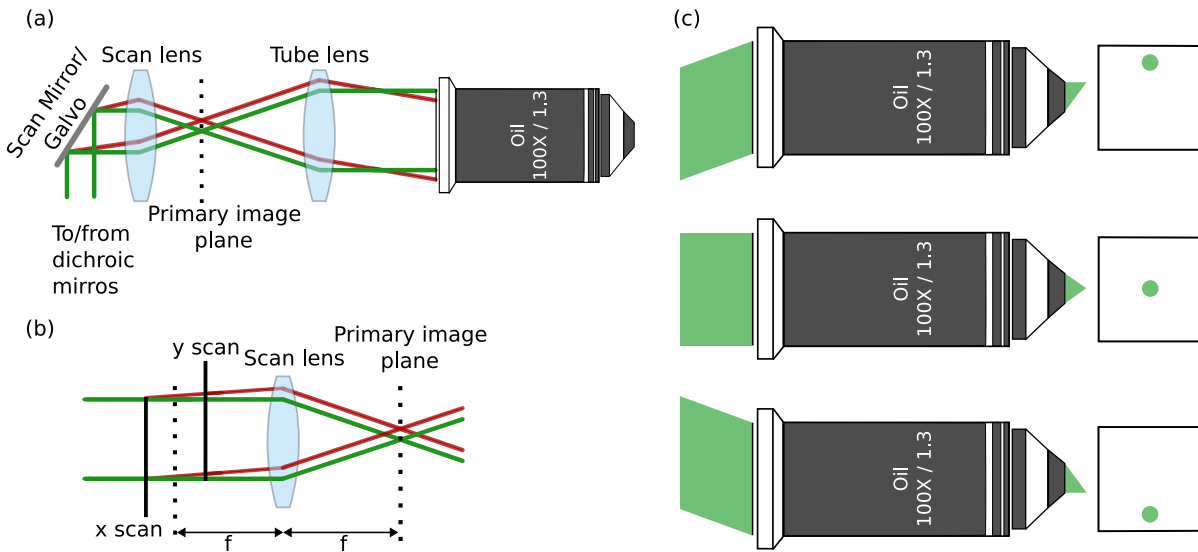


FIGURE 3.4. **Scanning confocal configure (a):** A simple arrangement of confocal scanning microscope with a single mirror (cardanic scanning), where the scan mirror is placed at the conjugate plane of the objective. **(b)** Closed coupled mirrors, separated by a small distance, require a slight change in lens placement to achieve satisfactory performance. **(c)** Raster scanning of the sample, where the angle of tilt introduced via galvos is transformed to a position change along the focal plane by the objective.

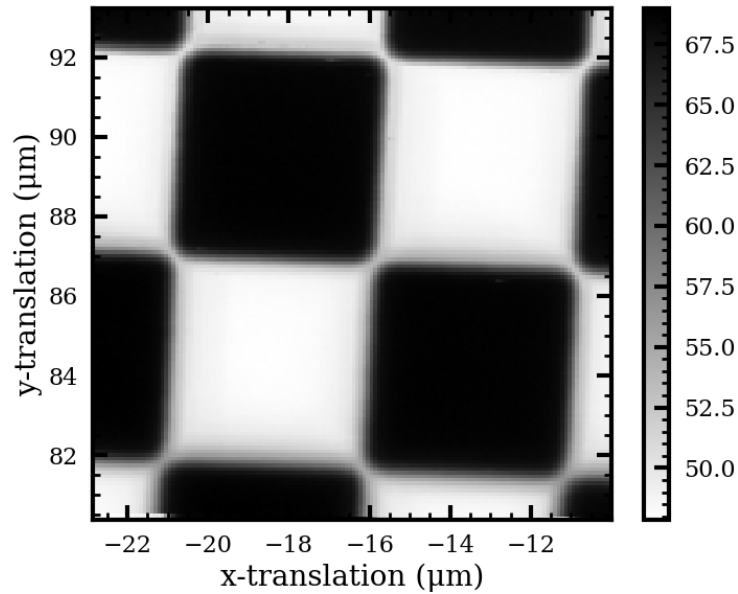
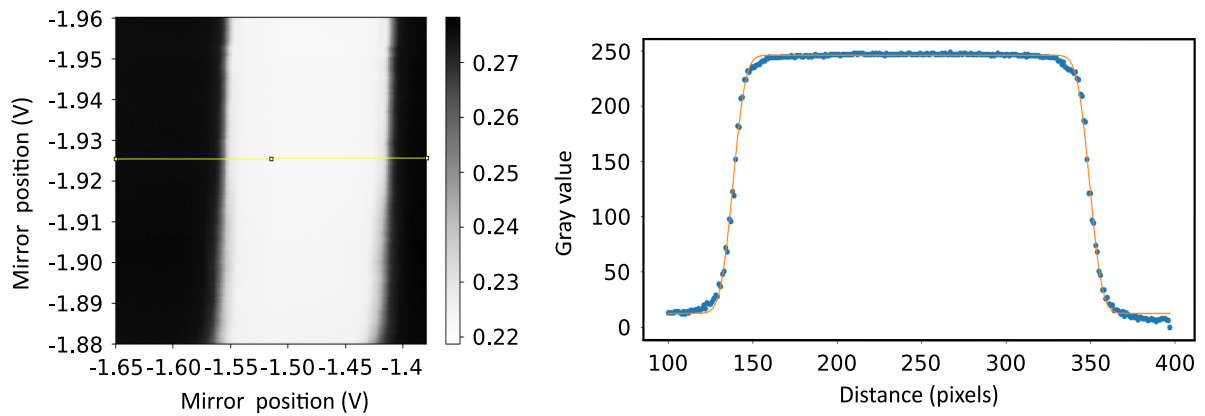
- Total scan range
- Mechanical vibrations

We tested the setup with a 10-um period checkerboard and a 100x air objective to find out the above-mentioned characteristics.

These checkerboard scans were performed using a photodiode (Thorlabs SM1PD1A with FDS1010 detector) controlled via the Labjack DAQ (U3-HV). During these scans, as we moved across the checkerboard surface, the photodiode's voltage recorded oscillations in intensity as a function of axial position. Using the formula below [222], we calculated the setup's confocal resolution.

$$(3.2) \quad FWHM = \frac{0.51\lambda}{NA}$$

In our case, when we used a 532 nm green laser and an objective with an  $NA = 0.9$ , our theoretical value (calculated from Eqn. 3.2) was about 302 nm. To calculate the confocal resolution experimentally, a line profile was taken across Fig. 3.6(a), fitting this line profile (Fig. 3.6(b) with a convolution of the grating function with the Gaussian beam we found the experimental confocal resolution to be  $326 \pm 5$ nm, with a minimum incremental step size of roughly 15 nm (see Appx. A.1 for more details).


 FIGURE 3.5. Microscope view of checkerboard with 10  $\mu\text{m}$  period.

 FIGURE 3.6. a) The yellow line represents the area where the line profile was taken across the checkerboard. b) Gaussian fitting of the obtained line profile using Python. Distance is pixel was converted to  $\mu\text{m}$  for confocal resolution calculation.

In the next step, we ran an overnight scan to figure out the scanning range; for this, a step size of 300 nm (0.00950V) was chosen. As shown in Fig. 3.7, our setup is capable of achieving a large axial displacement of about  $200\mu$  by  $240\mu\text{m}$ . It turned out that the checkerboard surface had smudges on it, which caused blurriness during this overnight scan, as shown in Fig. 3.7.

After characterising the setup's optical performance, we performed a test to check the me-

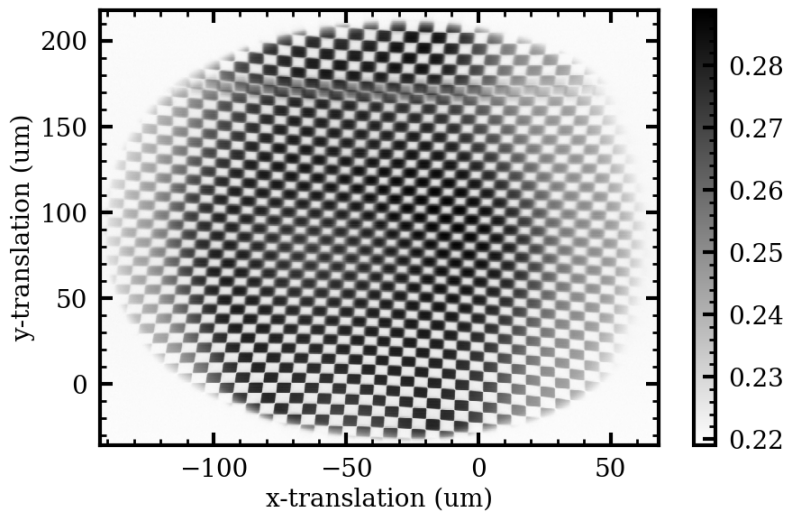


FIGURE 3.7. We achieved  $200\ \mu\text{m} \times 240\ \mu\text{m}$  axial displacement with our setup. Blurriness in this scan resulted from cleanliness issues with the checkerboard.

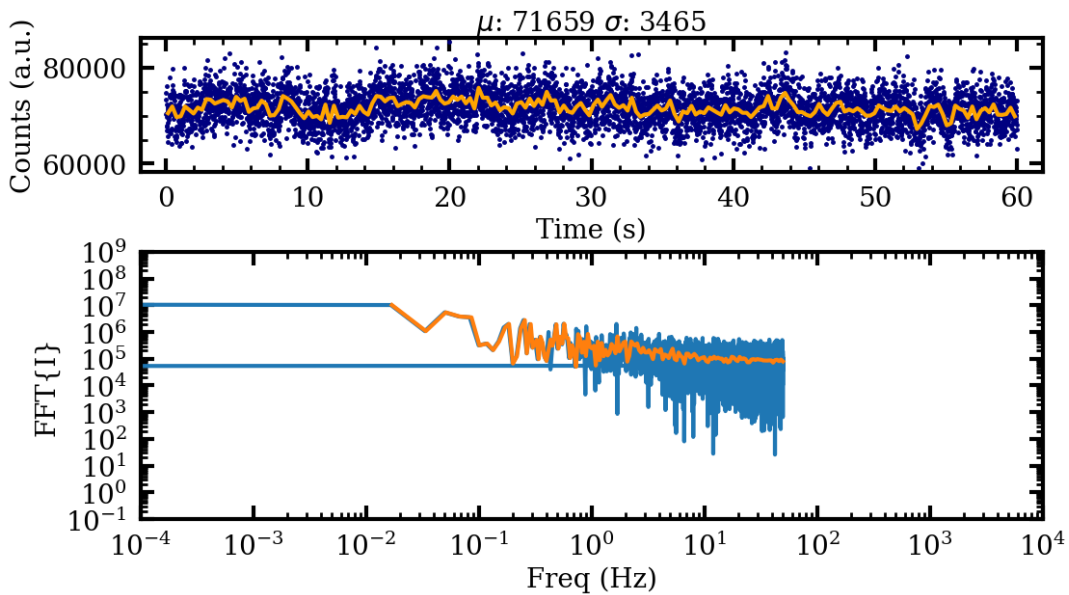


FIGURE 3.8. Time-tagged record of intensity from the NV centre b) Fourier transform of the acquired time-tagged signal.

chanical stability of the setup. Mechanical stability is important since we detect the NV electron spin signal as changes in photoluminescence intensity; changes in photon count rate induced by mechanical vibrations could therefore mask the spin signal. To characterise the stability of the setup, we recorded the intensity from an NV centre over a one-minute period, as shown in Fig. 3.8(top). By taking the Fourier transform of this recorded intensity, we observed no peaks

corresponding to any vibrations in the setup (see Fig. 3.8 bottom).

## 3.2 Optical pulsing system

An NV centre spin can be polarised and detected by  $\mu\text{s}$ -scale optical pulses of green laser. We implemented these pulses by modulating a CW laser with an acousto-optic modulator (AOM) from Isomet (1250C-829A).

An important parameter for an AOM system is the extinction ratio. Given that the NV spin can be polarised in about  $1 \mu\text{s}$ , a typical single-pass extinction ratio of  $10^2 - 10^3$  means that, with the AOM off, the NV spin would be polarised in  $100 \mu\text{s} - 1 \text{ ms}$ , shorter than the room-temperature spin  $T_1$  relaxation time. We, therefore, designed the AOM in a double-pass configuration to enhance the extinction ratio up to around  $10^5$ .

### 3.2.1 Working principles of an AOM

Bragg scattering is a good approximation for the modulation process in AOMs [224], where the modulation process is treated as a phonon-photon scattering process. According to the following energy-momentum conservation relation, incident light frequency is modulated during the scattering process due to the emission/absorption of the acoustic phonon.

$$(3.3) \quad \omega_{diff} = \omega_{inc} \pm \Omega_{phonon}$$

$$(3.4) \quad k_{diff} = k_{inc} \pm \kappa$$

here  $\Omega$  and  $\omega$ , shows the incident phonon and photon frequencies respectively. While the  $\kappa$  ( $\kappa = \frac{f}{v_{sound}}$ ),  $k$ , represents the phonon and photon wave vectors.

Generally, an acousto-optic device features a piezoelectric transducer on the side of the crystal material, which, upon being driven by a radio frequency (RF) signal, produces travelling acoustic waves within the crystal. These waves propagate at the speed of sound and have the same frequency as the applied RF signal. A modulation in refractive index that follows a periodic pattern (with modulation period  $\Lambda = \frac{2\pi v_s}{\Omega}$ ), due to the photo-elastic (compression and rarefaction) effect can be observed (see Fig. 3.9). It results in effects similar to those seen in diffraction

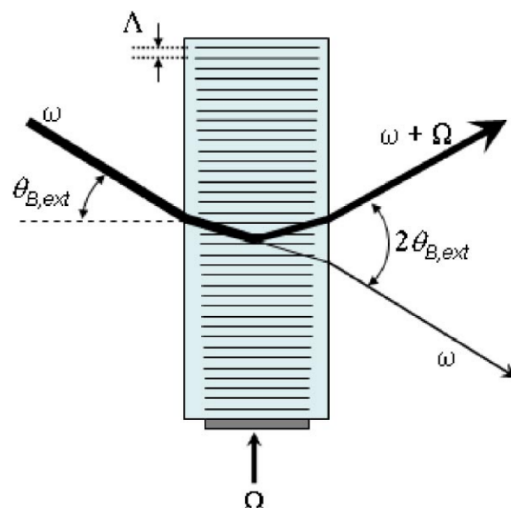


FIGURE 3.9. Schematic illustrating how phonon absorption leads to the diffraction of light resulting in the increase of the first-order frequency [223].

gratings. Hence we use a Bragg treatment (although care must be given, as this Bragg treatment can only be applied to plane acoustic waves with phonons that have a similar wave vector). To achieve optimal efficiency, input light must be injected at the  $\theta_{Bragg}$  for diffraction.

$$(3.5) \quad \theta_{Bragg} = \frac{n\lambda\Omega}{2v}$$

here  $n$  is the order of the diffraction peak,  $\lambda$  is the wavelength of the incoming light,  $\Omega$  is the radio frequency (RF), and  $v$  represents the acoustic velocity. In the case of an AOM, two essential control parameters include the radio drive frequency, responsible for controlling the angle of the diffracted beam, and the driving power of the RF input, which dictates the diffraction efficiency.

### 3.2.2 Double-pass AOM configuration

In a double-pass configuration, the input light is allowed to pass twice through the AOM with the help of a retroreflector. Using a double-pass scheme combined with a retroreflector configuration is primarily motivated by the enhancement it provides to the extinction ratio of a single device. The importance of a sufficient extinction ratio for our work can be attributed to the fact that any leakage of excitation green laser during spin manipulation will result in undesired initialisation of the spin state, ultimately reducing the fidelity of spin control. The extinction ratio of our AOM at 532nm was 53 dB, which satisfies the requirements [225]. Double pass configuration also helps tackle the challenges associated with coupling the output from the AOM to the fibre. The coupling into the fibre becomes ultra-sensitive when the RF drive frequency changes (jumps in the frequency).

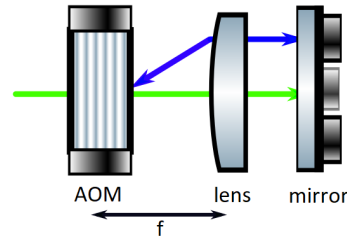


FIGURE 3.10. Schematic showing the retro-reflected light focused onto the AOM centre.

### 3.2.3 Design and performance of the AOM system

Input beam waist strongly affects the diffraction efficiency and the rise time of the AOM. Both of the entities increase with increasing beam waist, with efficiency levelling off around 90%. It is, therefore, necessary to make a trade-off between efficiency and rise time. An estimate of the Gaussian beam waist diameter for a plano-convex lens can be made by using  $d = 4\lambda f/\pi D$ . Two plano-convex lenses with a focal length of 125mm are being used to focus the light. They are both located at a distance of  $1f$  from the centre of the AOM (see Fig. 3.11). The zero-order diffraction beam (incidence beam) is blocked using a pinhole. In contrast, a mirror placed after a quarter-wave plate retro-reflects a beam of the  $1^{st}$  order. To optimize the AOM's throughput, a quarter-wave plate imparts a  $\lambda/2$  phase change, which helps separate the retro-reflected light

from the incident light using a polarizing beam splitter (PBS). In our setup, we mounted the AOM on top of a manual XYZ stage (DT12XYZ/M) to have freedom in alignment.

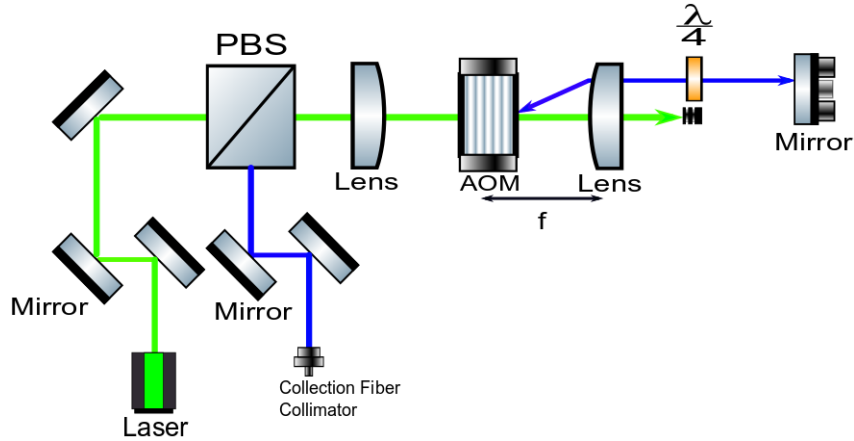


FIGURE 3.11. An overview of our AOM setup. (The different colours are used here to distinguish between light that is reflected (blue) and incoming light (green).

Based on experimental and theoretical calculations, the beam waist at the centre of our designed AOM was approximately  $34 \mu\text{m}$ . Hand-waving calculations based on geometric optics often do not provide sufficient information to design a suitable setup. The beam waist was calculated theoretically using a Gaussian beam tracing Python program to select the appropriate lens and components for the setup. The beam's full-width half maximum (FWHM) was calculated by fitting Gaussian functions to images taken at the regular distance between the two focusing plano-convex lenses. We calculated the diffraction efficiency to be approximately 55%, which agrees with the specification of the AOM. Additionally, the rise and fall time of the designed AOM was found to be about 10 ns.

### 3.3 Microwave (MW) chain

The zero-field splitting for an NV centre is about 2.87 GHz; the ground state spin transitions can therefore be driven by electromagnetic fields in the microwave regime. This section will describe the microwave (MW) chain we have developed for spin manipulation. Microwaves generated by a vector source and modulated by an arbitrary waveform generator are amplified and delivered to the diamond sample by a simple coplanar waveguide on a printed circuit board (PCB).

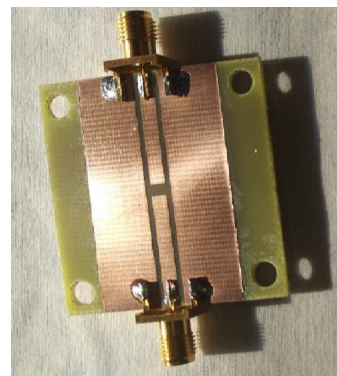


Figure 3.12: Designed coplanar waveguide for MW delivery. The break in the centre is used to mount the sample.

### 3.3.1 Design of coplanar waveguide

As shown in Fig. 3.12, the coplanar waveguide is constructed from an etched prototype circuit board with SMA connectors on either side. To design a microwave waveguide that has low reflection loss, the centre width of the waveguide and the spacing between the lines have been calculated using an online calculator (click). To deliver the MWs to the NV centre, the diamond sample is glued to the break in the centre conductor; a copper wire is then soldered across the break and over the sample (Fig 3.13). Due to the fact that the magnitude of the magnetic field introduced by the wire is proportional to the amount of current flowing through it, we use wires with a  $20\ \mu\text{m}$  diameter gauge to apply the magnetic field. To increase the strength of the field, we need to ensure that there is close contact between the wire and the sample because the strength of the field is proportional to the inverse square of the distance from the wire. Using a RIGOL RSA5065 network/spectrum analyser, we measured the S21 parameter, which is the fraction of power transmitted through the microwave waveguide. As seen in Fig. 3.14, there is less than a -5dB transmission loss across the range (1-3 GHz) we are interested in.

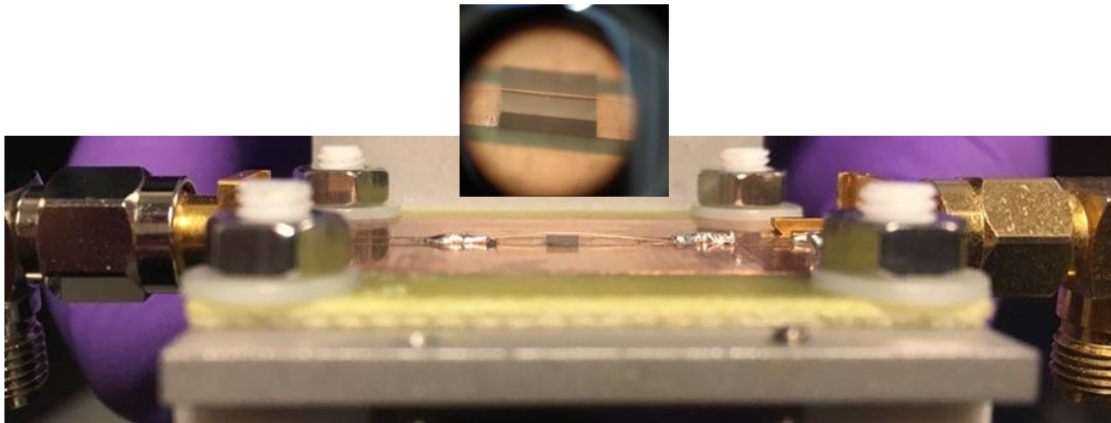


FIGURE 3.13. Diamond sample mounted on the PCB with a wire soldered to transmit microwaves.

### 3.3.2 Single-sideband Modulation

For effective excitation and manipulation of the spins, we need to control the amplitude and the phase of the MW pulses. Typical microwave pulses can be as short as a few tens of nanoseconds, and the microwave generator cannot be made to switch amplitude or phase so quickly. We, therefore, create a sequence of pulses controlled in amplitude and phase by modulating the CW microwave signal.

As shown in Fig. 3.15, using IQ modulation, a CW signal (carrier frequency) is split into two signals ( $\text{LO}_1$  and  $\text{LO}_2$ ) which differ by 90 degrees in phase, ‘quadrature’. These two signals ( $\text{LO}_1$  and  $\text{LO}_2$ ) are mixed with the two baseband signals  $I(t)$  and  $Q(t)$  via a mixer. The resulting signal from the mixer is an I/Q modulated signal at the carrier frequency of the local oscillator.

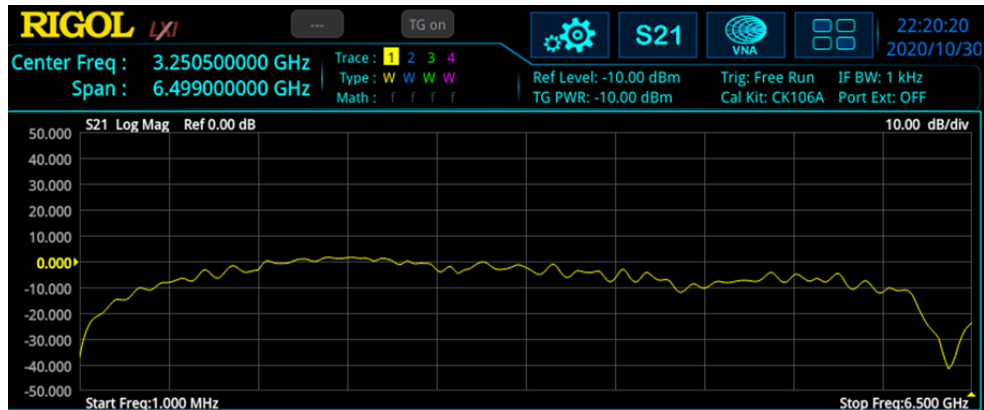


FIGURE 3.14. MW transmission spectrum across the wire over the sample in the range 0.001-6.5 GHz recorded with a spectrum analyser.

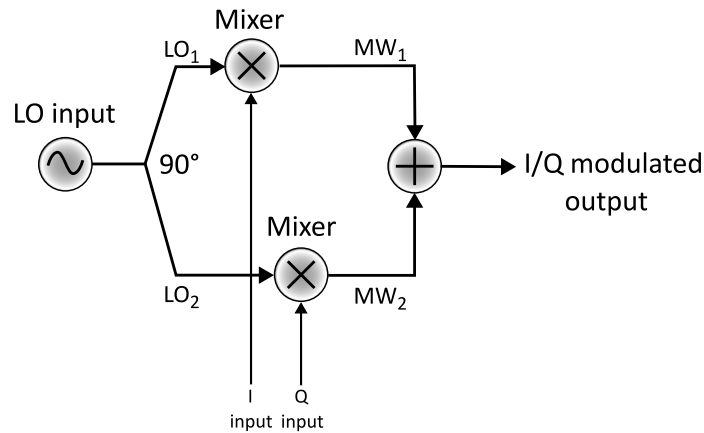


FIGURE 3.15. Block diagram of I/Q modulation.

In our setup, we use a ‘single-sideband’ modulation scheme. Two baseband signals, different in phase by 90 degrees, are applied to the I and Q channel, such that  $I(t) = A\sin(\omega_1 t)$  and  $Q(t) = A\cos(\omega_1 t)$ . While the split signals from the local oscillator are given as  $LO_1 = \sin(\omega_c t)$  and  $LO_2 = \cos(\omega_c t)$ . Such that the output from the mixers will be given as:

$$(3.6) \quad MW_1 = \sin(\omega_c t) * A\sin(\omega_1 t) = A/2\cos((\omega_c - \omega_1)t) - A/2\cos((\omega_c + \omega_1)t)$$

$$(3.7) \quad MW_2 = \cos(\omega_c t) * A\cos(\omega_1 t) = A/2\cos((\omega_c - \omega_1)t) + A/2\cos((\omega_c + \omega_1)t)$$

Summing the output of these two mixers will give the final output:

$$(3.8) \quad MW_{final} = MW_1 + MW_2 = A\cos((\omega_c - \omega_1)t)$$



To control the phase, we can modify the I and Q channel input to  $I(t) = A \sin(\omega_1 t + \alpha)$  and  $Q(t) = A \cos(\omega_1 t + \alpha)$  to get the following general result:

$$(3.9) \quad MW_{final} = MW_1 + MW_2 = A \cos((\omega_c - \omega_1)t + \alpha)$$

This is the required I/Q modulated signal (lower) sideband signal. Hence, we can control the final pulse's frequency, amplitude, and phase by controlling the I and Q signals.

Single-sideband modulation is advantageous in many ways. First of all, it enables detuning the oscillator frequency from the spin resonance, reducing the probability of unwanted spin transitions due to leakage from the source. A further advantage is that one can simultaneously address multiple lines using multiple detunings for the I and Q channels.

One challenge of this method is to ensure the output signal is as clean as possible. One of the common problems is the leakage of carrier signal into the output, as a result of two possible mechanisms:

1. the mixers not being matched and balanced in the same way, there is an effect of local oscillator (LO) leakage that is dependent on the carrier frequency.
2. A DC offset can cause the LO leakage at the I and/or Q inputs that are independent of the carrier frequency.

Additionally, one can have an LO quadrature error if the two LO signals aren't exactly 90 degrees apart from one another. The reason for this can be phase errors in the LO splitter or phase matching problems in the mixers. A consequence of this is that an undesired image signal is produced. If we examine the case of single sideband modulation, with a slight phase offset at the local oscillator ( $LO_1 = \sin(\omega_c t)$  and  $LO_2 = \cos(\omega_c t + \alpha)$ ) split signals, doing the calculation done above, we can get the final pulse as:

$$(3.10) \quad MW_{final} = MW_1 + MW_2 = A \cos(\alpha/2) \cos((\omega_c - \omega_1)t - \alpha/2) - A \sin(\alpha/2) \sin((\omega_c + \omega_1)t + \alpha/2)$$

This sort of error can be corrected by calibrating the internal I/Q settings of the source. I/Q mismatch errors can also result in an unwanted image. Generally, such errors are caused by a difference in amplitude, phase, and group delay (skew) between the I and Q signals. The issues can be accounted for using the internal settings of the Zurich Instruments HDAWG vector signal generator and the RF source settings, such as I/Q gain balance and quadrature adjustment. While the skewness can be corrected using the adjustable skew correction settings available on the HDAWG. An example of such issues was seen during the setting up of the I/Q modulation, as shown in Fig. 3.16 where an unwanted image is created at the frequency of  $LO + \omega_1$  along with the desired signal at  $LO - \omega_1$ .

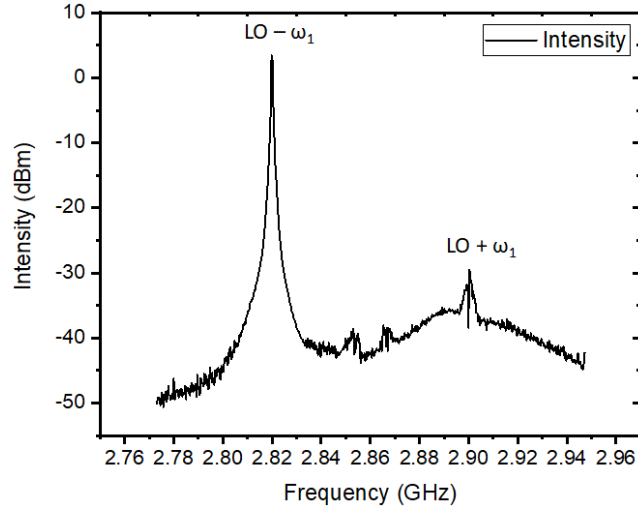


FIGURE 3.16. Spectrum of local oscillator (LO) with I/Q modulation. Here an unwanted image is created at  $LO + \omega_1$  along with the desired signal at  $LO - \omega_1$  due to an I/Q mismatch.

### 3.3.3 Microwave chain

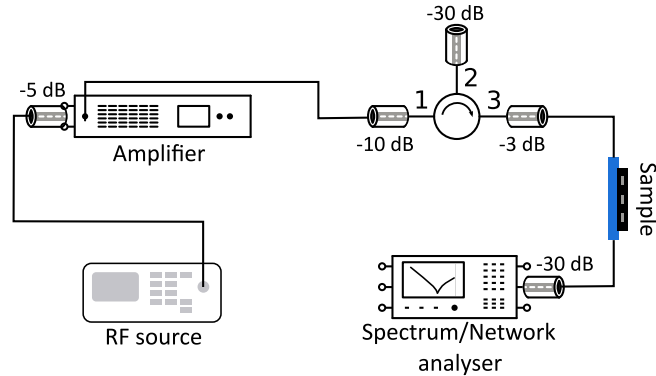


FIGURE 3.17. Circuit diagram of the microwaves (MWs) delivery setup.

In the context of the experiments detailed in Chap. 4 and 5, we employ a single-sideband modulated signal with a tone at 1.6 GHz, sourced via a vector signal generator (RohdeSchwarz SMBV100A). This signal is combined with a low-frequency baseband signal of 40 MHz generated by a Zurich Instruments high definition arbitrary waveform generator (HDAWG) (with specifications of 2.4 GSa/s, 16 bits vertical resolution, and signal bandwidth of 750 MHz). The modulated microwave signal is then amplified using an Amplifier Research 15S1G6 amplifier (0.7-6 GHz, 15 W) and passed through a circulator (Aaren Technology 11B-GX017027G-AF), which safeguards the amplifier from reflections while driving the ( $m_s = 0 \iff m_s = -1$ ) electron spin resonance. The configuration of the microwave circuit is outlined in Fig. 3.17. Within the MW circuit, we strategically employ attenuation to minimize reflections and prevent damage to the circuit's electronic components.

### 3.4 Nuclear spin assisted optical readout

Although for the measurements described in the thesis, single shot readout (SSR) was not available at room temperature. Methods such as nuclear spin-assisted readout can help achieve improved optical readout of NV electronic spin state, albeit with increased complexity in the system [226, 227]. In this section, I will briefly describe the physics behind such a method.

The electronic spin of the NV centre has the ability to interact with neighbouring nuclear spins. Notable nuclear species involved in this interaction include the intrinsic nitrogen nuclear spin of the NV centre, which possesses a total spin of either 1/2 or 1 for the isotopes  $^{15}\text{N}$  and  $^{14}\text{N}$ , respectively. Additionally, the carbon isotope  $^{13}\text{C}$ , with a total spin of 1/2, is also significant. The presence of  $^{13}\text{C}$  nuclei is generally stochastic in proximity to the NV centre having an isotopic abundance of 1.1%. Nuclear spins have significantly longer spin lifetimes compared to electrons [228]. Exploiting this property, they can be effectively employed as quantum memories [229].

Jiang et al. [226] was the first to showcase the basic concept behind nuclear spin-assisted readout for an NV centre. It involved capitalizing on the prolonged spin lifetime of nuclear spin and the capability to establish correlations between the states of the electron and nuclear spins using  $C_n\text{NOT}_e$  gates. This correlation enables the accumulation of photoluminescence (PL) signals over numerous consecutive readout cycles, thereby amplifying the signal-to-noise ratio (SNR). In preparation for measurement, the target electron spin state is transferred to the nucleus using a sequence of  $C_n\text{NOT}_e$  and  $C_e\text{NOT}_n$  gates (as depicted in Fig. 3.18). The subsequent readout procedure involves iteratively applying  $C_n\text{NOT}_e$  operations, which is followed by the usual PL readout of the electron spin state. In the initial readout cycle, the nuclear spin is projected into an eigenstate, and in an ideal scenario, each of the following cycles polarizes the electron spin while maintaining the nuclear spin unchanged. This permits the summation of photon counts from each readout cycle, enhancing the overall signal. However, in practice, the number of cycles is restricted due to the backaction from measurements, which eventually leads to the flipping of the nuclear spin.

In their experiment, Jiang et al. [226] employed a  $^{13}\text{C}$  nucleus exhibiting a relatively robust coupling of 14 MHz. The process of mapping and measuring was iterated 30 times, leading to a 2.2-fold enhancement in signal-to-noise ratio (SNR) compared to the conventional Photoluminescence (PL) technique. Later enhancements to the protocol, involving the utilization of a  $^{15}\text{N}$  nuclear spin, yielded a remarkable SNR increase of 6.8 times after performing 500 cycles [230]. However, the nuclear-assisted technique presents a significant technical challenge, demanding the implementation of intricate quantum-control pulse sequences for radio and microwave frequencies. It necessitates precise alignment of the externally applied DC magnetic field and the generation or identification of an NV centre coupled with a suitable  $^{13}\text{C}$  or  $^{15}\text{N}$  nucleus (where the natural abundance of  $^{15}\text{N}$  is 0.4%).

Despite their intricate nature, nuclear spin-assisted readout protocols have found widespread application in cutting-edge showcases of single-NV quantum sensors [231, 232]. In an ideal sce-

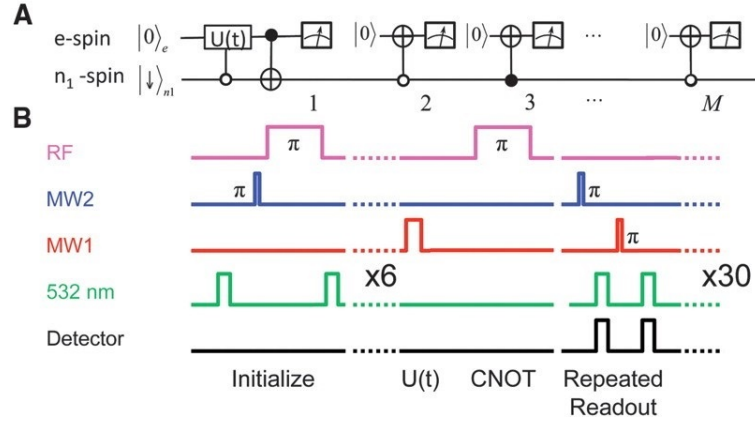


**FIGURE 3.18. Nuclear spin assisted repetitive readout.** (A) Quantum circuit implementing the repetitive readout scheme with  $M$  steps, enhanced by the interaction with spin  $n_1$ . (B) The procedures and pulse sequences for  $M = 60$  are as follows: The initial state  $|0\rangle_e |\downarrow\rangle_{n_1}$  is achieved using a 6-step process involving the manipulation of spins  $n_1$  and  $e$ . A microwave (MW1) pulse with a duration of  $t$  is applied, inducing Rabi nutation  $U(t)$  on electron spin. The parity information of this spin is then transferred to spin  $n_1$  through an RF  $\pi$  pulse, achieved by employing the  $C_e\text{NOT}_{n_1}$  gate. After reading the photoluminescence (PL) of the electron spin, repetitive readouts of  $n_1$  spin are carried out ( $M-1$ ) times. These readouts involve the utilization of either MW1 or MW2  $\pi$  pulses ( $C_{n_1}\text{NOT}_e$  gates), which are subsequently followed by PL readouts. However, the first readout iteration ( $m = 1$ ) does not precede a MW1 pulse. Figure adapted from [226].

nario, nuclear-assisted readout necessitates the fulfilment of certain criteria: the implementation of rapid  $C_n\text{NOT}_e$  operations to suppress measurement overhead, the involvement of a nuclear spin boasting a prolonged lifetime, and mitigation of non-secular components within the hyperfine Hamiltonian. These criteria somewhat conflict with each other, as swift gate operations tend to require relatively strong coupling, which, in turn, often results in shorter nuclear lifetimes and more substantial nonsecular terms. Nevertheless, these conditions can be practically satisfied using any of the common nuclear spins:  $^{14}\text{N}$ ,  $^{15}\text{N}$ , or  $^{13}\text{C}$ . The ultimate selection frequently hinges on the specific requirements of the experiment at hand. The main physical constraint in most experiments remains the presence of a small, yet non-negligible, likelihood of electron-nuclear flip-flops, particularly in the excited state of the NV centre. To mitigate these nonsecular terms, the option of utilizing coupled  $^{13}\text{C}$  nuclei aligned closely with the symmetry axis of the NV centre can be considered [233].

### 3.5 Characterisation of an NV centre

**Sample: Laser written NVs.** For the experiments discussed throughout this thesis, we used laser-written NV centres on an electronic-grade CVD diamond sample from Element Six. The concentration of natural NV centres in the bare high-purity samples was too low to find NV centres sufficiently close to the microwave wire.

The laser writing of the NV centres was carried out by our colleagues Dr Patrick Salter and

Prof Jason Smith at the University of Oxford. Typically, the laser writing process begins with a “seed pulse” to create an ensemble of vacancies. This pulse is followed by “annealing pulses” in the same region to induce vacancy diffusion. Which leads to the formation of the NV centres [234]. Another way to create NV centres is to place the sample with vacancies in a furnace with nitrogen atmosphere at 1000 °C [84].

Here, I examine the operation of our setup by performing an optical study of the laser-written NV sample. In Fig. 3.19, I have shown an example of a photoluminescence (PL) image of an NV centre taken with our scanning confocal microscope. Next, to verify that it is an NV centre, we used the Princeton Instruments IsoPlane SCT 320 triple-grating spectrometer in combination with liquid nitrogen-cooled PyLoN CCD to obtain a PL spectrum. The photoluminescence (PL) spectrum confirms the presence of an NV centre as shown in 3.20(a) [84, 235–237].

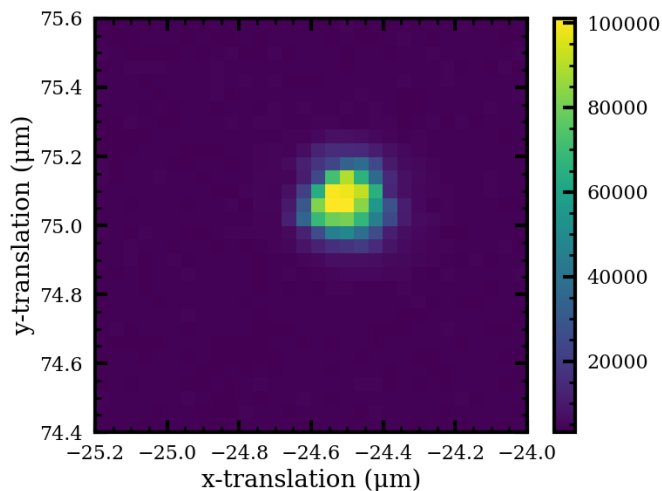


FIGURE 3.19. Photoluminescence (PL) image of an NV centre in diamond.

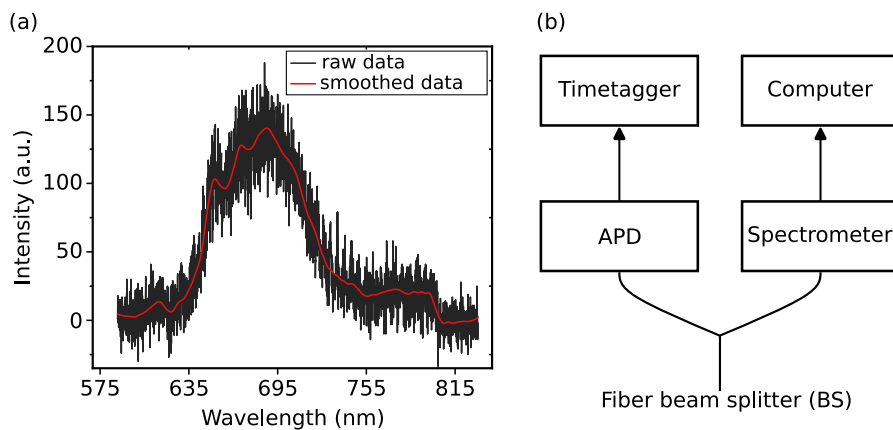


FIGURE 3.20. **(a)** Photoluminescence (PL) spectrum of an NV centre. **(b)** detection configuration utilising a 50:50 fibre beam splitter to track and record photoluminescence (PL) signal from an NV centre simultaneously.

It should be noted, however, that since the fluorescent spot size is significantly larger than the NV centre, more than one NV centre may exist within a single fluorescent spot. A well-known method of establishing that a fluorescence spot consists of a single photon emitter is to examine the photon statistics and observe anti-bunching dip [239–241]. This experiment requires an additional single photon counting module (SPCM), a fibre beam splitter (BS) (Thorlabs TW670R5F1), and a time tagger (see Fig. 3.21(b)). Using the arrangement shown in Fig. 3.21(b),

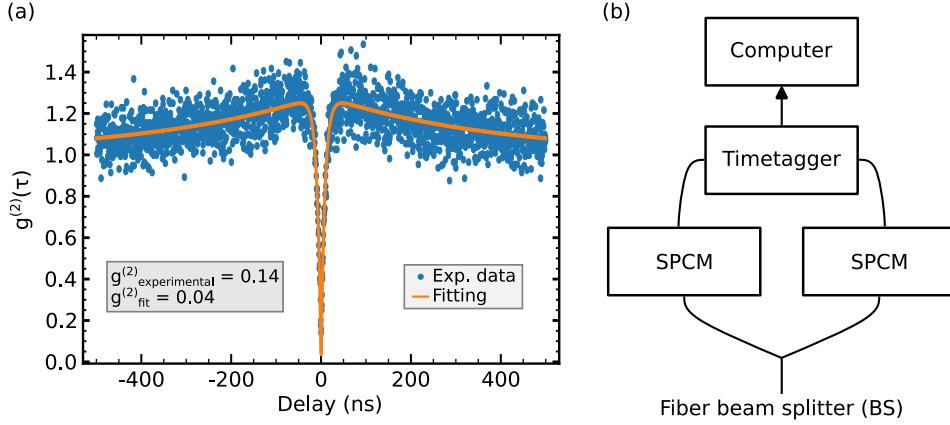


FIGURE 3.21. **Autocorrelation measurement.** (a) Second order correlation function of a single photon emitter showing a characteristic dip with  $g_{exp}^{(2)}(0) = 0.14$  and  $g_{fit}^{(2)}(0) = 0.04$ . The data was fitted to  $1 - (s + 1/2)e^{-\lambda_2 t} + (s - 1/2)e^{-\lambda_3 t}$ , which is derived from the rate equations of the NV centre [238]. The shoulders near 0 delay time are the signature of shelving in the singlet state with a bunching timescale of  $\sim 390$  ns. (b) Diagram illustrating the detection configuration for correlation measurements.

we measured the second-order correlation function, as shown in Fig. 3.21(a). The experimental value of the photon antibunching signal was found to be  $g_{exp}^{(2)}(0) = 0.14$ . The experimental data was fitted to  $1 - (s + 1/2)e^{-\lambda_2 t} + (s - 1/2)e^{-\lambda_3 t}$  [238]. Where this function is derived from the rate equations of the NV centre; for more details, refer to Chap. 2 in [238]. Using this fitting function, the value of  $g_{fit}^{(2)}(0)$  was found to be 0.04, with an anti-bunching and bunching timescale of  $\sim 8.6$  ns and 390 ns, respectively. A further correction to the data is possible by accounting for the incoherent background signal as done in [242, 243], but this correction has not been done in this case. This antibunching dip is a hallmark of a single quantum emitter. In Fig. 3.21(a), the delay time is characterized as the time interval between the moment when one single-photon counting module (SPCM) detects the arrival of a photon and the subsequent detection by the second SPCM.

Next, we performed a power saturation measurement to extract the saturating power. Fig. 3.22 shows a power saturation curve for the NV centre. The red line is the fitting done using the power dependence model,  $I(P) = I_{sat}/(1 + P_{sat}/P)$  [244].  $I$  is the recorded intensity,  $P$  is the applied laser power, and  $I_{sat}$  and  $P_{sat}$  are the corresponding saturation intensity and power. Fit gives a value of  $\sim 60 \pm 0.7$  kcps for saturation intensity and  $0.75 \pm 0.05$  mW for saturation power.

Following the discussion of the NV centre.

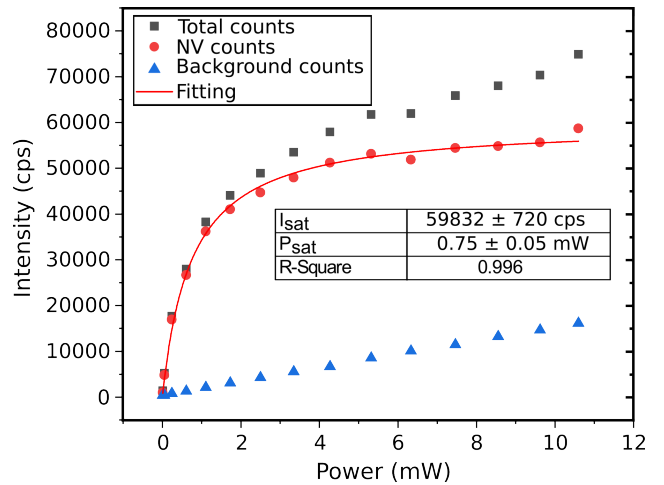


Figure 3.22: Power saturation curve of a single NV centre.

centre as a three-level system in Sec. 1.3, which leads to spin polarization and spin-dependent optical contrast, a similar picture can be used to explain this saturating behaviour as well. The relaxation rate between these levels varies based on the incident power and temperature [245]. According to [240], this power dependence is linear and  $\kappa_{23} > \kappa_{32}$ . Thus, with the increased power of the excitation laser, the system tends to be shelved into the intermediate level, which ultimately decreases total photon counts, as shown in Fig. 3.22.

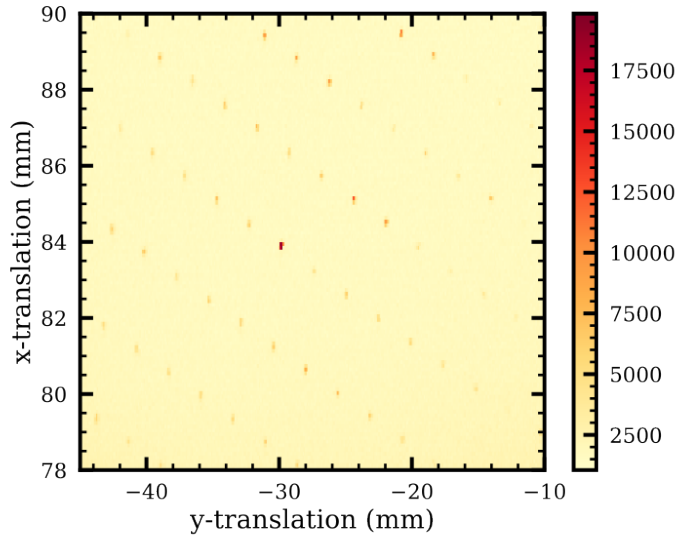


FIGURE 3.23. Large area photoluminescence (PL) map of the laser written sample, with bright spots showing the NV centres.

Our setup's wide lateral scan range is one of its important features (see Fig. 3.7). Using this, we performed a lateral scan of  $35 \times 12 \mu\text{m}^2$  area and mapped arrays of laser-written NV centres, as shown in Fig. 3.23.

### 3.5.1 Basic electron spin measurement and control

As discussed in Sec. 1.3, due to the presence of inter-system crossing, not only the NV centres can be optically polarised, but they also give a spin-state-dependent fluorescence signal. This polarization of the NV centres can be used to manipulate the associated spin via the application of microwaves (MWs). In the sections below, I will describe some of the basic spin experiments done on a single NV centre to test the working of microwaves and the electronics involved in our setup. A more detailed discussion on the electronics for adaptive experiments can be found in Sec. 3.8.

### 3.5.2 Optically detected magnetic resonance (ODMR)

As depicted in Fig. 1.10, the electronic ground state of an NV centre forms a spin triplet, exhibiting a zero-field splitting of 2.87 GHz between the states  $|m_s = 0\rangle$  and  $|m_s = \pm 1\rangle$ ,  $\hat{a}^{\text{TM}}$  at room temperature. The spin states  $|m_s = \pm 1\rangle$  are degenerate. This degeneracy can be lifted by applying an external magnetic field along the NV axis defined by the nitrogen-vacancy bond. The presence of such an external field can Zeeman split the spin states by  $\Delta f = 2 \gamma_{NV} B_z$ , with the NV gyromagnetic ratio given as  $\gamma_{NV} = 28.024 \text{ GHz/T}$  [95]. This change can be quantified through the implementation of an optically detected magnetic resonance (ODMR) experiment. During ODMR, a microwave signal is scanned in frequency under non-resonant illumination with a 532 nm green laser while counts from the NV centre are continuously monitored. In the absence of resonance between the microwave signal and any of the spin transitions, the NV centre remains consistently driven into its  $m_s = 0$  state. As the microwave frequency nears the resonance of the NV centre, the population transfer from the  $m_s = 0$  state to the  $m_s = +1$  or  $m_s = -1$  state increases, leading to lower photon emission as shown in Fig. 3.24. This difference in brightness is due to the longer lifetime of  $m_s = \pm 1$  states in comparison to  $m_s = 0$ .

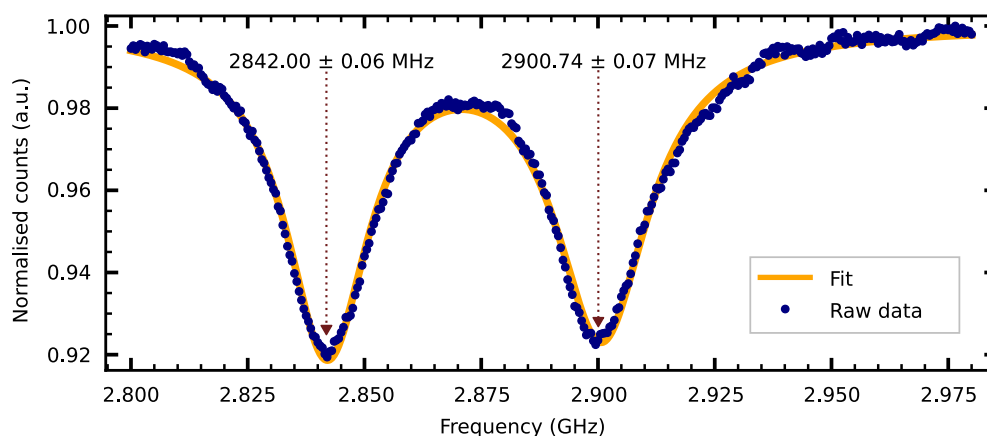


FIGURE 3.24. Optically detected magnetic resonance (ODMR) signal from an NV centre in diamond at an applied field of about 1.05 mT.

Three different mechanisms govern the linewidth of these resonances. Firstly, the natural linewidth of spin states, or  $1/T_2^*$ , sets a minimum limit for the linewidth of any measurement. Secondly, re-initialising the NV centre via a non-resonant optical driving of the system results in power broadening. Finally, microwaves for spin driving, similar to the optical drive, cause further power broadening. The total linewidth hence can be given as [105]:

$$(3.11) \quad \Delta\nu = \frac{\Gamma_c^\infty}{2\pi} \sqrt{\left(\frac{s}{1+s}\right)^2 + \frac{\Omega_R^2}{\Gamma_p^\infty \Gamma_c^\infty}}$$



where  $\Gamma_c^\infty, \Gamma_p^\infty$  are the optical cycle and polarisation rates at saturation, respectively.  $\Omega_R$  is the Rabi frequency. While  $s = P_{opt}/P_{sat}$  is a ratio of the transition's pump power and saturation power.

Although ODMR is probably the easiest way to measure the  $|m_s = 0\rangle \longleftrightarrow |m_s = \pm 1\rangle$  frequency change (see Sec. 3.5.2). A sensitive measurement of the ODMR dip frequency is usually achieved by parking the MW source at a frequency where the counts from the emitter are most sensitive to any change in resonance frequency, such as a point of the steepest slope. In such an ODMR measurement, the smallest detectable change in frequency is given as [238]:

$$(3.12) \quad \Delta f_{min} = \frac{\Gamma}{\sqrt{CT}\eta}$$

where  $\Gamma$  is the FWHM of the transition,  $T$  is the total acquisition time,  $C$  is the total photon count rate, and  $\eta$  is the resonance contrast. Hence for a typical case, with  $C = 80$  kHz,  $\eta = 20\%$ ,  $\Gamma = 20$  MHz, the maximum achievable sensitivity with CW ODMR is  $\Delta f_{min}/\gamma = 126 \mu\text{T}/\sqrt{\text{Hz}}$ . If we want to better this sensitivity by avoiding limitations enforced by power broadening, we must look towards interferometric measurement protocols such as Ramsey interferometry.

### 3.5.3 Rabi oscillations

Using microwave pulses to control electronic spins requires that we carefully characterize the AC magnetic field that drives the spins. Specifically, we need to know the times for  $\pi/2$  and  $\pi$  rotations since these will be used for the pulsed experiments. For a two-level spin system, the Hamiltonian can be written as:

$$(3.13) \quad \hat{H} = \hat{H}_0 + \hat{H}_I(t)$$

here,  $\hat{H}_0$  represents the unperturbed system's Hamiltonian, while  $\hat{H}_I(t)$  accounts for the time-varying interaction with the applied alternating field. Assuming that the system is polarised into  $m_s=0$ , to begin with, the general solution to Eqn. 3.13 can be given as [105]:

$$(3.14) \quad |c_1(t)|^2 = \frac{\Omega^2}{\Omega^2 + \Delta^2} \sin^2\left(\frac{\sqrt{\Omega^2 + \Delta^2}}{2}t\right)$$

where  $\Delta$  represents the detuning from the transition frequency, while the term  $\sin^2$  oscillates with a frequency of  $\sqrt{\Omega^2 + \Delta^2}$  in time. These oscillations are known as Rabi nutations, and for the case of NV centres, they were first observed by Jelezko et al. [246].

One thing to note is that the Hamiltonian given in Eqn. 3.13, does not capture the effect of decoherence. The Rabi oscillations are acquired by applying successive pulses of laser light for initialization of the spin state into  $m_s = 0$ , which is followed by a microwave (MW) pulse

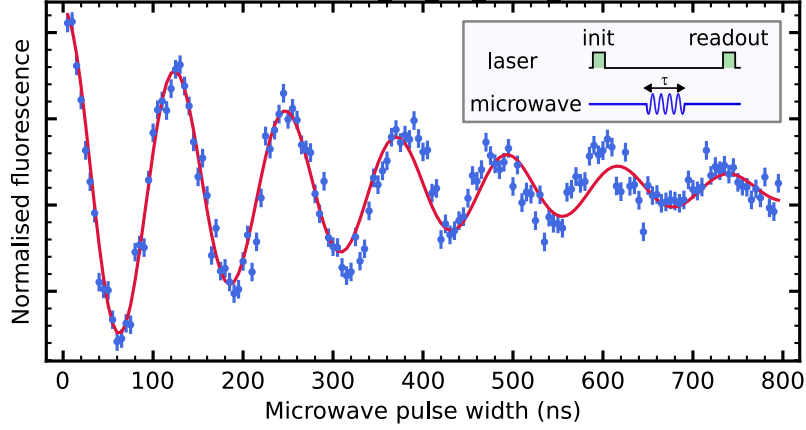


FIGURE 3.25. Rabi oscillations of an ensemble of spin qubits via the application of microwave (MW). Following the literature [247] the data was fitted to  $A \cdot \cos(2\pi\Omega t + \phi) \cdot \exp(\frac{t}{T_{rabi}}) + C$  with the  $T_{rabi}^{fit}$  value of  $297.8 \pm 18.1$  ns and  $\Omega_{rabi} = 8.12 \pm 0.03$  MHz. Here  $T_{rabi}^{fit}$  describes the duration up to which a spin transition in the ensemble can be driven before it dephases into a mixed state. **Inset:** Shows the pulse sequence used for the rabi oscillation experiment.

whose length is varied before a second pulse of laser light is applied to read out the spin state (see inset of Fig. 3.25). Rabi oscillations (for an NV ensemble) obtained for  $m_s = 0 \longleftrightarrow m_s = -1$  transition are displayed in Fig. 3.25. The data has been fitted to an exponentially decaying sinusoid equation given as [247]:

$$(3.15) \quad A * \cos(2\pi\Omega t + \phi) * \exp(\frac{t}{T_{rabi}}) + C$$

here  $A$  is the Rabi oscillation amplitude, and  $C$  is an offset.  $\Omega$  is the rabi frequency with the extracted value of  $\Omega = 8.12 \pm 0.03$  MHz and a characteristic decay time of  $T_{rabi} = 297.8 \pm 18.1$  ns.

### 3.5.4 Ramsey interferometry

As stated earlier, for an NV centre, an externally applied magnetic field causes a Zeeman splitting of its spin states, leading to the spin levels  $m_s = \pm 1$  being shifted by  $\Delta f = 2\gamma B_{ext,z}$ , here  $\gamma = 28.024$  GHz/T [95] is the electron's spin gyromagnetic ratio and  $B_{ext,z}$  is the component of external field along the NV axis. A similar effect is given by an external electric field which shifts the frequency of  $|m_s = 0\rangle \longleftrightarrow |m_s = \pm 1\rangle$  transition. For our case of this thesis, however, we are mainly focusing on the DC sensing of the magnetic field, so we will describe the Ramsey measurement in regards to that.

A Ramsey measurement begins with initialising the spin into the  $|0\rangle$  state via a 532 nm green laser pulse. This is followed by an application of a  $\pi/2$  (along  $\sigma_y$  for  $|0\rangle \longleftrightarrow |+1\rangle$  or along  $\sigma_x$  for  $|0\rangle \longleftrightarrow |-1\rangle$ ) MW pulse to create a superposition state. This state is allowed to evolve under the external field for a varying amount of time  $\tau$ , which leads to an acquisition of a phase  $\theta$  due to such an interaction. This phase is given as  $\theta = (\frac{g\mu_B}{\hbar}) B\tau$  [248], here  $\tau$  is the free evolution time,

$B$  is the applied field, and  $\mu_B$  is the Bohr magneton. This phase can be read out by applying another  $\pi/2$  pulse, which projects the phase gain into the population difference. This population difference is then converted into photon counts via the application of a final off-resonant laser pulse (see inset of Fig. 3.26). Hence, an interferometric pattern can be obtained by varying the time between the two  $\pi/2$  MW pulses, as shown in Fig. 3.26. During the Ramsey measurement, different phase gain for each run due to an oscillating environment is averaged out, leading to a diminished  $T_2^*$ . For such a measurement, the maximum achievable sensitivity is limited by  $T_2^*$  and an order of magnitude better than CW ODMR. A Ramsey interferometric pattern is shown in Fig. 3.26, which was fitted to  $y_0 + A \cdot \exp(-\frac{\tau}{T_2^*})^2$ . Here  $y_0$  is the offset,  $A$  represents amplitude, and  $\tau$  is the delay time. We extracted the corresponding value of  $T_2^{*fit}$  to be  $2.58 \pm 0.2 \mu\text{s}$ .

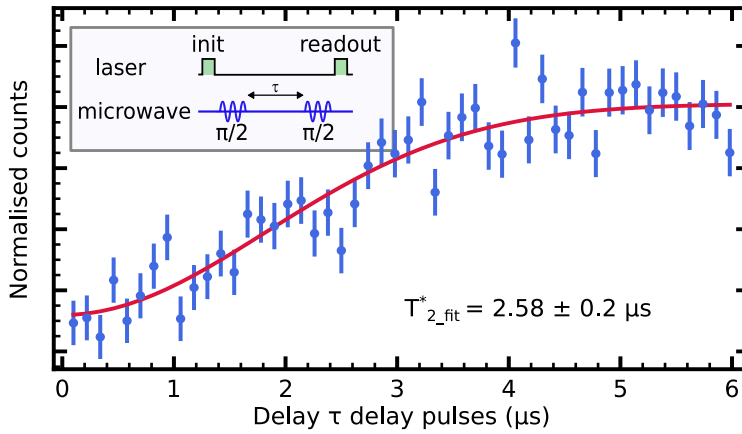


FIGURE 3.26. Ramsey decay of the NV spin qubit via the application of microwave (MW) on resonance with  $|m_s = 0\rangle$  to  $|m_s = -1\rangle$ . The data was fitted to  $y_0 + A \cdot \exp(-\frac{\tau}{T_2^*})^2$  with the  $T_2^{*fit}$  value of  $2.58 \pm 0.2 \mu\text{s}$ . Here the N nuclear spin is polarised by using an external magnetic field of  $\sim 512$  G. Inset: Shows the pulse sequence used for the Ramsey oscillation experiment.

### 3.5.5 Longitudinal relaxation time $T_1$

We characterised the  $T_1$  relaxation time for a single NV by polarising the spin into  $|m_s = 0\rangle$  spin state with a non-resonant 532 nm laser pulse, which was followed by another non-resonant pulse to read out the current population after some delay time  $\tau$  (see inset of Fig. 3.27). Repeating this measurement for different delay times  $\tau$  gives a decaying curve as shown in Fig. 3.27. The curve was fitted to  $y_0 + A \cdot \exp(-\frac{\tau}{T_1})^1$ , from which we extracted the spin relaxation time  $T_1$  to be  $4.36 \pm 0.92$  ms.

### 3.5.6 Hahn echo

To perform a Hahn echo experiment, an additional  $\pi$  pulse is applied between the two MW pulses used for the Ramsey measurement. This additional  $\pi$  pulse cancels out any acquired phase during

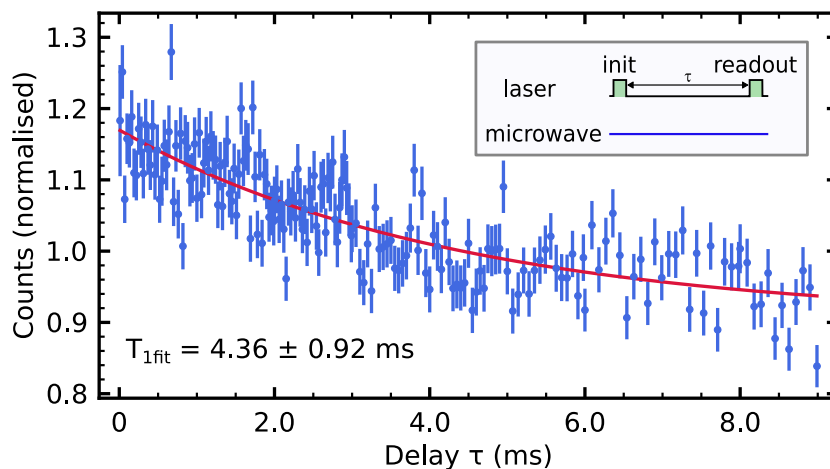


FIGURE 3.27.  $T_1$  measurement of a single NV centre. The data was fitted to  $y_0 + A \cdot \exp(-\frac{\tau}{T_1})$  with the  $T_1^{fit}$  value of  $4.36 \pm 0.92$  ms. Inset: Shows the pulse sequence used for the  $T_1$  estimation.  $\pi/2 \rightarrow \pi$  and  $\pi \rightarrow \pi/2$  intervals. Making this sequence non-sensitive to a DC/slowly varying field. The results obtained from such a measurement are shown in Fig. 3.28 with a corresponding pulse sequence shown in the inset. The data in Fig. 3.28 was fitted to  $y_0 + A \cdot \exp(-\frac{\tau}{T_2})$ . From this, we extract the coherence time  $T_2 = 87.1 \pm 8.3 \mu\text{s}$ .

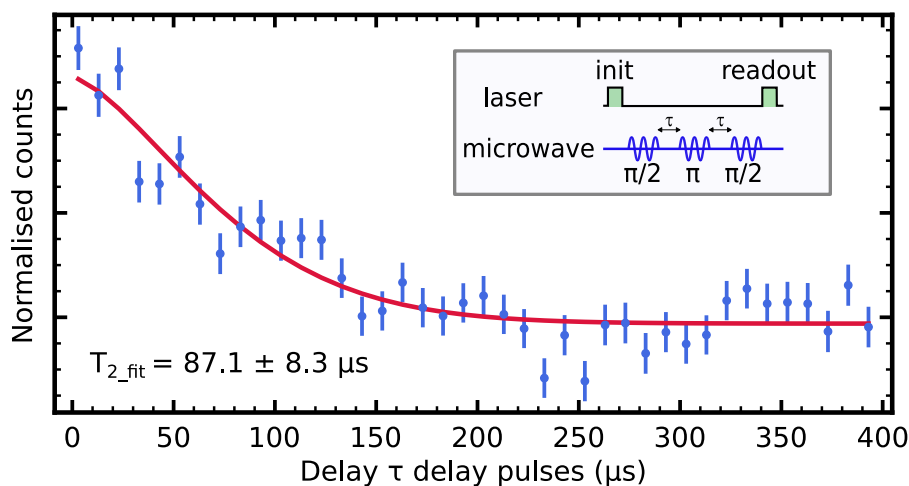


FIGURE 3.28. Spin echo  $T_2$  measurement of a single NV centre. The data was fitted to  $y_0 + A \cdot \exp(-\frac{\tau}{T_2})$  with the  $T_2^{fit}$  value of  $87.1 \pm 8.3 \mu\text{s}$ . Here the N nuclear spin is polarised by using an external magnetic field of  $\sim 512$  G. Inset: Shows the pulse sequence used for the  $T_2$  estimation.

### 3.6 Nuclear spin polarisation

The NV centre hosts a nitrogen atom, which can either be  $^{14}\text{N}$  (nuclear spin  $I = 1$ ) or  $^{15}\text{N}$  (nuclear spin  $I = 1/2$ ). In some cases, the nitrogen nuclear spin can be used as an ancillary qubit, for

example, as a quantum memory. In other situations, however, the presence of hyperfine lines in the electron spin resonance spectrum can be a problem, for example, when estimating frequencies associated with static magnetic fields (as it significantly complicates the signal). In such scenarios, it is possible to polarize the nitrogen nuclear spin in a manner that eliminates the presence of hyperfine frequencies.

In NV centres, nuclear spin polarisation has been successfully demonstrated for each of the  $^{14}\text{N}$  and  $^{15}\text{N}$  spins of the nitrogen atom [249, 250], along with ensembles of  $^{14}\text{N}$  spins at excited-state level anticrossing (ESLAC) around 512 G and even for the  $^{13}\text{C}$  spins proximal to the nitrogen atom [251, 252]. The hyperfine interaction close to the ESLAC points creates hyperfine states that couple the spins of electrons to the nucleus or from one nucleus to another. Several models have been developed to describe experimental results that measure nuclear spin polarization, including ones based on rate equations, [249] and those based on the Lindblad operator combined with the Liouville equation for the density matrix [253], as a method to describe how the spin projection states transition from one to another [250–252].

It has been shown that the nuclear spin polarization at the ESLAC is extremely sensitive to the angular deviation of the applied magnetic field from the NV axis [249]. Since the optical pumping polarises the spin into three hyperfine states  $|m_s = 0, m_I = 0, 1, -1\rangle$  while depleting the other three states  $|m_s = -1, m_I = 0, 1, -1\rangle$ , around the magnetic field value of  $\sim 512$  G, corresponding to the level anti-crossing. At that field, magnetic sub-levels of  $m_s = 0$  align with

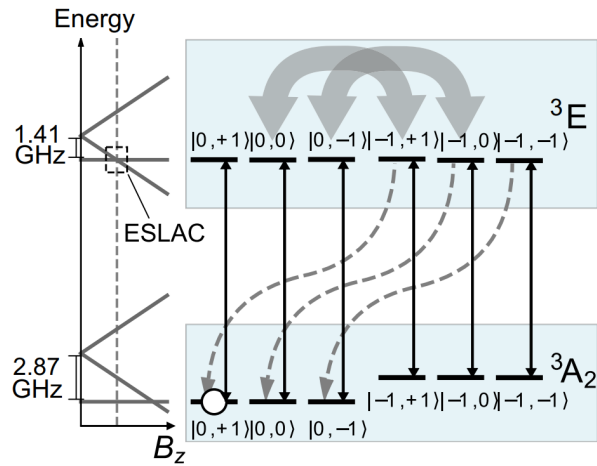


Figure 3.29: Nuclear spin polarisation at excited state level anticrossing. Figure adapted from [254].

As shown in Fig. 3.29, in the  $m_s = 0$  manifold, only the hyperfine spin level

$|m_s = 0, m_I = +1\rangle$  stays unmixed and hence protects its population. While due to the presence of the hyperfine interaction, the state  $|m_s = -1, m_I = +1\rangle$  is mixed with the  $|m_s = 0, m_I = 0\rangle$ , and the state  $|m_s = -1, m_I = 0\rangle$  is mixed with the  $|m_s = 0, m_I = -1\rangle$ . This mixing, along with the continuous excitation cycle and nonradiative decay, polarises the nuclear spin into the protected state  $|m_s = 0, m_I = 1\rangle$  (see Fig. 3.29). For this mixing to happen, projections of the electron angular momentum of the mixing partners should be equal to the sum of their nuclear angular momentum projections [255]. As a result, this level mixing close to the ESLAC causes the  $^{14}\text{N}$  nuclear spin to be polarised into the state  $|m_s = 0, m_I = +1\rangle$  since this is protected from level mixing.

As shown in Fig. 3.30(a), electron-nuclear hyperfine interaction can cause collapse and revivals

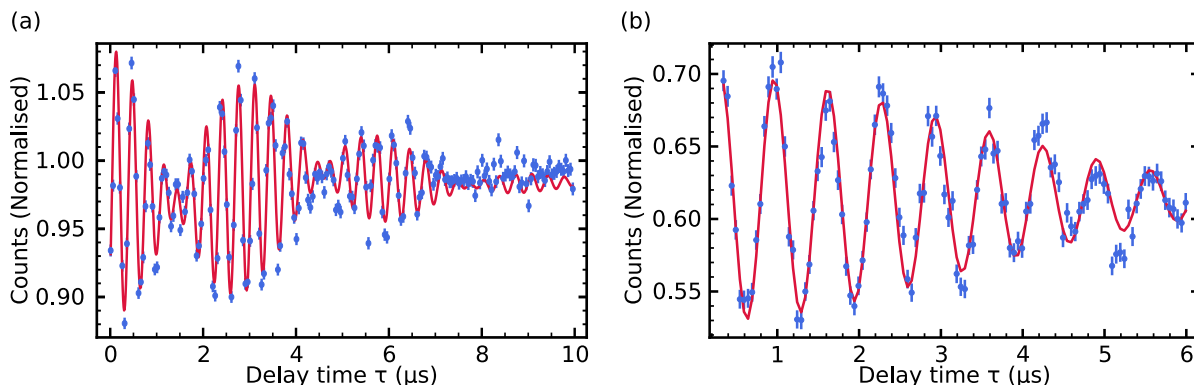


FIGURE 3.30. **Ramsey with and without nitrogen contribution.** **a** Collapse and revival in Ramsey plot due to nearby nuclear spin contributions. **b** Ramsey signal with polarised nuclear spin and applied detuning of 1.5 MHz showing clean oscillations.

in measurements like Ramsey and spin echo. Data in Fig. 3.30(a) is fitted according to

$$(3.16) \quad a_0 + e^{-\left(\frac{t}{T_2^*}\right)^2} \cdot \sum_{i=1}^3 (a_i \cos(2\pi(f_{det} - f_b) * t + \phi_i))$$

Our adaptive experiments discussed Chap. 4 and Chap. 5 requires the polarisation of nuclear spin to avoid beatings in the free induction decay signal. Once the nuclear spin is polarised, we can eliminate these beatings and get a clean oscillating signal at the applied detuning, as shown in Fig. 3.30(b), where a detuning of 1.5 MHz is applied.

### 3.6.1 Magnetic field alignment

High-fidelity operations on the NV centre spin require the externally applied magnetic field to be well-aligned along the NV quantization axis.

Any significant spin mixing that is caused by an off-axis magnetic field can result in a rapid reduction in the contrast of optically detected electron spin resonance (ESR) spectra since the spin-dependent photoluminescence (PL), and optically induced spin polarization are no longer effective because of the spin mixing. In addition to a decreased contrast in ESR, an increased off-axis magnetic field is also observed to decrease the effective excited state lifetime and the PL intensity [256, 257]. In a recent paper [258, 259], it was demonstrated that this property can be harnessed as a tool for performing all-optical mapping of magnetic fields through the scanning of an NV defect. We also exploit this property to align the externally applied magnetic field. In our setup, we have a magnetic field of 460 gauss, precisely aligned along the NV axis. This field is established using a permanent SmCo magnet situated on a motorized 3D translation stage (Standa 8MT173-30DCE2-XYZ).

We used SmCo magnets in place of more widely known neodymium since the output flux of the SmCo magnets varies three times less with temperature compared to the neodymium [260]. The magnetic field is precisely selected at the level anti-crossing point of the NV centre’s excited state to effectively polarize the nuclear spin of  $^{14}\text{N}$ . This polarization ensures the absence of collapse and revivals in the Ramsey signal (see Fig. 3.30).

Encased within a 3D-printed holder, the magnet is thermally stabilized using a Peltier element, controlled through a PID loop (Meerstetter TEC-1091), achieving thermal stability with an RMS temperature of 10 mK, which helps stabilise the ESR frequency to less than 100 kHz (see Sec. 3.7 for more details). To align the  $\mathbf{B}$  field, we scan the magnet across the sample and find the spot with the highest PL intensity as shown in Fig. 3.31, corresponding to the magnet aligned with the NV axis.

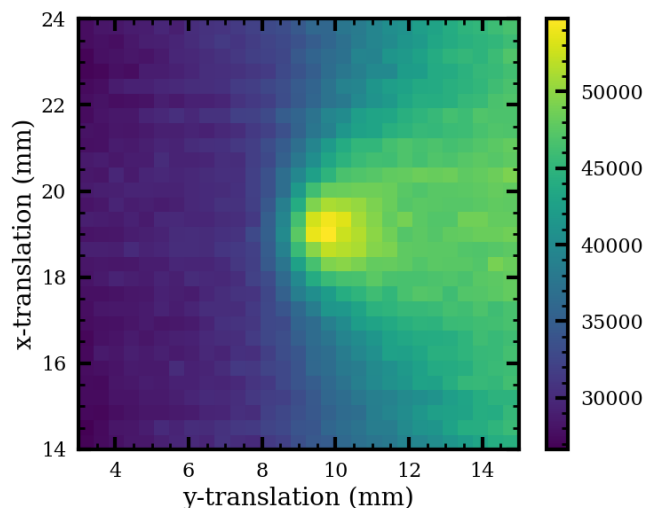


FIGURE 3.31. **Map of magnet scan across the sample.** Location with maximum counts highlights the position of maximum alignment of the field with the NV axis.

### 3.7 Temperature stability of the setup and magnet

Temperature stability has been one of the major issues we faced while setting up the optical setup in the lab. Our lab does not have any active temperature-controlling mechanisms installed. Additionally, the air conditioner used to cool/heat the lab blew air directly towards the optical table. This led to temperature instabilities in the experimental setup with a  $\sim 25$  minutes oscillation cycle, matching the cooling cycle of the air-conditioning system, as shown in Fig. 3.32(left). These temperature fluctuations were also reflected in the counts as shown in Fig. 3.32(right).

Along with these periodic fluctuations, our setup was also hampered by slow drifts of the XYZ sample stage. These drifts made the objective move out of focus from the position of the emitter leading to an unrecoverable drop in the PL intensity. These drifts in temperature with the corresponding change in the movement of the XYZ sample stage are highlighted in Fig. 3.33. Although the change in the XY direction is much less (few nm) than a change in the Z position (few  $\mu\text{m}$ ), and given the confocal resolution in the z-axis is much worse than xy resolution; still, this change was big enough that we lost a significant amount of the counts over a short time period as shown in Fig. 3.33(c). For clarity, the counts shown in Fig. 3.33(c) were not recorded precisely during the same time as the data shown in Fig. 3.33(a) or (b). However, the data in Fig.

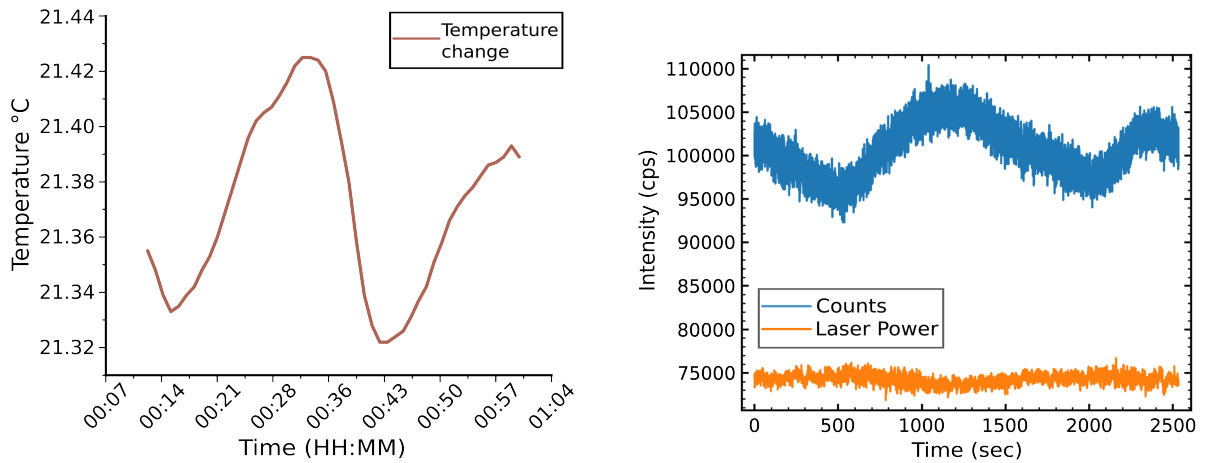


Figure 3.32: **Periodic counts fluctuations due to the air conditioner’s cooling cycle.** **Left:** Temperature oscillations in the lab recorded with a Tinytag Talk 2 - Temperature logger. **Right:** Counts fluctuations showing a periodic behaviour. Laser power has been plotted (without units) to rule out any fluctuations in laser intensity being the cause of these oscillations in counts.

3.33(c) indicates the effect of such temperature changes.

We designed a temperature stabilisation system to address these issues, which were preventing us from doing any meaningful measurements. First of all, we built a styrofoam-based box around the optical setup (see Fig. 3.34) to protect it from the air currents generated by the air conditioner blowing. This step was sufficient to eliminate the periodic oscillation of the counts but did not solve the full problem. Hence we decided to actively control the temperature of the platform holding the XYZ stage using a PID-controlled Peltier element (Meerstetter TEC-1092), stabilising the temperature down to less than 10 mK RMS (see Fig. 3.35).

Styrofoam box and temperature control solved the problem of count instability, as shown in Fig. 3.36. Our count rates are currently very stable even for measurements spanning several days.

### 3.7.1 Temperature stability of the magnet

Another issue with temperature fluctuations is that they induce changes in the magnetic field of permanent magnets. This is a big problem, as it changes the resonance frequency of the NV electron spin over time.

Although SmCo magnets that we used in the experiments done in Chap. 4 and 5 have a much better thermal response than neodymium magnets, with a temperature coefficient of approximately -0.04% per degree C. Still, the significant instability of the temperature in our lab meant we had to actively control the temperature of the magnets as well. We recorded the change in resonance frequency of  $|m_s = 0\rangle$  to  $|m_s = -1\rangle$  transition over a period of 6 hours as shown in Fig. 3.37(a), showing a peak to peak variation of  $\sim 800 - 900$  KHz. For experiments performed in Chap. 4 and Chap. 5, we wanted to control the field so that we get the minimum



### 3.7. TEMPERATURE STABILITY OF THE SETUP AND MAGNET

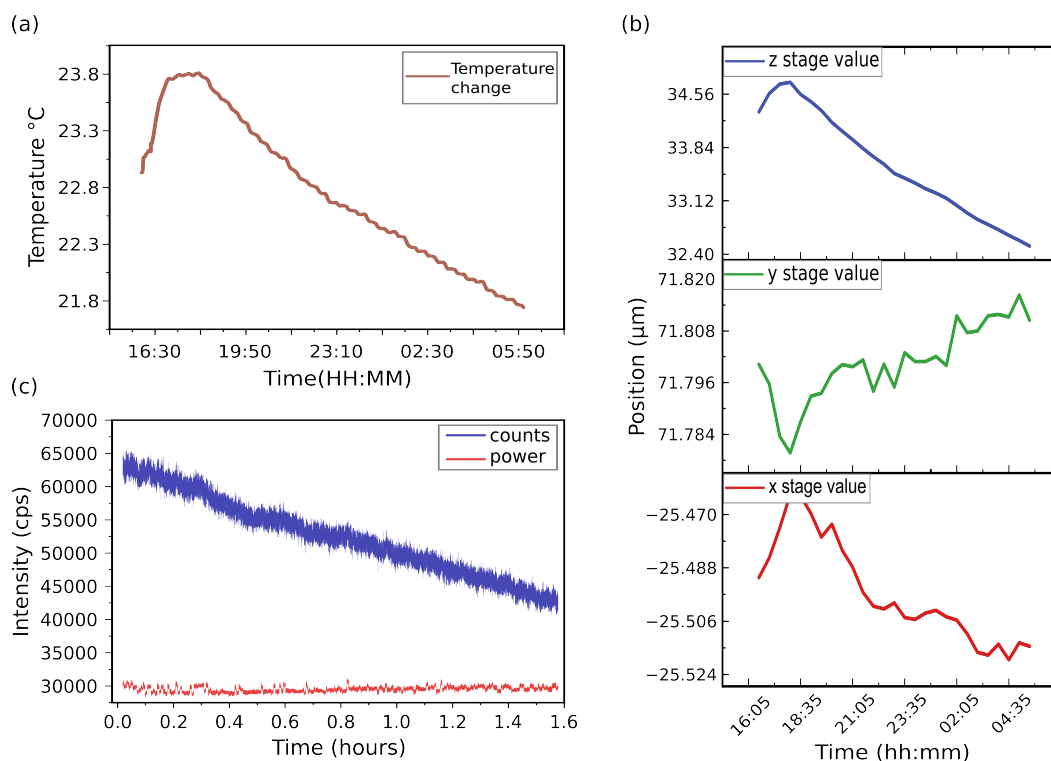


Figure 3.33: **Slow drift of XYZ stage.** (a) Change in lab temperature recorded during night time. (b) The corresponding change in position of XYZ stage. (c) Shows the effect of such temperature change on the counts from an NV centre; power has been multiplied by  $6.2e6$  to view it better on the graph. The temperature in the lab was recorded with a Tinytag Talk 2 - Temperature logger.

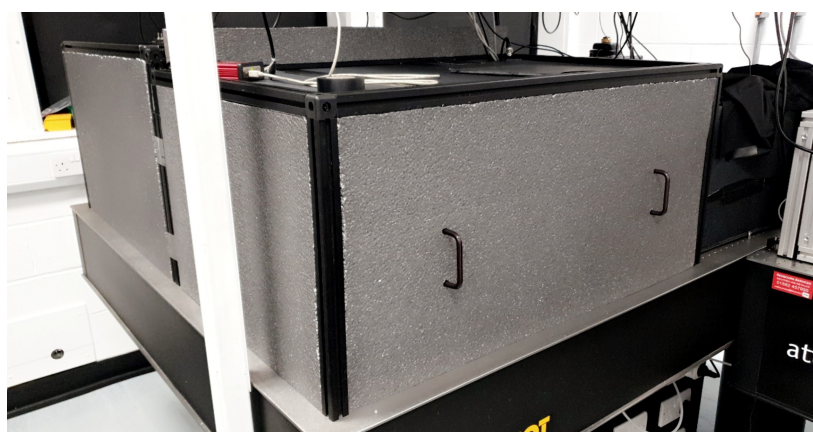


FIGURE 3.34. Styrofoam box built to isolate optical setup from direct air currents.

ESR frequency deviation. For this reason, we also installed another temperature controller (Meerstetter TEC-1091) to stabilise the magnets. After installing the TEC, we managed to get the frequency drifts to less than 100 kHz, as shown in Fig. 3.37(b).

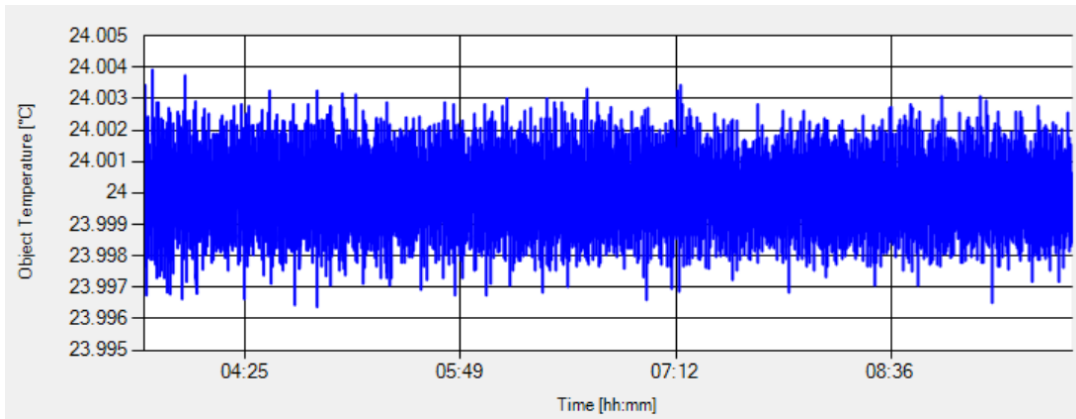


FIGURE 3.35. Temperature of the XYZ stage recorded over a period of 6 hours via the TEC software.

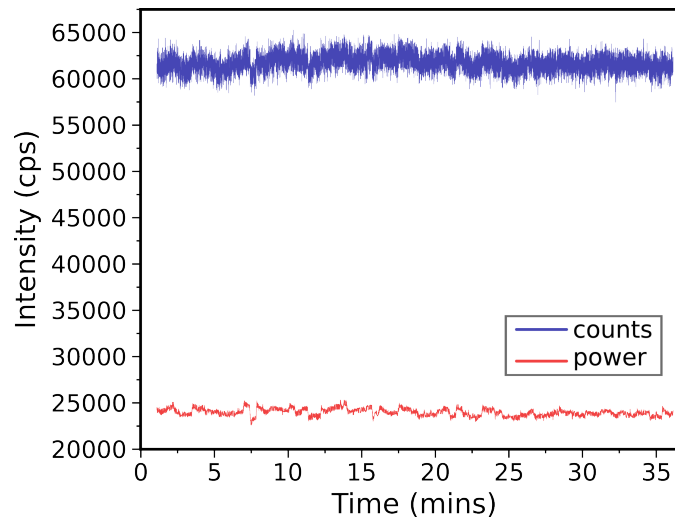


FIGURE 3.36. Stability of the counts recorded after installing the temperature controller and styrofoam box. Power has been multiplied by  $5.17 \times 10^6$  to view it better on the graph.

### 3.8 Adaptive electronics

This section details the electronic setup used to perform the adaptive experiments discussed in Chap. 4 and 5. This is the really innovative part of the setup, which enabled us to perform adaptive optimisation of experimental settings in less than  $100\mu\text{s}$ , an order of magnitude faster than the best reported in the literature (see Chap. 4). The main components of the adaptive electronics are shown in Fig. 3.38. In the sections below, we describe the details and working of each component separately.

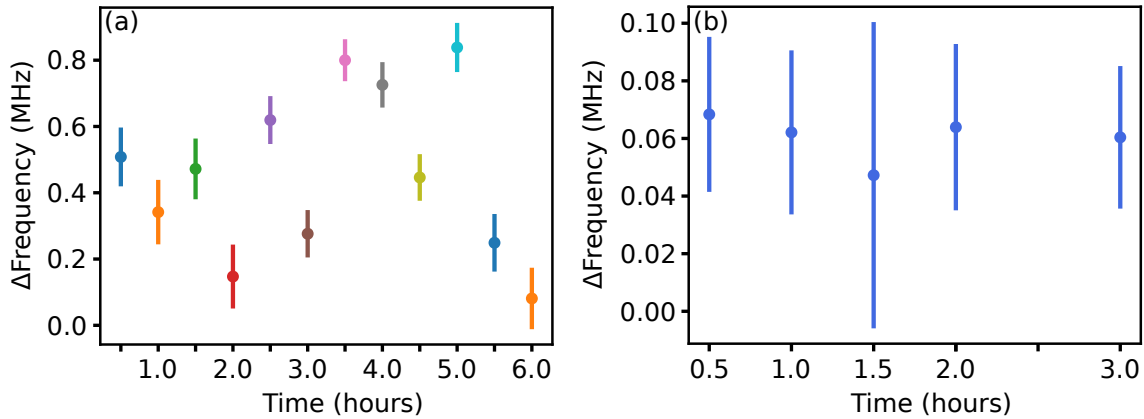


Figure 3.37: **Change in resonance frequency of  $|m_s = 0\rangle$  to  $|m_s = -1\rangle$  transition due to temperature change of magnets. (a):** Before installing the temperature controller. Frequency stability extracted via ODMR measurement. **(b):** After installing the temperature controller. Frequency stability extracted via Ramsey measurement.

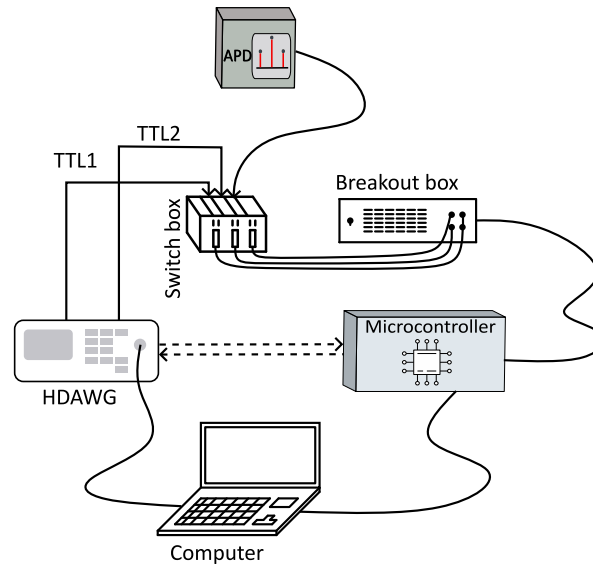


Figure 3.38: Schematic showing the connection of main electronics elements for adaptive sensing experiments described in Chap. 4 and 5.

### 3.8.1 Microcontroller - ADwin-Pro II

For the adaptive experiments described in Chap. 4 and 5, we employed a hard real-time microcontroller (ADwin Pro II) from Jäger Computergesteuerte Messtechnik, capable of achieving high performance using the new processor module T12 with a clock rate of 1 GHz, a memory of 1 GB, and a 64-bit FPU (double precision) for the calculation of floats. It is conveniently programmed in a proprietary version of BASIC.

As a result of the extremely short response times, even open and closed loop processes on the processor with cycle frequencies well over 1 MHz are reliably carried out on the processor with concise response times. The fast processor allowed us to update the probability distribution and calculate the optimal settings with minimum overhead time. Another advantage of the microcontroller comes with the analogue output modules. Using these synchronous data output can be achieved on four channels without the possibility of time offsets. The DACs offer a wide range of frequency responses and have a resolution of 16 bits. For our case of adaptive decoherence and frequency estimation, we use this micro-controller to process the information received from the photo-detectors, using that information and the specific likelihood function for each estimation (see Chap. 4 and 5 for more details on this) we update the probability distribution which characterises our knowledge about the unknown quantity. In our experiments, we use 100 particles to represent a probability distribution curve corresponding to the unknown quantity. During each iteration, we need to update this probability distribution. Using a microcontroller helps us achieve this update in less than 30  $\mu$ s (see Fig. 3.51). A time that is negligible compared to the total estimation cycle time, meaning little to no overhead is added to the total experiment time.



FIGURE 3.39. ADwin Pro II.

### 3.8.1.1 Communication of ADwin

ADwin has two 37-pin D-SUB sockets with 32 digital input and output (DIO 00 ... DIO 31) ports. All of these 32 ports are programmable via the ADbasic software in blocks of 8 bits as either inputs or output ports. The pin configuration of the DIO ports is shown in Fig. 3.40(left). Along with these 32 DIO ports, ADwin also has analogue outputs, allowing data extraction on 8 channels without any time offset.

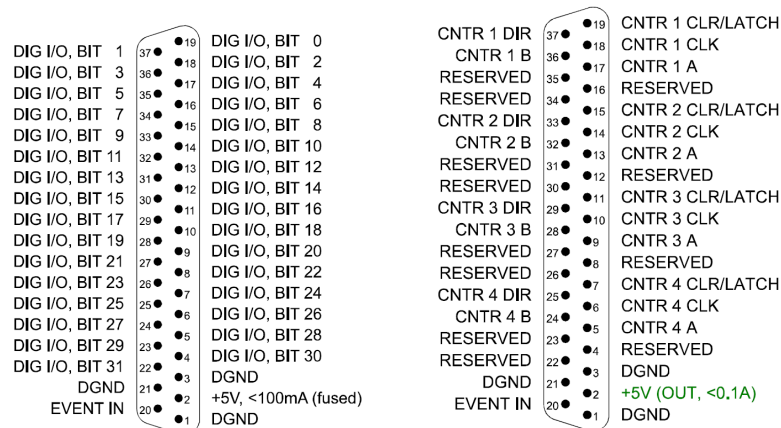


Figure 3.40: Pin assignment of the ADwin. **Left:** DIO module. **Right:** Counter module.

We use ADwin not only to perform the Bayesian update but to count the photons as well. For this purpose, we have a configurable 32-bit counter for event counting with a reference clock of 50 MHz. It takes in TTL signals as input and can be programmed via the ADbasic software. Fig. 3.40(right) shows the pin configuration of the counter module.

### 3.8.1.2 ADwin breakout box

The microcontroller unit requires a TTL signal (3.3V, 50 ns) on the counter module. Our detectors' output is not only smaller in amplitude (3 V) but also short in pulse length (20 ns). To condition the input signals accordingly, we designed a custom breakout box (a signal translation box) with 4 comparators and pulse stretchers based on a Schmitt trigger. The comparators feature a tuneable voltage divider to tune the threshold using a trimmer. We tested the breakout box using controllable pulses from a function generator.

### 3.8.2 High definition arbitrary waveform generator (HDAWG)

We chose Zurich Instruments HDAWG multi-channel Arbitrary Waveform Generator (see Fig. 3.41) for our adaptive experiments as it includes the possibility to modify pulse sequence parameters on-the-fly based on values passed through the Digital Input/Output (DIO) port. In our architecture, the ADwin performs the Bayesian update and chooses the optimal measurement settings, and then hands over the values to the HDAWG, which modifies the pulse sequence accordingly.

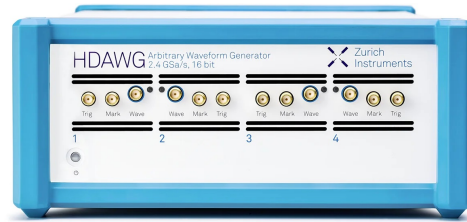


Figure 3.41: High definition arbitrary waveform generator from Zurich instrument.

The HDAWG can generate programmable signals with a bandwidth of up to 750 MHz. It comes with a 2.4 GSa/s sampling rate and can modulate digital signals at multiple frequencies. We have four DC-coupled, single-ended analogue output channels, each with a resolution of 16 bits vertically. In addition, output switching is supported between a direct mode which provides superior noise performance and maximum bandwidth, as well as an amplified mode which increases the output signal amplitude to a maximum of 5 Vpp.

This HDAWG can be controlled with the company-provided LabOne software, which provides a easy access to all the functionalities of the device and helps in creating any arbitrary waveforms. For our use in the lab, we have interfaced with this software using the Python APIs, which helped us to automate the measurement process and integrate it quickly into our existing Python control environment.

The HDAWG is interfaced with the external world through a VHDCI 68-pin connector (see Fig. 3.42). Here pin 42 to 66 work as DIO ports. These are used to communicate between HDAWG

and ADwin for the adaptive experiments discussed in Chap. 4 and 5.

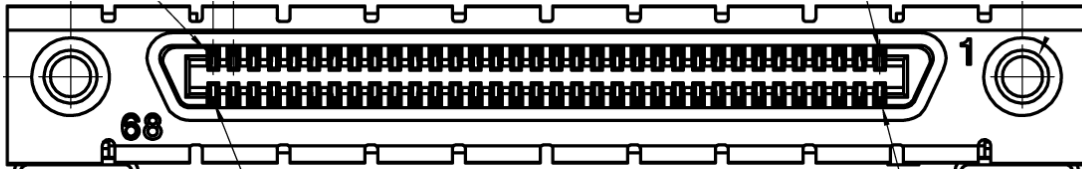


Figure 3.42: VHDCI 68 pin connector to interface HDAWG for DIO communication.

### 3.8.3 Photon pulse routing

Illumination of an NV centre with a green laser leads to the spin population initially in the  $m_s = \pm 1$  to be shelved in the singlet spin state (lifetime  $\sim 160$  ns [261]) after a few optical cycles. While the population in  $m_s = 0$  keeps cycling excited state (lifetime  $\sim 12$  ns [262]). This spin-dependent optical response leads to a PL contrast, as shown in Fig. 3.43, which shows a time-resolved fluorescence signal from an NV centre at room temperature for spin state  $m_s = 0$  and  $m_s = 1$ . However, this difference in spin-dependent PL intensity is short-lived, lasting only for about 300 ns due to the singlet population decaying back to the ground [263], resulting in a steady state of the system.

In our experiments, we use photon counts arriving in the first 300 ns as the signal and photon counts arriving in a later window as background counts for normalisation. Tracking the background counts is important as it allows us to monitor the stability of the system. In case instabilities are detected, one can either discard the measurement or re-normalise the number of detected counts based on the change in background counts.

To discriminate this spin-dependent signal from NV centres using the ADwin, we built a photon pulse routing box which combines two RF switches (Mini-Circuits ZASW-2-50DRA+) in series, powered by two 5V power supplies. The pin configuration of each RF switch is given in table 3.1. Here the signal on the control channel, which we apply based on our gating requirement of the signal, controls the desired state of the switch as given in table 3.2. As shown in Fig. 3.44 the box splits the input pulses from the APD (on the RF-IN port) into three different ports (RF1 out, RF2 out, and RF3 out), respectively corresponding to signal, normalisation and discarded

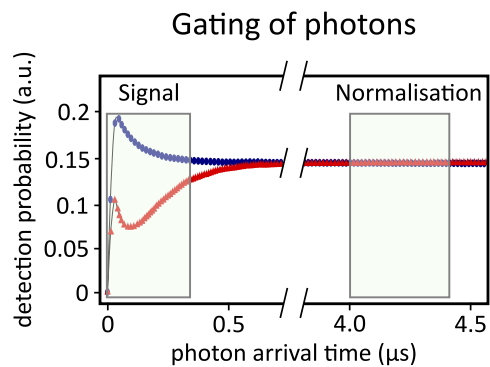


Figure 3.43: **Time resolved fluorescence signal from an NV centre.** Time resolved signal from spin state  $m_s = 0$  (blue) and  $m_s = 1$  (red). With the optimal counting duration for signal and normalisation indicated by the rectangular boxes.

photons (shown in Fig. 3.43). This home-built RF switch box was tested to verify its working using a test signal from a function generator.

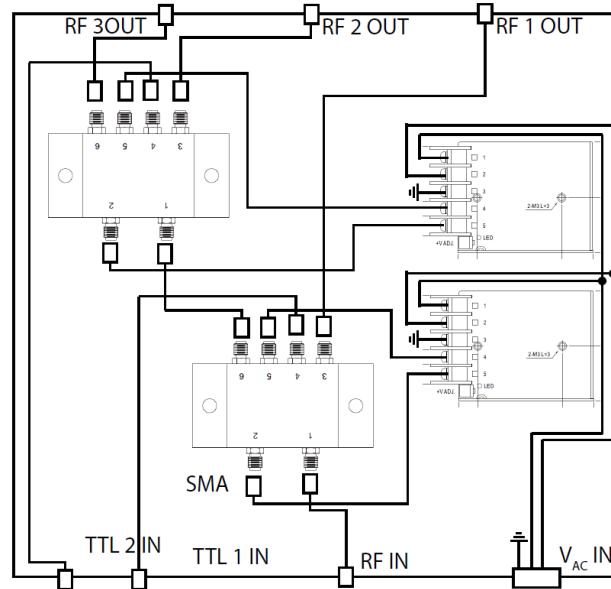


Figure 3.44: Design of RF switch box with two RF switches and 5V power supplies inside. TTL input ports are used to control the routing of the signal using RF switches to the output ports.

Coaxial connections		
Function	Port	Description
RF IN	1	RF common / Sum port
+5V	2	Positive supply voltage
RF1	3	RF out # 1 / In port # 1
Control	4	TTL control In
-5V	5	Negative supply voltage
RF2	6	RF out # 2 / In port # 2

Table 3.1: Functional description of the ports on an RF switch.

Truth table		
	Switch state - RF IN to	
	RF1	RF2
Low	ON	OFF
High	OFF	ON
ON - low insertion loss state OFF - isolation state		

Table 3.2: Truth table for signal routing by RF switch based on the input control signal.

### 3.8.4 Adaptive experiment at a glance

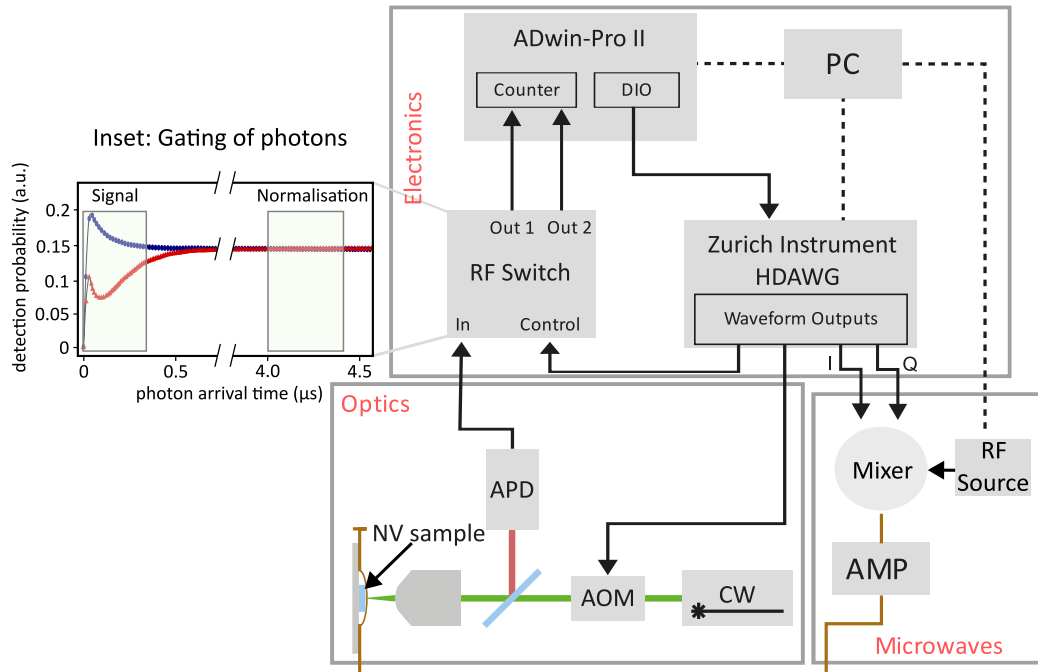


Figure 3.45: **Experimental schematic for adaptive experiment.** The hardware setup (optical, microwave, electronics) is depicted in the schematic, illustrating functional interconnections. Further elaboration on the electronics can be found in section 3.8. Key acronyms include CW (continuous wave) for the laser, NV (Nitrogen-vacancy), AOM (acousto-optic modulator), AMP (radio-frequency amplifier), APD (avalanche photodiode), PC (computer), and AWG (Arbitrary Waveform Generator). The computer orchestrates the overall measurement process but remains inactive during the experiment, with real-time control managed by the ADwin Pro II microcontroller. The inset portrays the utilization of RF switches to choose between the two shaded ranges: the first region, showing a difference in PL intensity between the two spin states, is used as the signal, while the second region, where there is no difference, functions as a background for drift monitoring.

After describing the main components of our adaptive electronics setup in the subsections above, Fig. 3.45 presents an overview of the adaptive experimental setup, including the optical, microwave and electronics parts of the setup.

## 3.9 Real-time Sequential Montecarlo implementation

In this section, I will describe the programming done to control the HDAWG along with the flowchart of ADwin.



### 3.9.1 HDWAG Programming

HDAWG code to illustrate how I generate pulse sequences in real-time. Fig. 3.46 shows the snippet of code used to pad the waveform. Since the HDAWG has a granularity of 16 samples, the length of any pulse needs to be a multiple of 16 for each sample, otherwise, it may lead to ill-defined samples causing issues with successive waveforms. Hence I pad the waveform to fulfil this requirement.

```
// Create padded microwave waveform
const padding = 32-(Samples_mw_pi % 32);
wave w_pad_l = 1*rect(round(padding/2),0);
wave w_pad_r = 1*rect(padding-round(padding/2),0);
wave w_mw_pi_padded = join(w_pad_l,w_mw_pi,w_pad_r);
```

Figure 3.46: **Wave padding for HDAWG.** Snippet of code used to pad the waveform to avoid ill-defined samples. Since HDAWG has a granularity of 16 samples, we need to ensure the length is multiple of 16.

Fig. 3.47 shows the code used to set the oscillator phase for the I and Q channel. HDAWG waits for a trigger from the ADwin, and the updated value of the adaptive parameter to build the sequence for the next run.

```
do{
// Waiting for the ADwin to be ready, AWG is ready at this point
setDIO(1<<AWG_ready_pin);

    resetOscPhase();
    setSinePhase(0, 0);
    setSinePhase(1, 90 + IQ_phase_correction);
    wait(30);

waitDIOTrigger();
var dio = getDIO();
```

Figure 3.47: **HDAWG ready and waiting for ADwin trigger.** Snippet of code showing the setting of the oscillator phase for I and Q channel for MWs. HDAWG waits for the trigger from the ADwin before building a real-time pulse sequence.

Fig. 3.48 shows the code used to mask the input received from the ADwin and convert it into decimal numbers to generate a real-time pulse sequence based on input from ADwin.

```
var pi_switch = (dio>>4) & 0b01;
wait(10);
var t1_delay = (dio>>ADwin_para) & 0xFF;
```

Figure 3.48: **Adaptive value received from ADwin trigger.** Snippet of code showing adaptive value received from the ADwin and converted to a decimal number to generate pulse sequence for the next run.

Fig. 3.49 shows the code used to make the pulse sequence for the next run based on input from ADwin. Here we show the use of a “command table” to generate a pulse sequence. The command table is a list of instructions that can be executed in a specific order, with each instruction specifying a particular waveform or operation to be performed. It can create complex signal sequences involving multiple waveforms and signal processing operations, such as filtering, mixing, modulation, and demodulation. For our experiments the use of the command table is motivated by the simplicity of its use and the ease of making complex and longer pulse.

```
var phase_8bit = (dio>>ADwin_para_2) & 0xFF;
setTrigger(AOM_channel);
wait(Cycles_rect);
setTrigger(0);

repeat(n_pulses)
{
  playZero(Samples_wait_after_pulse);
  resetOscPhase();

  executeTableEntry(300);

  playZero(t1_delay*scaling_factor-Samples_mw_pi-padding);

  executeTableEntry(phase_8bit);

  playZero(Samples_wait_after_pulse);

  waitWave();

  setTrigger(AOM_channel);
```

Figure 3.49: **Command table for HDAWG.** Snippet of code showing the use of adaptive parameter received from ADwin and combined with command table to generate pulse sequence for next run.

A video ([click](#)) shows the use of HDAWG to generate two I and Q modulation pulses. It shows a change in delay time between the two pulses and a change in the relative phase of the two pulses.

### 3.9.2 ADwin flow-chart

In Sec. 3.8.1, we described the general details of the microcontroller we used for the adaptive experiment in this thesis. This section provides details on the working of the ADwin in the form of a flowchart. This structure allows the series of events to work in a linear string. Each event spacing is determined by the process delay time, which can be adjusted during pre-experimental calibration. For details on how we code the ADwin, refer to Apx. A.2.

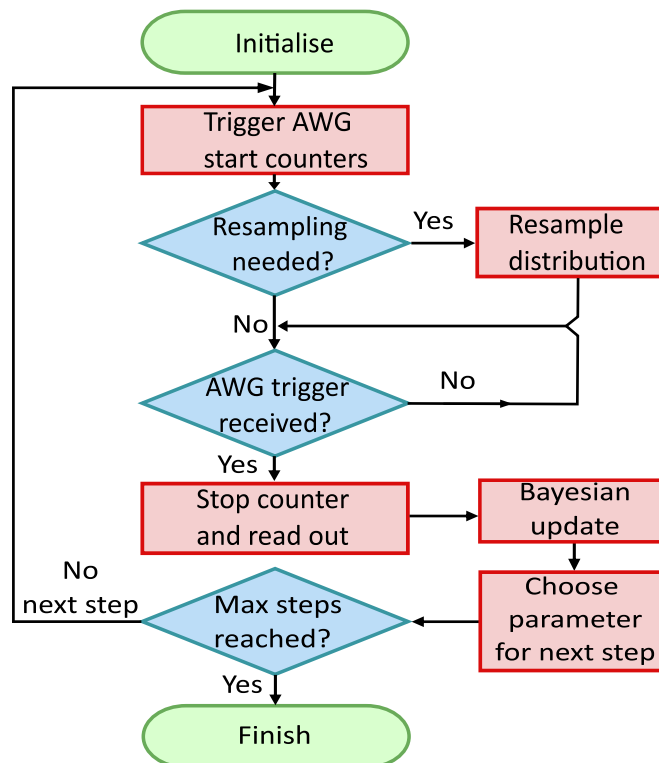


Figure 3.50: **Microcontroller flowchart.** A flowchart illustrates the sequence of steps carried out in the adaptive experiments. The microcontroller’s control process is independent of the specific measurement conducted, as it responds to trigger signals for activation. If required, resampling is executed concurrently with data acquisition, occurring between the initiation and stoppage of the counters. This approach ensures that no additional overhead is introduced to the procedure.

#### Details of microcontroller unit (MCU) operation flow.

The depicted flowchart delineates the MCU’s functioning in Fig. 3.50. During each iteration, the MCU initiates the AWG, which provides all the control pulse sequences and initializes the counters. If resampling is necessary, it is launched at this juncture, operating in tandem with data acquisition to prevent the introduction of extra overhead. Upon receiving a return trigger from the AWG, indicating the completion of all pulse sequences, the MCU stops and retrieves data from the two counters that have accumulated the total counts for all  $R$  repetitions. Subsequently, the MCU undertakes a Bayesian update of the probability distribution for the unknown parameter.

It then selects the optimal parameters for the subsequent iteration and conveys this value to the AWG to compile the next sequence for qubit control. The optimal setting value is handed over to the HDAWG as an 8-bit integer via its digital I/O port. In each set of  $R$  measurements, the AWG retrieves the value from the DIO port and subsequently designs the next pulse sequence. The AWG's functions extend beyond producing control pulses for the AOM and facilitating single-sideband modulation of the microwave (MW) signal. It also manages the switch that routes the signal from the detector towards the counter channels on the microcontroller.

### 3.9.2.1 Algorithm speed

We tested the speed of ADwin to update the probability distribution using the Bayes rule for a different number of particles representing that probability distribution (see Fig. 3.51). The experiment's timing was assessed in relation to the microcontroller's internal clock, revealing a benchmark of  $T_{\mu s} \sim 0.255 \cdot n$ , here  $n$  represents the number of particles used to discretize the probability distribution. For example, with  $n = 200$  particles, this translates to a probability distribution updating time of approximately  $50 \mu s$ .

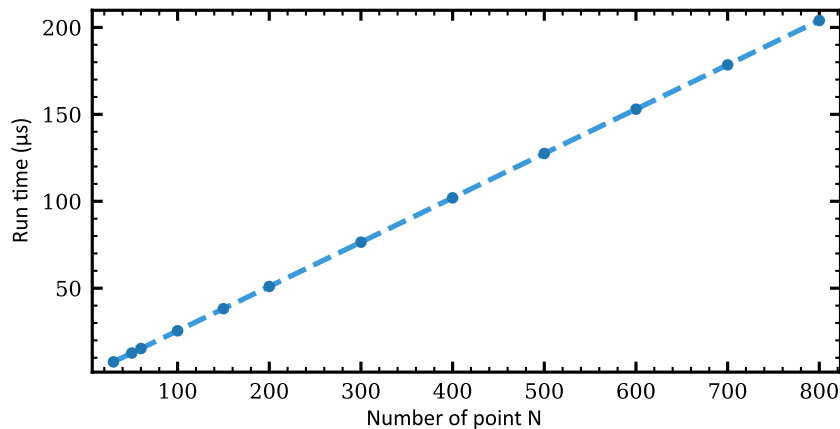


Figure 3.51: Time it takes ADwin to perform a Bayesian update of a probability distribution represented by  $N$  points.

## 3.10 Cryogenic setup for vanadium in SiC experiments

Here I discuss the experimental setup I used to study single vanadium centres in SiC in Chap. 6.

The basics of this confocal microscope are the same as discussed earlier, but the microscope here interfaces to a sample in a cryostat. Details of this homemade confocal microscopy setup are shown in Fig. 3.52.

We use a closed-cycle cryostat (Montana Cryostation S100) for the study of vanadium defects. This cryostat includes a 100x NIR objective (Olympus LCPLN100XIR) with a numerical aperture of 0.85. This objective is maintained at room temperature, inside the cryostat in a vacuum, via a

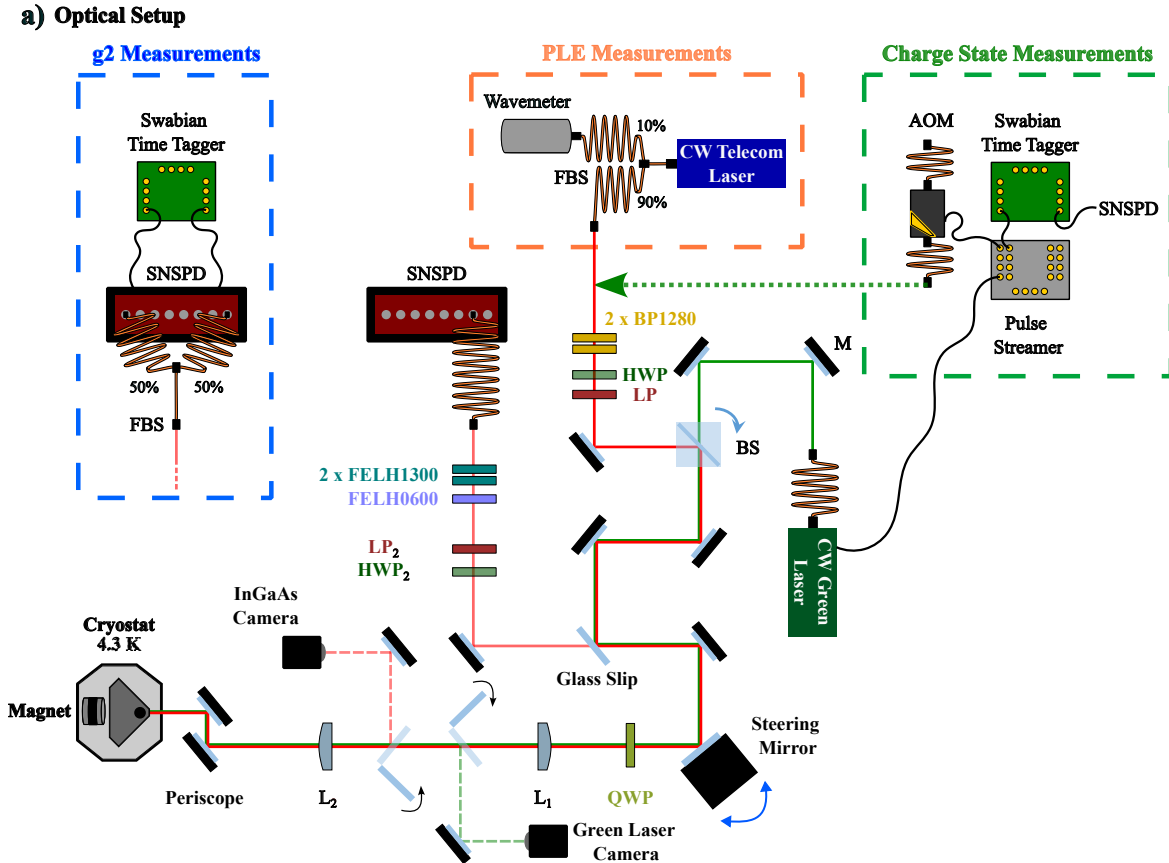
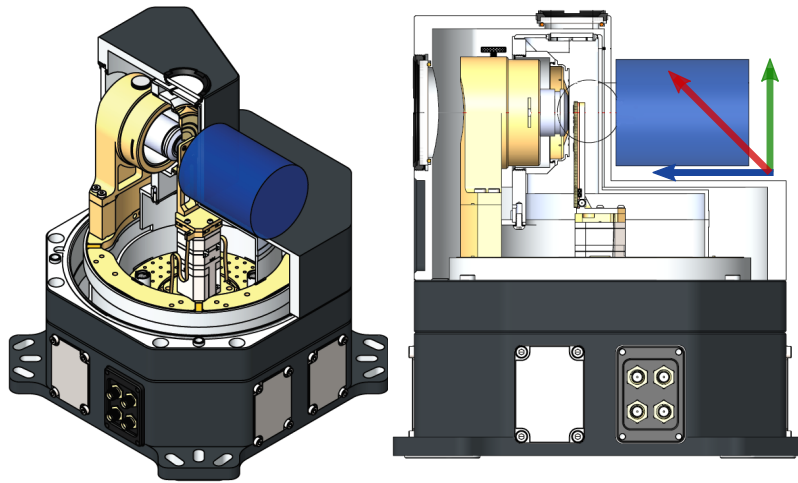


FIGURE 3.52. **Schematic of the optical setup used for vanadium study.** Shows the optical excitation (green and red path) and detection (orange path) for the study of vanadium. Where for different experimental studies, we used slightly different arrangements, as shown in the figure above: PLE measurement (orange box),  $g^2$  measurement (blue box), and charge state study (green box). Basic components are labelled as: **L<sub>1</sub>**, **L<sub>2</sub>** = Achromatic Doublet Lenses, **QWP** = Quarter-Wave Plate, **HWP** = Half-Wave Plate, **LP** = Linear Polarizer, **FELH0600** = Hard-Coated Long Pass Filter (Thorlabs), **FELH1300** = Hard-Coated Long Pass Filter (Thorlabs), **BS** = Beam Splitter, **M** = Mirror, **BP1280** = Band Pass Filter, **FBS** = Fiber Beam Splitter, **SNSPD** = Superconducting Nanowire Single-Photon Detector, **AOM** = Acousto-Optic Modulator. Where the flip mounts have been represented by a small arrow close to the optical component.

feedback-controlled heater. We mount the sample on a custom-made PCB, which is positioned on top of a stack of Attocube positioners (ANPx101). The cryostat shroud is custom-designed, allowing an external magnet to reach up to a distance of 20 mm from the sample position. We place a cylindrical (two inches in diameter and two inches thick) Neodymium magnet external to the cryostat to apply a magnetic field (see Fig. 3.52). Using this magnet we can generate fields of about 150 mT at the sample position. We have roughly aligned the magnet along the SiC c-axis. To determine the intensity of the applied field, we use a commercially available gaussmeter (Tunkia TD8620).

We study the  $\alpha$ -defect associated with the vanadium defect by optically exciting it with two lasers. The first one is a wavelength-tunable continuous wave (CW) telecom diode laser (Toptica DL Pro, 1270 nm-1350 nm), which is tuned in resonance with the zero-phonon line (ZPL) of the GS1-ES1 transition ( $\sim 1278.46$  nm). While the second is a green diode laser (Thorlabs PL520) used as repump laser to stabilise the  $V^{4+}$  charge state of the vanadium defect. Both of these lasers are collimated via aspheric lenses and coupled into two single-mode fibres (Thorlabs P3-980A-FC-2 and P3-460B-FC-2, respectively). To control the excitation power and polarisation of the telecom laser, we use a combination of a half-wave plate and a linear polarizer (as shown in Fig.3.52).



**FIGURE 3.53. Design of the cryostat used for vanadium study.** Our cryostat allows imaging of a sample attached to a coplanar waveguide. The custom-designed shroud of the cryostat helps us to bring a permanent magnet (blue cylinder in the schematic) within 20 mm of the sample. A permanent neodymium magnet (blue cylinder) can be mounted on a 3-axis stage, allowing us to achieve a 100 mT field at the sample location.

A Fizeau-Interferometer wavemeter (HighFinesse, WS7) monitors and stabilises the telecom laser frequency. To perform a raster scanning of the sample, we use a steering mirror (Newport FSM-300-NM) in combination with a 4f optical system composed of two plano-convex lenses,  $L_1$  (Newport - PAC35AR.16) and  $L_2$  (Newport - PAC13AR.16). The use of this 4f system is similar to what has been described earlier for room temperature setup. It expands the beam to fill the

objective's back pupil and ensure the confocal condition is maintained. The photoluminescence (PL) is collected via the same excitation objective, which is then coupled into a single-mode fibre (Thorlabs SMF-28) and detected with the help of a superconducting nanowire single-photon detector (SNSPD; Single Quantum EOS). In our setup, we use a combination of two cameras (Thorlabs camera (DCC1545M) for green and an InGaAs camera for telecom) and an iris diaphragm to align both the excitation and collection lasers. For the collection of the fluorescence phonon sidebands (PSB), we use a microscope glass slide with  $\sim 3\%$  reflection ("glass slip" in Fig.3.52) in combination with spectral filters. The telecom excitation laser is spectrally filtered via two 12 nm-FWHM bandpass filters centred at 1280 nm (Knightoptical, 1280DIB25, shown as "BP1280" in Fig.3.52). In addition to this, we use a combination of two longpass filters (Thorlabs FELH1300 and FELH0600) in the collection path to reject both excitation lasers and only collect photons with wavelength  $\geq 1300$  nm corresponding to the PSB of the V defects [264].

Coarse sample movement is achieved by low-temperature attocube piezo-positioners. These stages have a scan range of 5 mm with a minimum incremental step size of 10 nm. For xy scanning of the sample as described earlier, we steer the beam using the galvo mirrors, while the focus (z-axis) is fine-tuned using the Attocube positioners. For spin manipulation using microwaves (MW), four SMA feedthrough ports are added to the cryostat, which are connected to the sample mount internally.





## ADAPTIVE DECOHERENCE ESTIMATION

## 4.1 Introduction

This chapter describes an adaptive algorithm for decoherence estimation, with simulations and experimental results. We demonstrate an adaptive sensing scheme for a spin-based quantum sensor to estimate the decoherence timescales,  $\{T_1, T_2^*, \text{ and } T_2\}$  for a single qubit. The protocol described in this chapter has been implemented on an electron spin associated with an NV centre; however, this algorithm is general and can, in principle, be applied to any spin qubit. A motivation for this work stems from the fact that each spin-based quantum sensor has different decoherence properties; hence, a fast and reliable way to calibrate these is vital. Because decoherence occurs in quantum systems due to interaction with their environment, it is one of the key indicators of the efficiency of quantum technologies [65], such as quantum communication, quantum computation, and quantum sensing technologies. For quantum communication networks, an important metric is the decoherence timescale since it determines the length of time quantum memories and quantum repeaters can store information [10, 17, 265, 266]. Developing large-scale quantum computing architectures that use superconducting qubits [267, 268] and silicon spin qubits [269, 270] requires rapid benchmarking of decoherence timescales as a key step for validating and ensuring the quality of these systems. This may be crucial for ensuring the efficiency of error correction protocols as they approach fault tolerance thresholds in quantum computing systems. When it comes to quantum sensing, decoherence plays a double role. On the one hand, decoherence caps the maximum performance limits of the sensor [4]. While on the other hand, a quantum sensor can measure decoherence and provide information about the environment surrounding the sensor. This phenomenon can be seen in relaxometry, which determines information about physical processes in the environment by observing the rate at which a polarised quantum sensor approaches a thermal equilibrium configuration [97, 271–275]

It is possible to measure the decoherence rate of a quantum system by preparing it into a known quantum state, after which it can be probed at varying time delays to determine the probability of the system decaying from the initial state. To estimate the decoherence rate, the standard method involves taking a series of measurements over a predetermined range of time delays which is expected to contain the true value of the decoherence time. The data from such measurement is fitted with a decay function to extract the decoherence time. It is important to note that, following a predetermined time  $\tau$  range, some of the measurements will give little to no information about the decoherence time of the system. This is because the time delays are either very short, resulting in the system not decohering, or they are much longer, resulting in the complete decoherence of the system. Hence an adaptive scheme that makes an optimal choice of evolution time is desirable.

Our experiment utilizes a very simple analytical update rule, which is very different from other studies of adaptive protocols [211, 212, 276]. By using state-of-the-art fast electronics, the online processing takes a much shorter period, a mere  $50 \mu s$ , compared to the time it takes to perform each measurement. Furthermore, we investigate which quantity should be targeted to achieve the highest possible sensor performance, showing experimentally that optimizing sensitivity surpasses optimizing variance when it comes to ensuring the best sensor performance.

## 4.2 Fisher information of a qubit

A brief introduction to the Fisher information was given in Sec. 2.2.1. Here we will look at the maximisation of it for the case of estimating  $\{T_1, T_2^*, \text{ and } T_2\}$ . We use the general decay approximated by a power law as  $e^{-\left(\frac{\tau}{T_\chi}\right)^N}$ , with  $T_\chi$  and  $N$  as the parameter of specific noise spectrum [65]. The probability of finding the spin in a given state ( $|0\rangle$  or  $|1\rangle$ ) under time evolution will be [4]:

$$(4.1) \quad p(0|T_\chi) = \frac{1}{2} \left( 1 + e^{-\left(\frac{\tau}{T_\chi}\right)^N} \right)$$

$$(4.2) \quad p(1|T_\chi) = 1 - p(0|T_\chi) = \frac{1}{2} \left( 1 - e^{-\left(\frac{\tau}{T_\chi}\right)^N} \right)$$

For the case of spin-lattice relaxation ( $N = 1$ ), it will mean that, starting from spin up, i.e.  $|0\rangle$  with 100% probability. After the time  $\tau = T_1$ , this probability will drop to  $\sim 68\%$ .

$$(4.3) \quad p(0|T_\chi) = \frac{1}{2} (1 + e^{-1}) \sim 0.68$$

Hence Fisher information can provide a way to learn about the parameter  $T_\chi$  at a given evolution time  $\tau$ . Using the Eqn. 2.3, we can find the Fisher information as (see Apx. A.5 for details on derivation):

$$(4.4) \quad F_{T_\chi} = \frac{N^2 \left(\frac{\tau}{T_\chi}\right)^{2N}}{T_\chi^2 \left(e^{2\left(\frac{\tau}{T_\chi}\right)^N} - 1\right)}$$

### 4.2.1 Decay factor N

A dipolarly coupled electronic spin and its decay exponents have been examined in depth, and analytical solutions have been provided for various parameter regimes [277]. The decay exponent  $N$  varies greatly based on a specific noise power spectrum from the environment [278]. This decay factor describes the strength and correlation of the interaction between the electronic spin of the NV centre and entities such as the nuclear spin bath in the environment. This noise power spectrum generally depends on several factors, including the concentration and type of nuclear spins in the environment, the temperature, and the magnetic field. Consequently, if it is possible to ignore the coupling within the “bath”, the free induction decay (FID) of a single spin is approximately Gaussian ( $N = 2$ ) [76, 279, 280]. While for the case of a bath with white noise, the decay factor  $N$  saturates at 1. While a Hahn echo decay exponent takes a wide range, usually between  $N = 1$  to 4 [109]. This variation depends on the applied field and the bath parameters [277, 281]. In the experimental study shown below, we assume the decay exponent  $N$  to be known via the initial calibration of the system, and we focus on the estimation of a single unknown parameter,  $T_\chi$ . In many practical situations, this is the case as decay exponents  $N$  is usually known, at least approximately. For our study in this chapter, we found the decay factor  $N = 2$  for dephasing estimation via Ramsey measurement and  $N = 3/2$  for decoherence estimation via spin echo protocol. It must be noted, however, this decay factor is not the same for shallow and deep NVs, as for the shallow NVs that are closer to the surface than the average separation between the surface spins, study [282] has shown that for a free induction decay (FID) signal it is possible to have a decay factor  $N = 2$  at short times while the data fits well with  $N = 2/3$  at longer times (bi-exponential fit). In contrast, this condition of bi-exponential collapses to a single decay factor when the depth of the NV centres becomes greater than the average spin-spin separation.

### 4.2.2 Maximisation of Fisher information

Now, to maximise the Fisher information and, in return, find the optimal free evolution time  $t$ , we need to find the global maxima of the above equation. For this, we can either plot the Eqn. 4.4 as a function of  $\left(\frac{\tau}{T_\chi}\right)$  as shown in Fig. 4.1 and find the optimal  $\tau_{opt}$  from the maximum of the plot. Where from the plotted graphs, we can extract the optimal value for different  $N$  decay factors as given in Table 4.1.

The other approach is to solve Eqn. 4.4 numerically by taking the derivative of it as shown below.

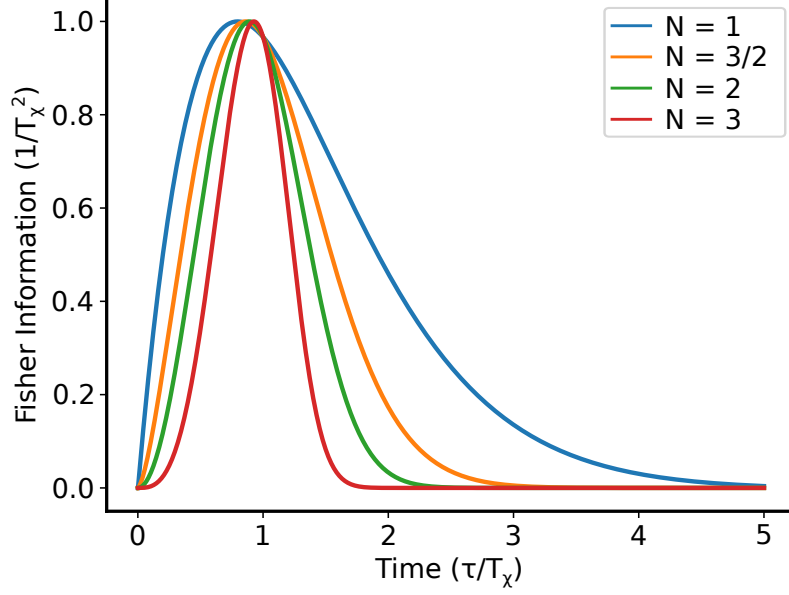


FIGURE 4.1. **Fisher information  $F$  in terms of  $\tau/T_\chi$  for different decay factors  $N = \{1, 3/2, 2, 3\}$ .** Here  $\tau$  is the probing time, while  $T_\chi$  is the targeted decoherence timescale. For each value of  $N$ ,  $\tau_{opt}$  is found in terms of  $T_\chi$  from the peak value of the plotted curves.

$$(4.5) \quad \frac{dF_\chi}{dt} = \frac{d}{dt} \left( \frac{N^2 \left(\frac{\tau}{T_\chi}\right)^{2N}}{T_\chi^2 \left(e^{2\left(\frac{\tau}{T_\chi}\right)^N} - 1\right)} \right) = \frac{N^2 \frac{d}{dt} \left[ \left(\frac{\tau}{T_\chi}\right)^{2N} \right] \left( e^{2\left(\frac{\tau}{T_\chi}\right)^N} - 1 \right) - \left(\frac{\tau}{T_\chi}\right)^{2N} \frac{d}{dt} \left[ e^{2\left(\frac{\tau}{T_\chi}\right)^N} - 1 \right]}{T_\chi^2 \left( e^{2\left(\frac{\tau}{T_\chi}\right)^N} - 1 \right)^2}$$

$$(4.6) \quad \frac{dF_\chi}{dt} = \frac{N^2 \left[ \frac{2N \left(\frac{\tau}{T_\chi}\right)^{2N-1} \left( e^{2\left(\frac{\tau}{T_\chi}\right)^N} - 1 \right)}{T_\chi} - \frac{2N \left(\frac{\tau}{T_\chi}\right)^{3N-1} e^{2\left(\frac{\tau}{T_\chi}\right)^N}}{T_\chi} \right]}{T_\chi^2 \left( e^{2\left(\frac{\tau}{T_\chi}\right)^N} - 1 \right)^2} = \frac{2N^3 \left(\frac{\tau}{T_\chi}\right)^{2N}}{t T_\chi^2 \left( e^{2\left(\frac{\tau}{T_\chi}\right)^N} - 1 \right)^2} - \frac{2N^3 \left(\frac{\tau}{T_\chi}\right)^{3N} e^{2\left(\frac{\tau}{T_\chi}\right)^N}}{t T_\chi^2 \left( e^{2\left(\frac{\tau}{T_\chi}\right)^N} - 1 \right)^2}$$

after simplification, we get:

$$(4.7) \quad \frac{dF_\chi}{dt} = - \frac{2N^3 \left(\frac{\tau}{T_\chi}\right)^{2N} \left[ \left( \left(\frac{\tau}{T_\chi}\right)^N - 1 \right) e^{2\left(\frac{\tau}{T_\chi}\right)^N} + 1 \right]}{t T_\chi^2 \left( e^{2\left(\frac{\tau}{T_\chi}\right)^N} - 1 \right)^2} = 0$$

Since there is no analytical solution to the above equation. We find an approximate solution via the Taylor expansion. Which for different decay factors  $N$ , gives us:

1. for  $N = 1$ ,  $\tau_{opt} = 0.79T_\chi$
2. for  $N = 2$ ,  $\tau_{opt} = 0.89T_\chi$
3. for  $N = 3/2$ ,  $\tau_{opt} = 0.86T_\chi$

Or a more generalised expression as:

$$(4.8) \quad \tau_{opt} = \xi \cdot T_\chi$$

Here  $\xi$  depends on the decay factor  $N$ . This simple numerical expression gives an easy way to adapt the evolution time  $\tau$ . That will give the maximum information about the decoherence time  $T_\chi$ . So for the adaptive protocol described in the later section, we choose the evolution time for each epoch based on the above numerical solution where the term  $T_\chi$  is the estimated value of decoherence time from the last epoch.

### 4.2.3 Optimising sensitivity

In the section above, we looked at the case of maximising the Fisher information to minimise the uncertainty of the unknown  $T_\chi$ . It must be noted, however, that this criterion does not consider the time it takes to perform a measurement. And since the adaptive experiment's objective is to minimize uncertainty in the shortest amount of time possible, if two measurements are taken from two different parameter values and have similar information gains, then the measurement which takes the shorter time to be performed should be favoured. Hence, it is also necessary to discuss an alternative approach that, rather than addressing the minimization of the mean squared error (MSE) as a goal, is instead focused on improving the sensitivity, defined as  $\eta^2 = MSE \cdot \tau$  [206]. Thus, we can come up with a new criterion that is based on Fisher information rescaled for probing time  $\tau$  as given below:

$$(4.9) \quad F_T = \frac{F(\tau)}{\tau} = \frac{N^2 \left( \frac{\tau}{T_\chi} \right)^{2N}}{\tau T_\chi^2 \left( e^{2 \left( \frac{\tau}{T_\chi} \right)^N} - 1 \right)}$$

Following a similar procedure as done in the section above, we can plot the Eqn. 4.9 as shown in Fig. 4.2 and extract the optimal  $\tau_{opt}$  values, or we can find a numerical solution for the optimal evolution time  $\tau_{opt} = \xi(F_T) \cdot T_\chi$ . Table 4.1 shows the multiplication factor  $\xi$  for Fisher information and optimal sensitivity protocol for different values of decay factor  $N$ . There was no maximum of Fisher information for the optimal sensitivity with  $N = 1$ .

If the parameter space is infinite or unbounded, the Fisher information might not have a maximum because the parameter values can become arbitrarily large or small. In such cases, the Fisher information might still provide information about the sensitivity of the likelihood function, but the concept of a maximum may not be applicable.

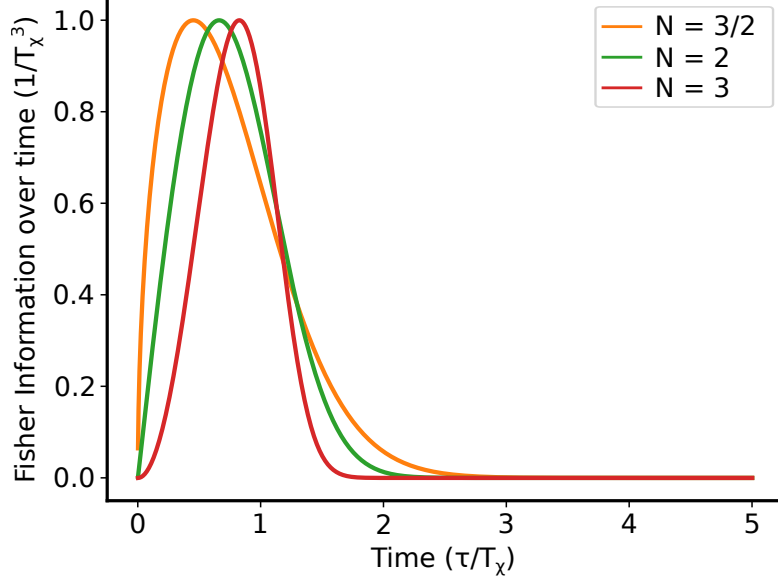


FIGURE 4.2. **Rescaled Fisher information  $F_T$  as a function of  $\tau/T_\chi$  for different decay factors  $\mathbf{N} = \{3/2, 2, 3\}$ .** Here  $\tau$  is the probing time, while  $T_\chi$  is the targeted decoherence timescale. For each value of  $\mathbf{N}$ ,  $\tau_{opt}$  is found in terms of  $T_\chi$  from the peak value of the plotted curves.

$N$	1	3/2	2	3
$\xi(F)$	0.79	0.86	0.89	0.93
$\xi(F_T)$	-	0.45	0.66	0.83

Table 4.1: **Selection of the optimal probing time  $\tau_{opt}$ .** The table presents numerically calculated  $\xi$  values for various decay exponents  $N$ . These values are obtained through the maximization of either the classical Fisher information ( $F$ ) (Eqn. 4.4) or the rescaled Fisher information ( $F_T$ ) (Eqn. 4.9) [283]. Similar results are found by taking the maxima of curves plotted in Fig. 4.1 and Fig. 4.2.

### 4.3 Adaptive estimation protocol

This section presents generalised steps involved in the estimation of an unknown quantum parameter  $\theta$ :

1. Quantum system is initialised into a state  $\hat{\rho}_{in}$  that experiences  $\theta$ -dependent evolution, resulting in a final state represented as  $\hat{\rho}_\theta$ . The information encapsulated in this final state  $\hat{\rho}_\theta$  is quantified using the Quantum Fisher Information (QFI) denoted as  $\mathcal{F}(\theta)$ .
2. After this, a measurement is carried out on the quantum system that results in a probability distribution-dependent outcome. As a result of this measurement QFI  $\mathcal{F}(\theta)$  is converted

into classical fisher information (CFI)  $F(\theta)$ .

$$(4.10) \quad F(\theta) \leq \mathcal{F}(\theta)$$

3. Using the measurement outcome, settings for the next measurement cycle are updated, e.g. choosing the optimal sensing time  $t_{opt} = 0.79T_\chi$  for the case of decoherence estimation.
4. Above mentioned steps are repeated  $N$  times to obtain  $N$  outcomes. Using these  $N$  outcomes, an estimator  $\theta_{est}$  is yielded to unknown parameter  $\theta$ . The accuracy of this estimation is quantified by the statistical error of the estimator [284]:

$$(4.11) \quad \delta\theta \equiv \sqrt{\langle (\theta_{est} - \theta)^2 \rangle}$$

The accuracy of an unbiased estimator, such as a Bayesian estimator, is constrained by the Cramér-Rao lower bound (CRLB) [285].

While working at room temperature, since a single shot measurement is unavailable, we have to perform the first two steps  $R$  number of times per measurement to yield an outcome.

## 4.4 Simulation results

Here I present the simulation results and the estimation algorithm.

### 4.4.1 Non-single shot readout

The adaptive protocol discussed above has been demonstrated on an electron spin linked to an NV centre in a diamond [70, 98]. Although optical measurements at room temperature are possible, in contrast with cryogenic temperatures [286], obtaining a binary readout from a single measurement is impossible (see Sec. 3.18 for details on nuclear spin-assisted optical readout). To circumvent the absence of single-shot reading, each measurement sequence was repeated  $R$  times to achieve statistical information about spin states. Such that after the  $n$ -th iteration, the total number of detected photons  $r_n$  can be employed to update the probability distribution of  $T_\chi$  via the Bayes rule as:

$$(4.12) \quad p(T_\chi|r_{1:n}, R) \propto p(r_n|T_\chi, R)p(T_\chi|r_{1:(n-1)}, R)$$

Based on the results of  $R$ -independent and identical Bernoulli experiments, the likelihood is a binomial distribution. During a single repetition, the probability that a photon click will be detected can be calculated as follows:

$$(4.13) \quad p_D(\tau, T_\chi, N) = \alpha \left( 1 + V e^{-(\tau/T_\chi)^N} \right)$$

where  $V$  and  $\alpha$  are the parameters of a specific experimental setup, and they can be calculated from the probability to detect a click as:

$$(4.14) \quad V = \frac{p_{clk}(|0\rangle) - p_{clk}(|1\rangle)}{p_{clk}(|0\rangle) + p_{clk}(|1\rangle)}$$

where  $p_{clk}(|i\rangle)$  is the probability to get a click from the state  $|i\rangle$ . Similarly,  $\alpha$  is given as:

$$(4.15) \quad \alpha = \frac{p_{clk}(|0\rangle) + p_{clk}(|1\rangle)}{2}$$

However, as the probability of getting photon clicks in a single measurement is quite small and the number of repetitions  $R$  is large, the likelihood function can be approximated with a Gaussian distribution as [213, 287]:

$$(4.16) \quad p(r_i | T_\chi, R) \approx \frac{1}{\sqrt{2\pi}\sigma} \exp \left[ -\frac{(r - R \cdot p_D(\tau, T_\chi, N))^2}{2\sigma^2} \right]$$

where  $\sigma = r(R - r)/R$ .

The estimation sequence is described in Algorithm 4. Initially, we establish a discretization of the  $T_\chi$  distribution, employing a set of  $K$  particles  $\{x_k\}$  distributed according to the prior probability  $p_0(T_\chi)$  (which in our case is uniform). The initial particle weights are assigned as  $1/K$ . In each iteration, the mean  $\hat{T}_\chi$  of the distribution is computed (line 5), and this mean is utilized to determine the subsequent probing time as  $\tau = \xi \cdot \hat{T}_\chi$  (line 6). Following this, the selected experiment is executed  $R$  times, resulting in the detection of  $r$  photons. Subsequently, the probability distribution  $p(T_\chi)$  is updated based on the Bayes rule (line 11), with normalization being applied to the distribution (line 12). At this juncture, if the distribution reveals big regions with low weights (as described by the condition in line 13), it undergoes re-sampling in accordance with the Liu-West algorithm [202]. We calculate the variance  $\sigma^2$ , and subsequently, we generate new particles through sampling (line 25) from a Gaussian distribution characterized by a variance of  $\sigma^2$  and a mean value given as:

$$(4.17) \quad \mu' = a_{LW} \cdot x_k + (1 - a_{LW}) \cdot \mu \quad ,$$

Here  $a_{LW}$  in the Liu-West parameter, which governs the balance between maintaining the original  $\{x_k\}$  and incorporating the properties (mean  $\mu$ ) of the current  $p(T_\chi)$  during the new



**Algorithm 4** Adaptive estimation algorithm**Input:**

$p_0(x)$ : prior probability distribution for  $x = T_\chi$ ;  
 $K$ : number of particles;  
 $N$ : number of epochs;  
 $a_{LW}$ : Liu-West re-sampling parameter;  
 $t_{RS}$ : re-sampling threshold

```

1: procedure ADAPTIVEESTIMATION( $n, p_0, N, a_{LW}, t_{RS}$ )
2:   draw  $\{x_k\}$  from  $p_0(x)$ 
3:    $\{\omega_k\} \leftarrow \{1/K\}$ 
4:   for  $i \in 1..N$  do
5:      $\hat{T}_\chi \leftarrow \sum_j \omega_k \cdot x_k$ 
6:      $\tau \leftarrow \xi \cdot \hat{T}_\chi$ 
7:     for  $j \in 1..R$  do
8:        $m_j \leftarrow \text{EXPERIMENT}(\tau)$ 
9:        $r_i \leftarrow \sum_{j=1}^R m_j$ 
10:       $\{\omega_k\} \leftarrow \{\omega_k \cdot p(r_i | T_\chi, R)\}$ 
11:       $\{\omega_k\} \leftarrow \{\omega_k / (\sum_k \omega_k)\}$ 
12:      if  $1/\sum \omega_k^2 < n \cdot t_{RS}$  then
13:         $\{x_k\} \leftarrow \text{RESAMPLE}(\{x_k\}, \{\omega_k\}, a_{LW})$ 
14:         $\{\omega_k\} \leftarrow \{1/K\}$ 
15:   return  $\hat{T}_\chi$ 
16:
17: procedure RESAMPLE( $\{x_k\}, \{\omega_k\}, a_{LW}$ )
18:    $\mu \leftarrow \sum_k x_k \cdot \omega_k$ 
19:    $\sigma^2 \leftarrow \sum_k x_k^2 \cdot \omega_k - \mu^2$ 
20:    $\mu' \leftarrow a_{LW} \cdot x_k + (1 - a_{LW}) \cdot \mu$ 
21:    $\{x_k\} \leftarrow \text{NORMAL}(\mu', \sigma^2)$ 
22:   return  $\{x_k\}$ 

```

sampling process. The resampling procedure occurs concurrently with data acquisition (see Fig. 3.50), ensuring that it does not introduce any extra delay to the total measurement duration.

The CRLB gives the fundamental performance limit for decoherence timescale learning for the Fisher information in Eqn. 4.4. In Fig. 4.3(a), we present the simulation results for the performance of our proposed algorithm in case of a perfect single-shot readout. We see that both adaptive approaches ( $F$  and  $F_T$ ) outshine the non-adaptive (random  $\tau$ ) protocol. With  $F_T$  even out-performing  $F$ . Here the CRLB is represented by the solid black line, where the best adaptive protocol will saturate this limit. In the absence of the single-shot readout, a condition that is true for our setup with NV centre at room temperature, the performance of the adaptive protocol is limited because of doing a readout averaged over  $R$  repetitions.

Looking at the simulation results shown in Fig. 4.3(c), we can see that due to this imperfect

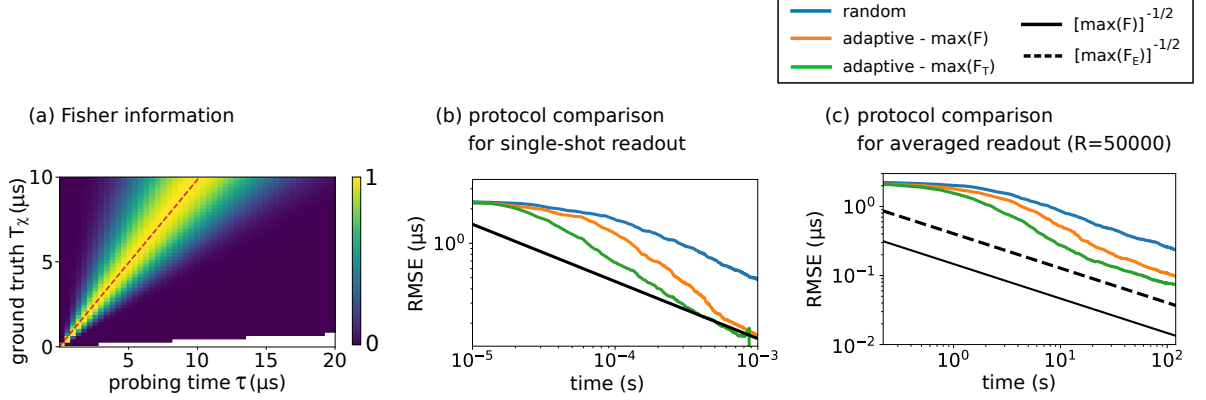


FIGURE 4.3. **Numerical simulations for estimation of  $T_2^*$ .** (a) Fisher information  $F$  in terms of the actual value of  $T_\chi = T_2^*$  and the probe time  $\tau$ , derived from Eqn. 4.4. Here  $F(\tau, T_2^*)$  is normalized by its maximum with respect to  $\tau$  for each value of  $T_2^*$ . A linear correlation between the maximum of  $F(\tau)$  and  $T_2^*$  is evident, with the maximum of Eqn. 4.4 indicated by a red dashed line in the plot. (b) Evaluation of the three strategies for  $T_2^*$  estimation in the presence of single-shot readout. The x-axis represents the cumulative probe time across all epochs, while the y-axis represents the root mean squared error (RMSE). The strategies include: random  $\tau$  selection (blue curve),  $\tau$  selection optimized by maximizing Fisher information  $F$  in Eqn. 4.4 (orange curve), and  $\tau$  selection optimized by maximizing the rescaled Fisher information  $F_T$  in Eq. 4.9 (green curve). The theoretical limit given by Cramér-Rao lower bound (CRLB) for Eqn. 4.4 is depicted by a solid black line. The protocol was averaged over 500 individual runs for each strategy for the estimation of  $T_2^*$ . The adaptive protocols perform better than the non-adaptive protocol in terms of lower uncertainty for any given probing time. (c) Simulations results in the absence of single shot readout with the probability of getting a photon for spin  $|0\rangle$  is equal 0.0187, and for  $|1\rangle$  is 0.0148 (data from experimental results). Here we have  $R = 50000$ . Cramér-Rao lower bound (CRLB) is shown in a black solid line with the dashed black line showing the CRLB limit for the Fisher information  $F_E$  in Eqn. 4.18.

readout, the performance of the adaptive protocol is far from the fundamental limit (solid black line). Such a performance is due to sub-optimal information retrieval from each measurement. To account for such a sub-optimal readout process and disentangle it from the performance of our proposed algorithm, we can encode this information into the algorithm. This can be computed from the Cramér-Rao bound by considering the modified likelihood function for non-SSR given in Eqn. 4.13 and its corresponding Fisher information  $F_E$ .

$$(4.18) \quad F_E(\tau) = - \frac{\alpha V^2 N^2 \left(\frac{\tau}{T_\chi}\right)^{2N}}{T_\chi^2 \left( \alpha V^2 + 2\alpha V e^{\left(\frac{\tau}{T_\chi}\right)^N} - V e^{\left(\frac{\tau}{T_\chi}\right)^N} + \alpha e^{2\left(\frac{\tau}{T_\chi}\right)^N} - e^{2\left(\frac{\tau}{T_\chi}\right)^N} \right)}.$$

Like before, the ultimate lower bound on the variance can be obtained from the inverse of Fisher information in the limit of many identical repetitions. Hence, we minimise the  $1/F_E$  for

given experimental values of  $\alpha$  and  $V$ , marking the optimal performance achievable for our protocol. This is displayed in 4.3(c) as a dotted black line.

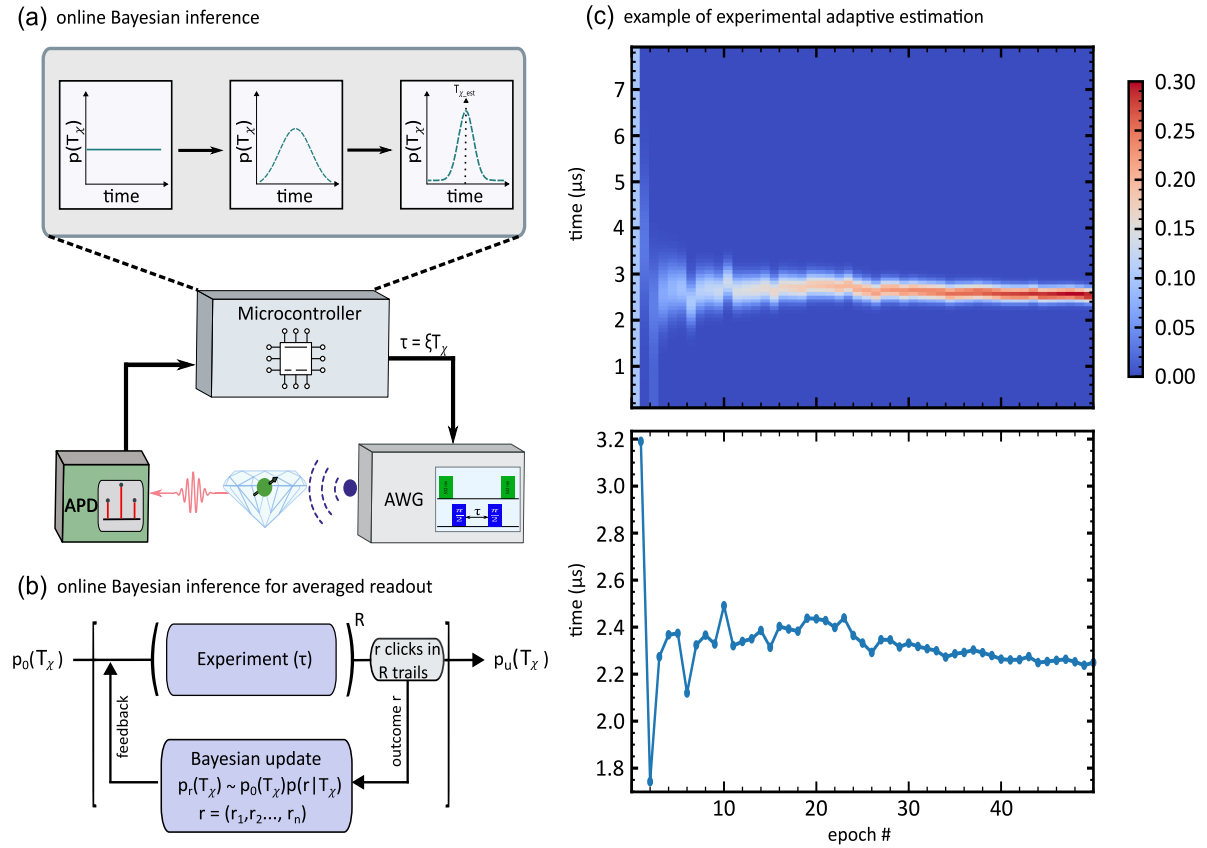
## 4.5 Experimental results

**Data acquisition details.** Before each batch of measurements, we implement a set of pre-measurement calibrations. We start by performing a Continuous-wave optical detected magnetic resonance (CW-ODMR) to extract the resonance frequency of the  $|0\rangle$ ,  $|1\rangle$  spin states. This is followed by Rabi oscillation and a Ramsey measurement to find the  $\pi$  pulse length and detuning frequency, respectively. After these pre-measurement calibrations, we perform the desired ( $T_1$ ,  $T_2$  or  $T_2^*$ ) measurements.

A schematic illustration of the experimental setup can be found in Fig. 4.4(a), where a real-time microcontroller performs the Bayesian update of the probability distribution  $T_\chi$  in a timescale of  $50 \mu\text{s}$ . We performed the measurement on the electron spin associated with an NV centre in diamond. We employed an arbitrary waveform generator (AWG) to create laser and MW pulse sequences. The spin state is optically measured, and the microcontroller uses the detected photon count rate to estimate the value of the decoherence timescale. Since a single interrogation cannot discriminate between qubit states in our experiments. We are required to perform  $R$  measurements, and the resulting number  $r$  of collected photons from these  $R$  measurements are then used to update  $p(T_\chi)$  via the Bayes' rule (see Fig. 4.4 (b)). The optimal probing time  $\tau_{opt}$  is chosen from the updated probability distribution. The value of the optimal probe time  $\tau_{opt}$  is then fed into the arbitrary waveform generator (AWG), which provides the appropriate pulse sequence (both microwave and laser) for the next measurement cycle. A computational latency of  $50 \mu\text{s}$  is a factor 20 faster than what has been previously reported for the real-time quantum sensing experiment at ambient conditions [212]. And this updating time is much smaller than the shortest measurement time (a few tens of ms, at  $\tau \sim 1\mu\text{s}$  and  $R = 10^4$ ) in our experiments.

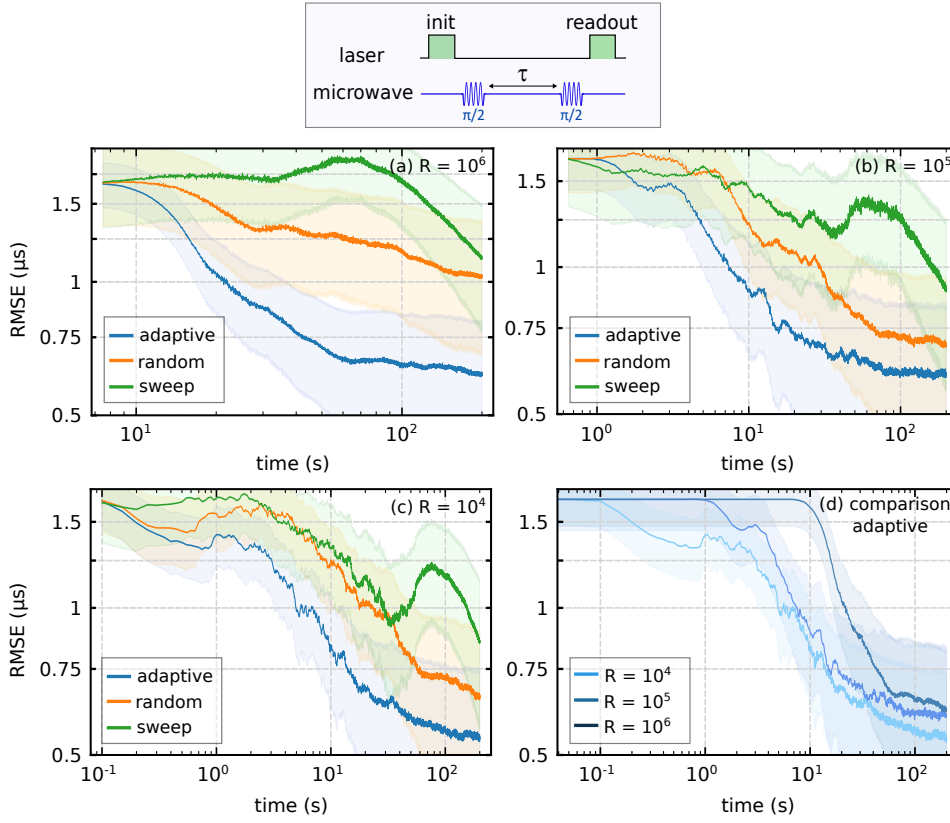
Fig. 4.4(c) provides an example of an experimental  $T_2^*$  estimation through an adaptive Ramsey experiment, depicting the evolution of  $p(T_2^*)$  across successive estimation epochs. Initially,  $p(T_2^*)$  encompasses a uniform distribution within the range of  $0\text{-}8 \mu\text{s}$ . As more measurement outcomes are processed, this distribution progressively converges to a singularly peaked distribution. For an NV centre in a high-purity diamond, the anticipated decay follows a Gaussian pattern ( $\beta = 2$ ) [76]. As such, an adaptive update rule is employed with  $\xi = 0.89$ . The selected  $\tau$  values are displayed in the lower plot, demonstrating their rapid convergence towards the optimal  $\tau_{opt} \sim 0.89 \cdot (T_2^*)_{true} \sim 2.23 \mu\text{s}$ .

Fig. 4.5 presents a comprehensive difference between the efficacy of adaptive and non-adaptive protocols for estimating the dephasing timescale  $T_2^*$ . This assessment encompasses a broader scope and involves three distinct values of readout repetitions  $R$  ( $R = 10^6$ ,  $R = 10^5$ ,  $R = 10^4$ ). With experimentally measured values of  $p_{cl}(|0\rangle) = 0.0186 \pm 0.0017$ , and  $p_{cl}(|0\rangle) = 0.0148 \pm 0.0016$ ,



**FIGURE 4.4. Online adaptive feedback.** (a) The figure illustrates the online adaptive approach implemented in this study. The investigation focuses on the electron spin associated with an NV center within diamond. An Arbitrary Waveform Generator (AWG) is responsible for generating pulses for spin manipulation. The spin state is measured optically, and the microcontroller uses the detected photon counts to estimate the decoherence timescale value. (b) In our experiment, a single measurement is insufficient for discriminating qubit states. Consequently,  $R$  measurements are conducted, yielding the number  $r$  of collected photons. These  $r$  photons are utilised to update  $p(T_\chi)$  via Bayes' rule and compute the probe time  $\tau$  for the subsequent iteration. (c) Experimental adaptive estimation sequence example, where  $p(T_\chi)$  signifies the probability at each measurement epoch. Beginning from a uniform, the probability  $p(T_\chi)$  starts converging towards a narrow peak as more measurement outcomes accumulate. The bottom plot displays the experimentally optimised values of  $\tau$  for each epoch.

denoting the number of detected photons per readout for the spin states  $\{|0\rangle, |1\rangle\}$ . The three varying readout repetition numbers  $R$  ( $R = 10^6$ ,  $R = 10^5$ , and  $R = 10^4$ ) correspond, to mean photon numbers  $\langle n \rangle \sim 16700$ ,  $\langle n \rangle \sim 1670$  and  $\langle n \rangle \sim 167$ , respectively. We implement two distinct non-adaptive protocols: one entails random  $\tau$  selection within the designated  $0-8 \mu\text{s}$  range (based on experimentally observed range), while the other involves uniform  $\tau$  sweeping across the range. To ensure a fair comparison, the total number of measurements  $N \cdot R$  (where  $N$  signifies the



**Figure 4.5: Comparing adaptive and non-adaptive experimental estimation of dephasing time  $T_2^*$ . RMSE is taken with respect to a ground true value of  $2.5 \mu\text{s}$ .** Dephasing time  $T_2^*$  is evaluated through a Ramsey experiment. The spin state, initially polarized in  $|0\rangle$  with a laser pulse, is prepared in a superposition state  $(|0\rangle + |1\rangle)/2$  using a microwave (MW)  $\pi/2$  pulse. A second  $\pi/2$  MW pulse, following a delay  $\tau$ , transforms phase information into population distribution of the  $|0\rangle$  state, which is subsequently detected optically. Our adaptive protocol (represented by the blue curve) showcases superior performance compared to non-adaptive protocols (sweeping  $\tau$  across a predefined range (indicated by the green curve) or randomly selecting  $\tau$  (shown by the orange curve)). This comparison encompasses varying readout repetitions  $R$  for each probing time: **(a)**  $R = 10^6$ , **(b)**  $R = 10^5$  and **(c)**  $R = 10^4$ . In each sub-plot, the root mean square error (RMSE) is depicted, averaged across 110 distinct experimental runs for  $T_2^*$  estimation. This RMSE is displayed as a function of the total probe time in seconds. **(d)** The adaptive protocol's performance is compared across different  $R$  values, using the experimental data from (a), (b), and (c) collectively presented for easy comparison. In all graphs, shaded regions represent 95% confidence intervals.

number of epochs) remained consistent across varying  $R$  values, thereby maintaining a fixed total measurement duration. All curves are the result of averaging over 100 iterations of the complete estimation sequence, thereby deriving the mean performance from an estimated ground truth value of  $2.5 \mu\text{s}$ , presented with a 95% confidence interval.

Fig. 4.5(a) shows the comparison of measurement uncertainty against the total measurement duration for  $R = 10^6$  repetitions per probing time. Commencing with a uniform prior, which

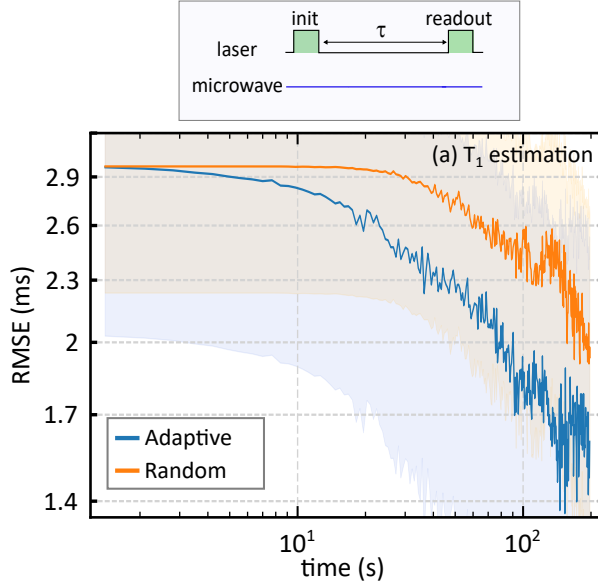
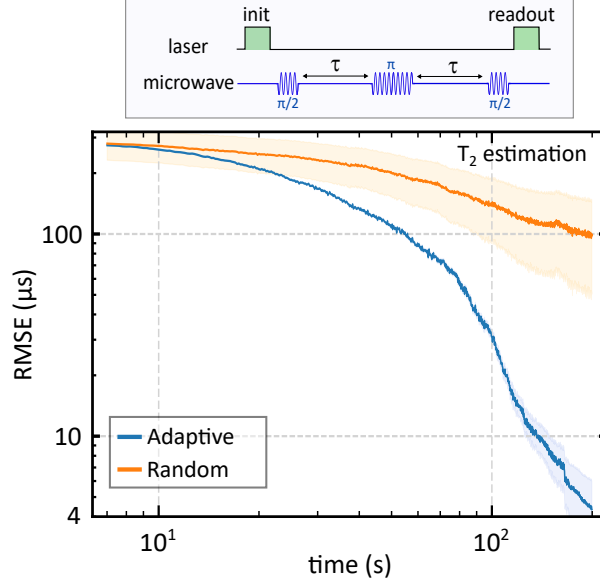


FIGURE 4.6. **Comparing adaptive and non-adaptive experimental estimation of  $T_1$  time.** RMSE is taken with respect to a ground true value of 1.45 ms. Root Mean Square Error (RMSE) with respect to probing time is analyzed for the estimation of spin relaxation time  $T_1$  ( $N = 1$ ). For the adaptive choice of  $\tau$ , we optimized  $F$  with  $\tau_{opt} = 0.8 \cdot T_{\chi}$ , while employing  $R = 10^4$  readout repetitions for each probing time. In each measurement, the electron spin is initialized in  $|0\rangle$  and subsequently assessed for its probability of being in  $|0\rangle$  after a delay  $\tau$ . The RMSE is averaged across 10 individual  $T_1$  measurements for each protocol. The shaded regions within the plot signify the 95% confidence interval. Comparatively, the confidence interval for  $T_1$  estimation is notably wider than that for  $T_2^*$  and  $T_2$  estimation. This difference arises due to the relatively limited number of protocol repetitions, owing to the extended time required for each measurement, given that the true value of  $T_1$  lies within the millisecond range.

serves as the common starting point for all three curves, the progression of uncertainty exhibits clear differences among the three protocols. Notably, the adaptive protocol initiates the process of learning the unknown parameter within only a few epochs, leading to a swift decline in uncertainty as opposed to the non-adaptive protocols. In the case of the random selection of delay  $\tau$ , the learning process falls in between the adaptive protocol and the non-adaptive sweep in terms of performance. The sweep protocol exhibits notably poor performance during the initial estimation epochs. It conducts measurements with probing times considerably shorter than the decoherence rate, leading to minimal information gain. As it eventually approaches probing times closer to the actual decoherence time, the reduction in uncertainty occurs at a quicker pace. Conversely, the protocol involving random probing times uniformly samples the entire expected range, enhancing the likelihood of obtaining significant information even in the initial epochs. In contrast, the adaptive protocol outperforms both non-adaptive approaches by swiftly learning the optimal probing time to extract maximum information about the decoherence time. A comparison among the three experimental curves underscores that, for instance, when targeting

an uncertainty of  $1 \mu\text{s}$ , the adaptive scheme proves approximately 10 times faster than either of the non-adaptive schemes.



**FIGURE 4.7. Comparing adaptive and non-adaptive experimental estimation of  $T_2$  time. RMSE is taken with respect to a ground true value of  $35 \mu\text{s}$ .** Root mean square error (RMSE) as a function of probing time in estimating the Hahn echo decay time  $T_2$  ( $N = 3/2$ ). The adaptive choice of optimal probing time  $\tau$  is based on maximising the Fisher information  $F$  as discussed in the main text, and the number of readout repetitions for each probing time  $\tau$  is  $R = 10^4$ . Every measurement involves the qubit’s preparation in the state  $(|0\rangle + |1\rangle)/2$ , followed by the detection of its overlap with the initial state after a duration of  $2 \cdot \tau$ . At the time  $\tau$ , a spin-flip is executed to realign the state evolution, effectively nullifying the impact of static magnetic fields. The RMSE is averaged over 40 individual measurements of  $T_2$  via each protocol. In the plot, shaded regions correspond to the 95% confidence interval.

Fig. 4.5b illustrates the comparison for  $R = 10^5$ , displaying a similar trend, with the adaptive protocol achieving learning about 4 times faster than the random protocol. However, the sweep protocol’s performance is approximately 20 times worse. This advantage of the adaptive protocol is also evident in the case of  $R = 10^4$ , as depicted in (Fig. 4.5c). In Fig. 4.5d, a comparative assessment of the adaptive scheme’s performance across various  $R$  values indicates that  $R = 10^4$  (corresponding to  $\langle n \rangle \sim 167$  photons detected on average) attains the lowest uncertainty for any measured probing time. This underscores the benefits of more frequent adaptive updates. Decreasing  $R$  further, within the Gaussian approximation in Eq. 4.16, does not lead to further performance enhancement due to increased shot noise in the number of detected photons at the lower value of  $R$ . Consequently, we fix  $R = 10^4$  for the subsequent experiments where we measure  $T_1$  and  $T_2$  (see Fig. 4.6 and Fig. 4.7). We also exclusively focus on the version of the non-adaptive protocol employing a random choice of  $\tau$ , as it surpasses the parameter sweeping approach.

In Fig. 4.6, we compare the adaptive and non-adaptive protocols for estimating  $T_1$  (relaxation)

timescales, revealing the superiority of the adaptive strategy over the non-adaptive counterpart. However, the gain achieved is comparatively less than that observed in  $T_2^*$  measurements. This discrepancy arises because  $T_1$  measurements take considerably longer to process (given true value in the ms range leading to ms probing time with  $R = 10^4$ ), and the statistical averaging of repetitions was small in this scenario.

Moving to Fig. 4.7, we compare the adaptive and non-adaptive protocols for estimating  $T_2$  (dephasing) timescales, where the superiority of the adaptive strategy is again evident. The final Root mean square error (RMSE) of the  $T_2$  value in the adaptive case is approximately 25 times lower than that in the non-adaptive case.

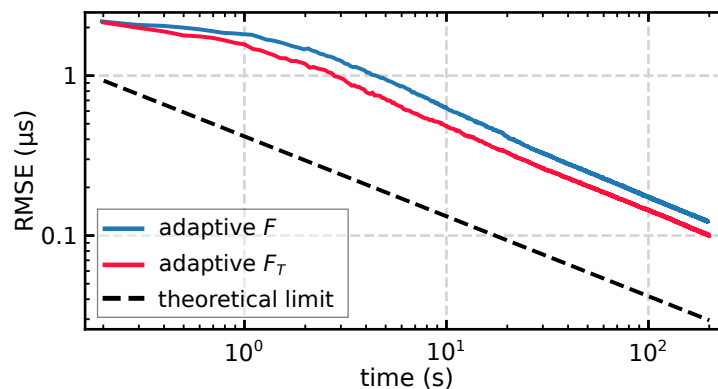


Figure 4.8: **Experimental comparison between maximizing  $F$  and  $F_T$ . RMSE is taken with respect to a ground true value of  $2.5 \mu\text{s}$ .** Root mean square error (RMSE) as a function of probing time in estimating the  $T_2^*$  ( $N = 2$ ) via the two different adaptive protocols. Calculating an adaptive choice through the maximization of the Fisher information divided by the total probing time ( $F_T$ ) (Eqn. 4.4) results in a reduced uncertainty for a specific probing time compared to the approach of simply maximizing the Fisher information ( $F$ ). The experimental estimations of  $T_2^*$  ( $N = 2$ ) is performed with  $R = 10^4$  readout repetitions of each probing time. The RMSE has been averaged over 35 individual measurements of  $T_2^*$  via each protocol. The dashed black line represents the theoretical limit as defined by  $F_E$  in Eq. 4.18. Both experimental curves conform to the scaling outlined by the Cramér-Rao Lower Bound (CRLB) for  $F_E$ .

Fig. 4.8 presents a comparison of adaptive estimation for the dephasing time  $T_2^*$ , achieved through the maximization of either the Fisher information ( $F$ ) or the Fisher information rescaled by the probing time ( $F_T$ ). As previously mentioned, this leads to a distinct multiplication factor  $\xi$  for the adaptive  $\tau$  choice, as outlined in Table 4.1. The plot in Fig. 4.8 demonstrates that as a function of the total probing time, maximizing  $F_T$  leads to approximately 2 times faster lowering of RMSE than maximizing  $F$ , with both experimental curves conforming to the scaling outlined by the Cramér-Rao Lower Bound (CRLB) for  $F_E$  in Eq. 4.18.



## 4.6 Multiparameter estimation

So far, in Chap. 4, we have discussed estimating a single parameter of the Hamiltonian. In this section, we will provide simulation and preliminary experimental results for the case of multiparameter estimation. Where instead of maximum Fisher information for a single parameter, we will have a Fisher information matrix (FIM) to be maximised. In such case, we start from Eqn. 4.1, where:

$$(4.19) \quad p(0|T_\chi, N) = \frac{1}{2} \left( 1 + e^{-\left(\frac{\tau}{T_\chi}\right)^N} \right) \quad \text{and} \quad p(1|T_\chi, N) = \frac{1}{2} \left( 1 - e^{-\left(\frac{\tau}{T_\chi}\right)^N} \right)$$

Here we will try to simultaneously estimate  $T_\chi$  and  $N$ . As mentioned in Sec. 2.2.1, in this case, we will have a Fisher information matrix (FIM), which for  $T_\chi$  and  $N$  takes the form:

$$\text{FIM} = \begin{pmatrix} \sum_{x \in X} \left( \frac{\partial^2}{\partial T_\chi \partial T_\chi} \log f(x|T_\chi, N) \right) f(x|T_\chi, N) & \sum_{x \in X} \left( \frac{\partial^2}{\partial T_\chi \partial N} \log f(x|T_\chi, N) \right) f(x|T_\chi, N) \\ \sum_{x \in X} \left( \frac{\partial^2}{\partial N \partial T_\chi} \log f(x|T_\chi, N) \right) f(x|T_\chi, N) & \sum_{x \in X} \left( \frac{\partial^2}{\partial N \partial N} \log f(x|T_\chi, N) \right) f(x|T_\chi, N) \end{pmatrix} \quad (4.20)$$

Following the similar procedure as done in Sec. 4.2, we can find terms of this FIM (see Apx. A.6 for details on calculation). Such that the final FIM for  $\{T_\chi, N\}$  is:

$$\text{FIM} = \begin{pmatrix} \frac{N^2 \left(\frac{\tau}{T_\chi}\right)^{2N}}{T_\chi^2 \left( e^{2\left(\frac{\tau}{T_\chi}\right)^N} - 1 \right)} & \frac{N \left(\frac{\tau}{T_\chi}\right)^{2N} \log\left(\frac{\tau}{T_\chi}\right)}{T_\chi \cdot \left( e^{2\left(\frac{\tau}{T_\chi}\right)^N} - 1 \right)} \\ \frac{N \left(\frac{\tau}{T_\chi}\right)^{2N} \log\left(\frac{\tau}{T_\chi}\right)}{T_\chi \cdot \left( e^{2\left(\frac{\tau}{T_\chi}\right)^N} - 1 \right)} & \frac{\left(\frac{\tau}{T_\chi}\right)^{2N} \left( \log\left(\frac{\tau}{T_\chi}\right) \right)^2}{\left( e^{2\left(\frac{\tau}{T_\chi}\right)^N} - 1 \right)} \end{pmatrix} \quad (4.21)$$

Using the D-optimality criteria discussed in Sec. 2.3, we find that the FIM is singular with a determinant of 0:

$$(4.22) \quad \Delta = \text{FIM}_{00}\text{FIM}_{11} - \text{FIM}_{01}\text{FIM}_{10} = 0$$

Hence to counter this issue, we devise a new strategy where we use two consecutive sensing times  $\tau = \{\tau_n, \tau_{n+1}\}$  to calculate optimal sensing time for “n + 2” iteration with  $\tau_{n+2} = \tau_{n+1} - \tau_n$ . We use the combined probability distribution of the two last measurements resulting in the following 4 elements:

$$(4.23) \quad p(0,0|T_\chi, N) = \frac{1}{2} \left( 1 + e^{-\left(\frac{\tau_1}{T_\chi}\right)^N} \right) \cdot \frac{1}{2} \left( 1 + e^{-\left(\frac{\tau_2}{T_\chi}\right)^N} \right)$$

$$(4.24) \quad p(0,1|T_\chi, N) = \frac{1}{2} \left( 1 + e^{-\left(\frac{\tau_1}{T_\chi}\right)^N} \right) \cdot \frac{1}{2} \left( 1 - e^{-\left(\frac{\tau_2}{T_\chi}\right)^N} \right)$$

$$(4.25) \quad p(1,0|T_\chi, N) = \frac{1}{2} \left( 1 - e^{-\left(\frac{\tau_1}{T_\chi}\right)^N} \right) \cdot \frac{1}{2} \left( 1 + e^{-\left(\frac{\tau_2}{T_\chi}\right)^N} \right)$$

$$(4.26) \quad p(1,1|T_\chi, N) = \frac{1}{2} \left( 1 - e^{-\left(\frac{\tau_1}{T_\chi}\right)^N} \right) \cdot \frac{1}{2} \left( 1 - e^{-\left(\frac{\tau_2}{T_\chi}\right)^N} \right)$$

In this case the *sum* ( $\Sigma$ ) in the FIM (see Eqn. 4.6) will be over the four probability distributions with  $X = \{p(0,0|T_\chi, N), p(0,1|T_\chi, N), p(1,0|T_\chi, N), p(1,1|T_\chi, N)\}$  for each entry of the FIM. The entries of the FIM can be calculated following the same process as done for a single sensing time (see Apx. A.6.1 for the final equations of this FIM).

Using four elements of the Fisher information matrix (FIM) mentioned in Apx. A.6.1 we find the determinant as:

$$(4.27) \quad \Delta = \frac{N^2 \left(\frac{\tau_1}{T_\chi}\right)^{2N} \left(\frac{\tau_2}{T_\chi}\right)^{2N} \left( \log\left(\frac{\tau_1}{T_\chi}\right)^2 - 2\log\left(\frac{\tau_1}{T_\chi}\right)\log\left(\frac{\tau_2}{T_\chi}\right) + \log\left(\frac{\tau_2}{T_\chi}\right)^2 \right)}{(T_\chi)^2 \left( -e^{2\left(\frac{\tau_1}{T_\chi}\right)^N} - e^{2\left(\frac{\tau_2}{T_\chi}\right)^N} + e^{2\left(\frac{\tau_1}{T_\chi}\right)^N} + 2\left(\frac{\tau_2}{T_\chi}\right)^N + 1 \right)}$$

An analytical method for determining the maxima of this function eluded us. Instead, we can calculate it numerically using probabilities for averaged readout. To implement this multi-parameter estimation scheme, we used a piece-wise linear approximation for both simulation and experiment (see Eqn. 4.28), which allows for a much faster calculation in real-time. On our microcontroller, the approximation takes  $\sim 200$  ns per iteration compared to  $\sim 60$   $\mu$ s per iteration for the full calculation. The approximation works well for  $N < 5$  and is given by:

$$(4.28) \quad \tau_{1_{opt}} = \begin{cases} 0.313\tau_0 + 1.04\hat{T}_\chi, & \text{if } \tau_0 < 0.83\hat{T}_\chi \\ 0.7\tau_0, & \text{if } 0.83\hat{T}_\chi < \tau_0 < 0.96\hat{T}_\chi \\ 0.109\tau_0 + 0.55\hat{T}_\chi, & \text{if } 0.96\hat{T}_\chi < \tau_0 \end{cases}$$

Using this method, we performed simulations for simultaneous estimation of decay factor ( $N$ ) and dephasing time ( $T_2^*$ ) with  $R = 10^5$ . We chose the detector click probability for state  $|0\rangle$  and  $|1\rangle$  as  $p_{clk}(|0\rangle) = 0.01$ ,  $p_{clk}(|1\rangle) = 0.008$ . To highlight the performance of both schemes, we plot the root mean squared error (RMSE) as a function of time in Fig. 4.9. Looking at the figure, we find

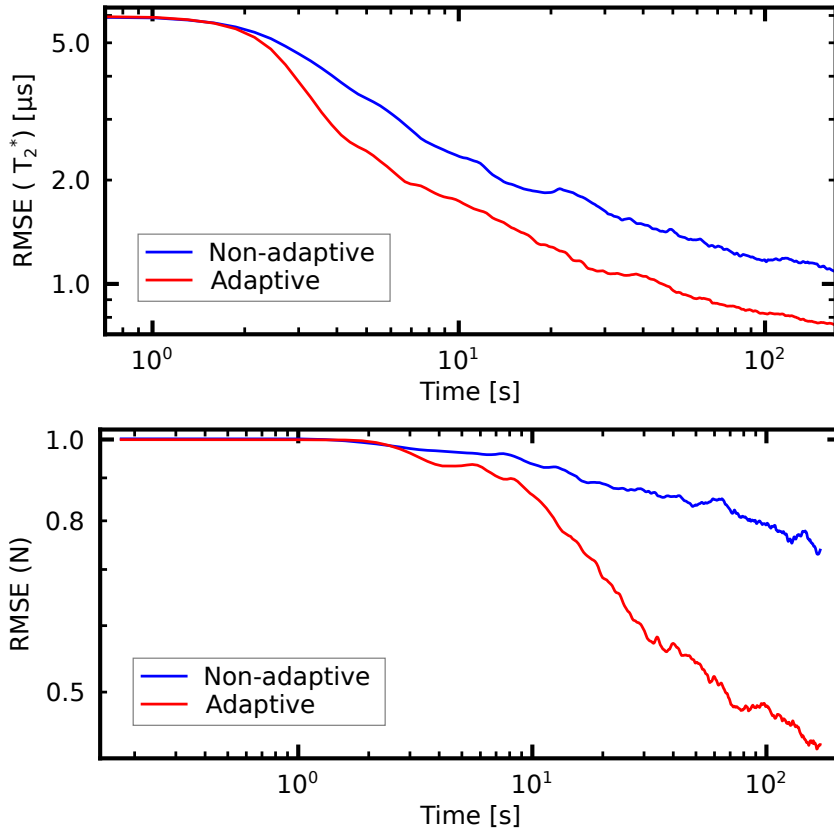


Figure 4.9: **Simulations for simultaneous estimation of  $T_2^*$  top and  $N$  (bottom). RMSE is taken with respect to a ground truth value of  $T_2^* = 4.15 \mu\text{s}$  and  $N = 2$ .** RMSE in the estimation of  $T_2^*$  and  $N$  for adaptive vs non-adaptive protocol. For these simulations, we choose the detector click probability for state  $|0\rangle$  and  $|1\rangle$  as  $p_{clk}(|0\rangle) = 0.01$ ,  $p_{clk}(|1\rangle) = 0.008$ . Both protocols had  $R = 10^5$  readout repetitions at each probing time. The piece-wise linear approximation mentioned in Eqn. 4.28 for the adaptive protocol is used in this estimation.

that the performance of the adaptive protocol for simultaneous estimation of  $\{T_2^*, N\}$  is about  $\sim 4$  times better than the non-adaptive protocol, giving smaller errors at all times.

Using Ramsey measurement ( $\hat{T}_\chi = T_2^*$ ), we experimentally confirm the gain of this adaptive algorithm against the random non-adaptive measurement scheme. To more effectively sample the two-parameter space, the Bayesian update is carried out over 500 particles with the parameter search range set to be  $T_2^* \in [2 \times 10^{-7}, 2 \times 10^{-5}]$  and  $N \in [1, 5]$ . Fig. 4.10 illustrates the experimental results for simultaneous estimation of  $T_2^*$  and  $N$ , indicating about  $\sim 4$  times better performance for estimation of  $N$  similar to simulation results. While the gain for  $T_2^*$  is comparatively less compared to the simulations. These are preliminary results, with more investigation and analysis underway in the lab.

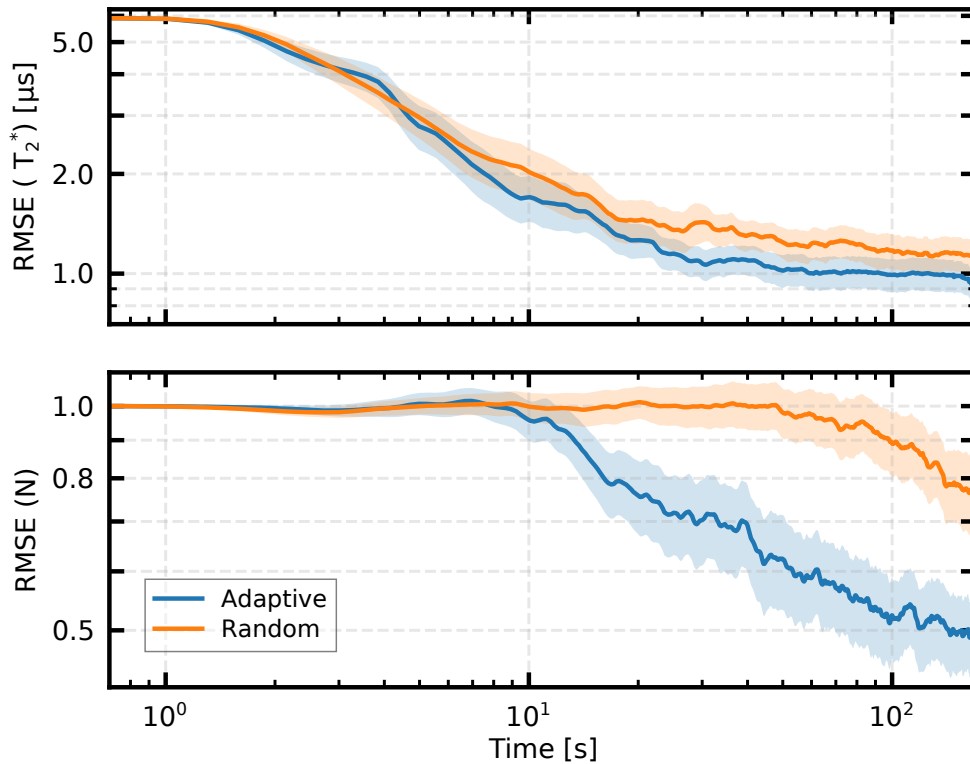


FIGURE 4.10. **Concurrent experimental estimation of  $T_2^*$  (top) and  $N$  (bottom). RMSE is taken with respect to a ground truth value of  $T_2^* = 4.15 \mu\text{s}$  and  $N = 2$ .** The number of readout repetitions for each probing time is  $R = 10^5$ . The results are averaged across 140 individual estimations of  $T_2^*$  and  $N$  via each protocol. The piece-wise linear approximation mentioned in Eqn. 4.28 for the adaptive protocol is used in this estimation. In all plots, the shaded regions represent a 95% confidence interval. Credit to Ben Haylock for data acquisition.

## ADAPTIVE FREQUENCY ESTIMATION EXPERIMENT

## 5.1 Introduction

The goal of this chapter is to improve frequency estimation related to measuring a static magnetic field with a single spin over a large dynamic range using adaptive protocols.

Phase estimation is not only a central idea in quantum metrology [13]; many important quantum algorithms are also based on phase estimation algorithms, for example, Shor's factorization algorithm [2]. Cleve et al. quantum phase estimation algorithm (QPEA) [288], and Kitaev et al. [203, 289] phase estimation algorithm (PEA) have been widely studied to date. Extensions of Kitaev's quantum phase estimation protocol have been shown to be quite successful in measuring frequency over a wide dynamic range [205–207]. The dynamic range ( $f_{max}/\sigma_f$ ) is defined as the ratio of maximum detectable frequency ( $f_{max}$ ) to frequency uncertainty ( $\sigma_f$ ). The precision in a conventional (classical) measurement is limited by the shot-noise limit, which depends on the total measurement time  $T$  as  $\propto 1/\sqrt{\tau T}$  [205, 206, 290]. This scaling happens because  $T/\tau$  repeated measurements are made with the constant sensing time  $\tau$ . One can achieve a more precise measurement with longer sensing time  $\tau \sim T_2$ , but the dynamic range will suffer due to the  $2\pi$  periodicity of the phase. To tackle the problem of  $2\pi$  phase ambiguity, protocols designed on quantum phase estimation algorithms have been used to achieve Heisenberg-limited scaling of uncertainty ( $\sigma_f$ ) with improved dynamic range [205, 291] (refer to Sec. 2.5 for more details on this). Please note that in the literature concerning high dynamic range sensing, it is important to distinguish between the Heisenberg-limited scaling for a single particle and the Heisenberg limit for a system of  $N$  particles. While the Heisenberg-limited scaling for a single particle is limited to  $1/T$  in classical sensing, the Heisenberg limit for a system of  $N$  particles can be surpassed through the utilization of entanglement.

Using protocols based on a quantum phase estimation algorithm, the phase accumulated by the quantum sensor due to interaction with the environment can be efficiently estimated. If this interaction is dictated by the frequency  $f$ , the total sensing time ( $\tau$ ) grows exponentially,  $\tau = 2^k \tau_0$ , where the index  $k$  ranges from 0 to  $K$ . In this chapter, we term this as an adaptive frequency estimation algorithm (FEA). While  $\tau_0$ , the shortest sensing time, limits the sensor's dynamic range to  $= \left[ -\frac{1}{2\tau_0}, \frac{1}{2\tau_0} \right]$ ,  $T_2^*$  bounds the longest sensing time as  $2^K \tau_0 < T_2^*$  [205].

## 5.2 Adaptive frequency estimation algorithm (FEA)

The performance of a frequency estimation protocol can be improved by using a real-time feedback approach which chooses the optimal measurement settings for the next run based on the information from the previous outcomes [206, 292, 293]. An adaptive phase estimation algorithm (PEA) has been realised to achieve Heisenberg-limit scaling [187].

According to theoretical and numerical work [207, 294], it may be possible to increase sensitivities by adaptively controlling the sensing time  $\tau$  or the phase  $\phi$ . Experimental studies with spin sensors for magnetic field estimations have been done as well [206, 211]. However, all of these studies were either performed experimentally with a single-shot readout (SSR) scheme [206] or have simulated the availability of SSR [211].

SSR is unfortunately not currently available in our setup for NV centre experiments at room temperature, which is important, for example, for biological samples requiring ambient conditions (see Sec. 3.4 for details on nuclear spin-assisted readout). Hence an adaptive scheme working with non-SSR sensors is most desirable. This chapter discusses our experimental progress towards implementing an adaptive frequency estimation algorithm (FEA) on a non-SSR sensor using a binomial distribution to describe measurement outcomes. We have shown that by using this adaptive algorithm, the sensitivity of real-time experiments can be greatly improved in contrast to standard non-adaptive techniques.

A problem with non-SSR sensors is the strong overlap of the measurement outcome histograms, as shown in Fig. 5.1(left). This makes it impossible to assign an outcome to either state in a single readout shot with high fidelity. To counter this issue for a non-SSR sensor, measurement step (1) is performed several times to gain information about the sensor's spin state via "averaged" detection [4], yet with a non-negligible error. The most commonly used method to determine the spin state is to use a threshold, known as "majority voting" [295, 296]. Although this approach results in a binary outcome, it is more prone to environmental noise as it disregards most possible outcomes by simply thresholding the photons [213]. A more informative approach is to use all the positive outcomes,  $r$ , from a batch of  $R$  repeated measurements [213] (see Sec. 4.4.1 for details). Such probability can then be represented by the binomial distribution as:

$$(5.1) \quad P(f|r) = \binom{R}{r} P_d(1|f)^r [1 - P_d(1|f)]^{R-r}$$

where  $P_d(1|f)$  is the probability of getting a positive outcome for a given unknown parameter  $f$ , with  $r$  being the number of positive outcomes from  $R$  repetitions [213]. The term  $P_d$  contains information regarding the accumulated phase because of the external target parameter. Since we access the full range of possible outcomes using this method, our measurements are less prone to any mistakes due to the noise from the environment. Which leads to a more sensitive estimation [213].

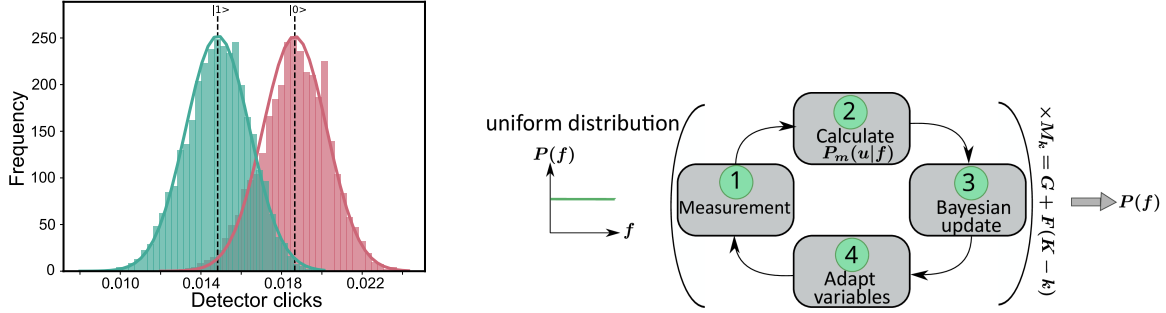


**Figure 5.1: Left: Histogram of measurement outcomes ‘0’ and ‘1’.** Probability of detecting a detector click per readout from spin state  $m_s = 0$  and  $m_s = -1$ . The mean value for spin state ‘0’ was  $0.0187 \pm 0.0019$ , while for ‘1’ was  $0.0148 \pm 0.0016$ . The histogram was taken with  $R = 10000$ . **Right: Adaptive frequency estimation algorithm (FEA).** Graph illustrating the four steps of the adaptive frequency estimation algorithm. This begins by applying the desired experimental pulse sequence (1). Based on the outcome from the previous step, the probability distribution  $P_m(u|f)$  is updated (2), which is followed by the Bayesian update of the probability distribution of the unknown quantity of interest (3). Lastly, the optimal values are extracted, and the next sequence is updated accordingly (4). Inset: We begin with a uniform probability distribution which converges to the estimated value of the unknown quantity after several runs of the protocol [287].

A cyclic process is used to apply adaptive FEA, as shown in Fig. 5.1 (right). Where beginning from a uniform distribution, a set of four steps leads to a final estimation of the unknown quantity. In the first step (1), we apply a Ramsey pulse sequence (see Sec. 3.5.4 for more details) with an exponentially growing time delay, as discussed previously. After each sensing time, we perform a measurement resulting in an outcome ( $u$ ), which could be either one of the two possible outcomes (0 or 1) for SSR or a majority voting case. While for the binomial distribution method, we model the probability distribution as given in Eqn. 5.4. Using this outcome in step (2), we update the probability function expressing the likelihood of detecting an outcome  $u$  due to unknown frequency  $f$ . Step (3) is where we update our estimation of the unknown quantity using the Bayesian inference (see Sec. 2.1.1 for more details). Given as [63, 206]:

$$(5.2) \quad P(f|u) \propto P_m(u|f)P(f|u)$$

where  $P(f|u)$  is the posterior probability distribution of the unknown quantity of interest  $f$ . The total number of iterations for each sensing time is given by  $M_k = G + (K - k)F$ , where  $G$

and  $F$  are optimised parameters, while  $k$  is the sensing time index. Hence as the sensing time grows, the number of iterations shrinks. The rationale for selecting such a number of iterations is that shorter sensing times distinguish frequencies across a wider range, making errors more detrimental to the variance. Thus, to mitigate errors, a greater number of repetitions are required to achieve stronger suppression.

### 5.2.1 Rundown of the adaptive FEA experiment

Step 1 begins with applying a Ramsey interferometry pulse sequence to sense a DC magnetic field. As discussed in Sec. 3.5.4, a  $\frac{\pi}{2}$  pulse prepares the system into initial superposition state of  $|\phi(t=0)\rangle = 2^{-\frac{1}{2}}(|0\rangle + |1\rangle)$ . After this, the system is allowed to evolve under the external field applied ( $\Delta B$ ), resulting in the accumulation of phase proportional to the external field in the rotating frame,  $|\phi(t)\rangle = 2^{-\frac{1}{2}}(|0\rangle + e^{-i2\pi f_{\Delta B}t}|1\rangle)$ . After this, another  $\frac{\pi}{2}$  pulse is applied to project the spin to the eigenstate of  $\sigma_z$ . Which is followed by an optical readout of the spin state.

Step 2 is to update the probability function based on the outcome from Step 1. This function is modelled as follows:

$$(5.3) \quad P_m(u|f) = \frac{1}{2} \left[ 1 + (-1)^u e^{-\left(\frac{t}{T_2^*}\right)^2} \cos(2\pi f_{\Delta B}t - \phi) \right]$$

Where  $T_2^*$  is the dephasing time of the sensor. This model has been widely used for SSR or majority voting non-SSR cases; however, for our experiments, as discussed earlier, we want to use binomial distribution; hence we have an updated probability distribution function  $P_d(1|f)$  given as

$$(5.4) \quad P_d(1|f) = \alpha \left[ 1 + V e^{-\left(\frac{t}{T_2^*}\right)^2} \cos(2\pi f_{\Delta B}t - \phi) \right]$$

Where  $\alpha$  is the threshold given as  $\alpha = \frac{1}{2}[P_d(1|m_0) + P_d(1|m_1)]$ , and  $V$  gives the visibility of the sensor,  $V = \frac{P_d(1|m_0) - P_d(1|m_1)}{P_d(1|m_0) + P_d(1|m_1)}$ . Here  $P_d(1|m_i)$ , for  $i = 0$  or  $1$  is the probability of getting a detector to click for each spin state. For complete derivation, refer to [213].

In the experimental results discussed below for DC magnetometry, our adaptive scheme relies on finding the optimal readout phase. This is achieved by minimising the reachable variance of an unbiased estimator of phase  $\phi$ , known as Cramér-Rao lower bound (CRLB) or maximising the Fisher information  $I$  to improve the estimation of phase  $\phi$  (see Sec. 2.2 for more details on this). Hence utilising this idea, we calculate the Fisher information of the probability function, written as:

$$(5.5) \quad I(f_{\Delta B}) = E \left[ \left( \frac{\partial}{\partial f_{\Delta B}} \log(P(r|f_{\Delta B})) \right)^2 \right]$$



Here  $E$  represent the expectation value. Maximising it for the phase  $\phi$ , such that :

$$(5.6) \quad \frac{\partial}{\partial \phi} I(f_{\Delta B}) = 0$$

we find the optimal phase value to be given as:

$$(5.7) \quad \phi_{opt} = 2\pi \hat{f}_B \tau - \arccos \left( \frac{\sqrt{A^2 - B^2} - A}{B} \right)$$

See Apx. A.7 for a complete derivation of this. In the next section, I will detail the experimental demonstration of implementing a Bayesian approach utilising the full binomial distribution over thresholding the distribution through a majority voting technique to deliver a binary outcome.

### 5.3 Majority voting vs Binomial distribution

This section describes the use of two contrasting approaches to infer the state of the spin sensor after  $R$  repetitions from the number of collected photons  $r$ . Following the discussion about these methods for a non-SSR sensor from Sec. 4.4.1 and Sec. 5.2, we perform an experimental evaluation of the two methods and highlight the gain of binomial distribution method over majority voting. We experimentally performed these measurements using the confocal setup described in Chap. 3 on a single NV centre in a laser-written diamond sample.

As shown in Fig. 5.2, we performed non-adaptive Ramsey measurement (Step 1) to perform DC magnetometry using the externally applied magnetic field at the level anti-crossing. We randomly choose 500 different magnetic field detunings  $f_{\Delta B}$  in the range  $[-2, +2]$  MHz.  $R = 2500$  repetitions

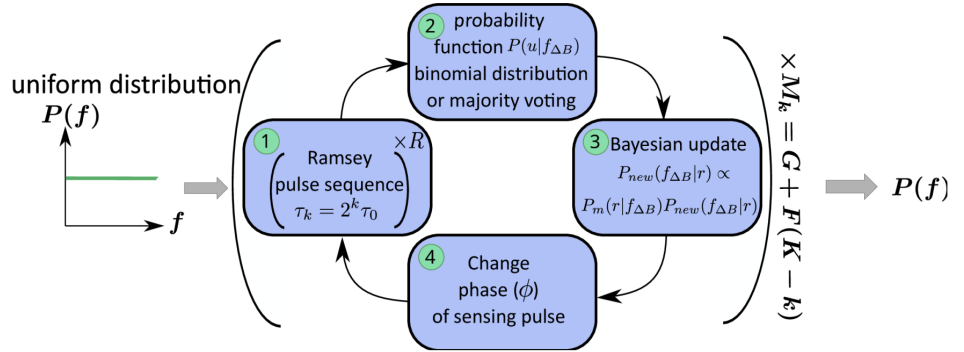


Figure 5.2: **DC magnetometry for non-SSR case.** A visual representation of the phase estimation algorithm used for measuring DC magnetic fields via Ramsey interferometry in the absence of single shot readout (i.e. non-SSR) [287].

were performed for each detuning using both majority voting and binomial distribution scheme (Step 2). The probability distribution in each case was updated using the Bayesian inference (Step 3). While the phase of the second  $\pi/2$  pulse was swept linearly from 0 to  $\pi$  (Step 4). Measurements times are chosen based on Kitaev's algorithm [203, 289] and are given by  $\tau_{k \leq K} = 2^k \tau_0$ . The

number of measurements at each time step is given by  $M_{k \leq K} = F + G(K - k)$ , where  $F$ ,  $G$ , and  $K$  are integers. Set to  $G = 3$ ,  $F = 5$ , and  $K = 5$  for this comparison.

The performance of these two methods was calculated via estimation error:

$$(5.8) \quad \text{Estimation error} = \sqrt{\langle (\tilde{f}_B - f_B)^2 \rangle}$$

Here  $\tilde{f}_B$  is the estimated frequency extracted from the probability distribution at each iteration, while  $f_B$  is the true frequency. In Fig. 5.3 (a), we present our experimental finding for comparison between the two methods. It was found that binomial distribution achieved a more precise estimate than majority voting across all the iterations for both theory and experimental results. Particularly after 32 iterations, binomial methods reach an uncertainty of  $\sim 0.33$  MHz in about 12.81 ms ( $\tau = 125$  ns for the first 23 iterations and then  $\tau = 250$  ns for the next 9), while to reach the same level of uncertainty majority voting takes about 54 iterations with total sensing time of 34.69 ms resulting in the binomial method being  $\sim 2.7$  faster in that case. The small discrepancy between the theory and experimental results is mainly attributed to the uncertainty in the calculation of detection probability for the two states, i.e.  $P_d(1|m_0)$  and  $P_d(1|m_1)$ .

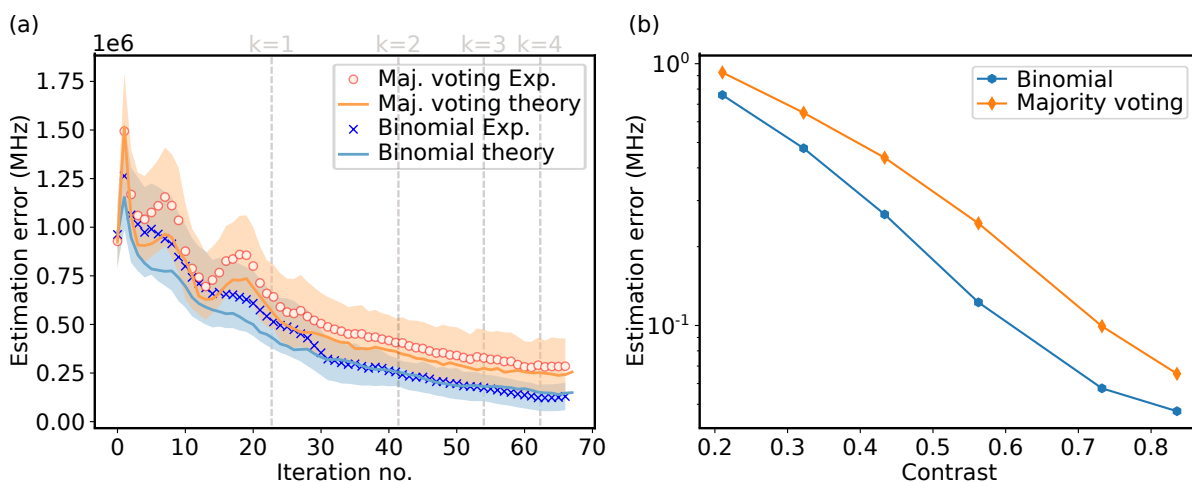


Figure 5.3: **Majority voting vs Binomial distribution. (a) Experimental result:** Estimation error as a function of the number of iterations for majority voting (orange) and binomial distribution (blue). Measurements were performed for 500 randomly chosen detuning with  $R = 2500$  repetitions. The shaded region on the curve corresponds to the 95% confidence interval. Dotted vertical lines mark the increment in the ‘k’ value signalling a change in sensing time (or the number of iterations). **Note** the theory curves in this plot have added Gaussian noise with 2% standard deviation to  $P_d(1|m_0)$  and  $P_d(1|m_1)$  to most closely emulate the experimental results. **(b) Simulation result:** Estimation error as a function for the contrast (see Eqn. 5.9) of the two spin states. Binomial distribution outperforms the majority voting for all contrast values. Credit to Ben Haylock for data acquisition.

The performance of these methods was also compared against the contrast of the states. The contrast is given as [72, 206]:

$$(5.9) \quad C = \left[ 1 + \frac{2(P_d(1|m_0) + P_d(1|m_1))}{(P_d(1|m_0) - P_d(1|m_1))^2 R} \right]^{-1/2}$$

here  $P_d(1|m_0)$ ,  $P_d(1|m_1)$  is the number of photons per shot from spin state  $m_s = 0$  and  $m_s = 1$ , respectively, and  $R$  is the number of repetitions for each detuning.

In Fig. 5.3 (b), we show simulation results comparing the performance of majority voting and binomial distribution methods in terms of estimation error vs contrast. We find that the performance gain of binomial over the majority voting persists across contrast ranging from 0.2 to 0.85.

## 5.4 Adaptive frequency estimation algorithm result

This section describes the simulation and the experimental results for the estimation of the frequency via the application of adaptive and non-adaptive frequency estimation protocols. The simulations described in this section are different in a way that these were done using the parameters ( $P_d(1|m_0)$ ,  $P_d(1|m_1)$ ) of the NV centre extracted from real-time experiments. Using these parameters, we simulated the counts, which are then used for the update and adaptation. We employed a binomial distribution approach to calculate the probability function in both cases. Similar to before, measurement times are chosen according to the Kitaev phase estimation algorithm [203, 289], with measurement times given by  $\tau_{k \leq K} = 2^k \tau_0$ . The number of measurements at each time step is given by  $M_{k \leq K} = F + G(K - k)$ , where  $F$ ,  $G$ , and  $K$ , are integers, here set to  $F = 5$ ,  $G = 3$ ,  $K = 5$ . In the non-adaptive case, for each  $\tau_k$  the phase is swept through a full  $2\pi$ . After reaching the end of the prescribed steps,  $\tau$  is set to  $T_2^*$  and measurement phases are chosen in the range  $[0, 2\pi]$  at random. The non-adaptive protocol does not take advantage of information learned from previous measurements in any way. While for the case of adaptive protocol, optimal phase choices are made based on the Eqn. 5.7.

Looking at Fig. 5.4, we can see that the phase values for the adaptive scheme start converging in a small number of iterations, much faster than  $M_k$  iterations calculated theoretically.

To see the performance of this adaptive frequency estimation protocol, we performed experimental measurements in the lab using our room temperature confocal setup. For the measurement, we randomly choose 500 different values of magnetic field values  $f_{\Delta} B$  in the range  $[-2, +2]$  MHz and the performance of frequency estimation protocols was compared in regards to the estimation error (see Eqn. 5.8) from the actual detuning magnetic applied to the system. Fig. 5.5 shows the simulation and experimental results for the frequency estimation via the proposed adaptive phase estimation scheme protocol with  $R = 10000$ . As seen in the figure, the adaptive protocol outperforms the non-adaptive scheme. The final error in frequency estimation is  $\sim 4$  times smaller for the adaptive than the non-adaptive scheme. Here the theory curves are plotted by running simulations offline using the experimental settings ( $P_d(1|m_0)$  and  $P_d(1|m_1)$ ) obtained

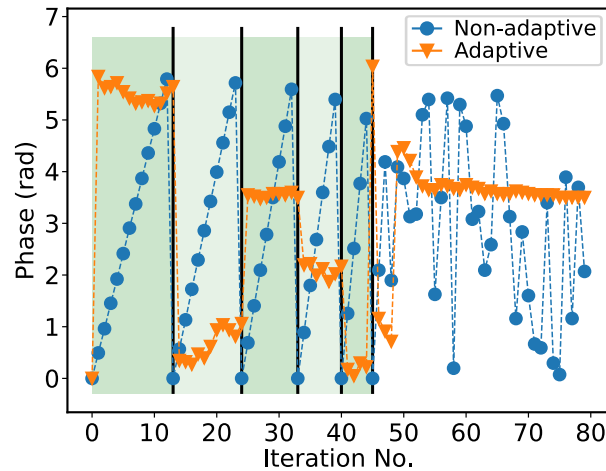


Figure 5.4: **Phase values for frequency estimation via Ramsey measurement.** Phase value in each iteration of the adaptive and non-adaptive scheme. Credit to Ben Haylock for data acquisition.

from pre-calibration measurements. One thing to note here is that there is a difference between theory and experimental results for both protocols. We attributed this issue to the instability of the counts (change in the value of  $P_d(1|m_0)$  and  $P_d(1|m_1)$ ) over time for experimental data.

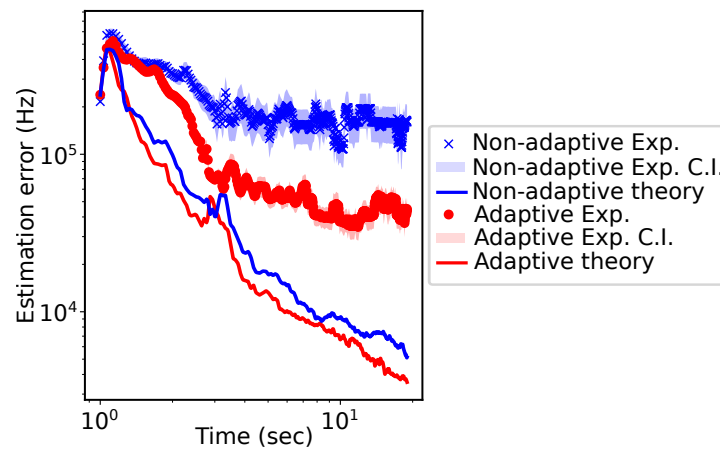


Figure 5.5: **Simulations and experimental results for frequency estimation. Error is calculated using Eqn. 5.8 from the true magnetic field detuning  $f_B$  applied in the range  $[-2,+2]$  MHz.** Frequency estimation with  $R = 10000$  repetitions. Here the theory curves are plotted by running simulations offline using the experimental settings ( $P_d(1|m_0)$  and  $P_d(1|m_1)$ ) obtained from pre-calibration measurements. The difference between theory and experimental results for both protocols was attributed to the instability of the counts (change in the value of  $P_d(1|m_0)$  and  $P_d(1|m_1)$ ) over time for experimental data. The shaded region gives a confidence interval of 95%. Credit to Ben Haylock for data acquisition.

To test the protocol's robustness, we applied it to  $R = 4000$  repetitions, as shown in Fig. 5.6. Here again, we see that even though the total number of detected counts is smaller due to  $R = 4000$  iterations, the adaptive scheme for both simulations and experiment is better than the

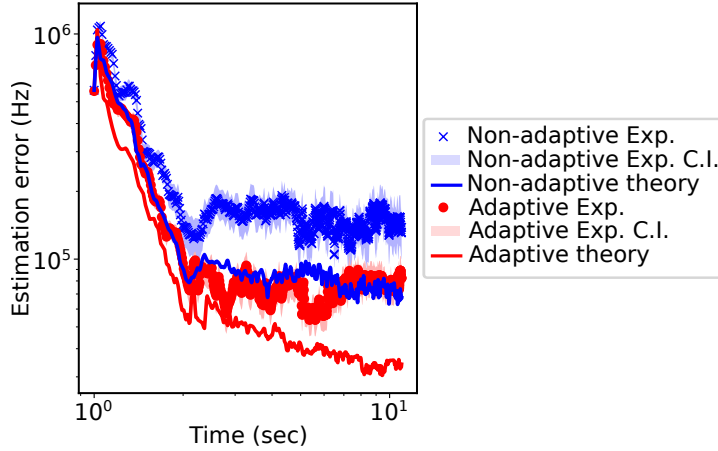


Figure 5.6: **Simulations and experimental results for frequency estimation. Error is calculated using Eqn. 5.8 from the true magnetic field detuning  $f_B$  applied in the range  $[-2,+2]$  MHz.** Frequency estimation with  $R = 4000$  repetitions. Here the theory curves are plotted by running simulations offline using the experimental settings ( $P_d(1|m_0)$  and  $P_d(1|m_1)$ ) obtained from pre-calibration measurements. The shaded region gives a confidence interval of 95%. Credit to Ben Haylock for data acquisition.

non-adaptive scheme, leading to an almost 2 times smaller error in the final estimate. For the case of  $R = 100000$  (see Fig. 5.7), the experimental results for both adaptive and non-adaptive cases are not only far from the theoretical predictions, but the adaptive gain is also much smaller compared with lower  $R$  values. We attributed this issue to the count's instability (change in detection probability from each state,  $P_d(1|m_0)$  and  $P_d(1|m_1)$ ) leading to experimental poor performance of both protocols in comparison to theory.

We also compared the performance of this adaptive FEA protocol against the scheme already present in the literature along with the adaptive-optimised scheme proposed in our paper [287], which in this chapter we name as "Double adaptive protocol".

**1/sigma adaptive protocol:** This protocol is described in [212]. In this scheme, the first measurement time is chosen as  $\tau_0$ , while the subsequent times are chosen by  $\tau = \frac{1}{2\pi\sigma}$ , where  $\sigma$  is the standard deviation in the Bayesian estimate of the detuning frequency. Once  $\tau \geq T_2^*$ ,  $\tau$  is set to a random value selected from a Gaussian distribution of standard deviation  $T_2^*/20$  centred at  $0.7T_2^*$ . The phase is kept constant at zero, and averaged readout is via majority voting (for more details, refer to Sec. 2.5).

**Double adaptive protocol:** This protocol is proposed in [287]. Where the estimation proceeds the same as the adaptive scheme, except when the optimal phase estimate is stable (defined as when the variance of three consecutive phase choices is less than  $\frac{0.1}{\pi}$ , see Fig. 4b in [287]), the update rule then proceeds immediately to the next value of  $\tau$  without completing  $M_{k \leq K}$  measurements.

Fig. 5.8, and 5.9 show the performance of the adaptive FEA protocol against these protocols for different repetitions ( $R$ ). Where we find that the adaptive FEA protocol performs quite well

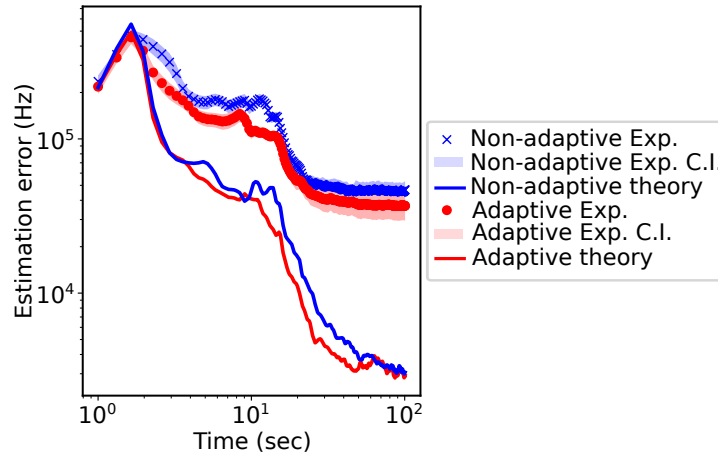


Figure 5.7: **Simulations and experimental results for frequency estimation. Error is calculated using Eqn. 5.8 from the true magnetic field detuning  $f_B$  applied in the range  $[-2,+2]$  MHz.** Frequency estimation with  $R = 100000$  repetitions. Here the theory curves are plotted by running simulations offline using the experimental settings ( $P_d(1|m_0)$  and  $P_d(1|m_1)$ ) obtained from pre-calibration measurements. The difference between theory and experimental results for both protocols was attributed to the instability of the counts (change in the value of  $P_d(1|m_0)$  and  $P_d(1|m_1)$ ) over time for experimental data. The shaded region gives a confidence interval of 95%. Credit to Ben Haylock for data acquisition.

against the other protocols, see Fig. 5.8.

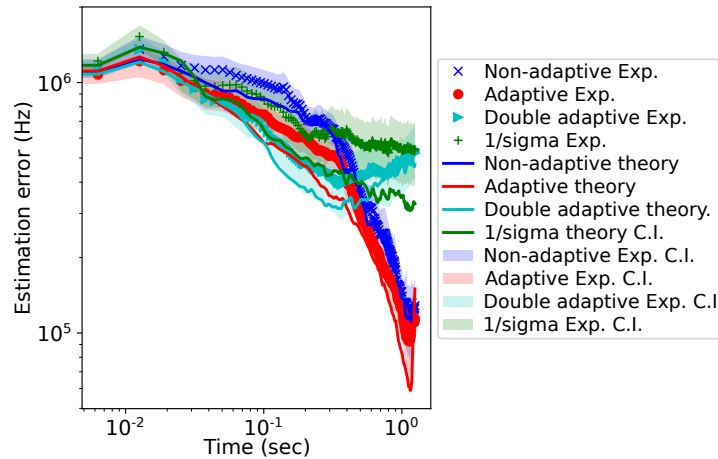


Figure 5.8: **Simulations and experimental results for frequency estimation for different protocols.** Frequency estimation with  $R = 2000$  repetitions. Here the double adaptive scheme performs on par with the adaptive scheme, but as time gets longer, it starts to saturate, and both adaptive and non-adaptive schemes surpass it. The shaded region gives a confidence interval of 95%. Credit to Ben Haylock for data acquisition.

But as the number of repetitions increases, when  $R = 20000$  (see Fig. 5.9), adaptive FEA protocol is outperformed by other protocols, especially the double adaptive becomes significantly better. Hence, we find that with different  $R$ , the performance gain of the protocols changes and

certain protocols perform better than others (more details on this in Sec. 5.5).

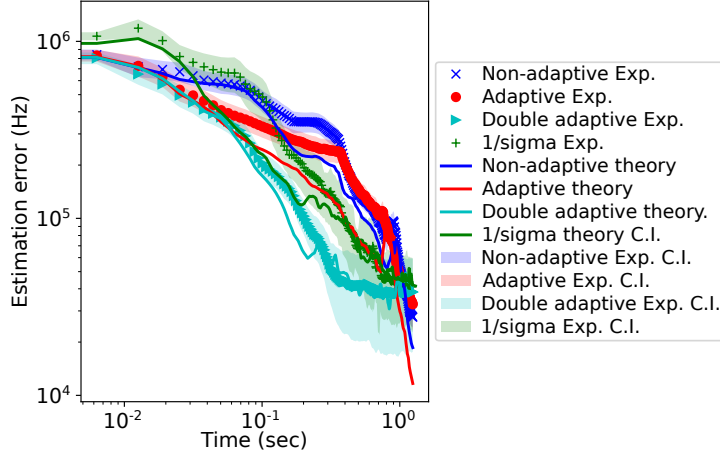


Figure 5.9: **Simulations and experimental results for frequency estimation for different protocols.** Frequency estimation with  $R = 20000$  repetitions. In this case, the double adaptive scheme performs much better than any other scheme for the whole duration, with adaptive performing marginally better than the non-adaptive scheme. The shaded region gives a confidence interval of 95%. Credit to Ben Haylock for data acquisition.

## 5.5 Simulations: Performance of adaptive protocols for different experimental settings

In this section, we performed simulations to better understand the contrasting behaviour of the above-described protocols across different repetitions  $R$ . For these simulations; we used the values which emulated the experimental values closely. For these simulations, the detection probabilities for the two spin states were set to  $P_d(1|m_0) = 0.016$  and  $P_d(1|m_1) = 0.011$ . The value of  $T_2^*$  was set to  $5.5\mu\text{s}$  and  $N = 2$  for a Ramsey measurement. Here each trial was run over 500 epochs to ensure convergence has been reached, and 500 trials of each simulation were performed to reduce statistical uncertainty. In addition to the above-mentioned schemes, we propose two new adaptive schemes and compare them with the schemes already discussed in Sec. 5.4. These two additional schemes are:

**Dual adaptive variance rule:** in this protocol, measurement times are chosen as per the 1/sigma protocol update rule, while the measurement phase is chosen as described for the Adaptive FEA update rule (Eqn. 5.7).

**Step adaptive variance:** In this scheme, the selection of measurement phases follows the process outlined in the adaptive FEA rule (Eqn. 5.7). However, updates to the measurement times occur only after the phase estimate has stabilized. The 1/sigma update rule governs these time updates when they do occur.

Figure 5.10 displays the results for two different values of  $R$ . We observe that in both cases adaptive FEA rule performs quite well at long time scales. For  $R = 25000$  at short time scales, all three multi-adaptive protocols (double adaptive, dual adaptive variance, and step adaptive variance) outperform both adaptive FEA and non-adaptive schemes, with the double adaptive being a clear winner. While at longer timescales, the performance of adaptive FEA and the double adaptive is almost the same. Conversely, at  $R = 2500$ , only the two multi-adaptive protocols based on  $1/\sigma$  briefly outperform the non-adaptive scheme, but they do not reach anywhere near the final absolute error. Here the adaptive FEA scheme is a clear winner. Furthermore, at  $R = 2500$ , the double adaptive rule seems to be the worst performer.

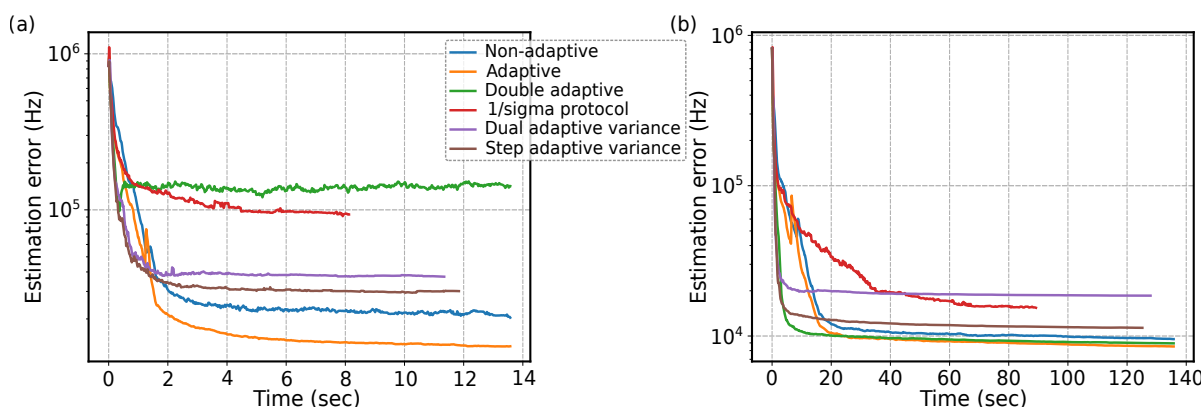


Figure 5.10: **Simulations comparing different protocols for frequency estimation. (a)** Estimation with  $R = 2500$ . **(b)** The same estimation with  $R = 25000$ .

This settings-dependent performance for simulations discussed above along with the varied performance for experimental estimation discussed in Sec. 5.4 was quite intriguing. Hence to further understand it, we performed simulations in terms of contrast (see Eqn. 5.9). In our model, the probability equation 5.4, is dependent on the parameters  $\alpha$  and  $V$  which in return are dependent on the detection probabilities ( $P_d(1|m_0)$  and  $P_d(1|m_1)$ ) from the spin state. Since we find these detection probabilities from pre-calibration measurements and they stay constant throughout each of these protocol runs, the performance of the protocols gets strongly affected if there is any change in these values during the measurement. Hence we performed simulations, where we compared all these adaptive rules across different experimental parameters expressed in terms of contrast. In Fig. 5.11 we plot the performance of all these schemes in terms of estimation error vs contrast.

In these simulations against contrast, the contrast is varied by adjusting the value of  $R$  (see Eqn. 5.9). The number of iterations is held constant for each rule at every contrast level. However, the number of iterations varies when moving between contrast levels. Therefore, performance comparisons between different contrast levels should not be made directly.

There are features of the estimation that are not captured by this contrast plot which are captured by Fig. 5.10 or by Fig. 5.8. One of the most significant limitations is that Fig. 5.11 only



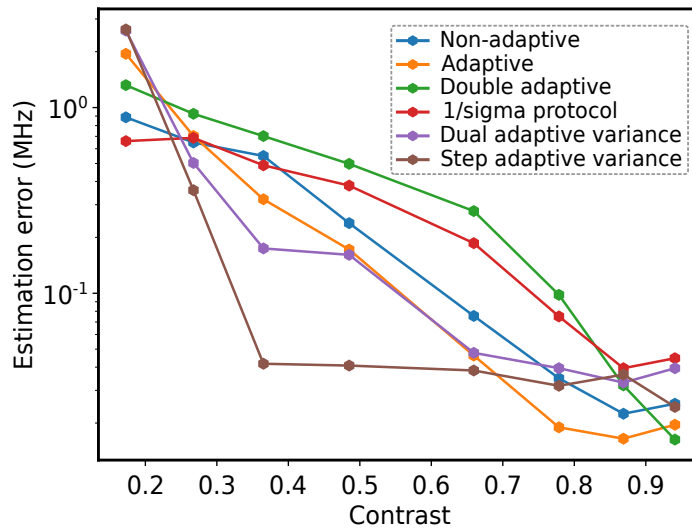


Figure 5.11: **Simulations comparing different protocols performance against contrast.** In this plot number of iterations ( $M_k$ ) is the same for all protocols at one particular value of contrast.  $M_k$  changes between different contrast values.

plots the final value, disregarding any intermediate values. However, as seen in experimental and simulation results there are certain experimental parameters (contrast values) where alternative protocols perform significantly better over certain time intervals. For example in Fig. 5.10(b), the dual adaptive variance algorithm reaches a value close to the best achieved by any other algorithm in  $\sim 10$ s vs 20s for others, and then maintains that value. Therefore, if the  $R = 25000$  experiment were run for only 10 seconds, the dual adaptive variance algorithm would seem like a better choice than the Adaptive FEA algorithm. Hence, the findings of these initial experimental and simulation results dictate that when selecting the optimal algorithm, all experimental conditions must be carefully evaluated.

One thing that we observed across our experimental and simulation results was sometimes poor convergence of the protocols based 1/sigma rule, which skews the average performance upward. The limiting factor for these algorithms has previously been observed experimentally by Joas et al. [212] as well. With no clear explanation for why such runs occur and no practical method for preventing them, even in theory, all of the runs had to be taken into account. Although such runs can be identified and eliminated post-experiment, in such a case, the additional overhead of failed runs must be factored into the average run time of the remaining successful runs. This calculation has not been performed here.



## SINGLE VANADIUM CENTRES IN SiC

## 6.1 Introduction

A number of the most successful applications of quantum networking primitives have been based on using single optically-active spin defects and impurities [182]. In general, such systems can be described as having an electron spin that is associated with a point defect, such as a nitrogen-vacancy (NV) in diamonds [17, 34, 297] (see Sec. 1.3 for details) or silicon vacancies [298, 299] along with other related systems such as in SiC [157, 163] (see Sec. 1.4.1 for details) or 2D materials [300, 301], interfaced with optical photons by means of spin-selective optical transitions that are spectrally stable and atomic-like in nature. As an electron spin couples to several nuclear spins, these spins are used to store the quantum states over a long period of time. They can also be used for implementing quantum error-correction codes to achieve fault-tolerant operation. A direct interface between optical photons and nuclear spins is possible in some systems with a long optical lifetime [302, 303] as in such systems, the hyperfine interaction may be larger than the optical linewidth, allowing for optical photons to interact directly. A spin-photon interface in the telecom wavelength region can be useful for quantum network applications since it is compatible with standard optical fibre networks that cover the same wavelength range. Although nonlinear processes can convert emissions at other frequencies into the telecom range [36, 127, 304], the requirement for additional optics in the system to implement such protocols reduces the system's overall efficiency. The inhomogeneity of the optical transition frequencies is one of the most important parameters for analyzing the optical transition for different emitters. The emission frequencies of quantum emitters are typically spread over a wide range in response to local variations in strain and electric field in the solid-state matrix. However, to ensure high-visibility quantum interference, quantum networking protocols require

the emission to be indistinguishable. To overcome this problem, either strain or electric fields have been used to tune the optical transitions. On small-length scales, strain is not an easy process to implement. It can have a detrimental impact on other properties, including the mixing of excited states, which impacts the spin relaxation time and the fidelity of optical spin readouts [286]. While by applying an electric field through small electrical contacts on the surface of the chip, it is possible to tune optical transition in a reproducible manner, with experiments showing a very large tuning range [166, 305, 306]. However, scalability is not easy; adding more electrical contacts while reducing crosstalk is a technical complexity that is not trivial. A potential alternative to this approach is to utilize the quantum frequency process employed for frequency conversion to the telecom range. The pump laser can be tuned to finely control the output telecom frequency so that all emitters are in resonance [307]. This approach involves considerable technological complexity for each emitter in the network.

In this chapter, we study the vanadium (V) defect's optical, electronic and charge state properties ( $V^{4+}$ ) with an excited state lifetime of 167 ns in an isotopically-purified 4H-SiC (sample A) as well as in standard high-purity semi-insulating (HPSI) 4H-SiC sample (sample B). This study gives the first experimental confirmation of optical transitions that conserve spin and their corresponding dependence on the externally applied magnetic field. Our study involves a comprehensive analysis of the optical emission from numerous  $V^{4+}$  centres, examining their distribution patterns in both standard and isotopically-purified samples. An ultra-narrow ( $\sim 100$  MHz) inhomogeneous distribution is observed in the isotopically-purified sample, in contrast to the several GHz spectral distribution found in SiC with natural isotopic composition. This small distribution can be attributed to the decrease in local stress due to the lack of isotopic mass variation. In the last section of this chapter, I will discuss our findings of charge state dynamics of  $V^{4+}$  centre, where we show that for a high-purity semi-insulating (HPSI) sample, we can achieve charge state stability of more than a few seconds. The results discussed in this chapter highlight the potential of  $V^{4+}$  centres for promising applications as a telecom-ready quantum networking platform.

### 6.1.1 Sample

We make use of two SiC samples designated as 'A' and 'B' in this study.

**Sample A:** The material used for this sample was a  $\sim 110 \mu\text{m}$  thick isotopically-enriched 4H- $^{28}\text{Si}^{12}\text{C}$  layer. This layer was grown by chemical vapour deposition (CVD) on the Si-face of a standard 4-degree off-cut (0001) 4H-SiC substrate. The isotope purity was estimated to be about  $\sim 99.85\%$  for  $^{28}\text{Si}$  and about  $\sim 99.98\%$  for  $^{12}\text{C}$ . These purities were then confirmed by secondary ion mass spectroscopy (SIMS) for one of the wafers in the series. To confirm the n-type nature of the layer, current-voltage measurements were carried out using a mercury probe station. The measurement showed a free carrier concentration of about  $6 \cdot 10^{13} \text{ cm}^{-3}$ . This value is quite close to the concentration of the residual nitrogen (N), which is a shallow donor of  $\sim 3.5 \cdot 10^{13}$

$\text{cm}^{-3}$  concentration as determined from low-temperature photoluminescence (PL) [308, 309]. The concentration of the B shallow acceptor is expected to be in the low  $10^{13} \text{ cm}^{-3}$  range due to contamination from the susceptor. Deep-level transient spectroscopy (DLTS) measurements indicated that the primary electron trap within the layer was associated with the carbon vacancy  $V_C$ , exhibiting a concentration within the lower range of  $10^{13} \text{ cm}^{-3}$ .

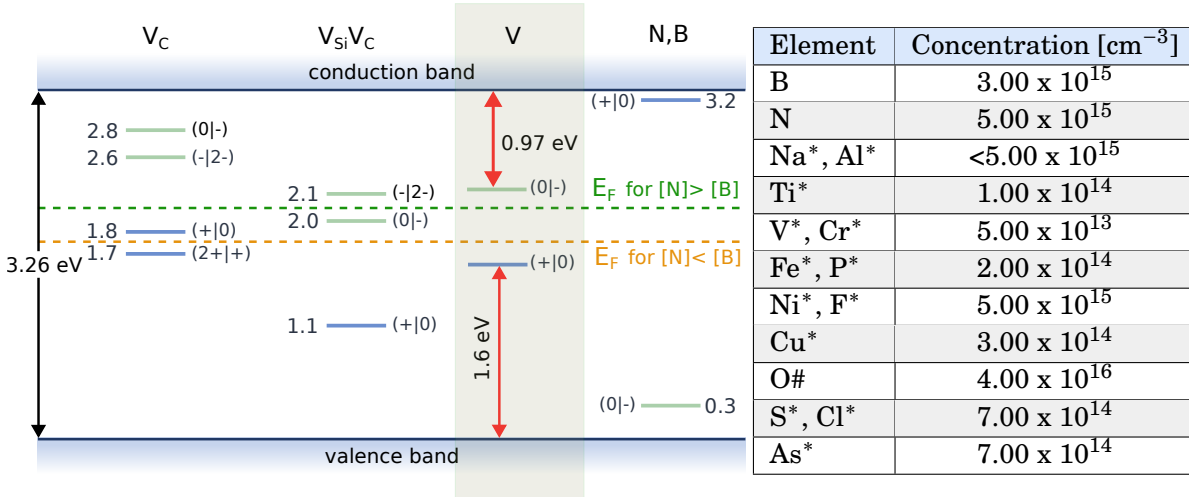


**FIGURE 6.1. Transition levels scheme in SiC and impurity concentration in HPSI 4H-SiC. (Left)** An energy diagram showing the levels at which carbon vacancy ( $V_C$ ), divacancy ( $V_{Si}V_C$ ), vanadium (V), nitrogen (N) and boron (B) charge transition are in SiC. For the case of the HPSI sample, depending on whether the upper level is occupied or not for the case when  $[N] < [B]$ , the Fermi level can be positioned above either the  $(2+|+)$  or  $(+|0)$  level of  $V_C$ . This same concept applies to the acceptor levels of divacancy for the case when  $[N] > [B]$ . To indicate the location of the Fermi level, dotted lines are placed within the levels. Hence depending on the concentration of N and B, the Fermi level will be found at either the donor levels of  $V_C$  or the acceptor levels of the divacancy. The transition levels for  $V_C$  are extracted via DLTS, EPR and calculations [310–312] (see details in the main text). **Right:** Analysis of impurities in high-purity semi-insulating (HPSI) 4H-SiC material using secondary ion mass spectrometry (SIMS). Data adapted from [313].

**Sample B:** This is a high-purity semi-insulating (HPSI) silicon carbide (4H-SiC) obtained from Cree. It was used to stabilise the charge state of single vanadium emitters. The residual N donor and B acceptor in this HPSI material are present in compatible concentrations in the low-mid  $10^{15} \text{ cm}^{-3}$  range. Meanwhile, the dominant intrinsic defects in the material are C vacancy and divacancy, which are present in the high  $10^{15} \text{ cm}^{-3}$  range. One thing to note here is that this difference in impurity concentration between two different samples leads to a change in the Fermi level (as shown in Fig. 6.1 (left)). While, the main contributor to the reduction of inhomogeneous broadening is the purity of the sample from isotopic variations. Assuming a higher concentration of N donors than B acceptors, the Fermi level will reside at approximately  $\sim E_C - 1.35 \text{ eV}$  on the  $(0|-)$  acceptor level of the divacancy. In the case where B acceptors are more

concentrated and can compensate for the N donors, the Fermi level will instead occupy the (+|0) donor level of  $V_C$  at approximately  $\sim E_C - 1.35$  eV. The Fermi level is situated between the (+|0) and (0|-) levels of V in both scenarios, with the neutral charge state  $V^{4+}$  being stable (see Fig. 6.1). However, in the first scenario, the single  $V^{4+}$  emitters' photoluminescence decay may still be minimally affected by electrons trapped at the divacancy's (0|-) acceptor level.

In Fig. 6.1(left), we depict the energy levels of the various defects in the 4H-SiC sample. By monitoring the transmutation of implanted radioactive  $^{51}\text{Cr}$  isotope to  $^{51}\text{V}$  using deep-level transient spectroscopy (DLTS) techniques [314, 315], it has been determined that the single acceptor level (0|-) of V in 4H-SiC is  $\sim 0.97$  eV below the conduction band ( $E_C - 0.97$  eV). A study by Ewvaraye et al. [316] has reported the (+|0) donor level of V in 6H-SiC at 1.55 eV measured using optical admittance spectroscopy (OAS). While based on photoexcitation electron paramagnetic resonance (photo-EPR) measurement of the 4H and 6H polytypes, it was reported that the single donor (+|0) level of V was located  $\sim 1.6$  eV above the valence band (VB) ( $E_V + 1.6$  eV) [317], further supporting the OAS results. As a result of a subsequent study of V-doped semi-insulating (SI) 4H-SiC, Mitchel et al. [318] found the activation energy of free carriers to be about 1.6 eV from temperature dependence measurement. This value was assigned to the (+|0) donor level of V with energy distance as  $E_C - 1.6$  eV [318]. A deep donor level cannot compensate shallow donors in n-type materials. Thus, it does not help pin the Fermi level in sample A. Hence the activation energy should be associated with the valence band, and the (+|0) level of V should be at  $\sim E_V + 1.6$  eV in accordance with the results of photo-EPR studies [317], OAS results and the Langer-Heinrich rule [319].

In both samples, vanadium ions were implanted at an energy of 100 keV, which corresponds to a depth of about 58 nm. Single emitter studies were enabled by a low implantation dose of  $10^8$   $\text{cm}^{-2}$ . The damage created to the lattice due to the implantation process can be repaired by annealing the sample at 1400 °C under an Ar atmosphere for 30 minutes. This annealing was done without a C-cap layer, and no noticeable surface morphology degradation was observed.

The vanadium (V) defect formation happens when a V atom substitutes a silicon atom in the lattice of SiC [180, 264, 320]. Three possible charge states of vanadium can exist within the 4H-SiC:  $V^{4+}$  (neutral),  $V^{5+}$  (positively charged), and  $V^{3+}$  (negatively charged). Out of these three, only one charge state exhibits luminescence in the telecom region and possesses an electron spin of  $S = 1/2$  that is required for quantum networking applications. Two zero-phonon lines are observed in 4H-SiC for the neutral charge state ( $V^{4+}$ ), encoded as  $\alpha$  and  $\beta$ , respectively, corresponding to the impurity in the (k) site or the (h) site, respectively [320]. For the study done in this chapter, we will focus on the  $\alpha$  site of the  $V^{4+}$ . A zero-phonon line at  $\sim 1278.8$  nm characterises this site.

### 6.1.2 Optical measurements

All of the optical measurements discussed in the later part of this chapter were performed with the sample at 4.3K. This sample was mounted in a closed-cycle cryostat (Montana Cryostation s100) with a custom-made external shroud, allowing us to bring an external SmCo permanent magnet as close as 20 mm from the sample. These measurements were conducted using a custom-built standard confocal microscopy setup. Where we used a CW telecom tunable diode laser, in resonance with the  $\alpha$  site of the vanadium [320]), and a 520 nm green repump laser [264]. We employed a series of long-pass filters in the detection path, allowing us to filter out the excitation laser and only collect the emission's phonon sideband (PSB) (1280 nm - 1600 nm). This PSB is detected by a superconducting nanowire single-photon detector (SNSPD from Single Quantum EOS). Sec. 3.10 discusses more details about this optical setup.

The following sections will identify a single vanadium defect by performing an auto-correlation measurement. We will follow this by studying the defect's electronic structure via the polarisation-resolved photoluminescence excitation (PLE) and give a first experimental demonstration of the spin-conserving optical selection rules [321]. We have systematically studied the optical emission of more than 150 defects (sample A) and more than 300 defects (sample B). We found that for sample A, the emission wavelengths spread of the defects within each region had a standard deviation as small as 100 MHz with an overall standard deviation of less than 1 GHz. Compared to any other quantum emitter reported in the literature, these numbers are much smaller, greatly reducing the need for any additional frequency conversion or tuning processes.

## 6.2 Optical spectroscopy of a single vanadium centre

A home-built confocal microscopy setup (described in Sec. 3.10) has been used to conduct the optical measurements at a temperature of 4.3K. As part of our optical spectroscopy, we use two lasers to excite the system: a narrowband (20 kHz) telecom laser that can be tuned to a wavelength between 1270 and 1350 nm in resonance with the zero phonon line of the V  $\alpha$ -line [320] as well as a green repump laser (520 nm) which is used to compensate for ionisation caused by lasers [264]. To simplify the discussion, we express the frequency of the resonant excitation throughout the entire chapter in terms of detuning (in GHz) from a base frequency  $f_0 = 234425.0$  GHz, which corresponds to a wavelength of 1278.8417 nm. A photoluminescence (PL) map of the sample is acquired by scanning an excitation laser across the x-y plane of the sample, thus identifying the V defects, as shown in Fig. 6.2(a), where the vanadium defects are visible as bright ( $\sim 10^3$  counts per second) localized spots. The PL map shown in Fig. 6.2(a) contains 389 spots that are detected using an automated detection algorithm (see Sec. 6.3) over a map area of  $1600 \mu\text{m}^2$ . This corresponds to having about  $0.29 \text{ spots}/\mu\text{m}^2$ . Since the algorithm does not detect every spot, and all of these spots do not correspond to single emitters, this number is a rather lower bound.

To confirm the presence of a single emitter among these spots, we performed a second-order

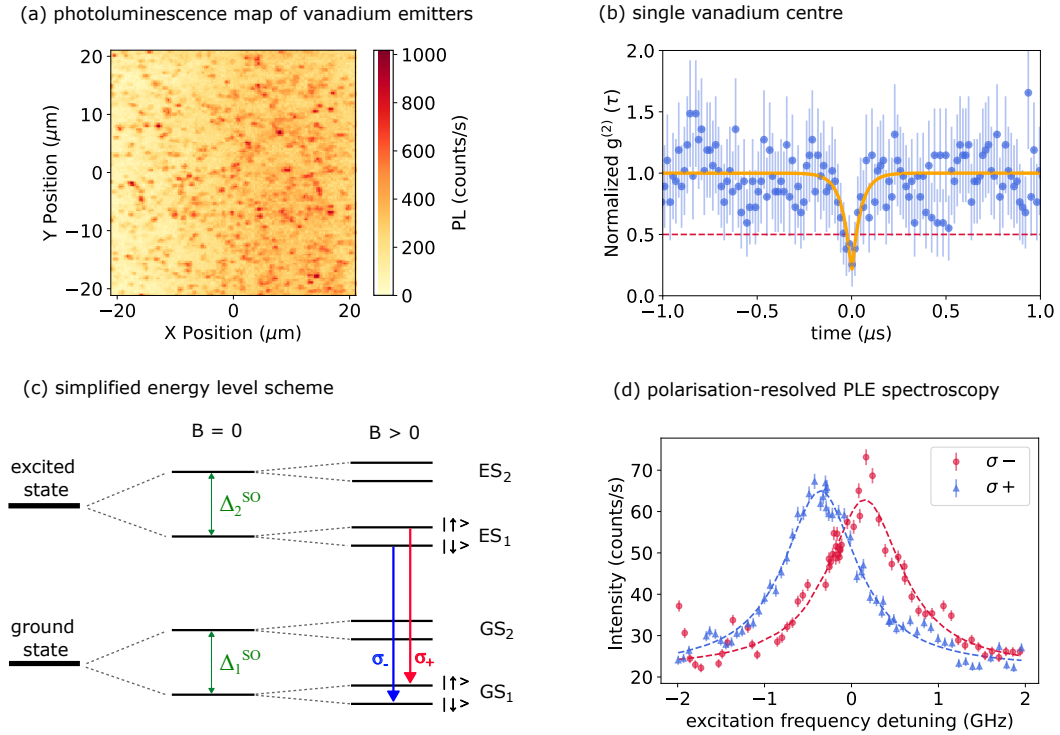


**FIGURE 6.2. Optical spectroscopy of a single vanadium  $V^{4+}$  centre in 4H-SiC.** (a) The photoluminescence (PL) intensity map obtained by scanning an excitation laser across the sample in resonance ( $1278.84 \text{ nm}$ ,  $234.42457 \text{ THz}$ ) with the zero phonon line (ZPL) of the V defects. These vanadium defects are marked by the localised spots in the map ( $\sim 1000$  counts per second). (b) Shows a second-order autocorrelation measurement  $g^2(\tau)$  performed for one of the defects as a function of time delay ( $\tau$ ). The measured experimental value of  $g^2(0) = 0.255 \pm 0.180$  signalling the presence of a single vanadium defect. Experimental data (blue) was fitted with a single exponential function (orange line) given in Eqn. 6.1. (c) Vanadium impurities in SiC can be represented using the following simplified energy level diagram. The presence of spin-orbit couplings (represented by  $\Delta_1^{SO} = 529(1) \text{ GHz}$  [264] and  $\Delta_2^{SO} = 181(1) \text{ GHz}$  [264] in the figure) lifts the degeneracy of the ground and excited state set by  $C_{3v}$  symmetry [321, 322]. The degeneracy between the electron spin levels is further removed by applying a magnetic field  $B$ . Two circularly-polarised transitions are permitted  $\sigma_+$  and  $\sigma_-$ , indicated by the red and blue arrows, respectively. (d) Shows the performed polarisation-resolved photoluminescence excitation (PLE) measurements where we scanned the frequency of the resonant excitation laser and recorded the resultant photoluminescence at an applied field of about 1000 Gauss. Here red circle corresponds to a  $\sigma_-$  circular polarisation, while a blue triangle corresponds to a  $\sigma_+$  circular polarization. The frequency of the laser on the x-axis has been expressed as a detuning from the base frequency  $f_0 = 234425 \text{ GHz}$ .

correlation  $g^2(\tau)$  measurement. For this, we used a Hanbury-Brown and Twiss configuration to perform the  $g(2)$  measurements. As shown in Fig. 3.52, the PL emission from the defects is split between 50:50 using a fibre beam splitter ("FBS", Thorlabs TW1300R5F1). This split signal



is then passed on to the two channels of the superconducting nanowire single-photon detector (SNSPD). The output of which is counted via a TimeTagger (Swabian Instrument). We use the Timetagger to record and time correlate the photon arrival on the two channels. To verify the working of the Hanbury-Brown and Twiss configuration, we used a signal from a single NV centre before performing a measurement with a single vanadium defect. Switching back to the vanadium signal, we observed an experimental value of  $g^2(0) = 0.255 \pm 0.180$  (see Fig. 6.2 (b)). The experimental data were fitted with a single exponential function given as:

$$(6.1) \quad g^{(2)}(\tau) = 1 - Ae^{-\tau/\tau_c}$$

the values for fitting in Fig. 6.2 (b) were  $A = 0.828 \pm 0.163$  and  $\tau_c = 0.048 \pm 0.013 \mu\text{s}$ .

After characterising the emitter with  $g^{(2)}(\tau)$  measurement. Our next step was to study its electronic structure by using a method known as photoluminescence excitation spectroscopy (PLE). We carried out the theoretical calculations described in the section below.

### 6.2.1 Theoretical study of electronic structure

Based on a combination of the theories presented in [321–323], we present a theoretical analysis of the optical transitions with the help of the lowest ground and excited Kramers doublets (KDs). Our approach is based on the KD Hamiltonians to model the energies of the KDs, given as:

$$(6.2) \quad H_k = E_k + \frac{1}{2}\mu_B \vec{B} \mathbf{g}_k \vec{\sigma}_k + \frac{1}{2}\vec{\sigma}_k \mathbf{A}_k \vec{I} + \mu_N g_N \vec{B} \cdot \vec{I},$$

where in the above equation,  $k$  labels are used for KDs, while the zero-field energies of the  $k$ -th KD are represented by  $E_k$  (in MHz). With  $\mu_B$  being the Bohr magneton and  $\mu_N$  the nuclear magneton (in MHz/Gauss). The nuclear  $g$ -factor is given by  $g_N$ , the strongly KD dependent  $g$ -tensor as  $\mathbf{g}_k$ , and the hyperfine tensor as  $\mathbf{A}_k$ , see Table 6.1 for the values of these parameters from literature.

KD $k$	$g_k^z$	$\alpha_k^{zz}/h$ (MHz)	$a_k^{xx,yy}/h$ (MHz)	$\alpha_k^{xz}/h$ (MHz)
$g$ ( $1, \Gamma_4$ )	1.748	232	165	0
$e$ ( $2, \Gamma_{5/6}$ )	2.24	213	0	75

Table 6.1: A review of related KDs parameters from literature for the Vanadium  $\alpha$  defect in 4H-SiC. Ground states (GS) parameters are derived from [323], which are based on [264]. While for the excited state (ES), we use parameters from [185]. The signs of  $\alpha^z z_k$  are chosen to describe the data best. In addition to these components, there are no other components of the  $g$ - and hyperfine-tensors (i.e. they are 0).

It is possible to describe the coupling to an electric field with a frequency in the vicinity of the crystal field splitting  $\Delta_{cr} = E^e - E^g$  by using the Hamiltonian formula, given as:

$$(6.3) \quad H_d^\sigma \approx \mathcal{E}(t)\epsilon|e, -\sigma\rangle\langle g, -\sigma| + \text{h.c.}$$

where the pseudo-spin of the KDs along with the polarisation of the electric field  $\mathbf{E}$  having an amplitude  $\mathcal{E}(t)$  is described by  $\sigma = \pm = \uparrow, \downarrow$  within the rotating wave approximation (RWA). In this case, we only take into consideration the dominant part of the transition, that's spin conserving, and by doing so, we ignore the much weaker spin-flipping transition that may occur due to the spin-orbit coupling process. Where for the RWA the driving field must fulfil  $|\epsilon\mathcal{E}| \ll \min_i |\Delta_{so}^i|$ . The first step of modelling the spectra is assuming the width of each of the hyperfine transitions,  $\gamma$ , is the same. As a result, we can quantify the transition intensity of each of the hyperfine transitions as:

$$(6.4) \quad a|\langle g, \sigma_g, m_g || g, \sigma \rangle \langle e, \sigma | | e, \sigma_e, m_e \rangle|^2 \frac{\gamma}{\left[4(\omega - E_{\sigma_e, m_e}^e + E_{\sigma_g, m_g}^g)^2 + \gamma^2\right]}$$

In this case, we use (a) as a fitting parameter that is independent of the hyperfine states (but still dependent on  $\mathbf{B}$ ). The hyperfine states are grouped by their main spin ( $\sigma_k$ ) as well as their nuclear contribution ( $m_k$ ). Nevertheless, the hyperfine states are composed of spin, orbital, and nuclear states that are different from each other. The analytical expressions for the states and energies are contained in the reference [323].

## 6.2.2 Experimental results for PLE

To perform polarisation-resolved PLE measurements, the excitation laser frequency is scanned across the zero-phonon line with selected polarisations, the excitation laser is prepared in one of the two circularly polarisation basis ( $\sigma+$  or  $\sigma-$ ), and the detection is carried out in the co-polarised state. For these measurements, we use a Fizeau-Interferometer wavemeter (HighFinesse, WS7) with a resolution of 1 Angstrom to measure and scan the wavelength of the excitation telecom laser. As shown in the "PLE measurements" box in Fig. 3.52, with the help of a fibre beam splitter (FBS), we will split the excitation laser and send 10% of the power from the excitation laser to the wavemeter. To control the excitation power and fix the polarisation of the excitation laser, we use a half-wave plate and a linear polarizer, which are referred to as "HWP" and "LP" in Fig. 3.52, respectively. The excitation laser is then passed through a quarter-wave plate (QWP), with its fast axis set at  $45^\circ$  with respect to the incident linear polarisation. It is thus possible to circularly polarize the excitation beam before the excitation of a sample in this way. A polarimeter, composed of the same quarter-wave plate ("QWP"), a half-wave plate, and a linear polarizer (marked as the "HWP2" and "LP2" in Fig. 3.52) is then used to analyze the PL

Parameter	0 Gauss	600 Gauss	1000 Gauss
Amplitude $a(B)$ (GHz/s)	22.6±0.2	19.5±0.2	23.1±0.2
Offset $o(B)$ (1/s)	24.9±0.3	23.4±0.3	27.6±0.3

Table 6.2: Fitting parameters dependent on the measurement setup.

emission from the V defects before being detected by the SNSPD. This physics of  $V^{4+}$  charge state is largely determined by a single active electron placed in a  $3d$  orbital, which has, as a result, a  $C_{3v}$  symmetry imposed by the crystal field of SiC. By coupling spin-orbits into Kramer doublets, which are pairs of states with the degeneracy connected through time inversion, the  $C_{3v}$  symmetry is further broken. An externally applied magnetic field is the only thing that can lift the degeneracy of Kramer doublets. Theoretical calculations [321, 322] have predicted that the Kramers doublet in the ground and excited states will undergo spin-selective circularly polarized optical transitions. Theoretical calculations predict spin-selective circularly-polarized optical transitions between Kramers doublets in the ground and excited states (Fig. 6.2(c)). There are two distinct peaks observed with orthogonal circular polarisations when PLE is performed at a magnetic field of 1000 Gauss, roughly aligned along the SiC c-axis (Fig. 6.2(d)). We fitted the data to a Lorentzian function with a centre at  $0.155 \pm 0.015$  GHz for  $\sigma+$  and with  $-0.335 \pm 0.011$  GHz for  $\sigma-$ . In agreement with our theoretical predictions (see Sec. 6.2.1), we have extracted a relative Zeeman splitting of  $\sim 510$  MHz from the fittings. The two peaks shown in Fig. 6.2(d) are because of the circular polarisation-dependent selection rules [322]. These peaks are related to the spin-conserving transitions, as schematically shown in Fig. 6.2(c), between the first ground ( $GS_1$ ) and the first excited state ( $ES_1$ ).

Further investigation was carried out on how the spectrum of PLE is affected by the externally applied magnetic field  $\mathbf{B}$  along the sample c-axis (Fig. 6.3). In the case of  $B = 0$  Gauss, the two transitions are superimposed onto each other without visible splitting between them. A small amount of splitting can be observed at  $B = 600$  Gauss, and this splitting increases further at  $B = 1000$  Gauss. In a remarkable finding, the linewidth of the resonance appears to decrease with increasing magnetic field strength. To complete a study, we compare our data with the existing theoretical models[322, 323]. For example, we calculate the frequency and hyperfine transitions strength based on the previously measured experimental values [185, 264, 323], as shown in Fig. 6.3(d). For each hyperfine allowed transition, we assume that the shape is a Lorentzian with the same width  $\gamma$ . As part of our fitting model, we treat the width  $\gamma \approx 1$  GHz, the central (or zero-field) transition frequency  $\Delta_{cr}$  for each defect, along with the amplitude of peak and background offset parameters as the fitting parameters (more details are given in Sec. 6.2.1). Setup-dependent fitting values of these parameters are given in Table. 6.2.

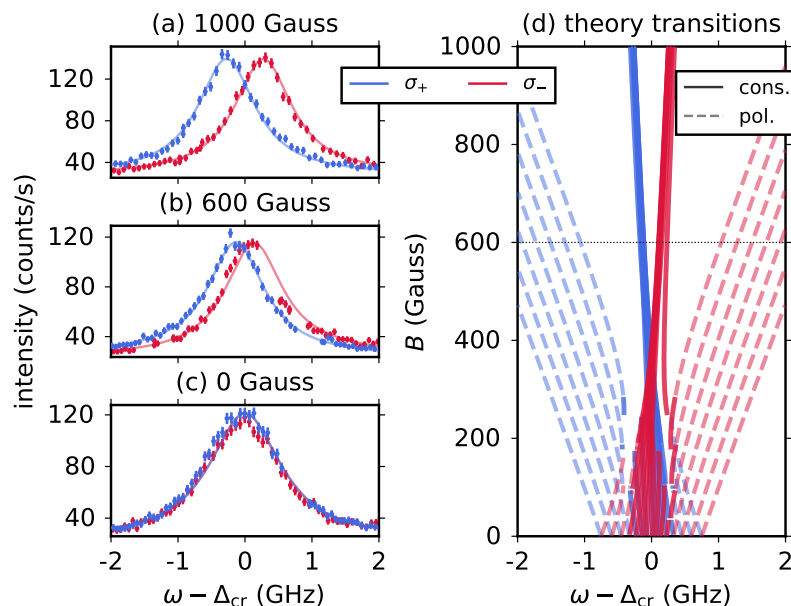


**FIGURE 6.3. Magnetic field-dependent PLE spectroscopy.** (a), (b), (c) show the magnetic field-dependent spectroscopy of the same vanadium defect at various applied  $\mathbf{B}$  fields along the  $c$ -axis of the sample. While in (d) shows the predicted hyperfine transitions based on the model described in Sec. 6.2.1 and the hyperfine parameters were taken from [185, 264, 323]. The main transitions (solid lines) start narrowing as the magnitude of the magnetic field increases with the conservation of the nuclear and KD spin. On the other hand, the hyperfine-allowed transitions (dashed lines) flip the KD spin and can polarize the nuclear spin. The fit [solid lines in (a)-(c)] allows for different backgrounds and amplitudes for each of the measurements but shares the same width  $1038 \pm 7$  MHz and central transition frequency  $\Delta_{cr} = 234425594 \pm 4$  MHz for all transition frequencies [see (d)]. Where the legends of the figure give information about the polarization.

As part of fitting the data in Fig. 6.3, we sum all the possible transitions within a given polarisation ( $\sigma$ ) and a global offset ( $o$ ) (dependent on  $B$ ), using the hyperfine parameters from [185, 322], we determine the hyperfine linewidth  $\gamma$ , magnetic field dependent fit parameters  $\{a(B), o(B)\}$  along with the crystal splitting  $\Delta_{cr}$  (which can vary from one defect to another). Hence using the least square fitting weighted by the inverse Poisson error of data, we extract  $\gamma = 1038 \pm 7$  MHz with the fitted central frequency of  $\Delta_{cr} = 234425594 \pm 4$  MHz. It is important to stress that under the same signs of the  $zz$  component of the hyperfine tensors, the model using values from the literature predicts the narrowing of the linewidth due to the bunching of the main hyperfine transitions for higher magnetic fields. Where the splitting of the two peaks in Fig. 6.3 can be approximated by  $\mu_B |g_e - g_g| B$  when we have large magnetic fields  $B \gg 100$  Gauss, both of the predictions of the theory are true for our measurement results.

### 6.3 Ultra-narrow inhomogeneous distribution

It is noticeable from the previous experiments [264] that the zero-phonon lines in vanadium ensembles have an asymmetry, with the tails being longer at higher frequencies and the lines being duplicated at higher frequencies as well. It has been suggested that this is due to isotope shifts of the nearby  $^{13}\text{C}$ ,  $^{29}\text{Si}$ , and  $^{30}\text{Si}$  isotopes. This isotope shift is a phenomenon caused by a change in the mass of nearby atoms, thereby affecting the local strain or bandgap [324, 325], resulting in a change in the frequency of the zero-phonon line due to the variation in the mass of nearby atoms. For the linewidth fitting method, a shift of  $22 \pm 3$  GHz per unit mass has been observed for nearest-neighbour carbon isotopes and  $2.0 \pm 0.5$  GHz per unit mass for silicon isotopes. To support this, it was recently shown by Hendriks et al. [184] that tuning the optical excitation wavelength of a vanadium ensemble can result in a change in the optically-detected magnetic resonance spectrum. Where the excitation at a wavelength of 1278.86 nm (with a detuning of approximately -3 GHz compared to our base frequency  $f_0$ ) only produced a dip corresponding to the vanadium electron spin resonance, excitation at 1278.76 nm (approximately +15 GHz from  $f_0$ ) showed side peaks that could be attributed to hyperfine couplings with the neighbouring  $^{29}\text{Si}$  atomic nuclei. There is, therefore, a suggestion that in contrast to the case where natural abundance isotope composition is present, the inhomogeneous distribution of zero-phonon lines should become narrower in the case of isotopically enriched SiC, with the removal of the majority of  $^{13}\text{C}$ ,  $^{29}\text{Si}$  and  $^{30}\text{Si}$  isotopes.

In this work, we investigated this quantitatively using a dataset derived from a sequence of photoluminescence maps taken at different excitation frequencies for both samples (see Fig. 6.4(a) and Fig. 6.4(b)).

For sample A, the spectral distribution of more than 150 PL spots was statistically analysed to gain a quantitative understanding of the data. To do this, we took a series of maps at different detunings across 4 different regions of the sample, each about  $100 \mu\text{m}^2$  wide (see Sec. A.8 for more details). These maps were processed by automatically detecting the spots associated with emitters. This was done by convolving the image with a Gaussian function of a size comparable to the diffraction limit of the microscope and detecting the local maxima. Then we computed the counts for each spot by integrating the signal over a square of the area as large as the confocal width for each spot. For every spot position, we plot the total counts in each map as a function of excitation laser detuning, which was then fitted with a Gaussian function to extract the centre frequency of the transition. Fig. 6.4(c) shows the histograms for inhomogeneous distributions of central frequencies for sample A and sample B.

For sample A, we found that all of the spots associated with  $\text{V}^{4+}$  defects appear and disappear on relatively similar excitation frequencies, with a standard deviation of about 100 MHz in the central frequencies of these emitters. The frequency shift of optical transitions in  $\text{V}^{4+}$  emitters can be attributed to the local strain generated by nearby isotopes [182]. In theory, the impact of stress on the spin characteristics of  $\text{V}^{4+}$  can be explained by a coupling between the energy

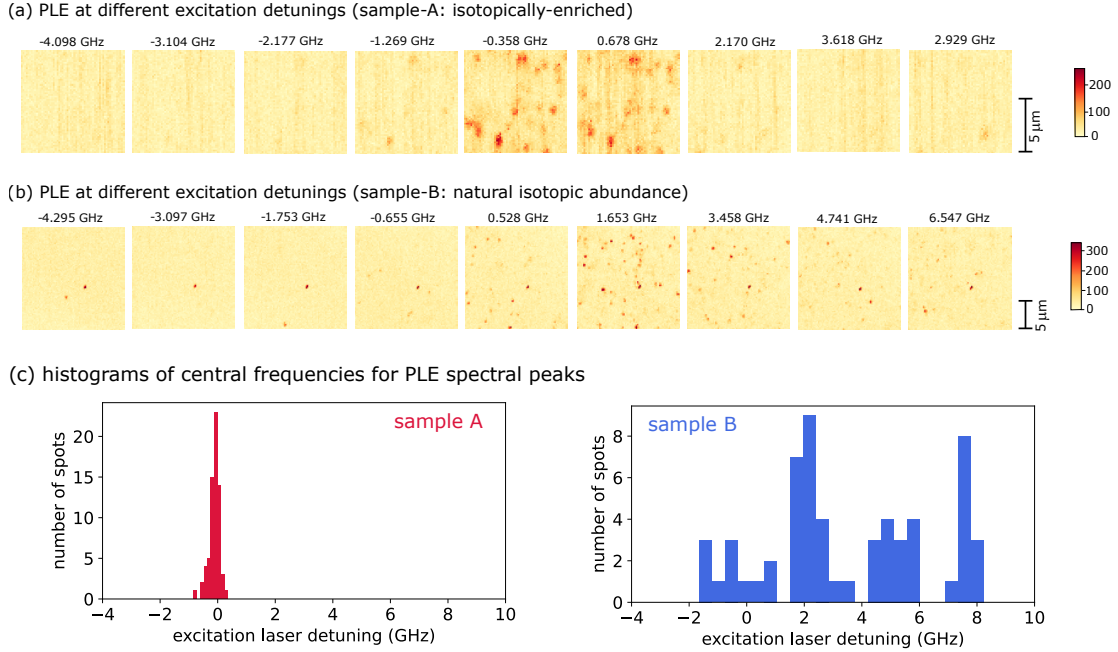


**FIGURE 6.4. Inhomogeneous distribution study of Vanadium emitter for sample A and sample B.** (a), (b): Shows an example of series of PLE maps taken at different excitation laser detunings for two samples. Maps in (a) have an area of  $10 \times 10 \mu\text{m}$ , while maps in (b) have an area of  $20 \times 20 \mu\text{m}$ . Sample A shows evidence that most emitters are only visible at a narrow frequency range. While for sample B there is a big spread of frequency distribution for different emitters. (c) Shows central frequencies histogram with a standard of more than 150 vanadium centres across 4 different sample regions for sample A (left). The standard deviation of the inhomogeneous distributions within these regions is approximately 100 MHz. While for the standard sample containing isotopes of Si and C in natural abundance, the frequency distribution spans several GHz.

levels of  $V^{4+}$  and the local strain produced by lattice distortion resulting from nearby isotopes. Particularly, strain coupling satisfies the time-reversal symmetry, and this leads to two strain tensor elements which transform like an electric field in the ( $z$ )-direction within ( $C_{3v}$ ) symmetry: ( $\epsilon_{zz}$ ) and ( $\epsilon_{xx} + \epsilon_{yy}$ ) [326]. As in the electric field case, these elements can directly influence the energy spacing of the Kramers doublets [321]. The other strain-tensor elements can also affect these spacings at a higher order. Hence, we are able to assign the different transition frequencies to different values of local strain, and we note that strain engineering may be used in the future to tune the transition frequencies of vanadium emitters into resonance with specific applications.

For sample B, we analysed more than 300 emitters. We found an excitation frequencies window of a couple of GHz consistent with the anticipated  $\sim 2$  GHz per unit mass for Si isotopes [264]. One could explore the possibility of measuring the hyperfine coupling for different detunings of the zero-phonon line by correlating optical spectroscopy with optically-detected electron spin

resonance measurements. Such an investigation could yield interesting results. Despite our efforts, we were unable to observe optically-detected magnetic resonance on individual centres, which is probably because the electron spin relaxation timescales for vanadium are too short at 4K [185].

centre	wavelength	lifetime	Fourier linewidth	inhomogen. distr.	$\eta$
NV:diamond (single)	637 nm	12 ns	13 MHz	~40-50 GHz [327]	>3000
SiV:diamond (single)	637 nm	1.7 ns	94 MHz	~10 GHz [328, 329]	107
V <sub>Si</sub> :SiC (single)	861 nm	6 ns	27 MHz	~15 GHz[330]	565
V:SiC (single)	1278 nm	167 ns	0.95 MHz	>10 GHz	>10,000
<b>V:<sup>28</sup>Si<sup>12</sup>C (single)</b>	<b>1278 nm</b>	<b>167 ns</b>	<b>0.95 MHz</b>	<b>~100 MHz</b>	<b>105</b>
Er <sup>3+</sup> :Si (single)	1536 nm	~ 0.186 ms [331]	~ 856 Hz	~0.5 GHz [331]	~ 0.6 · 10 <sup>6</sup>
T centre:Si (single)	1326 nm	940 ns [332]	169 kHz	~1 GHz [333]	5900
T centre: <sup>28</sup> Si (ensemble)	1326 nm	940 ns [332]	169 kHz	60 MHz (0.25 $\mu$ eV) [332]	355
G centre: <sup>28</sup> Si (ensemble)	1280 nm	5.9 ns [334]	27 MHz	72 MHz [334]	3
G centre:Si (single)	1280 nm	5.9 ns [335]	27 MHz	>100 GHz [335]	>3000
<sup>171</sup> Yb <sup>3+</sup> :Y <sub>2</sub> SiO <sub>5</sub> (ensemble)	~ 980 nm	~ 1ms [336]	~ 160 Hz	~ GHz [336]	> 6 · 10 <sup>6</sup>
<sup>153</sup> Eu <sup>3+</sup> :EuCl <sub>3</sub> · 6H <sub>2</sub> O (ensemble)	579.7 nm	~ 2ms [337]	~ 80 Hz	25 MHz [338]	> 3 · 10 <sup>5</sup>

TABLE 6.3. An overview of the inhomogeneous distribution of a number of spin-active quantum emitters. In the table above,  $\eta$  is the ratio between the inhomogeneous broadening and transform-limited linewidth.

The local inhomogeneous distribution of the order of 100 MHz for the studied vanadium emitter is very favourable compared to other quantum emitters (see Table.6.3). In Table 6.3, we compare the inhomogeneous broadening and lifetime-limited linewidth for various quantum emitters across different materials platforms. The observed value for vanadium defect is several orders of magnitude smaller than what is found for the nitrogen-vacancy (NV) centres (~ 40 - 50 GHz [327]). A more narrow inhomogeneous distribution has been reported for silicon vacancy centres SiV in diamond [328, 329], and silicon carbide (V<sub>Si</sub>) [330] on the order of 10-20 GHz. The vanadium distribution in SiC can even be compared favourably to that of rare-earth ions, which can show even narrower distributions down to the MHz-GHz level [336, 338, 339]. In this case, a better measure of merit would be the ratio  $\eta$  between the inhomogeneous broadening and transform-limited linewidth. This ratio can be used to quantify how many linewidths the frequencies of two emitters need to be shifted to bring them in resonance with each other. We see that in Table 6.3, that vanadium defect in SiC performs equally well with the silicon-vacancy centre in diamond ( $\eta \sim 100$ ) while being an order of magnitude better than the nitrogen-vacancy (NV) centre in diamond ( $\eta > 3000$ ). A recent study conducted on the T centre (ensemble) in Si has revealed an exceptionally low level of inhomogeneous broadening, reaching as narrow as 60 MHz, with  $\eta \sim 350$  [332]. Rare-earth ions exhibit remarkable coherence in their optical transitions, with some cases showing inhomogeneous broadening as low as the MHz range (see Table 6.3). However, their long optical lifetimes lasting in the ms range and linewidths limited by their lifetime in the few tens of Hz range result in relatively high values for  $\eta$ .

### 6.3.1 Narrowest linewidth

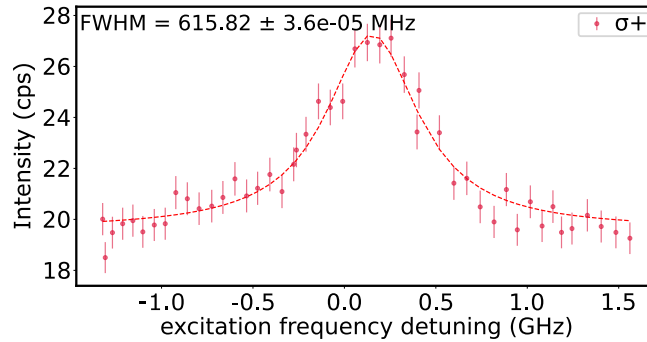


FIGURE 6.5. **PLE spectrum of a single vanadium impurity  $V^{4+}$  in SiC.** The smallest linewidth of  $615.82 \pm 3.6e-5$  MHz was observed at a resonant telecom excitation power of  $0.1 \mu\text{W}$ . The defects central frequency was  $234.425152 \pm 1.2e-5$  THz. Red symbols show experimental data.

This section presents the PLE spectrum with the narrowest emission linewidth of a single vanadium V defect. For this, we performed our measurements at 3.5 K and at a telecom excitation laser power of  $0.1 \mu\text{W}$ . The value of the applied magnetic field was about 1000 Gauss, and we used + polarisation of the incident light. The obtained PLE spectrum is shown in Fig. 6.5; the data was fitted to a Lorentzian function to extract the FWHM of  $615.82 \pm 3.6e-5$  MHz.

In contrast to a predicted lifetime limited linewidth of less than 1 MHz, at the lowest excitation power, we observe a linewidth of  $\sim 600$  MHz (see Fig. 6.5). To account for this discrepancy, the presence of eight hyperfine lines due to an interaction with  $I = 7/2$   $^{51}\text{V}$  nuclear spin results in electronic and optical transition being broadened with respect to the lifetime limit, with the hyperfine splitting on the order of 200 MHz. Additionally, power broadening may also have limited our results here, but we could not reduce the optical power any further, as this leads to a poor signal-to-noise ratio due to the low emission rate of a single vanadium centre. It should also be noted that temperature can also affect linewidth through the process of phonon-assisted dephasing. We cannot fully assess the impact of phonon dephasing in our system because we are limited to experiments at about 4 K. Additional measurements at lower temperatures will be required to assess this phenomenon fully. There is also the possibility that the spectral diffusion caused by fluctuating electric fields associated with charge traps near the vanadium emitters could play a role in the phenomenon. The implantation process is quite aggressive for heavier atomic species such as vanadium. Hence, despite the sample being annealed at a very high-temperature post-implantation, it is possible that the crystal lattice of the SiC has not been fully repaired.



## 6.4 Charge state stability $V^{(4+)}$

As discussed previously, there are three different possible charge states in which vanadium can exist in 4H-SiC, including  $V^{(3+)}$  (negatively charged),  $V^{(4+)}$  (neutral), and  $V^{(5+)}$  (positively charged) [317]. Only the  $V^{(4+)}$  state can emit luminescence in the telecom region and has an  $S = 1/2$  electron spin, which is essential for quantum networks. Therefore, it is important to ensure the  $V^{(4+)}$  state is prepared well and is stable over a long period.

Hence in this section, we discuss the measurements performed for the charge state study of the vanadium defect in both samples. To investigate the dynamics of the charge state of V defects, we performed time-resolved PL measurements by pulsing the telecom laser and/or the repump laser and time-tagging the emitted photons. A fibre-coupled acousto-optic modulator (AOM, Aerodiode - 1310-AOM-2) is used to pulse the telecom laser. While for the green laser, we use the current controller (Thorlabs LDC205C) for pulsing. During these experiments, the control pulse and the time tagger trigger signals are generated with the help of a waveform generator (Streamer 8/2 by Swabian Instruments). To time tag the signal from V defects, we used Swabian Instruments time tagger directly connected to the Pulse Streamer and the SNSPDs.

For vanadium defect, a resonant excitation induced by a 1278 nm laser results in a quenching of the luminescence because of a change in the charge state of V. This luminescence can be recovered by shining a green (520 nm) repump laser, which leads to recovery of the charge state. In the following discussion, we will show the experiment carried out to study this effect under different excitation-repump conditions. The first experiment we performed on both samples was the study of the ionisation of V defect due to the resonant (telecom) laser. For this experiment, we prepared the  $V^{4+}$  state with the help of a green laser pulse of 300 ms, where the resonant 1278 nm laser was used to probe the system (see Fig. 6.6(a)). Here the repump laser is repeated after 700 ms to allow enough time for the counts to decay completely. We repeat this measurement sequence at varying resonant excitation power and fit the data to a single exponential decaying function to extract the decay time for each resonant laser power. For sample A the values for decay rate  $T_{fit}$  are given as  $T_{fit} = 80.30 \pm 0.19$  ms for  $P = 0.5\mu\text{W}$ ,  $T_{fit} = 50.33 \pm 0.29$  ms for  $P = 4.0\mu\text{W}$  and  $T_{fit} = 35.64 \pm 0.44$  ms for  $P = 8.0\mu\text{W}$ . While for sample B, we see a decay rate decreasing from  $>300$  ms to  $\sim 150$  ms as the power increases from  $2\mu\text{W}$  to  $25\mu\text{W}$ . We observed that these decay rates have an exponential decay dependence on the resonant power.

The next experiment we performed was to study the lifetime of the charge state in the absence of any optical excitation (Fig. 6.6(b)). This is an important case for quantum memory applications since the electron spin qubit is maintained with no excitation. The microwave pulse sequences can be applied to extend its  $T_2$  coherence time, with the storage time being limited by the presence of the  $S = 1/2$  electron. For this case study, we used the pulse sequence depicted in (Fig. 6.6(b)) where we used a green pulse laser of 300 ms to initialise the charge state, which is followed by a resonant excitation laser at varying time delays  $\tau$  to read out the charge state. Applying this pulse sequence for different delays  $\tau$  leads to a decaying photoluminescence signal (Fig. 6.6(b)).

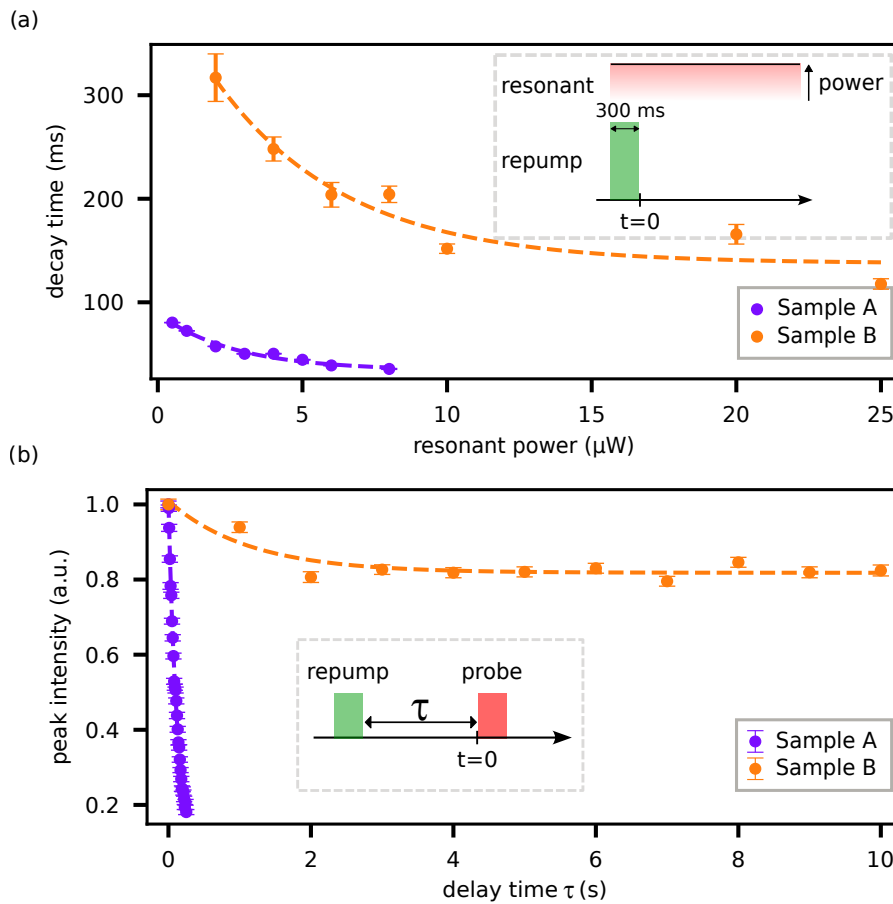


FIGURE 6.6. **Charge state stability study of vanadium  $V^{4+}$  in SiC.** (a) Inset depicts the pulse sequence used to study the PL decay over time of  $V^{4+}$  as a function of resonant power.  $V^{4+}$  is prepared using a 300 ms repump pulse, while the resonant laser is used to read the PL intensity. The repump pulse is repeated every 700 ms, a time enough for the PL intensity to decay completely. The exponential decay of the count rate is observed as evidence of ionisation resulting from resonant excitation, and the decay constant varies exponentially for both samples depending on the applied excitation power. Sample A has a much stronger response to an increase in laser power, with the decay rate going down from 80 ms to 50 ms in about 8  $\mu\text{W}$  increase of power. While for sample B, this decay is relatively slow as the decay rate decreases from  $\sim 300$  ms to  $\sim 100$  ms over 20-25  $\mu\text{W}$  increase of power. (b) Inset depicts the pulse sequence used to study the lifetime of the  $V^{4+}$  charge state in the absence of any optical excitation. Here again, the system is prepared in the  $V^{4+}$  state by a repump pulse of 300 ms, and the PL emission intensity is then recorded as a function of the delay time ( $\tau$ ) between the pump and probe pulse. The peak intensity gives the initial probability of V to be in  $V^{4+}$  state. In the absence of optical excitation, there is a strong exponential decay of the initial amplitude with increasing delay time  $\tau$  for sample A (purple curve) as the electrons excited from traps to the conduction band by resonant excitation accelerate the process to convert  $V^{4+}$  to  $V^{3+}$  in about  $129 \pm 6$ . While for sample B, with mostly empty electron traps, the impact of the resonant excitation on the PL decay is weaker, helping to stabilize  $V^{4+}$  charge state, and the lifetime of the charge state is at least a few seconds.

Where for each delay,  $\tau$  starting amplitude reflects the probability of the system being in  $V^{4+}$ . We observe that for sample A, the peak intensity decays exponentially with the charge state lifetime of  $129 \pm 6$  ms as the delay time is swept (purple curve in Fig. 6.6(b)). While for sample B, due to the Fermi level pinning between the  $(+|0)$  and  $(0|-)$  levels of V, the neutral charge state  $V^{4+}$  is stable and we find a charge state lifetime of several seconds.

In the n-type layer we use for sample A, V is expected to be in the negative charge state  $V^{3+}$  in equilibrium. The small implantation dose ( $1 \cdot 10^8 \text{ cm}^{-2}$ ), required to observe single isolated vanadium emitters, cannot change the Fermi level in the n-type layer. When a green repump laser is applied, the electrons from the acceptor levels of V,  $V_C$  and the shallow nitrogen N donor are excited to the conduction band, leading to neutral charge states. However, when the repump laser is stopped, free electrons in the conduction band are captured back to the defects' acceptor levels. As a result, V exists in both neutral and negative charge states, with the latter being the predominant state, and the acceptor levels of the carbon vacancy ( $V_C$ ) are also populated. This electron-capturing process turns V to the negative charge state, leading to the decay of the PL intensity of the neutral  $V^{4+}$  centre. In principle, if the photon energy of the resonant laser could excite electrons from the  $(0|-)$  acceptor level of V to activate the neutral charge state, then the photoluminescence quenching may not occur. Hence, the green repump laser would not be needed. However, from the decrease of the PL decay time with an increase of the red laser power, as shown in Fig. 6.6(a), it is likely that the resonant laser (1278.84 nm or 0.9695 eV) cannot efficiently excite electrons from the  $(0|-)$  level of V (at EC - 0.97 eV) to the conduction band, while it can efficiently remove electrons from the higher-lying  $(0|-)$  and  $(-|2-)$  levels of  $V_C$  (at  $\sim 0.5$  eV and  $\sim 0.7$  eV below the conduction band, respectively). With higher power, the red laser removes electrons from the acceptor levels of  $V_C$  more efficiently, leading to a higher concentration of free electrons in the conduction band. This, in turn, enhances the process of capturing electrons to the acceptor level of V, leading to a higher photoluminescence quenching rate.

Hence to summarise the results we found for the experiments discussed above, the decay of PL we see in Fig. 6.6(a) reflects the depletion of these free-electrons in the conduction band created by the green repump laser as the excitation laser is applied. The decay we see in Fig. 6.6(b) further supports this notion. The peak PL intensity exponentially decays as the delay time  $\tau$  increases since the population of the  $V^{4+}$  state is decaying exponentially along with the free-electron concentration. For sample A, electrons excited from traps to the conduction band by resonant excitation accelerate the process of charge state conversion. Hence, we observed a charge state lifetime for the  $V^{4+}$  of about  $129 \pm 6$  ms. While by using the HPSI sample B with mostly empty electron traps, the impact of the resonant excitation on the PL decay is weaker, helping to stabilize the charge state. For this sample, we find a charge state lifetime that extends to several seconds.

## 6.5 Summary

As a result of our study, we gained insight into the optical properties of single vanadium defects in SiC. As the first experimental evidence for spin-dependent selection rules of the optical spectroscopy of photoluminescence, we observe surprising inhomogeneous distributions of photoluminescence in the sub-GHz range, which are critical for applications in the field of telecom quantum technology. We provide the first experimental verification of its spin-dependent selection rules and observe surprising sub-GHz photoluminescence inhomogeneous distributions, critical for telecom quantum technology applications. The narrowness of the inhomogeneous distribution can be an essential element for creating remote entanglement between different emitters within the nodes of a quantum network since perfect indistinguishability between the photons in a quantum network is necessary for high visibility quantum interference. In addition, it also has the potential to be useful for superradiance experiments, which also require indistinguishability. The ultra-narrow inhomogeneous distribution was achieved by isotopically enhancing the sample, as the isotope shift effect is responsible for the local change in emission frequencies. It is possible to use this property to pre-select emitters with a specific configuration of nearby nuclear spins using optical spectroscopy, which could facilitate selecting specific emitters for implementing a quantum memory. The charge state study for sample A revealed a charge state lifetime of  $129 \pm 6$  ms for the neutral  $V^{4+}$  state. While this timescale is not particularly long, it can be explained by the Fermi level (n-type) in our sample, stabilising the negatively charged vanadium state. While for sample B, with no trapped electrons, we were able to extend this lifetime to several seconds.

To conclude, the findings presented in this study, in combination with recent work on the measurement of long spin coherence time ( $T < 2$  K) [184], suggest that a vanadium centre embedded in SiC could make an attractive candidate for quantum networking. The direct emission at telecom O-band wavelengths, stable charge state and the demonstration of an ultra-narrow inhomogeneous distribution enable the practical realisation of multi-V colour centre entanglement without using complex additional hardware for conversion and tuning. This broadening also enables efficient interfacing between multiple emitters. Additionally, the emission of quantum signals in the telecom O-band can open up doors to wavelength-multiplexing of the quantum signals in the O-band with classical signals in the C-band over a standard telecom fibre. The combination of these results and the fact that there is an electronic spin in vanadium with a long coherence time leads to the conclusion that vanadium in SiC might make an appealing candidate for the demonstration of quantum repeaters and quantum networking nodes for telecom wavelengths.

## CONCLUSION/OUTLOOK

## 7.1 Conclusion

This dissertation presents the results of experimental work about novel characterisation tools and spin systems for spin-based quantum technology.

Chapter 4 presented the development and implementation of our adaptive protocols for the estimation of decoherence timescales associated with a qubit. Our study showed improved performance of the proposed protocols compared to the non-adaptive protocols. In this study, we first focused on estimating a single noise parameter, i.e.  $T_\chi$ , while calibrating the other parameters, such as decay factor  $N$ , from measurements in the lab. We presented simulation results to characterise the performance of these adaptive protocols vs the non-adaptive scheme: in the case of single-shot readout (SSR), our adaptive protocols saturated the theoretical limit set by the CRLB, while for the case of the non-SSR regime, we found a modified theoretical limit and showed the gain of adaptive protocols over the non-adaptive one. To verify these results, we also performed experimental measurements for three different timescales  $\{T_1, T_2, \text{ and } T_2^*\}$ . The adaptive protocols achieved more precise estimation at a given time in comparison to the non-adaptive protocol for  $\{T_2, \text{ and } T_2^*\}$ . The gain for  $T_1$  was, however, undermined due to long delay times and few iterations of the protocol. In the final section of Chap. 4 we presented the generalisation of our adaptive protocol to two-parameter estimation. Where we experimentally studied the performance of adaptive protocol versus the non-adaptive scheme for the estimation of  $T_\chi, N$ . While these protocols were implemented at room temperature on a single spin associated with the nitrogen-vacancy (NV) centre, they are generalisable and applicable to any qubit system. The methods showcased in this study will directly lead to the enhancement of quantum relaxometry, where the measurement of qubit decoherence derives valuable insights into environmental noise.

An example of this is the application of single spins within nano-diamonds to assess radical levels. This strategy leverages the fact that radicals induce magnetic noise, consequently diminishing the  $T_1$  timescale of the sensor spin. It has been employed in diverse applications, including the examination of particular chemical reactions [340] and the determination of radical oxygen species concentration within living cells [275, 341].

We followed up our study of decoherence timescales with the use of adaptive learning for frequency estimation. In Chap. 5, we presented our adaptive frequency estimation protocol. We compared it against the other frequency estimation protocols already present in the literature, along with a few modified new methods that we proposed in this study. We found that our proposed method outperforms the non-adaptive as well as previously studied adaptive frequency estimation methods. We also studied the effect of change in experimental conditions and found that our proposed methods perform better than the non-adaptive method. The study done in this chapter showcased how non-SSR sensors can be employed as effective instruments in adaptive frequency estimation algorithms and establish a proof of concept for a non-SSR sensor based on NV centre in diamond. However, the approach holds general applicability and can also be implemented in other sensing systems as well [342].

In Chapter 6, we performed optical spectroscopy measurements to study the optical, electronics and charge state properties of implanted vanadium ions in SiC. Vanadium presents a promising platform for quantum networking applications, with the ability to emit light directly in the telecom O-band. This presents an opportunity to use wavelength-multiplexing on the same standard telecom fibre to combine quantum signals in the O-band with classical signals in the C-band. We studied an isotopically purified sample implanted with V and observed ultra-narrow inhomogeneous broadening ( $\sim 100$  MHz) along with the charge state that lasts more than  $129 \pm 6$  ms. By using the high-purity semi-insulating (HPSI) sample, we showed that this lifetime can increase to several seconds. These results will enable entanglement among multiple V colour centres and eliminate the need for intricate wavelength conversion and tuning equipment.

## 7.2 Outlook

While I have had the opportunity to gain knowledge and expertise in the field of adaptive sensing and spin-based quantum technology, there are many ideas that my PhD study has not encompassed and are yet to be explored.

### 7.2.1 Adaptive learning prospects

In terms of adaptive learning, in the final section (Sec. 4.6) of chapter 4, we present preliminary experimental results for the simultaneous estimation of  $T_2^*$  and  $N$  at  $R = 10^5$ . The next short-term goal will be to perform these measurements for different repetitions  $R$  (contrast values) to analyse the gain of the adaptive scheme for different experimental conditions. The use of

adaptive multi-parameter estimation schemes will provide a more comprehensive picture of each spin qubit, making these techniques more general for future implementation.

As a mid-term term goal, although the adaptive schemes we have discussed in this thesis have provided gain over the standard non-adaptive measurement techniques, the experimental uncertainties, such as a fluctuation of counts and stability of the setup, severely limit their benefits. Hence as a next step, it will be helpful to include these errors as part of the learning process. The idea of incorporating information from a system has been applied for quantum sensing [213], where information about photon arrival times is incorporated to achieve a more sensitive measurement. Similar studies have been done, which include noise for approximate Bayesian computation of a dynamical system [343, 344]. Hence Bayesian inference schemes with the incorporation of system noise will lead to a more efficient estimation in future.

Another challenge that we need to address is that the complexity of the problem scales with an increase in the number of parameters to be estimated. We saw in Chap. 4, as we went from single parameter to two-parameter estimation, the equation (see Eqn. 4.27) to be maximised became quite complex. Maximising such an equation in each measurement iteration would be too computationally intensive. Additionally, if one wants to estimate more than two parameters, it will become even more complex and intensive. Hence a better method for multi-parameter estimation was recently proposed by Fiderer et al. [345]. In their paper, they make use of a reinforcement learning technique to devise efficient experiment-design heuristics in Bayesian quantum estimation. This scheme results in a significant improvement over the previously developed slow algorithms [208, 346]. Particularly, some of the key features of this approach are (a) its versatility in adapting to various types of estimation problems, (b) its utilization of a neural network as a broad ansatz for the experiment-design heuristic, and (c) the ability to achieve global optimization by finding heuristics that are optimal for all upcoming experiments, as opposed to local strategies that merely optimize the next experiment. However, these studies still depend on either a complete understanding of the system's quantum state or the explicit likelihood function that characterizes the system's output probabilities. Hence a more robust method that can answer both of our original problems, namely the incorporation of noise and handling the complexity of the estimation problem with an increase in the number of parameters, can be addressed by a more recent study by Cimini et al. [347]. They propose a method extending and combining the power of the two machine learning algorithms discussed in [345] and [348]. Their approach employs deep-learning-based methods and does not require any prior knowledge of the system to execute practical Bayesian quantum metrology estimation proficiently. Implementing such a scheme for quantum sensing can help to include the system's imperfections, and being model-free will help scale up the multi-parameter estimation problem.

As a long-term goal for this adaptive learning work, I believe an artificial intelligence-based Nano-MRI method holds great promise. As discussed in Chap. 1, a lot of effort is being spent on using solid-state spin-based sensors for detecting and imaging nearby nuclear and electron

spins with unprecedented resolutions [57, 58]. Such experiments usually involve gathering huge amounts of data and post-processing with manual efforts. Although studies in this domain using machine learning have shown a potential to outperform manual human input [349]. Achieving the ability to image larger and more intricate systems requires the development of machine learning techniques that are both optimal in data acquisition and data analysis. The goal is to extract meaningful information from complex and noisy spectra, which is not possible by humans using standard techniques. Additionally, machine learning methods can not only be used to choose optimal measurements to be performed but may also predict new spectroscopy techniques, which will help to achieve an even more detailed study of complex systems.

With these fascinating prospects yet to be achieved, I believe there are exciting times ahead, and the future holds great promise for machine learning-based estimation techniques across the board.

### 7.2.2 SiC-based quantum technologies

A technical goal for future studies in the project is to answer an open question about the linewidth of the optical transitions observed during the experiments presented in Chap. 6. In contrast to a predicted lifetime limit of less than 1 MHz at the lowest excitation power, we observe a linewidth of  $\sim 600$  MHz. The presence of eight hyperfine lines due to an interaction with  $I = 7/2$   $^{51}\text{V}$  nuclear spin results in electronic and optical transition being broadened with respect to the lifetime limit, with the hyperfine splitting on the order of 200 MHz. Including the hyperfine transitions, however, would result in a set of multiple separate lines with MHz-linewidth allowing direct access to the nuclear spin through optical means. Although power broadening may have limited our results discussed in Chap. 6, we could not reduce the optical power any further, as this leads to a poor signal-to-noise ratio due to the low emission rate of a single vanadium centre. An idea about addressing this issue in future is either to embed the emitter in a photonic structure such as a solid immersion lens (SIL) [350] or to build a nanopillar to enhance collection efficiency. It should also be noted that temperature can also affect linewidth through the process of phonon-assisted dephasing. We cannot fully assess the impact of phonon dephasing in our system because we are limited to experiments at about 4 K. Additional measurements at lower temperatures will be required to assess this phenomenon fully. There is also the possibility that the spectral diffusion caused by fluctuating electric fields associated with charge traps near the vanadium emitters could play a role in the phenomenon. The implantation process is quite aggressive for heavier atomic species such as vanadium. Hence, despite the sample being annealed at a very high-temperature post-implantation, it is possible that the crystal lattice of the SiC has not been fully repaired. For future experiments, it may be possible to assess and even address the contribution of this factor by embedding the vanadium centres into a p-i-n diode structure. By applying a large electric field, we can empty all the charge traps in the structure, which will lead to a stabilised local electromagnetic environment [166]. This has been shown to strongly reduce



spectral diffusion, resulting in coherent optical transitions and stable spin-photon interfaces [132, 351].

Moreover, in future, emissions from vanadium can be enhanced by using a resonant photonic structure. Recent studies involving rare-earth ions have shown that Purcell factors of more than 500 could be achieved by using photonic crystals [302] or open microcavity [352] architectures. Since the spin-photon interface is built on a circularly-polarised optical transition, preserving the polarisation degeneracy of the cavity modes is important. This will require controlling the birefringence and shape in the case of open cavities or control over the symmetry of the geometry for photonic crystals [353]. Since vanadium centres host a  $^{51}\text{V}$  nuclear spin with hyperfine interaction on the order of 200 MHz, it can provide a fast quantum memory. A study has proposed protocols to polarise these nuclear spin [322].

A long-term goal will include demonstrating a quantum network based on colour centres in SiC photonics. To this end, the integration of defects into photonic structures holds the key. Such integration of spin defects can enhance their interaction with identical photons, thereby facilitating the effective entanglement of distant defects. Although significant advancements have been made in the development of the cavity-defect node, there still exists a substantial disparity in performance between integrated quantum photonics and their classical counterparts [354]. In this regard, SiC-on-insulator demonstrates exceptional suitability in closing the gap between classical and quantum photonics [355–357]. Furthermore, it shows great potential for realizing a quantum photonic processor based on defects, which would incorporate fully-integrated high Q/V photonic crystal cavities, integrated detectors and rapid cryogenic optical modulators [354].

Additionally, photonics inverse design [358] is a promising device engineering technique that is likely to impact the advancement of scalable quantum photonic circuits significantly. Especially for complex systems, inverse design presents a unique approach for accomplishing intricate tasks by enabling targeted optimization across multiple metrics, which includes enhancing robustness to fabrication imperfections (thereby boosting yield) and overcoming fabrication constraints [359]. In the future, integrated spin-based photonic structures hold great promise for scalable quantum communication platforms and SiC with successful demonstrations of integration of emitters into semiconductor junctions on a wafer-scale [166], utilization of isotope engineering for nuclear spin registers [360], creation of a SiC-on-Insulator material suitable for quantum applications [357, 361], and production of indistinguishable single photon emission [361] shows great potential in the years to come.





## A.1 Smallest incremental step size calculation

To measure the smallest incremental step size, we used Fig. 3.5 to extract that  $0.14 \text{ V} = 5 \mu\text{m}$  or  $0.028 \text{ V} = 1 \mu\text{m}$ . The Labjack we used to control the Glavos mirror has an instrumental resolution of  $= \frac{20V_{pip}(-10V \text{ to } 10V)}{2^{16}} = 0.00030517578 \text{ V} = 10.89 \text{ nm}$ . In comparison, the Galvo system has a repeatability of  $0.0008^\circ$  ( $14 \mu\text{rad}$  or about  $14 \text{ nm}$ ). To extract the smallest incremental step, we divided the optimal scan step voltage of  $0.00042 \text{ V}$  by  $0.028 \text{ V}$  ( $1 \mu\text{m}$ ), giving us the minimum incremental step of  $\sim 15 \text{ nm}$ . The choice of optimal scan step was based on looking at the line profile across the checkerboard and seeing at what point we start seeing multiple y data points at the same level for different values of applied voltage (see Fig. A.1).

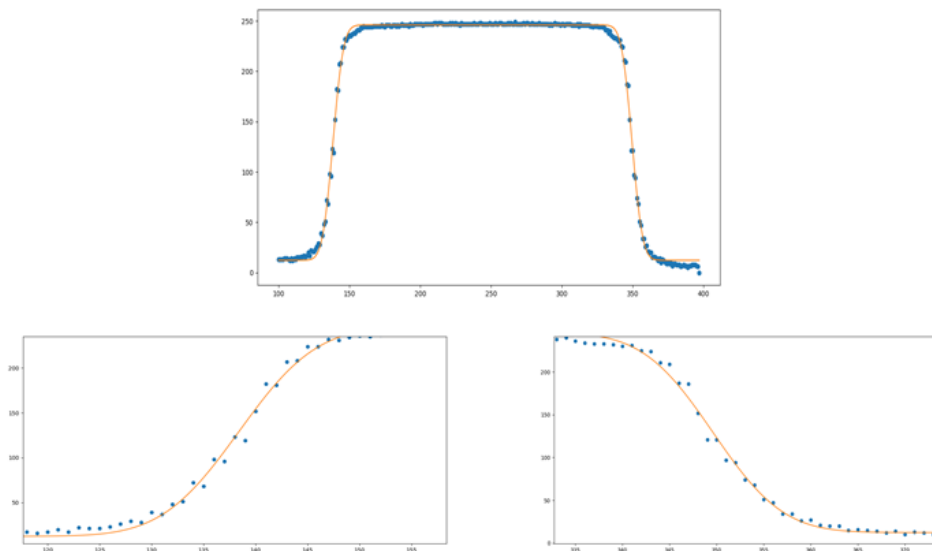


FIGURE A.1. Line profile across the checkerboard scan. Zoomed in image of the profile shows the presence of multiple y data points at the same level for two different values of voltage (x-axis).

## A.2 Code for ADwin

Here I will describe the case-by-case programming of the ADwin. ADwin code for adaptive measurements is divided into 8 cases, each describing one particular microcontroller function.

### case 0: Update DIO parameters and values for the next run.

```

CASE 0 'Update Parameters and DIO for this run
'<REGION> Set Parameter values for this run
  ''Choose which parameter is swept
  IF (adaptive_true = 1) THEN
    par_1_value = Round((curr_t * sampling_rate) /scaling_factor)
  ELSE
    par_1_value = Data_11[curr_epoch]
    curr_t = par_1_value * scaling_factor/ sampling_rate
  ENDIF
  '' Assign parameters in DIO, other outputs set to zero
  P2_DIGOUT_LONG(DIO_MODULE,Shift_Left(par_1_value+Shift_Left(par_2_value,8),par_DIO_start))
  'Set DIO value for adaptive_output, buts 8-16
  mode = 1
'<ENDREGION>

```

Figure A.2: Case 0, where the parameter for the current estimation run is chosen, and this value is set on the DIO ports.

### case 1: Check if resampling is needed.

```

CASE 1 'Check if resampling needed
  Q = 0 'Reset sum of probabilities
  FOR i=1 TO N 'For loop to populate Q
    Q = Q + (P[i]^2)
  NEXT i
  Neff = 1/Q 'Calculate support

  IF (Neff<resampling_threshold) THEN
    'Perform Resampling
    mode = 100
  ELSE
    'Move on to next step
    mode = 2
  ENDIF

```

Figure A.3: Case 1, Where the protocol checks if the re-sampling is needed

### case 2: Activate the Counter and trigger the AWG.

```

CASE 2 'Activate Counter and Trigger AWG

    processdelay = cycle_duration_long

    IF ((Shift_right(P2_DIGIN_LONG(DIO_MODULE), AWG_ready_DI_channel) AND 1b) > 0) THEN
        'Shift the inputs by the value of the AWG done channel, and code mask to one channel

        P2_Cnt_Clear(CNTR_MODULE,111b)          'reset counters 1+2+3 to 0
        P2_Cnt_Enable(CNTR_MODULE,111b)        'start counters 1+2+3, stop 4

'<REGION> Trigger
    P2_DIGOUT(DIO_MODULE,AWG_start_DO_channel,1) 'Enable AWG Trigger
'<ENDREGION>
    mode = 3
ENDIF

```

Figure A.4: Case 2, Where the protocol opens up the counter channels for the ADwin and triggers the AWG.

### case 3: Wait for AWG to complete its sequence.

```

CASE 3 'Wait for AWG trigger
    processdelay = cycle_duration_normal 'Check as quickly as possible

    IF ((Shift_right(P2_DIGIN_LONG(DIO_MODULE), AWG_done_DI_channel) AND 1b) > 0) THEN
        'Shift the inputs by the value of the AWG done channel, and code mask to one channel

        P2_DIGOUT(DIO_MODULE,AWG_start_DO_channel,0) 'Disable AWG Trigger
        mode = 4
    ENDIF

```

Figure A.5: Case 3, where the protocol waits for the AWG to finish its sequence run.

### case 4: Stop counters, read out results and assign values to Data arrays.

```

CASE 4 'Stop Counters and read out

    processdelay = cycle_duration_long

'<REGION> Counter Readout
    P2_Cnt_Enable(CNTR_MODULE,0)          'Disable Counters

    Par_21 = P2_Cnt_Read(CNTR_MODULE,1) 'Read out Counter 1 (Drop)
    Par_22 = P2_Cnt_Read(CNTR_MODULE,2) 'Read out Counter 2 (Discriminator)
    Par_23 = P2_Cnt_Read(CNTR_MODULE,3) 'Read out Counter 3 (Normaliser)
'<ENDREGION>
'<REGION> Check the Bayesian update we want to perform
    IF (maj_voting = 1 ) THEN
        mode = 5
    ELSE
        mode = 6
    ENDIF
'<ENDREGION>

```

Figure A.6: Case 4, where the protocol, after receiving the trigger from AWG signalling the measurement has finished, stops the counters and readouts the value on each of them. Based on the choice of adaptive scheme decided, it either goes to Bayesian updating via majority voting (case 5) or binomial distribution (case 6).

**case 5: Bayesian update based on majority.**

```

CASE 5
  processdelay = cycle_duration_N_Xtralong  'Requires more processing time
  A = 0
  Avg = 0
  IF (m > maj_thr) THEN
    M=0
  ELSE
    M=1
  ENDIF

  For i=1 TO N
    P[i] = P[i]*0.5*(1+((-1)^M)*EXP(-curr_t/X[i])^2)
    IF (P[i] < 2) Then
      A = A + P[i]
    Else
      P[i] = 0
    ENDIF
  NEXT i
  mode=7

```

Figure A.7: Case 5, where the protocol performs a Bayesian updating via majority voting for a binary outcome. This case was used only in the experiments discussed in Chap. 5.

**case 6: Bayesian update based on the averaged readout.**

```

CASE 6
  processdelay = cycle_duration_N_Xtralong  'Requires more processing time
  A = 0
  Avg = 0
  For i=1 TO N
    L = alpha*(1+((-1)^0)*V*EXP(-curr_t/X[i])^1)
    IF (R<1000) THEN
      Lk = ((L)*(1-L))^m*(1-L)^(R-2*m)
    ELSE
      Lk = EXP(-(R/(2*m*(R-m)))*(m - R*L)^2)
    ENDIF

    P[i] = P[i]*Lk
    A = A + P[i]
  NEXT i
  mode = 7

```

Figure A.8: Case 6, where the protocol performs a Bayesian updating based on the averaged readout. This case was used for the experiments discussed in both Chap. 4 and Chap. 5.

**case 7: Normalisation, data extraction and incrementation of an epoch.**

### A.3. CODE FOR HIGH DEFINITION ARBITRARY WAVEFORM GENERATOR (HDAWG)

```
Case 7
processdelay = cycle_duration_N_long

IF (first_point = 0) THEN
  first_point = 1
ELSE
  'Normalise and find the Average of the probability distribution
  FOR i=1 TO N
    P[i] = F[i]/A
    Avg = Avg + X[i]*P[i] 'Current estimate of T1
  NEXT i

  curr_t= 0.8 * Avg

  Inc(curr_epoch)
  IF (curr_epoch > nr_epochs) THEN
    End 'Exit EVENT section and execute FINISH before stopping process
  ENDIF
ENDIF
```

Figure A.9: Case 7, where the protocol normalises the updated probability distribution and extracts the optimal parameter for the next measurement cycle.

#### case 100: Resampling procedure

```
CASE 100 'Re-sampling

  processdelay = cycle_duration_long 'Extra computational time required

'<REGION> Calculate Gaussian variance of probability distribution
  S = 0

  For i=1 to N
    S = S + X[i]*X[i]*P[i]
  NEXT i

  sigma = SQR(S-Avg^2)
'<ENDREGION>

'Re-generate x values based on Gaussian estimation, and set a uniform probability distribution
FOR i=1 TO N[...]
```

```
mode = 2
```

Figure A.10: Case 100, where the protocol estimates the variance of the current probability distribution and re-generates x-values to represent the probability distribution.

## A.3 Code for High definition arbitrary waveform generator (HDAWG)

Here is the code we use to make pulses for T1 relaxometry with HDAWG based on feedback from the ADwin.

```
{ {
//This sequence is for adaptive T1 relaxometry.

//Constants/variables for the sequence
```

```

const ClockCycle = 3.3333e-9; //Time length of one clock cycle-wait command
const SeqCycle = 1/2.4e9; //One cycle in the sequence, limited by sampling
    rate

//1 = 1st channel, 2 = 2nd channel, 4 = 3rd channel, 8 = 4th channel

const TTagger_trigger_cycles = 30;
const AOM_channel = 0b0001; // TTL channel for laser pulsing
const sig_channel = 0b0100; // TTL for the signal from marker of channel 3
const nor_channel = 0b1100; // TTL for the normalisation from marker of
    channel 4
const I_channel = 1; //I and Q microwave channels -- these need to be 1 and
    2 for amplitude/
const Q_channel = 2; // phase control using the command table version Red
    1.0.
const IQ_factor= 1; // to compensate for differnce in heights in outputs of
    IQ channels
const IQ_phase_correction=-1; // to compensate for the difference in phase
    of the IQ channels
const AWG_done_pin = 24; // Pin in DIO to toggle AWG finished
const AWG_ready_pin = 25; // Pin to signal HDAWG ready
const ADwin_pin_pi = 4;
const ADwin_para = 8;
//var ADwin_pin_start = 0;

const rect_duration = {pulse_duration}; //Duration of rectangular pulse in
    seconds
const rect_amp = 1; //Amplitude of rectangular pulse
const n_pulses = {n_pulses}; //Number of iterations of the sequence loop
    before exiting
const wait_between_sequences = 50e-6; //Wait time in-between sequences, in
    seconds
const pulse_delay = {pulse_delay}; //Wait time (delay) between pulses, in s
const wait_after_pulse = 600e-9; //Delay between laser pulse and microwave
    pulse, in s
const sig_gate_length= {sig_gate_length}; // Gate length for signal in
    seconds
const nor_gate_length= {norm_gate_length}; // Gate length for normalisation
    in seconds
const sig_buffer = {sig_buffer}; // Buffer at the start of the aom pulse
    before the signal gating
const nor_buffer = {norm_buffer}; // Buffer at the end of the aom pulse
    after the normalisation gate
const scaling_factor = {scaling_factor}; // scaling factor -- in T1, applies
    to delays and is in units of samples, i.e. 16 == 6.667 ns per step in
    DIO

```



### A.3. CODE FOR HIGH DEFINITION ARBITRARY WAVEFORM GENERATOR (HDAWG)

```
const mw_amp = {mw_amplitude}/100; //Initial amplitude of microwave pulse,
    in %
const mw_pi_duration = {mw_pulse_duration}; //Length of microwave pi pulse

// Calculations

const Cycles_rect = rect_duration/ClockCycle; // Number of clock cycles for
    rectangular pulse
const Cycles_sequence_wait = wait_between_sequences/ClockCycle; // Wait
    between sets of sequences
const Samples_rect = rect_duration/SeqCycle; // Number of samples in the
    rectangular pulse
const Samples_pulse_delay = pulse_delay/SeqCycle; //Convert delay into units
    of samples
const Samples_wait_after_pulse = wait_after_pulse/SeqCycle; // Wait after
    optical pulse before microwave pulse
const Cycles_sig_gate_length = sig_gate_length/ClockCycle; // Signal gate
const Cycles_nor_gate_length = nor_gate_length/ClockCycle; // Norm gate
const Cycles_sig_buffer= sig_buffer/ClockCycle; // signal buffer
const Cycles_nor_buffer= nor_buffer/ClockCycle; // norm buffer
const Cycles_wait_after_pulse = wait_after_pulse/ClockCycle; // wait between
    laser pulse and mw
const Samples_mw_pi = mw_pi_duration/SeqCycle; // Number of samples in
    microwave pulse

// Generate possible waveforms

// wave w_rect = 1*rect(Samples_rect, rect_amp);
wave w_mw_pi = 1*rect(Samples_mw_pi, mw_amp); // this changes the length of
    the mw pi pulse - pad it below

// Create padded microwave waveform
const padding = Samples_mw_pi % 32;
wave w_pad_l = 1*rect(round(padding/2),0);
wave w_pad_r = 1*rect(padding-round(padding/2),0);
wave w_mw_pi_padded = join(w_pad_l,w_mw_pi,w_pad_r);

do{{
// Waiting for the ADwin to be ready, AWG is ready at this point
setDIO(1<<AWG_ready_pin);

    resetOscPhase();
    setSinePhase(0, 0);
    setSinePhase(1, 90 + IQ_phase_correction);
    wait(30);

waitDIOTrigger();
```

```

var dio = getDIO();

// get the value of the rabi length (parameter we are trying to sweep with
  ADwin)
var pi_switch = (dio>>4) & 0b01;
wait(10);
var t1_delay = (dio>>ADwin_para) & 0xFF;

//Programming the sequence

setTrigger(AOM_channel);
wait(Cycles_rect);
setTrigger(0);

repeat(n_pulses)
{{
  if(pi_switch==0) {{
    playZero(t1_delay*scaling_factor+Samples_wait_after_pulse);
    waitWave();
  }}
  else{{
    playZero(Samples_wait_after_pulse);
    resetOscPhase(); // added to make sure every pulse start with same
      phase each time
    setSinePhase(0, 0);
    setSinePhase(1, 90 + IQ_phase_correction);
    playWave(I_channel, w_mw_pi_padded, Q_channel, w_mw_pi_padded*
      IQ_factor);
    playZero(t1_delay*scaling_factor+round(Samples_wait_after_pulse/10))
      ;
    waitWave();
  }}

  setTrigger(AOM_channel);
  wait(Cycles_sig_buffer);
  //Triggers
  setTrigger(AOM_channel+sig_channel);
  wait(Cycles_sig_gate_length);
  setTrigger(AOM_channel);
  wait(Cycles_rect-Cycles_sig_buffer-Cycles_sig_gate_length-
    Cycles_nor_gate_length-Cycles_nor_buffer);
  setTrigger(AOM_channel+nor_channel);
  wait(Cycles_nor_gate_length);
  setTrigger(AOM_channel);
  wait(Cycles_nor_buffer);
  setTrigger(0);
}}

```

```
//Send DIO finished to ADwin
setDIO(1<<AWG_done_pin);
wait(Cycles_sequence_wait);
}} while(1);
}}
```

## A.4 Use of HDAWG and ADwin for adaptive experiments

To interface the adaptive electronics with each other, we wrote a Python wrapper for both HDAWG and ADwin. Here in this section, we will give a snippet of code used to initialise these devices and perform a simple adaptive  $T_1$  measurement (for example of a code, see Appx. A.3). Communication between the two devices exploits the 32-bit DIO ports available on both ADwin and HDAWG. The first 16 bits are reserved for back-and-forth communication about the readiness of each device, while the next 16 bits are used to pass the adaptively-optimised experimental settings.

```
if initialise_HDAWG:
    """
    To boot/prepare the HDAWG for running - instrumen
    """

    device = 'dev8236' #device ID for the Bay 5 RT NV
    awgMod = HDAWG_PLSer(device) #Create a session on

    #TO TEST: Changing a node value
    awgMod.set_value(f"/{device}/awgs/0/outputs/0/amp
```

Figure A.11: Snippet of the code to initialise HDAWG via Python.

```
if initialise_adwin:
    """
    To boot/prepare the adwin for running - instrum
    """

    # Generate an instance of the ADwin class, rais
    adw = ADwin(DeviceNo=1, raiseExceptions=1)

    try:
        adw.Boot(adw.ADwindir + '\\ADwin12.bt1')
        print('ADwin Initialised')
    except:
        print('ADwin Boot Failed')
```

Figure A.12: Snippet of the code to initialise ADwin via Python wrapper that we wrote.

## A.5 Fisher information calculation for single parameter estimation

This section gives the mathematical derivation of the Fisher information for the case of single parameter estimation ( $T_\chi$ ). Beginning from Eqn. 2.3 in the main text, we can find the Fisher

```

if combined_communication_process:
    #Set the parameter for the first adaptive value to
    adw.Set_Par(20,0) #This parameter controls whether
    adw.Set_Par(21,1000) #This sets the process delay

    #The binary file generated for my process ia compi
    Filename = "ADwin_code/Adaptive_trigger_python.TC1

    #Importing sequencer code from file to upload to A
    with open("AWG Sequences/Early_adaptive_T1_manual"
        awg_string = file.read()
        awg_program = awg_string.format() #Used to inp

    #Compile processes for both machines
    adw.Load_Process(Filename)
    awgMod.compile(device, awg_program)

```

Figure A.13: **Snippet of the code to upload file to ADwin and HDAWG.** *Filename* contains the address to the ADwin file for a specific measurement run. While the *awg\_program* contains the code to be uploaded to HDAWG.

information as:

$$(A.1) \quad \left( \frac{\partial}{\partial T_\chi} \ln(p(0|T_\chi)) \right)^2 = \left( \frac{\partial}{\partial T_\chi} \ln \left( \frac{1}{2} \left( 1 + e^{-\left(\frac{\tau}{T_\chi}\right)^N} \right) \right) \right)^2$$

$$(A.2) \quad = \left( \frac{\frac{\partial}{\partial T_\chi} e^{-\left(\frac{\tau}{T_\chi}\right)^N}}{1 + e^{-\left(\frac{\tau}{T_\chi}\right)^N}} \right)^2 = \left( \frac{N \left(\frac{\tau}{T_\chi}\right)^{N-1} e^{-\left(\frac{\tau}{T_\chi}\right)^N}}{T_\chi \left( 1 + e^{-\left(\frac{\tau}{T_\chi}\right)^N} \right)} \right)^2$$

$$(A.3) \quad = \left( \frac{N \left(\frac{\tau}{T_\chi}\right)^{N-1} e^{-\left(\frac{\tau}{T_\chi}\right)^N}}{T_\chi e^{-\left(\frac{\tau}{T_\chi}\right)^N} \left( \frac{1}{e^{-\left(\frac{\tau}{T_\chi}\right)^N} + 1} \right)} \right)^2$$

resulting in the final solution as:

$$(A.4) \quad \left( \frac{\partial}{\partial T_\chi} \ln(p(0|T_\chi)) \right)^2 = \frac{N^2 \left(\frac{\tau}{T_\chi}\right)^{2N}}{T_\chi^2 \left( e^{\left(\frac{\tau}{T_\chi}\right)^N} + 1 \right)^2}$$

similar steps can be taken to find the solution for spin state  $|1\rangle$ .

$$(A.5) \quad \left( \frac{\partial}{\partial T_\chi} \ln(p(1|T_\chi)) \right)^2 = \frac{N^2 \left( \frac{\tau}{T_\chi} \right)^{2N}}{T_\chi^2 \left( 1 - e^{\left( \frac{\tau}{T_\chi} \right)^N} \right)^2}$$

with the total Fisher information given as:

$$(A.6) \quad F_{T_\chi} = p(0|T_\chi) \times \frac{N^2 \left( \frac{\tau}{T_\chi} \right)^{2N}}{T_\chi^2 \left( e^{\left( \frac{\tau}{T_\chi} \right)^N} + 1 \right)^2} + p(1|T_\chi) \times \frac{N^2 \left( \frac{\tau}{T_\chi} \right)^{2N}}{T_\chi^2 \left( 1 - e^{\left( \frac{\tau}{T_\chi} \right)^N} \right)^2}$$

solving this will lead to the following general equation for the Fisher information of a two-level system subject to decoherence.

$$(A.7) \quad F_{T_\chi} = \frac{1}{2} \left( 1 + e^{-\left( \frac{\tau}{T_\chi} \right)^N} \right) \times \frac{N^2 \left( \frac{\tau}{T_\chi} \right)^{2N}}{T_\chi^2 \left( e^{\left( \frac{\tau}{T_\chi} \right)^N} + 1 \right)^2} + \frac{1}{2} \left( 1 - e^{-\left( \frac{\tau}{T_\chi} \right)^N} \right) \times \frac{N^2 \left( \frac{\tau}{T_\chi} \right)^{2N}}{T_\chi^2 \left( 1 - e^{\left( \frac{\tau}{T_\chi} \right)^N} \right)^2}$$

$$(A.8) \quad F_{T_\chi} = \frac{N^2 \left( \frac{\tau}{T_\chi} \right)^{2N}}{2T_\chi^2} \left( \frac{1 + e^{-\left( \frac{\tau}{T_\chi} \right)^N}}{\left( e^{\left( \frac{\tau}{T_\chi} \right)^N} + 1 \right)^2} + \frac{1 - e^{-\left( \frac{\tau}{T_\chi} \right)^N}}{\left( 1 - e^{\left( \frac{\tau}{T_\chi} \right)^N} \right)^2} \right)$$

$$(A.9) \quad F_{T_\chi} = \frac{N^2 \left( \frac{\tau}{T_\chi} \right)^{2N}}{2T_\chi^2} \left( \frac{e^{-\left( \frac{\tau}{T_\chi} \right)^N} \left( e^{\left( \frac{\tau}{T_\chi} \right)^N} + 1 \right)}{\left( e^{\left( \frac{\tau}{T_\chi} \right)^N} + 1 \right)^2} - \frac{e^{-\left( \frac{\tau}{T_\chi} \right)^N} \left( 1 - e^{\left( \frac{\tau}{T_\chi} \right)^N} \right)}{\left( 1 - e^{\left( \frac{\tau}{T_\chi} \right)^N} \right)^2} \right)$$

taking minus out from the denominator of the second fraction, we get:

$$(A.10) \quad F_{T_\chi} = \frac{N^2 \left( \frac{\tau}{T_\chi} \right)^{2N}}{2T_\chi^2} \left( \frac{e^{-\left( \frac{\tau}{T_\chi} \right)^N}}{\left( e^{\left( \frac{\tau}{T_\chi} \right)^N} + 1 \right)} + \frac{e^{-\left( \frac{\tau}{T_\chi} \right)^N}}{\left( e^{\left( \frac{\tau}{T_\chi} \right)^N} - 1 \right)} \right)$$

$$(A.11) \quad F_{T_\chi} = \frac{N^2 \left( \frac{\tau}{T_\chi} \right)^{2N}}{2T_\chi^2} \left( \frac{e^{-\left( \frac{\tau}{T_\chi} \right)^N} \left( e^{\left( \frac{\tau}{T_\chi} \right)^N} - 1 \right) + e^{-\left( \frac{\tau}{T_\chi} \right)^N} \left( e^{\left( \frac{\tau}{T_\chi} \right)^N} + 1 \right)}{\left( e^{\left( \frac{\tau}{T_\chi} \right)^N} + 1 \right) \left( e^{\left( \frac{\tau}{T_\chi} \right)^N} - 1 \right)} \right)$$

$$(A.12) \quad F_{T_\chi} = \frac{N^2 \left(\frac{\tau}{T_\chi}\right)^{2N}}{2T_\chi^2} \left( \frac{\left(1 - e^{-\left(\frac{\tau}{T_\chi}\right)^N} + 1 + e^{-\left(\frac{\tau}{T_\chi}\right)^N}\right)}{\left(e^{2\left(\frac{\tau}{T_\chi}\right)^N} - 1\right)} \right) = \frac{N^2 \left(\frac{\tau}{T_\chi}\right)^{2N}}{2T_\chi^2} \left( \frac{2}{\left(e^{2\left(\frac{\tau}{T_\chi}\right)^N} - 1\right)} \right)$$

This results in the final general solution given in Eqn. 4.4.

## A.6 FIM matrix calculations

This section describes the mathematical steps performed to calculate the FIM matrix for the case of multiparameter estimation  $(N, T_\chi)$  discussed in Sec. 4.6.  $\text{FIM}_{00}$  has been derived in the section above (see Apx. A.5). Here I will only derive  $\text{FIM}_{10}$ , and  $\text{FIM}_{11}$  as  $\text{FIM}_{10} = \text{FIM}_{01}$ .

$$(A.13) \quad \text{FIM}_{10} = p(0|T_\chi, N) \times \left( \frac{\partial^2}{\partial N \partial T_\chi} \log p(0|T_\chi, N) \right) + p(1|T_\chi, N) \times \left( \frac{\partial^2}{\partial N \partial T_\chi} \log p(1|T_\chi, N) \right)$$

$$(A.14) \quad \frac{\partial^2}{\partial N \partial T_\chi} \log p(0|T_\chi, N) = \frac{\partial^2}{\partial N \partial T_\chi} \left( \log \left( \frac{1 + e^{-\left(\frac{\tau}{T_\chi}\right)^N}}{2} \right) \right) = \frac{\partial}{\partial T_\chi} \left( \frac{\partial}{\partial N} \log \left( \frac{1 + e^{-\left(\frac{\tau}{T_\chi}\right)^N}}{2} \right) \right)$$

$$(A.15) \quad = \frac{\partial}{\partial T_\chi} \left( - \frac{e^{-\left(\frac{\tau}{T_\chi}\right)^N} \left(\frac{\tau}{T_\chi}\right)^N \log \left(\frac{\tau}{T_\chi}\right)}{1 + e^{-\left(\frac{\tau}{T_\chi}\right)^N}} \right)$$

$$(A.16) \quad = - \frac{-N e^{-\frac{\tau^N}{T_\chi^N}} \tau^N T_\chi^N \log \left(\frac{\tau}{T_\chi}\right) - e^{-\frac{\tau^N}{T_\chi^N}} \tau^N T_\chi^N - N e^{-\frac{2\tau^N}{T_\chi^N}} \tau^N T_\chi^N \log \left(\frac{\tau}{T_\chi}\right) - e^{-\frac{2\tau^N}{T_\chi^N}} \tau^N T_\chi^N + N e^{-\frac{\tau^N}{T_\chi^N}} \tau^{2N} \log \left(\frac{\tau}{T_\chi}\right)}{T_\chi^{2N+1} \left(1 + e^{-\left(\frac{\tau}{T_\chi}\right)^N}\right)^2}$$

similarly we can find that:

$$(A.17) \quad \frac{\partial^2}{\partial N \partial T_\chi} \log p(1|T_\chi, N) = \frac{\partial^2}{\partial N \partial T_\chi} \left( \log \left( \frac{1 - e^{-\left(\frac{\tau}{T_\chi}\right)^N}}{2} \right) \right) = \frac{\partial}{\partial T_\chi} \left( \frac{\partial}{\partial N} \log \left( \frac{1 - e^{-\left(\frac{\tau}{T_\chi}\right)^N}}{2} \right) \right)$$

$$(A.18) \quad = \frac{\partial}{\partial T_\chi} \left( \frac{e^{-\left(\frac{\tau}{T_\chi}\right)^N} \left(\frac{\tau}{T_\chi}\right)^N \log \left(\frac{\tau}{T_\chi}\right)}{1 - e^{-\left(\frac{\tau}{T_\chi}\right)^N}} \right)$$

$$(A.19) \quad = \frac{-Ne^{-\frac{\tau}{T_\chi}} \tau^N T_\chi^N \log\left(\frac{\tau}{T_\chi}\right) - e^{-\frac{\tau}{T_\chi}} \tau^N T_\chi^N + Ne^{-\frac{2\tau}{T_\chi}} \tau^N T_\chi^N \log\left(\frac{\tau}{T_\chi}\right) + e^{-\frac{2\tau}{T_\chi}} \tau^N T_\chi^N + Ne^{-\frac{\tau}{T_\chi}} \tau^{2N} \log\left(\frac{\tau}{T_\chi}\right)}{T_\chi^{2N+1} \left(1 - e^{-\left(\frac{\tau}{T_\chi}\right)^N}\right)^2}$$

substituting Eqn. A.19 and Eqn. A.16 into Eqn. A.13, and simplifying it we get the final solution for  $FIM_{10}$  as:

$$(A.20) \quad FIM_{10} = - \frac{Ne^{-\frac{\tau}{T_\chi}} \tau^{2N} \log\left(\frac{\tau}{T_\chi}\right) - Ne^{-\frac{\tau}{T_\chi}} \tau^{N^2 T_\chi} \log\left(\frac{\tau}{T_\chi}\right) - e^{-\frac{\tau}{T_\chi}} \tau^{N^2 T} - Ne^{-\frac{2\tau}{T_\chi}} \tau^{N^2 T} \log\left(\frac{\tau}{T_\chi}\right) - e^{-\frac{2\tau}{T_\chi}} \tau^{N^2 T}}{2T^{2N+1} \left(e^{-\left(\frac{\tau}{T}\right)^N} + 1\right)} + \frac{-Ne^{-\frac{\tau}{T_\chi}} \tau^{N^2 T} \log\left(\frac{\tau}{T_\chi}\right) - e^{-\frac{\tau}{T_\chi}} \tau^{N^2 T} + Ne^{-\frac{2\tau}{T_\chi}} \tau^{N^2 T} \log\left(\frac{\tau}{T_\chi}\right) + e^{-\frac{2\tau}{T_\chi}} \tau^{N^2 T} + Ne^{-\frac{\tau}{T_\chi}} \tau^{2N} \log\left(\frac{\tau}{T_\chi}\right)}{2T^{2N+1} \left(-e^{-\left(\frac{\tau}{T}\right)^N} + 1\right)}$$

$$(A.21) \quad FIM_{10} = \frac{N \left(\frac{\tau}{T_\chi}\right)^{2N} \log\left(\frac{\tau}{T_\chi}\right)}{T_\chi \cdot \left(e^{2\left(\frac{\tau}{T_\chi}\right)^N} - 1\right)}$$

Following the similar approach we can find the value for  $FIM_{11}$  as:

$$(A.22) \quad FIM_{11} = p(0|T_\chi, N) \times \left(\frac{\partial}{\partial N} \log p(0|T_\chi, N)\right)^2 + p(1|T_\chi, N) \times \left(\frac{\partial}{\partial N} \log p(1|T_\chi, N)\right)^2$$

$$(A.23) \quad \frac{\partial}{\partial N} \log p(0|T_\chi, N) = \frac{1}{\frac{1+e^{-\left(\frac{\tau}{T_\chi}\right)^N}}{2}} \frac{\partial}{\partial N} \left(\frac{1+e^{-\left(\frac{\tau}{T_\chi}\right)^N}}{2}\right) = \frac{1}{\frac{1+e^{-\left(\frac{\tau}{T_\chi}\right)^N}}{2}} \left(-\frac{1}{2} e^{-\left(\frac{\tau}{T_\chi}\right)^N} \left(\frac{\tau}{T_\chi}\right)^N \log\left(\frac{\tau}{T_\chi}\right)\right)$$

$$\frac{\partial}{\partial N} \log p(0|T_\chi, N) = -\frac{\left(\frac{\tau}{T_\chi}\right)^N \log\left(\frac{\tau}{T_\chi}\right)}{1+e^{-\left(\frac{\tau}{T_\chi}\right)^N}}$$

(A.24)

While

$$(A.25) \quad \frac{\partial}{\partial N} \log p(1|T_\chi, N) = \frac{\left(\frac{\tau}{T_\chi}\right)^N \log\left(\frac{\tau}{T_\chi}\right)}{e^{\left(\frac{\tau}{T_\chi}\right)^N} - 1}$$

Substituting the above two results in Equ. A.22, we get:

$$(A.26) \quad \text{FIM}_{11} = \frac{\left(1 + e^{-\left(\frac{\tau}{T_\chi}\right)^N}\right) \tau^{N \cdot 2} \log^2\left(\frac{\tau}{T_\chi}\right)}{2T_\chi^{N \cdot 2} \left(e^{\left(\frac{\tau}{T_\chi}\right)^N} + 1\right)^2} + \frac{\left(1 - e^{-\left(\frac{\tau}{T_\chi}\right)^N}\right) \tau^{N \cdot 2} \log^2\left(\frac{\tau}{T_\chi}\right)}{2T_\chi^{N \cdot 2} \left(e^{\left(\frac{\tau}{T_\chi}\right)^N} - 1\right)^2}$$

$$(A.27) \quad \text{FIM}_{11} = \frac{\left(\frac{\tau}{T_\chi}\right)^{2N} \left(\log\left(\frac{\tau}{T_\chi}\right)\right)^2}{\left(e^{2\left(\frac{\tau}{T_\chi}\right)^N} - 1\right)}$$

The other two terms of the FIM matrix are:

$$(A.28) \quad \text{FIM}_{00} = \frac{N^2 \left(\frac{\tau}{T_\chi}\right)^{2N}}{T_\chi^2 \left(e^{2\left(\frac{\tau}{T_\chi}\right)^N} - 1\right)}$$

$$(A.29) \quad \text{FIM}_{01} = \frac{N \left(\frac{\tau}{T_\chi}\right)^{2N} \log\left(\frac{\tau}{T_\chi}\right)}{T_\chi \cdot \left(e^{2\left(\frac{\tau}{T_\chi}\right)^N} - 1\right)}$$

### A.6.1 FIM entries for two consecutive sensing times

This subsection gives the entries of Fisher information matrix (FIM) for the case of two parameter  $(N, T_\chi)$  estimation. As described in the main text when we choose single sensing time  $\tau$ , the determinant of the matrix is 0, hence we modified out adaptive strategy to take two consecutive sensing time  $\tau_1$  and  $\tau_2$ . This section provides the element of FIM for that. These entries have been calculated following the same method as done for the single sensing time  $\tau$  above (see Apx. A.6). The entries we found for the FIM were:

$$(A.30) \quad \text{FIM}_{00} = \frac{N^2 \left( \left(\frac{\tau_1}{T_\chi}\right)^{2N} e^{2\left(\frac{\tau_2}{T_\chi}\right)^N} - \left(\frac{\tau_1}{T_\chi}\right)^{2N} + \left(\frac{\tau_2}{T_\chi}\right)^{2N} e^{2\left(\frac{\tau_1}{T_\chi}\right)^N} - \left(\frac{\tau_2}{T_\chi}\right)^{2N} \right)}{T_\chi^2 \left( -e^{2\left(\frac{\tau_1}{T_\chi}\right)^N} - e^{2\left(\frac{\tau_2}{T_\chi}\right)^N} + e^{2\left(\frac{\tau_1}{T_\chi}\right)^N} + 2\left(\frac{\tau_2}{T_\chi}\right)^N + 1 \right)}$$



$$(A.31) \quad \text{FIM}_{01} = \frac{N \left( -\left(\frac{\tau_1}{T_\chi}\right)^{2N} e^{2\left(\frac{\tau_2}{T_\chi}\right)^N} \log\left(\frac{\tau_1}{T_\chi}\right) + \left(\frac{\tau_1}{T_\chi}\right)^{2N} \log\left(\frac{\tau_1}{T_\chi}\right) - \left(\frac{\tau_2}{T_\chi}\right)^{2N} e^{2\left(\frac{\tau_1}{T_\chi}\right)^N} \log\left(\frac{\tau_2}{T_\chi}\right) + \left(\frac{\tau_2}{T_\chi}\right)^{2N} \log\left(\frac{\tau_2}{T_\chi}\right) \right)}{T_\chi \left( -e^{2\left(\frac{\tau_1}{T_\chi}\right)^N} - e^{2\left(\frac{\tau_2}{T_\chi}\right)^N} + e^{2\left(\frac{\tau_1}{T_\chi}\right)^N + 2\left(\frac{\tau_2}{T_\chi}\right)^N} + 1 \right)}$$

$$(A.32) \quad \text{FIM}_{10} = \frac{N \left( -\left(\frac{\tau_1}{T_\chi}\right)^{2N} e^{2\left(\frac{\tau_2}{T_\chi}\right)^N} \log\left(\frac{\tau_1}{T_\chi}\right) + \left(\frac{\tau_1}{T_\chi}\right)^{2N} \log\left(\frac{\tau_1}{T_\chi}\right) - \left(\frac{\tau_2}{T_\chi}\right)^{2N} e^{2\left(\frac{\tau_1}{T_\chi}\right)^N} \log\left(\frac{\tau_2}{T_\chi}\right) + \left(\frac{\tau_2}{T_\chi}\right)^{2N} \log\left(\frac{\tau_2}{T_\chi}\right) \right)}{T_\chi \left( -e^{2\left(\frac{\tau_1}{T_\chi}\right)^N} - e^{2\left(\frac{\tau_2}{T_\chi}\right)^N} + e^{2\left(\frac{\tau_1}{T_\chi}\right)^N + 2\left(\frac{\tau_2}{T_\chi}\right)^N} + 1 \right)}$$

$$(A.33) \quad \text{FIM}_{11} = \frac{\left(\frac{\tau_1}{T_\chi}\right)^{2N} e^{2\left(\frac{\tau_2}{T_\chi}\right)^N} \log\left(\frac{\tau_1}{T_\chi}\right)^2 - \left(\frac{\tau_1}{T_\chi}\right)^{2N} \log\left(\frac{\tau_1}{T_\chi}\right)^2 + \left(\frac{\tau_2}{T_\chi}\right)^{2N} e^{2\left(\frac{\tau_1}{T_\chi}\right)^N} \log\left(\frac{\tau_2}{T_\chi}\right)^2 - \left(\frac{\tau_2}{T_\chi}\right)^{2N} \log\left(\frac{\tau_2}{T_\chi}\right)^2}{-e^{2\left(\frac{\tau_1}{T_\chi}\right)^N} - e^{2\left(\frac{\tau_2}{T_\chi}\right)^N} + e^{2\left(\frac{\tau_1}{T_\chi}\right)^N + 2\left(\frac{\tau_2}{T_\chi}\right)^N} + 1}$$

## A.7 Optimal phase calculation

In this section, we drive the optimal phase for the adaptive frequency estimation. We begin by defining a likelihood model  $L$  expressing the probability of a frequency  $f_B$  for a given phase  $\phi$ .

$$(A.34) \quad L(f_B, \phi) = \alpha [1 + V \cos(2\pi f_B \tau - \phi)]$$

With the corresponding derivative given as:

$$(A.35) \quad L'(f_B, \phi) = \frac{\partial}{\partial f_B} L(f_B, \phi) = -2\alpha V \pi \tau \sin(2\pi f_B \tau - \phi)$$

Using the binomial probability distribution, given as:

$$(A.36) \quad P(f|r) = \binom{R}{r} P_d(1|f)^r [1 - P_d(1|f)]^{R-r}$$

We can write the mean and variance as:

$$(A.37) \quad \mu_r = E[r|f_B] = R \cdot L(f_B, \phi)$$

$$(A.38) \quad \sigma_r^2 = E[(r - \mu_r)^2|f_B] = R \cdot L(f_B, \phi) [1 - L(f_B, \phi)]$$

for  $\Delta \ll 1$ , we can approximate  $L(f_B, \phi) = \frac{r}{R} + \Delta$ . Using we can write the variance as:

$$\begin{aligned}
 \sigma_r^2 &= R.L(f_B, \phi)[1 - L(f_B, \phi)] = RL - RL^2 = R \left[ \left( \frac{r}{R} + \Delta \right) - \left( \frac{r}{R} + \Delta \right)^2 \right] \\
 (A.39) \quad &= R \left[ \left( \frac{r}{R} + \Delta \right) - \left( \frac{r^2}{R^2} + 2\Delta \frac{r}{R} + \Delta^2 \right) \right] \approx R \left[ \left( \frac{r}{R} + \Delta \right) - \frac{r^2}{R^2} - 2\Delta \frac{r}{R} \right] \\
 &= R \left[ L - \frac{r^2}{R^2} - 2 \left( L - \frac{r}{R} \right) \frac{r}{R} \right] = R \left[ L + \frac{r^2}{R^2} - 2 \frac{r}{R} L \right] = R \left[ L \left( 1 - 2 \frac{r}{R} \right) + \frac{r^2}{R^2} \right]
 \end{aligned}$$

for simplicity we have replaced we have replaced  $L(f_B, \phi) = L$ . For  $\sigma_r^2 \geq 0$ : it can be shown that  $L(f_B, \phi) + \frac{r^2}{R^2} - 2 \frac{r}{R} L(f_B, \phi) \geq L^2(f_B, \phi) + \frac{r^2}{R^2} - 2 \frac{r}{R} L(f_B, \phi) \geq 0$ .

Taking the logarithm of the model (likelihood function), we get:

$$(A.40) \quad K(r, f_B) \equiv \log P(r|f_B) = \log \binom{R}{r} + r \log L(f_B, \phi) + (R - r) \log(1 - L(f_B, \phi))$$

Taking the partial derivative of Eqn. A.40 with respect to  $f_B$ , we get:

$$(A.41) \quad \frac{\partial}{\partial f_B} K(r, f_B) = \frac{rL'}{L} - \frac{(R-r)L'}{1-L} = \left[ \frac{r}{L} - \frac{R-r}{1-L} \right] L' = \left[ \frac{r-RL}{L(1-L)} L' \right] = \frac{R}{\sigma_r^2} (r - \mu_r) L'$$

Using Eqn. A.41 we can now calculate the Fisher information below:

$$\begin{aligned}
 (A.42) \quad I(f_B) &= E \left[ \left( \frac{\partial}{\partial f_B} K(r, f_B) \right)^2 \right] = E[(r - \mu_r)^2] \frac{R^2}{\sigma_r^4} (L')^2 = \frac{R^2}{\sigma_r^2} (L')^2 \\
 &\approx \frac{RL'^2}{\frac{r^2}{R^2} + (1 - 2 \frac{r}{R})L} = 4R\alpha^2 V^2 \pi^2 \tau^2 \frac{\sin^2(2\pi f_B \tau - \phi)}{\frac{r^2}{R^2} + (1 - 2 \frac{r}{R})\alpha[1 + V \cos(2\pi f_B \tau - \phi)]}
 \end{aligned}$$

rewriting the above equation in a more compact form, we get the following:

$$(A.43) \quad I(f_B) = C \frac{\sin^2(2\pi f_B \tau - \phi)}{A + B \cos(2\pi f_B \tau - \phi)}$$

Where A, B and C are given as:

$$(A.44) \quad A = \frac{r^2}{R^2} + \left( 1 - 2 \frac{r}{R} \right) \alpha$$

$$(A.45) \quad B = \left( 1 - 2 \frac{r}{R} \right) \alpha V$$

$$(A.46) \quad C = 4R\alpha^2V^2\pi^2\tau^2$$

Using Eqn. A.43, we can maximise it to get the optimal phase  $\phi$  as:

$$(A.47) \quad \frac{\partial}{\partial\phi}I(f_B) = 0$$

$$(A.48) \quad \frac{\partial}{\partial\phi} \left( C \frac{\sin^2(2\pi f_B\tau - \phi)}{A + B\cos(2\pi f_B\tau - \phi)} \right) = 0$$

$$(A.49) \quad C \frac{\frac{d}{dx}(\sin^2(2\pi f_B\tau - \phi))(A + B\cos(2\pi f_B\tau - \phi)) - \frac{d}{dx}(A + B\cos(2\pi f_B\tau - \phi))\sin^2(2\pi f_B\tau - \phi)}{(A + B\cos(2\pi f_B\tau - \phi))^2} = 0$$

$$(A.50) \quad = C \frac{(-\sin(2(2\pi f_B\tau - \phi)))(A + B\cos(2\pi f_B\tau - \phi)) - B\sin(2\pi f_B\tau - \phi)\sin^2(2\pi f_B\tau - \phi)}{(A + B\cos(2\pi f_B\tau - \phi))^2}$$

$$(A.51) \quad = \frac{C(-\sin(2(2\pi f_B\tau - \phi))(A + B\cos(2\pi f_B\tau - \phi)) - B\sin^3(2\pi f_B\tau - \phi))}{(A + B\cos(2\pi f_B\tau - \phi))^2}$$

$$(A.52) \quad = \frac{C \cdot (B\sin^3(\phi - 2\pi f_B\tau) + 2\cos(\phi - 2\pi f_B\tau)(B\cos(\phi - 2\pi f_B\tau) + A)\sin(\phi - 2\pi f_B\tau))}{(A + B\cos(2\pi f_B\tau - \phi))^2}$$

simplifying the above equation, we get:

$$(A.53) \quad \frac{C \cdot (\cos(\phi - 2\pi f_B\tau)(B\cos(\phi - 2\pi f_B\tau) + 2A) + B)\sin(\phi - 2\pi f_B\tau)}{(A + B\cos(2\pi f_B\tau - \phi))^2} = 0$$

Where this Eqn. A.53 has two solutions. First one is for  $\phi = 2\pi f_B\tau$ , while the second solution is:

$$(A.54) \quad B\cos^2(2\pi f_B\tau - \phi) + 2A\cos(2\pi f_B\tau - \phi) + B = 0$$

hence by defining  $z = \cos(2\pi f_B\tau - \phi)$ , we can find that :

$$(A.55) \quad z = \frac{-A + \sqrt{A^2 - B^2}}{B} \rightarrow \cos(2\pi f_B\tau - \phi) = \frac{\sqrt{A^2 - B^2} - A}{B}$$

Leading to a final optimal value of phase as Eqn. 5.7, mentioned in the main text.

$$(A.56) \quad \phi_{opt} = 2\pi\hat{f}_B\tau - \arccos\left(\frac{\sqrt{A^2 - B^2} - A}{B}\right)$$

where  $\hat{f}_B = E[f_B]$ .

## A.8 Inhomogeneous distribution calculation

This section discusses the statistical analyses done to give quantitative results about the inhomogeneous broadening in our isotropically purified (sample A) and standard (sample B) samples. For sample A, we chose four different regions (one shown here) of the sample and took a series of PL maps at different detunings (see, for example, Fig. A.14). An automated detection was done to find out the spot's comparable to the size of the diffraction limit. The total counts were integrated for each spot and plotted as a function of detuning (see, for example, Fig. A.15). Fitting the peaks in these plots for four different regions, we analyse more than 150 vanadium defects in sample A and plot the distribution of inhomogeneous broadening in Fig. 6.4(c) in Chap. 6.

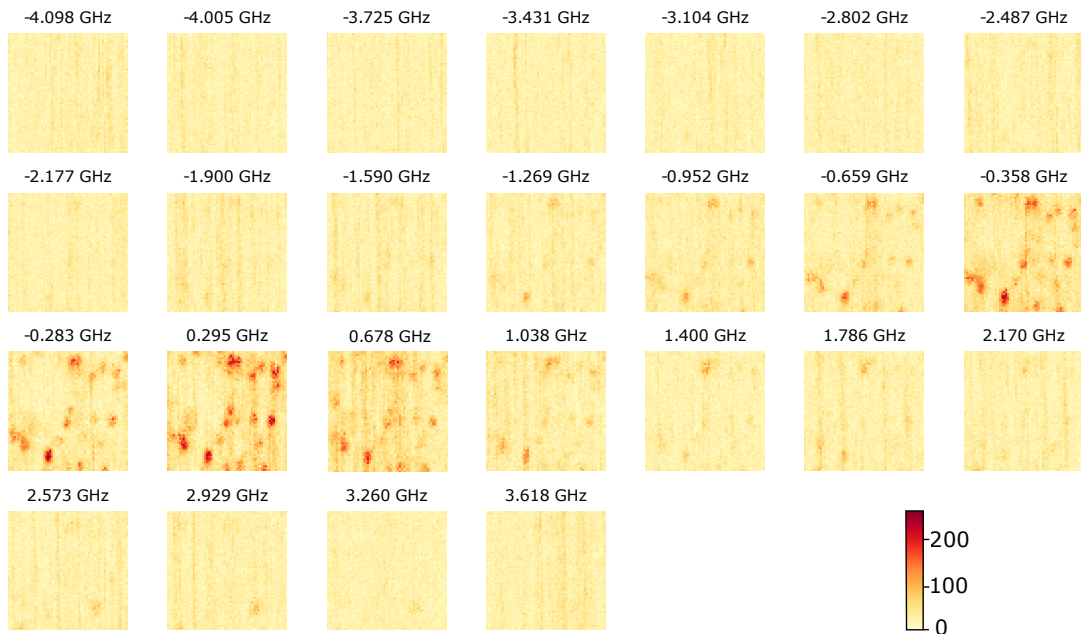


FIGURE A.14. **Series of PLE maps in region A of sample A.** An illustration of photoluminescence maps with different laser detunings.

A similar analysis was done for sample B. In this sample, we analysed more than 300 PL spots. Here I show one such PLE map taken in that sample across an excitation frequency of -4.3 to +1.4 GHz as shown in Fig. A.16. The corresponding spectra of automatically detected spots in these PLE maps are shown in Fig. A.17.

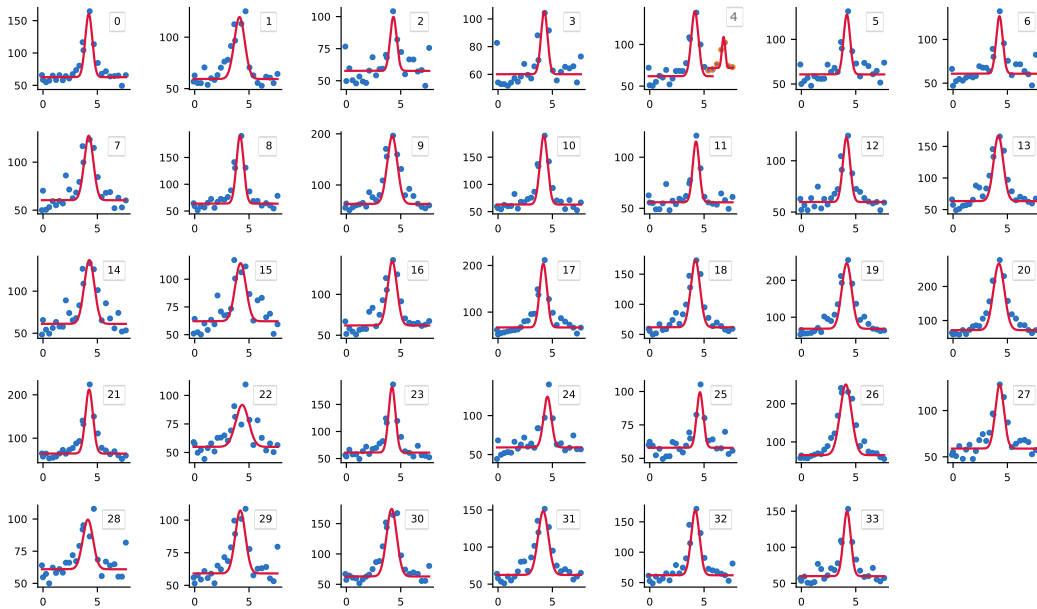


FIGURE A.15. **Series of PLE spectra in region A of sample A.** Spectra of the 33 spots in Fig A.14 fitted with Gaussian function. In each subplot, the x-axis represents the frequency of the excitation in GHz, while the y-axis represents the total detected counts.

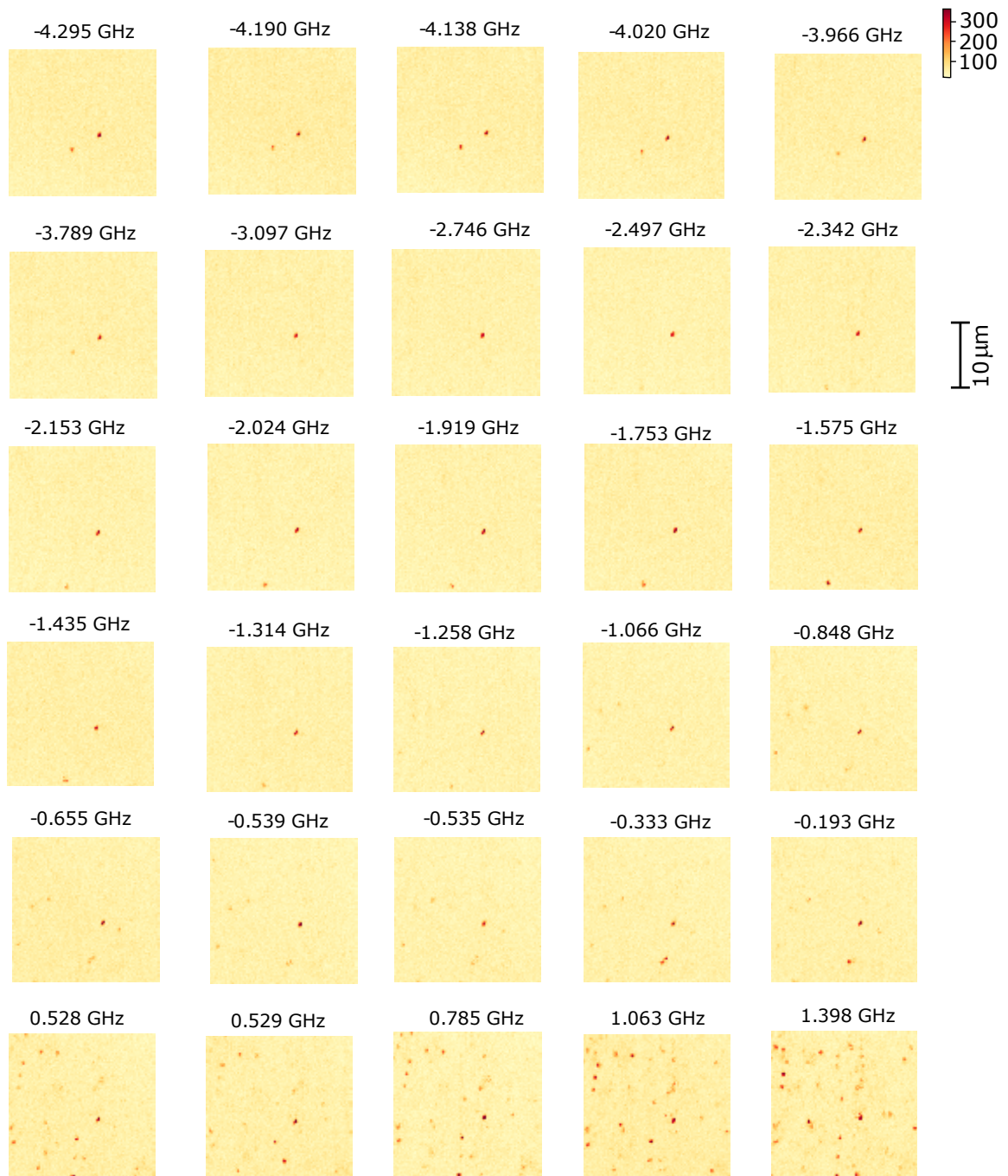
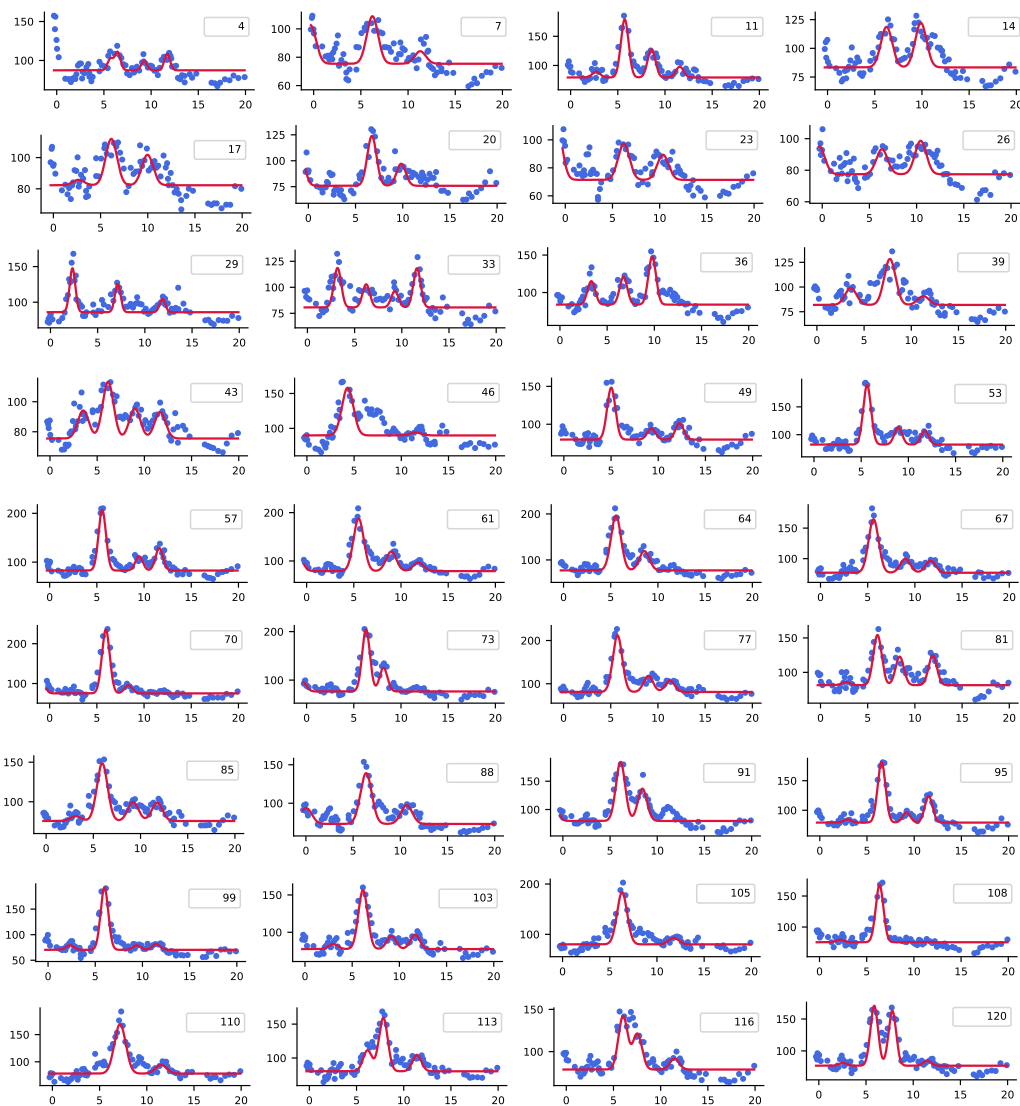


FIGURE A.16. **Series of PLE maps in sample B with a natural abundance of isotopes.** An illustration of photoluminescence maps with different laser detunings.



**FIGURE A.17. Series of PLE spectra in sample B with a natural abundance of isotopes.** Spectra of the PL spots in Fig A.16 fitted with Gaussian function. In each subplot, the x-axis represents the frequency of the excitation in GHz, while the y-axis represents the total detected counts.





## BIBLIOGRAPHY

- [1] L. B. Kish, “End of Moore’s law: thermal (noise) death of integration in micro and nano electronics,” *Physics Letters A*, vol. 305, no. 3-4, pp. 144–149, 2002.
- [2] P. W. Shor, “Algorithms for quantum computation: discrete logarithms and factoring,” in *Proceedings 35th Annual Symposium on Foundations of Computer Science*, pp. 124–134, Ieee, 1994.
- [3] C. H. Bennett and G. Brassard, “Quantum cryptography: Public key distribution and coin tossing,” *Theoretical Computer Science*, vol. 560, pp. 7–11, 2014.
- [4] C. L. Degen, F. Reinhard, and P. Cappellaro, “Quantum sensing,” *Reviews of Modern Physics*, vol. 89, no. 3, p. 035002, 2017.
- [5] N. Aslam, H. Zhou, E. K. Urbach, M. J. Turner, R. L. Walsworth, M. D. Lukin, and H. Park, “Quantum sensors for biomedical applications,” *Nature Reviews Physics*, vol. 5, no. 3, pp. 157–169, 2023.
- [6] S. Zaiser, T. Rendler, I. Jakobi, T. Wolf, S.-Y. Lee, S. Wagner, V. Bergholm, T. Schulte-Herbrüggen, P. Neumann, and J. Wrachtrup, “Enhancing quantum sensing sensitivity by a quantum memory,” *Nature Communications*, vol. 7, no. 1, p. 12279, 2016.
- [7] W. Wieczorek, R. Krischek, N. Kiesel, C. Schmid, and H. Weinfurter, “Entanglement enhanced quantum sensing,” in *Quantum Sensing and Nanophotonic Devices VII*, vol. 7608, pp. 213–217, SPIE, 2010.
- [8] S.-H. Wei, B. Jing, X.-Y. Zhang, J.-Y. Liao, C.-Z. Yuan, B.-Y. Fan, C. Lyu, D.-L. Zhou, Y. Wang, G.-W. Deng, *et al.*, “Towards Real-World Quantum Networks: A Review,” *Laser & Photonics Reviews*, vol. 16, no. 3, p. 2100219, 2022.
- [9] H. J. Kimble, “The quantum internet,” *Nature*, vol. 453, no. 7198, pp. 1023–1030, 2008.
- [10] S. Wehner, D. Elkouss, and R. Hanson, “Quantum internet: A vision for the road ahead,” *Science*, vol. 362, no. 6412, p. eaam9288, 2018.
- [11] Y. Li and S. C. Benjamin, “High threshold distributed quantum computing with three-qubit nodes,” *New Journal of Physics*, vol. 14, no. 9, p. 093008, 2012.

## BIBLIOGRAPHY

---

- [12] P. Komar, E. M. Kessler, M. Bishof, L. Jiang, A. S. Sørensen, J. Ye, and M. D. Lukin, “A quantum network of clocks,” *Nature Physics*, vol. 10, no. 8, pp. 582–587, 2014.
- [13] V. Giovannetti, S. Lloyd, and L. Maccone, “Quantum-enhanced measurements: beating the standard quantum limit,” *Science*, vol. 306, no. 5700, pp. 1330–1336, 2004.
- [14] J. Wallnöfer, M. Zwerger, C. Muschik, N. Sangouard, and W. Dür, “Two-dimensional quantum repeaters,” *Physical Review A*, vol. 94, no. 5, p. 052307, 2016.
- [15] J. Cramer, N. Kalb, M. A. Rol, B. Hensen, M. S. Blok, M. Markham, D. J. Twitchen, R. Hanson, and T. H. Taminiau, “Repeated quantum error correction on a continuously encoded qubit by real-time feedback,” *Nature Communications*, vol. 7, no. 1, p. 11526, 2016.
- [16] B. Hensen, H. Bernien, A. E. Dréau, A. Reiserer, N. Kalb, M. S. Blok, J. Ruitenberg, R. F. Vermeulen, R. N. Schouten, C. Abellán, *et al.*, “Loophole-free Bell inequality violation using electron spins separated by 1.3 kilometres,” *Nature*, vol. 526, no. 7575, pp. 682–686, 2015.
- [17] M. Pompili, S. L. Hermans, S. Baier, H. K. Beukers, P. C. Humphreys, R. N. Schouten, R. F. Vermeulen, M. J. Tiggelman, L. dos Santos Martins, B. Dirkse, *et al.*, “Realization of a multinode quantum network of remote solid-state qubits,” *Science*, vol. 372, no. 6539, pp. 259–264, 2021.
- [18] W. Pfaff, B. J. Hensen, H. Bernien, S. B. van Dam, M. S. Blok, T. H. Taminiau, M. J. Tiggelman, R. N. Schouten, M. Markham, D. J. Twitchen, *et al.*, “Unconditional quantum teleportation between distant solid-state quantum bits,” *Science*, vol. 345, no. 6196, pp. 532–535, 2014.
- [19] I. V. Inlek, C. Crocker, M. Lichtman, K. Sosnova, and C. Monroe, “Multispecies trapped-ion node for quantum networking,” *Physical Review Letters*, vol. 118, no. 25, p. 250502, 2017.
- [20] R. Van Meter, *Quantum networking*. John Wiley & Sons, 2014.
- [21] K. Azuma, K. Tamaki, and H.-K. Lo, “All-photonic quantum repeaters,” *Nature Communications*, vol. 6, no. 1, p. 6787, 2015.
- [22] L. Jiang, J. M. Taylor, K. Nemoto, W. J. Munro, R. Van Meter, and M. D. Lukin, “Quantum repeater with encoding,” *Physical Review A*, vol. 79, no. 3, p. 032325, 2009.
- [23] E. Diamanti, H.-K. Lo, B. Qi, and Z. Yuan, “Practical challenges in quantum key distribution,” *npj Quantum Information*, vol. 2, no. 1, pp. 1–12, 2016.

- 
- [24] T. Inagaki, N. Matsuda, O. Tadanaga, M. Asobe, and H. Takesue, “Entanglement distribution over 300 km of fiber,” *Optics Express*, vol. 21, no. 20, pp. 23241–23249, 2013.
- [25] W. K. Wootters and W. H. Zurek, “A single quantum cannot be cloned,” *Nature*, vol. 299, pp. 802–803, 1982.
- [26] W. Dür and H. J. Briegel, “Entanglement purification and quantum error correction,” *Reports on Progress in Physics*, vol. 70, no. 8, p. 1381, 2007.
- [27] S. Castelletto, A. Peruzzo, C. Bonato, B. C. Johnson, M. Radulaski, H. Ou, F. Kaiser, and J. Wrachtrup, “Silicon carbide photonics bridging quantum technology,” *ACS Photonics*, vol. 9, no. 5, pp. 1434–1457, 2022.
- [28] G. Calusine, A. Politi, and D. D. Awschalom, “Cavity-enhanced measurements of defect spins in silicon carbide,” *Physical Review Applied*, vol. 6, no. 1, p. 014019, 2016.
- [29] C. Babin, R. Stöhr, N. Morioka, T. Linkewitz, T. Steidl, R. Wörnle, D. Liu, V. Vorobyov, A. Denisenko, M. Hentschel, *et al.*, “Nanofabricated and integrated colour centres in silicon carbide with high-coherence spin-optical properties,” in *Frontiers in Optics*, pp. FM6D–2, Optical Society of America, 2021.
- [30] C.-K. Hong, Z.-Y. Ou, and L. Mandel, “Measurement of subpicosecond time intervals between two photons by interference,” *Physical Review Letters*, vol. 59, no. 18, p. 2044, 1987.
- [31] A. Csóré, I. Ivanov, N. Son, and A. Gali, “Photoluminescence lineshapes and charge state control of divacancy qubits in silicon carbide,” *arXiv preprint arXiv:2107.01971*, 2021.
- [32] R. Hab-arrih, A. Jellal, and A. Merdaci, “Classical Instability Effects on Photon Excitations and Entanglement,” *arXiv preprint arXiv:2102.10470*, 2021.
- [33] A. Reiserer, N. Kalb, M. S. Blok, K. J. van Bemmelen, T. H. Taminiou, R. Hanson, D. J. Twitchen, and M. Markham, “Robust quantum-network memory using decoherence-protected subspaces of nuclear spins,” *Physical Review X*, vol. 6, no. 2, p. 021040, 2016.
- [34] H. Bernien, B. Hensen, W. Pfaff, G. Koolstra, M. S. Blok, L. Robledo, T. H. Taminiou, M. Markham, D. J. Twitchen, L. Childress, *et al.*, “Heralded entanglement between solid-state qubits separated by three metres,” *Nature*, vol. 497, no. 7447, pp. 86–90, 2013.
- [35] M. Degen, S. Loenen, H. Bartling, C. Bradley, A. Meinsma, M. Markham, D. Twitchen, and T. H. Taminiou, “Entanglement of dark electron-nuclear spin defects in diamond,” *Nature Communications*, vol. 12, no. 1, p. 3470, 2021.

## BIBLIOGRAPHY

---

- [36] A. Dréau, A. Tchebotareva, A. El Mahdaoui, C. Bonato, and R. Hanson, “Quantum frequency conversion of single photons from a nitrogen-vacancy center in diamond to telecommunication wavelengths,” *Physical Review Applied*, vol. 9, no. 6, p. 064031, 2018.
- [37] F. K. Asadi, N. Lauk, S. Wein, N. Sinclair, C. O’Brien, and C. Simon, “Quantum repeaters with individual rare-earth ions at telecommunication wavelengths,” *Quantum*, vol. 2, p. 93, 2018.
- [38] S. K. Joshi, D. Aktas, S. Wengerowsky, M. Lončarić, S. P. Neumann, B. Liu, T. Scheidl, G. C. Lorenzo, Ž. Samec, L. Kling, *et al.*, “A trusted node-free eight-user metropolitan quantum communication network,” *Science Advances*, vol. 6, no. 36, p. eaba0959, 2020.
- [39] X.-Y. Luo, Y. Yu, J.-L. Liu, M.-Y. Zheng, C.-Y. Wang, B. Wang, J. Li, X. Jiang, X.-P. Xie, Q. Zhang, *et al.*, “Postselected entanglement between two atomic ensembles separated by 12.5 km,” *Physical Review Letters*, vol. 129, no. 5, p. 050503, 2022.
- [40] P. Drmota, D. Main, D. Nadlinger, B. Nichol, M. Weber, E. Ainley, A. Agrawal, R. Srinivas, G. Araneda, C. Ballance, *et al.*, “Robust Quantum Memory in a Trapped-Ion Quantum Network Node,” *Physical Review Letters*, vol. 130, no. 9, p. 090803, 2023.
- [41] A. Kumar, A. Suleymanzade, M. Stone, L. Taneja, A. Anferov, D. I. Schuster, and J. Simon, “Quantum-enabled millimetre wave to optical transduction using neutral atoms,” *Nature*, vol. 615, no. 7953, pp. 614–619, 2023.
- [42] J. V. Rakonjac, S. Grandi, S. Wengerowsky, D. Lago-Rivera, F. Appas, and H. de Riedmatten, “Transmission of light-matter entanglement over a metropolitan network,” *arXiv preprint arXiv:2304.05416*, 2023.
- [43] D. Lago-Rivera, J. V. Rakonjac, S. Grandi, and H. d. Riedmatten, “Long distance multiplexed quantum teleportation from a telecom photon to a solid-state qubit,” *Nature Communications*, vol. 14, no. 1, p. 1889, 2023.
- [44] D. Lago-Rivera, S. Grandi, J. V. Rakonjac, A. Seri, and H. de Riedmatten, “Telecom-heralded entanglement between multimode solid-state quantum memories,” *Nature*, vol. 594, no. 7861, pp. 37–40, 2021.
- [45] S. Hermans, M. Pompili, H. Beukers, S. Baier, J. Borregaard, and R. Hanson, “Qubit teleportation between non-neighbouring nodes in a quantum network,” *Nature*, vol. 605, no. 7911, pp. 663–668, 2022.
- [46] A. Boaron, G. Boso, D. Rusca, C. Vulliez, C. Autebert, M. Caloz, M. Perrenoud, G. Gras, F. Bussièrès, M.-J. Li, *et al.*, “Secure quantum key distribution over 421 km of optical fiber,” *Physical Review Letters*, vol. 121, no. 19, p. 190502, 2018.

- [47] M. Minder, M. Pittaluga, G. L. Roberts, M. Lucamarini, J. Dynes, Z. Yuan, and A. J. Shields, “Experimental quantum key distribution beyond the repeaterless secret key capacity,” *Nature Photonics*, vol. 13, no. 5, pp. 334–338, 2019.
- [48] X. Zhong, J. Hu, M. Curty, L. Qian, and H.-K. Lo, “Proof-of-principle experimental demonstration of twin-field type quantum key distribution,” *Physical Review Letters*, vol. 123, no. 10, p. 100506, 2019.
- [49] G. Vallone, D. Bacco, D. Dequal, S. Gaiarin, V. Luceri, G. Bianco, and P. Villoresi, “Experimental satellite quantum communications,” *Physical Review Letters*, vol. 115, no. 4, p. 040502, 2015.
- [50] Y. Yu, F. Ma, X.-Y. Luo, B. Jing, P.-F. Sun, R.-Z. Fang, C.-W. Yang, H. Liu, M.-Y. Zheng, X.-P. Xie, *et al.*, “Entanglement of two quantum memories via fibres over dozens of kilometres,” *Nature*, vol. 578, no. 7794, pp. 240–245, 2020.
- [51] S. Wang, W. Chen, Z.-Q. Yin, H.-W. Li, D.-Y. He, Y.-H. Li, Z. Zhou, X.-T. Song, F.-Y. Li, D. Wang, *et al.*, “Field and long-term demonstration of a wide area quantum key distribution network,” *Optics Express*, vol. 22, no. 18, pp. 21739–21756, 2014.
- [52] M. Sasaki, M. Fujiwara, H. Ishizuka, W. Klaus, K. Wakui, M. Takeoka, S. Miki, T. Yamashita, Z. Wang, A. Tanaka, *et al.*, “Field test of quantum key distribution in the Tokyo QKD Network,” *Optics Express*, vol. 19, no. 11, pp. 10387–10409, 2011.
- [53] J. Yin, Y. Cao, Y.-H. Li, S.-K. Liao, L. Zhang, J.-G. Ren, W.-Q. Cai, W.-Y. Liu, B. Li, H. Dai, *et al.*, “Satellite-based entanglement distribution over 1200 kilometers,” *Science*, vol. 356, no. 6343, pp. 1140–1144, 2017.
- [54] G. Xueshi, R. B. Casper, B. Johannes, I. Shuro, V. L. Mikkell, G. Tobias, C. Matthias, S. Jonas, and L. A. Ulrik, “Distributed quantum sensing in a continuous-variable entangled network,” *Nature Physics*, vol. 16, no. 3, pp. 281–284, 2019.
- [55] V. Giovannetti, S. Lloyd, and L. Maccone, “Advances in quantum metrology,” *Nature Photonics*, vol. 5, no. 4, pp. 222–229, 2011.
- [56] D. P. DiVincenzo and D. Loss, “Quantum computers and quantum coherence,” *Journal of Magnetism and Magnetic Materials*, vol. 200, no. 1-3, pp. 202–218, 1999.
- [57] M. Abobeih, J. Randall, C. Bradley, H. Bartling, M. Bakker, M. Degen, M. Markham, D. Twitchen, and T. H. Taminiau, “Atomic-scale imaging of a 27-nuclear-spin cluster using a quantum sensor,” *Nature*, vol. 576, no. 7787, pp. 411–415, 2019.
- [58] K. S. Cujia, K. Herb, J. Zopes, J. M. Abendroth, and C. L. Degen, “Parallel detection and spatial mapping of large nuclear spin clusters,” *Nature Communications*, vol. 13, no. 1, p. 1260, 2022.

- [59] S. Saijo, Y. Matsuzaki, S. Saito, T. Yamaguchi, I. Hanano, H. Watanabe, N. Mizuochi, and J. Ishi-Hayase, “AC magnetic field sensing using continuous-wave optically detected magnetic resonance of nitrogen-vacancy centers in diamond,” *Applied Physics Letters*, vol. 113, no. 8, p. 082405, 2018.
- [60] Z. Wang, C. McPherson, R. Kadado, N. Brandt, S. Edwards, W. Casey, and N. Curro, “ac sensing using nitrogen-vacancy centers in a diamond anvil cell up to 6 gpa,” *Physical Review Applied*, vol. 16, no. 5, p. 054014, 2021.
- [61] T. Yamaguchi, Y. Matsuzaki, S. Saito, S. Saijo, H. Watanabe, N. Mizuochi, and J. Ishi-Hayase, “Bandwidth analysis of AC magnetic field sensing based on electronic spin double-resonance of nitrogen-vacancy centers in diamond,” *Japanese Journal of Applied Physics*, vol. 58, no. 10, p. 100901, 2019.
- [62] G. Wang, Y.-X. Liu, J. M. Schloss, S. T. Alsid, D. A. Braje, P. Cappellaro, *et al.*, “Sensing of arbitrary-frequency fields using a quantum mixer,” *Physical Review X*, vol. 12, no. 2, p. 021061, 2022.
- [63] V. Gebhart, R. Santagati, A. A. Gentile, E. M. Gauger, D. Craig, N. Ares, L. Banchi, F. Marquardt, L. Pezzè, and C. Bonato, “Learning quantum systems,” *Nature Reviews Physics*, pp. 1–16, 2023.
- [64] R. Hanson and D. D. Awschalom, “Coherent manipulation of single spins in semiconductors,” *Nature*, vol. 453, no. 7198, pp. 1043–1049, 2008.
- [65] D. Suter and G. A. Álvarez, “Colloquium: Protecting quantum information against environmental noise,” *Reviews of Modern Physics*, vol. 88, no. 4, p. 041001, 2016.
- [66] F. Perona Martínez, A. C. Nusantara, M. Chipaux, S. K. Padamati, and R. Schirhagl, “Nanodiamond relaxometry-based detection of free-radical species when produced in chemical reactions in biologically relevant conditions,” *ACS Sensors*, vol. 5, no. 12, pp. 3862–3869, 2020.
- [67] D. Kawahara and Y. Nagata, “T1-weighted and T2-weighted MRI image synthesis with convolutional generative adversarial networks,” *Reports of Practical Oncology Radiotherapy*, vol. 26, no. 1, pp. 35–42, 2021.
- [68] J. R. Petta, A. C. Johnson, J. M. Taylor, E. A. Laird, A. Yacoby, M. D. Lukin, C. M. Marcus, M. P. Hanson, and A. C. Gossard, “Coherent manipulation of coupled electron spins in semiconductor quantum dots,” *Science*, vol. 309, no. 5744, pp. 2180–2184, 2005.
- [69] X. Wu, D. R. Ward, J. Prance, D. Kim, J. K. Gamble, R. Mohr, Z. Shi, D. Savage, M. Lagally, M. Friesen, *et al.*, “Two-axis control of a singlet–triplet qubit with an integrated micro-

- magnet,” *Proceedings of the National Academy of Sciences*, vol. 111, no. 33, pp. 11938–11942, 2014.
- [70] J. F. Barry, J. M. Schloss, E. Bauch, M. J. Turner, C. A. Hart, L. M. Pham, and R. L. Walsworth, “Sensitivity optimization for NV-diamond magnetometry,” *Reviews of Modern Physics*, vol. 92, no. 1, p. 015004, 2020.
- [71] F. Rozpędek, K. Goodenough, J. Ribeiro, N. Kalb, V. C. Vivoli, A. Reiserer, R. Hanson, S. Wehner, and D. Elkouss, “Parameter regimes for a single sequential quantum repeater,” *Quantum Science and Technology*, vol. 3, no. 3, p. 034002, 2018.
- [72] J. Taylor, P. Cappellaro, L. Childress, L. Jiang, D. Budker, P. Hemmer, A. Yacoby, R. Walsworth, and M. Lukin, “High-sensitivity diamond magnetometer with nanoscale resolution,” *Nature Physics*, vol. 4, no. 10, pp. 810–816, 2008.
- [73] T. Ishikawa, K.-M. C. Fu, C. Santori, V. M. Acosta, R. G. Beausoleil, H. Watanabe, S. Shikata, and K. M. Itoh, “Optical and spin coherence properties of nitrogen-vacancy centers placed in a 100 nm thick isotopically purified diamond layer,” *Nano Letters*, vol. 12, no. 4, pp. 2083–2087, 2012.
- [74] R. de Sousa, “Electron spin as a spectrometer of nuclear-spin noise and other fluctuations,” in *Electron Spin Resonance and Related Phenomena in Low-Dimensional Structures*, pp. 183–220, Springer, 2009.
- [75] R. Hanson, F. Mendoza, R. Epstein, and D. Awschalom, “Polarization and readout of coupled single spins in diamond,” *Physical Review Letters*, vol. 97, no. 8, p. 087601, 2006.
- [76] R. Hanson, V. Dobrovitski, A. Feiguin, O. Gywat, and D. Awschalom, “Coherent dynamics of a single spin interacting with an adjustable spin bath,” *Science*, vol. 320, no. 5874, pp. 352–355, 2008.
- [77] R. Hanson, O. Gywat, and D. Awschalom, “Room-temperature manipulation and decoherence of a single spin in diamond,” *Physical Review B*, vol. 74, no. 16, p. 161203, 2006.
- [78] P. L. Stanwix, L. M. Pham, J. R. Maze, D. Le Sage, T. K. Yeung, P. Cappellaro, P. R. Hemmer, A. Yacoby, M. D. Lukin, and R. L. Walsworth, “Coherence of nitrogen-vacancy electronic spin ensembles in diamond,” *Physical Review B*, vol. 82, no. 20, p. 201201, 2010.
- [79] G. Davies, *Properties and growth of diamond*. INSPEC, 1994.
- [80] A. M. Zaitsev, *Optical properties of diamond: a data handbook*. Springer Science & Business Media, 2013.

- [81] S. Pezzagna, D. Rogalla, D. Wildanger, J. Meijer, and A. Zaitsev, "Creation and nature of optical centres in diamond for single-photon emission-overview and critical remarks," *New Journal of Physics*, vol. 13, no. 3, p. 035024, 2011.
- [82] E. Pereira, L. Santos, L. Pereira, D. Hofmann, P. Christmann, W. Stadler, and B. Meyer, "Slow emission of the 2.56 eV centre in synthetic diamond," *Diamond and Related Materials*, vol. 4, no. 1, pp. 53–58, 1994.
- [83] E. van Oort, P. Stroomeer, and M. Glasbeek, "Low-field optically detected magnetic resonance of a coupled triplet-doublet defect pair in diamond," *Physical Review B*, vol. 42, no. 13, p. 8605, 1990.
- [84] Y.-C. Chen, P. S. Salter, S. Knauer, L. Weng, A. C. Frangeskou, C. J. Stephen, S. N. Ishmael, P. R. Dolan, S. Johnson, B. L. Green, *et al.*, "Laser writing of coherent colour centres in diamond," *Nature Photonics*, vol. 11, no. 2, pp. 77–80, 2017.
- [85] T. Luo, L. Lindner, J. Langer, V. Cimalla, X. Vidal, F. Hahl, C. Schreyvogel, S. Onoda, S. Ishii, T. Ohshima, *et al.*, "Creation of nitrogen-vacancy centers in chemical vapor deposition diamond for sensing applications," *New Journal of Physics*, vol. 24, no. 3, p. 033030, 2022.
- [86] P. B. Karki, R. Timalisina, M. Dowran, A. E. Aregbesola, A. Laraoui, and K. Ambal, "An efficient and low-cost method to create high-density nitrogen-vacancy centers in CVD diamond for sensing applications," *arXiv preprint arXiv:2301.08712*, 2023.
- [87] J. R. Maze, A. Gali, E. Togan, Y. Chu, A. Trifonov, E. Kaxiras, and M. D. Lukin, "Properties of nitrogen-vacancy centers in diamond: the group theoretic approach," *New Journal of Physics*, vol. 13, no. 2, p. 025025, 2011.
- [88] R. D. McMichael and S. Blakley, "Diamond NV Center Magnetometry," *NIST*, 2019.
- [89] M. W. Doherty, N. B. Manson, P. Delaney, and L. C. Hollenberg, "The negatively charged nitrogen-vacancy centre in diamond: the electronic solution," *New Journal of Physics*, vol. 13, no. 2, p. 025019, 2011.
- [90] A. Gali, E. Janzén, P. Deák, G. Kresse, and E. Kaxiras, "Theory of spin-conserving excitation of the N- V- center in diamond," *Physical Review Letters*, vol. 103, no. 18, p. 186404, 2009.
- [91] B. Deng, R. Zhang, and X. Shi, "New insight into the spin-conserving excitation of the negatively charged nitrogen-vacancy center in diamond," *Scientific Reports*, vol. 4, no. 1, p. 5144, 2014.



- [92] M. L. Goldman, M. Doherty, A. Sipahigil, N. Y. Yao, S. Bennett, N. Manson, A. Kubanek, and M. D. Lukin, “State-selective intersystem crossing in nitrogen-vacancy centers,” *Physical Review B*, vol. 91, no. 16, p. 165201, 2015.
- [93] M. Gulka, D. Wirtitsch, V. Ivády, J. Vodnik, J. Hruby, G. Magchiels, E. Bourgeois, A. Gali, M. Trupke, and M. Nesladek, “Room-temperature control and electrical readout of individual nitrogen-vacancy nuclear spins,” *Nature Communications*, vol. 12, no. 1, p. 4421, 2021.
- [94] V. R. Horowitz, B. J. Alemán, D. J. Christle, A. N. Cleland, and D. D. Awschalom, “Electron spin resonance of nitrogen-vacancy centers in optically trapped nanodiamonds,” *Proceedings of the National Academy of Sciences*, vol. 109, no. 34, pp. 13493–13497, 2012.
- [95] A. Kuwahata, T. Kitaizumi, K. Saichi, T. Sato, R. Igarashi, T. Ohshima, Y. Masuyama, T. Iwasaki, M. Hatano, F. Jelezko, *et al.*, “Magnetometer with nitrogen-vacancy center in a bulk diamond for detecting magnetic nanoparticles in biomedical applications,” *Scientific Reports*, vol. 10, no. 1, pp. 1–9, 2020.
- [96] M. J. Ku, T. X. Zhou, Q. Li, Y. J. Shin, J. K. Shi, C. Burch, L. E. Anderson, A. T. Pierce, Y. Xie, A. Hamo, *et al.*, “Imaging viscous flow of the Dirac fluid in graphene,” *Nature*, vol. 583, no. 7817, pp. 537–541, 2020.
- [97] T. Zhang, G. Pramanik, K. Zhang, M. Gulka, L. Wang, J. Jing, F. Xu, Z. Li, Q. Wei, P. Cigler, *et al.*, “Toward Quantitative Bio-sensing with Nitrogen-Vacancy Center in Diamond,” *ACS Sensors*, vol. 6, no. 6, pp. 2077–2107, 2021.
- [98] R. Schirhagl, K. Chang, M. Loretz, and C. L. Degen, “Nitrogen-vacancy centers in diamond: nanoscale sensors for Physics and Biology,” *Annual Review of Physical Chemistry*, vol. 65, no. 1, pp. 83–105, 2014.
- [99] L. Rondin, J.-P. Tetienne, T. Hingant, J.-F. Roch, P. Maletinsky, and V. Jacques, “Magnetometry with nitrogen-vacancy defects in diamond,” *Reports on Progress in Physics*, vol. 77, no. 5, p. 056503, 2014.
- [100] G. Balasubramanian, I. Chan, R. Kolesov, M. Al-Hmoud, J. Tisler, C. Shin, C. Kim, A. Wojcik, P. R. Hemmer, A. Krueger, *et al.*, “Nanoscale imaging magnetometry with diamond spins under ambient conditions,” *Nature*, vol. 455, no. 7213, pp. 648–651, 2008.
- [101] P. C. Maurer, G. Kucsko, C. Latta, L. Jiang, N. Y. Yao, S. D. Bennett, F. Pastawski, D. Hunger, N. Chisholm, M. Markham, *et al.*, “Room-temperature quantum bit memory exceeding one second,” *Science*, vol. 336, no. 6086, pp. 1283–1286, 2012.

- [102] C. Degen, “Scanning magnetic field microscope with a diamond single-spin sensor,” *Applied Physics Letters*, vol. 92, no. 24, p. 243111, 2008.
- [103] G. Balasubramanian, P. Neumann, D. Twitchen, M. Markham, R. Kolesov, N. Mizuochi, J. Isoya, J. Achard, J. Beck, J. Tissler, *et al.*, “Ultralong spin coherence time in isotopically engineered diamond,” *Nature Materials*, vol. 8, no. 5, pp. 383–387, 2009.
- [104] C. A. Meriles, L. Jiang, G. Goldstein, J. S. Hodges, J. Maze, M. D. Lukin, and P. Cappellaro, “Imaging mesoscopic nuclear spin noise with a diamond magnetometer,” *The Journal of Chemical Physics*, vol. 133, no. 12, p. 124105, 2010.
- [105] A. Dréau, M. Lesik, L. Rondin, P. Spinicelli, O. Arcizet, J.-F. Roch, and V. Jacques, “Avoiding power broadening in optically detected magnetic resonance of single NV defects for enhanced dc magnetic field sensitivity,” *Physical Review B*, vol. 84, no. 19, p. 195204, 2011.
- [106] F. Dolde, H. Fedder, M. W. Doherty, T. Nöbauer, F. Rempp, G. Balasubramanian, T. Wolf, F. Reinhard, L. C. Hollenberg, F. Jelezko, *et al.*, “Electric-field sensing using single diamond spins,” *Nature Physics*, vol. 7, no. 6, pp. 459–463, 2011.
- [107] L. T. Hall, C. D. Hill, J. H. Cole, and L. C. Hollenberg, “Ultrasensitive diamond magnetometry using optimal dynamic decoupling,” *Physical Review B*, vol. 82, no. 4, p. 045208, 2010.
- [108] G. de Lange, D. Ristè, V. Dobrovitski, and R. Hanson, “Single-spin magnetometry with multipulse sensing sequences,” *Physical Review Letters*, vol. 106, no. 8, p. 080802, 2011.
- [109] E. Skorokhodov and B. V. Fine, “Electronic spin-echo envelope of NV-centers in diamond,” *Masters Thesis*, 2020.
- [110] J. R. Maze, P. L. Stanwix, J. S. Hodges, S. Hong, J. M. Taylor, P. Cappellaro, L. Jiang, M. G. Dutt, E. Togan, A. Zibrov, *et al.*, “Nanoscale magnetic sensing with an individual electronic spin in diamond,” *Nature*, vol. 455, no. 7213, pp. 644–647, 2008.
- [111] P. Siyushev, F. Kaiser, V. Jacques, I. Gerhardt, S. Bischof, H. Fedder, J. Dodson, M. Markham, D. Twitchen, F. Jelezko, *et al.*, “Monolithic diamond optics for single photon detection,” *Applied Physics Letters*, vol. 97, no. 24, p. 241902, 2010.
- [112] J. Hadden, J. Harrison, A. Stanley-Clarke, L. Marseglia, Y.-L. Ho, B. Patton, J. O’Brien, and J. Rarity, “Strongly enhanced photon collection from diamond defect centers under microfabricated integrated solid immersion lenses,” *Applied Physics Letters*, vol. 97, no. 24, p. 241901, 2010.

- 
- [113] T. M. Babinec, B. J. Hausmann, M. Khan, Y. Zhang, J. R. Maze, P. R. Hemmer, and M. Lončar, “A diamond nanowire single-photon source,” *Nature Nanotechnology*, vol. 5, no. 3, pp. 195–199, 2010.
- [114] D. Le Sage, L. M. Pham, N. Bar-Gill, C. Belthangady, M. D. Lukin, A. Yacoby, and R. L. Walsworth, “Efficient photon detection from color centers in a diamond optical waveguide,” *Physical Review B*, vol. 85, no. 12, p. 121202, 2012.
- [115] L. M. Pham, N. Bar-Gill, D. Le Sage, C. Belthangady, A. Stacey, M. Markham, D. Twitchen, M. D. Lukin, and R. L. Walsworth, “Enhanced metrology using preferential orientation of nitrogen-vacancy centers in diamond,” *Physical Review B*, vol. 86, no. 12, p. 121202, 2012.
- [116] L. M. Pham, N. Bar-Gill, C. Belthangady, D. Le Sage, P. Cappellaro, M. D. Lukin, A. Yacoby, and R. L. Walsworth, “Enhanced solid-state multispin metrology using dynamical decoupling,” *Physical Review B*, vol. 86, no. 4, p. 045214, 2012.
- [117] B. Naydenov, F. Dolde, L. T. Hall, C. Shin, H. Fedder, L. C. Hollenberg, F. Jelezko, and J. Wrachtrup, “Dynamical decoupling of a single-electron spin at room temperature,” *Physical Review B*, vol. 83, no. 8, p. 081201, 2011.
- [118] J. Weber, W. Koehl, J. Varley, A. Janotti, B. Buckley, C. Van de Walle, and D. D. Awschalom, “Quantum computing with defects,” *Proceedings of the National Academy of Sciences*, vol. 107, no. 19, pp. 8513–8518, 2010.
- [119] L. Childress and R. Hanson, “Diamond NV centers for quantum computing and quantum networks,” *MRS Bulletin*, vol. 38, no. 2, pp. 134–138, 2013.
- [120] D. D. Sukachev, A. Sipahigil, C. T. Nguyen, M. K. Bhaskar, R. E. Evans, F. Jelezko, and M. D. Lukin, “Silicon-vacancy spin qubit in diamond: a quantum memory exceeding 10 ms with single-shot state readout,” *Physical Review Letters*, vol. 119, no. 22, p. 223602, 2017.
- [121] M. K. Bhaskar, D. D. Sukachev, A. Sipahigil, R. E. Evans, M. J. Burek, C. T. Nguyen, L. J. Rogers, P. Siyushev, M. H. Metsch, H. Park, *et al.*, “Quantum nonlinear optics with a germanium-vacancy color center in a nanoscale diamond waveguide,” *Physical Review Letters*, vol. 118, no. 22, p. 223603, 2017.
- [122] S. Häußler, G. Thiering, A. Dietrich, N. Waasem, T. Teraji, J. Isoya, T. Iwasaki, M. Hatano, F. Jelezko, A. Gali, *et al.*, “Photoluminescence excitation spectroscopy of SiV- and GeV-color center in diamond,” *New Journal of Physics*, vol. 19, no. 6, p. 063036, 2017.

- [123] H. Kaupp, C. Deutsch, H.-C. Chang, J. Reichel, T. W. Hänsch, and D. Hunger, “Scaling laws of the cavity enhancement for nitrogen-vacancy centers in diamond,” *Physical Review A*, vol. 88, no. 5, p. 053812, 2013.
- [124] D. Riedel, I. Söllner, B. J. Shields, S. Starosielec, P. Appel, E. Neu, P. Maletinsky, and R. J. Warburton, “Deterministic enhancement of coherent photon generation from a nitrogen-vacancy center in ultrapure diamond,” *Physical Review X*, vol. 7, no. 3, p. 031040, 2017.
- [125] J. Wolters, A. W. Schell, G. Kewes, N. Nüsse, M. Schoengen, H. Döscher, T. Hannappel, B. Löchel, M. Barth, and O. Benson, “Enhancement of the zero phonon line emission from a single nitrogen vacancy center in a nanodiamond via coupling to a photonic crystal cavity,” *Applied Physics Letters*, vol. 97, no. 14, p. 141108, 2010.
- [126] R. Ikuta, T. Kobayashi, S. Yasui, S. Miki, T. Yamashita, H. Terai, M. Fujiwara, T. Yamamoto, M. Koashi, M. Sasaki, *et al.*, “Frequency down-conversion of 637 nm light to the telecommunication band for non-classical light emitted from NV centers in diamond,” *Optics Express*, vol. 22, no. 9, pp. 11205–11214, 2014.
- [127] C. L. Morrison, M. Rambach, Z. X. Koong, F. Graffitti, F. Thorburn, A. K. Kar, Y. Ma, S.-I. Park, J. D. Song, N. G. Stoltz, *et al.*, “A bright source of telecom single photons based on quantum frequency conversion,” *Applied Physics Letters*, vol. 118, no. 17, p. 174003, 2021.
- [128] S. Chakravarthi, C. Pederson, Z. Kazi, A. Ivanov, and K.-M. C. Fu, “Impact of surface and laser-induced noise on the spectral stability of implanted nitrogen-vacancy centers in diamond,” *Physical Review B*, vol. 104, no. 8, p. 085425, 2021.
- [129] M. Ruf, M. IJspeert, S. Van Dam, N. De Jong, H. Van Den Berg, G. Evers, and R. Hanson, “Optically coherent nitrogen-vacancy centers in micrometer-thin etched diamond membranes,” *Nano Letters*, vol. 19, no. 6, pp. 3987–3992, 2019.
- [130] L. V. Rodgers, L. B. Hughes, M. Xie, P. C. Maurer, S. Kolkowitz, A. C. Bleszynski Jayich, and N. P. de Leon, “Materials challenges for quantum technologies based on color centers in diamond,” *MRS Bulletin*, vol. 46, no. 7, pp. 623–633, 2021.
- [131] T. Kimoto and J. A. Cooper, *Fundamentals of silicon carbide technology: growth, characterization, devices and applications*. John Wiley & Sons, 2014.
- [132] M. Widmann, M. Niethammer, T. Makino, T. Rendler, S. Lasse, T. Ohshima, J. Ul Hassan, N. Tien Son, S.-Y. Lee, and J. Wrachtrup, “Bright single photon sources in lateral silicon carbide light emitting diodes,” *Applied Physics Letters*, vol. 112, no. 23, p. 231103, 2018.

- [133] P. Mélinon, B. Masenelli, F. Tournus, and A. Perez, “Playing with carbon and silicon at the nanoscale,” *Nature Materials*, vol. 6, no. 7, pp. 479–490, 2007.
- [134] M. Radulaski, M. Widmann, M. Niethammer, J. L. Zhang, S.-Y. Lee, T. Rendler, K. G. Lagoudakis, N. T. Son, E. Janzen, T. Ohshima, *et al.*, “Scalable quantum photonics with single color centers in silicon carbide,” *Nano Letters*, vol. 17, no. 3, pp. 1782–1786, 2017.
- [135] M. Atatüre, D. Englund, N. Vamivakas, S.-Y. Lee, and J. Wrachtrup, “Material platforms for spin-based photonic quantum technologies,” *Nature Reviews Materials*, vol. 3, no. 5, pp. 38–51, 2018.
- [136] M. Bhatnagar and B. J. Baliga, “Comparison of 6H-SiC, 3C-SiC, and Si for power devices,” *IEEE Transactions on Electron Devices*, vol. 40, no. 3, pp. 645–655, 1993.
- [137] G. Liu, B. R. Tuttle, and S. Dhar, “Silicon carbide: A unique platform for metal-oxide-semiconductor physics,” *Applied Physics Reviews*, vol. 2, no. 2, p. 021307, 2015.
- [138] P. Xing, D. Ma, K. J. Ooi, J. W. Choi, A. M. Agarwal, and D. Tan, “CMOS-compatible PECVD silicon carbide platform for linear and nonlinear optics,” *ACS Photonics*, vol. 6, no. 5, pp. 1162–1167, 2019.
- [139] H. Matsunami, “Current SiC technology for power electronic devices beyond Si,” *Microelectronic Engineering*, vol. 83, no. 1, pp. 2–4, 2006.
- [140] B. J. Baliga, “Silicon carbide power devices,” in *Springer Handbook of Semiconductor Devices*, pp. 491–523, Springer, 2022.
- [141] L. F. Alves, R. C. Gomes, P. Lefranc, R. d. A. Pegado, P.-O. Jeannin, B. A. Luciano, and F. V. Rocha, “SiC power devices in power electronics: An overview,” in *2017 Brazilian Power Electronics Conference (COBEP)*, pp. 1–8, IEEE, 2017.
- [142] P. M. Sarro, “Silicon carbide as a new MEMS technology,” *Sensors and Actuators A: Physical*, vol. 82, no. 1-3, pp. 210–218, 2000.
- [143] S. Dimitrijević and P. Jamet, “Advances in SiC power MOSFET technology,” *Microelectronics Reliability*, vol. 43, no. 2, pp. 225–233, 2003.
- [144] F. Martini and A. Politi, “Linear integrated optics in 3C silicon carbide,” *Optics Express*, vol. 25, no. 10, pp. 10735–10742, 2017.
- [145] H. Ou, Y. Ou, A. Argyraki, S. Schimmel, M. Kaiser, P. Wellmann, M. K. Linnarsson, V. Jokubavicius, J. Sun, R. Liljedahl, *et al.*, “Advances in wide bandgap SiC for optoelectronics,” *The European Physical Journal B*, vol. 87, no. 3, pp. 1–16, 2014.

- [146] N. Wright and A. Horsfall, “SiC sensors: a review,” *Journal of Physics D: Applied Physics*, vol. 40, no. 20, p. 6345, 2007.
- [147] D. D. Awschalom, R. Hanson, J. Wrachtrup, and B. B. Zhou, “Quantum technologies with optically interfaced solid-state spins,” *Nature Photonics*, vol. 12, no. 9, pp. 516–527, 2018.
- [148] C. J. Cochrane, J. Blacksberg, M. A. Anders, and P. M. Lenahan, “Vectorized magnetometer for space applications using electrical readout of atomic scale defects in silicon carbide,” *Scientific Reports*, vol. 6, no. 1, pp. 1–13, 2016.
- [149] A. Lohrmann, N. Iwamoto, Z. Bodrog, S. Castelletto, T. Ohshima, T. Karle, A. Gali, S. Prawer, J. McCallum, and B. Johnson, “Single-photon emitting diode in silicon carbide,” *Nature Communications*, vol. 6, no. 1, pp. 1–7, 2015.
- [150] F. Fuchs, V. Soltamov, S. V ath, P. Baranov, E. Mokhov, G. Astakhov, and V. Dyakonov, “Silicon carbide light-emitting diode as a prospective room temperature source for single photons,” *Scientific Reports*, vol. 3, no. 1, pp. 1–4, 2013.
- [151] S.-i. Sato, T. Honda, T. Makino, Y. Hijikata, S.-Y. Lee, and T. Ohshima, “Room temperature electrical control of single photon sources at 4H-SiC surface,” *ACS Photonics*, vol. 5, no. 8, pp. 3159–3165, 2018.
- [152] S. Castelletto, B. C. Johnson, and A. Boretti, “Quantum effects in silicon carbide hold promise for novel integrated devices and sensors,” *Advanced Optical Materials*, vol. 1, no. 9, pp. 609–625, 2013.
- [153] N. Mizuochi, S. Yamasaki, H. Takizawa, N. Morishita, T. Ohshima, H. Itoh, and J. Isoya, “Continuous-wave and pulsed EPR study of the negatively charged silicon vacancy with  $S = 3/2$  and  $C 3v$  symmetry in n-type 4H-SiC,” *Physical Review B*, vol. 66, no. 23, p. 235202, 2002.
- [154] P. Udvarhelyi, G. Thiering, N. Morioka, C. Babin, F. Kaiser, D. Lukin, T. Ohshima, J. Ul-Hassan, N. T. Son, J. Vučković, *et al.*, “Vibronic states and their effect on the temperature and strain dependence of silicon-vacancy qubits in 4H-SiC,” *Physical Review Applied*, vol. 13, no. 5, p. 054017, 2020.
- [155] D. Simin, H. Kraus, A. Sperlich, T. Ohshima, G. Astakhov, and V. Dyakonov, “Locking of electron spin coherence above 20 ms in natural silicon carbide,” *Physical Review B*, vol. 95, no. 16, p. 161201, 2017.
- [156] M. Widmann, S.-Y. Lee, T. Rendler, N. T. Son, H. Fedder, S. Paik, L.-P. Yang, N. Zhao, S. Yang, I. Booker, *et al.*, “Coherent control of single spins in silicon carbide at room temperature,” *Nature Materials*, vol. 14, no. 2, pp. 164–168, 2015.

- [157] R. Nagy, M. Niethammer, M. Widmann, Y.-C. Chen, P. Udvarhelyi, C. Bonato, J. U. Hassan, R. Karhu, I. G. Ivanov, N. T. Son, *et al.*, “High-fidelity spin and optical control of single silicon-vacancy centres in silicon carbide,” *Nature Communications*, vol. 10, no. 1, pp. 1–8, 2019.
- [158] S. Majety, P. Saha, V. A. Norman, and M. Radulaski, “Quantum information processing with integrated silicon carbide photonics,” *Journal of Applied Physics*, vol. 131, no. 13, p. 130901, 2022.
- [159] S. Castelletto and A. Boretti, “Silicon carbide color centers for quantum applications,” *Journal of Physics: Photonics*, vol. 2, no. 2, p. 022001, 2020.
- [160] C. Babin, R. Stöhr, N. Morioka, T. Linkewitz, T. Steidl, R. Wörnle, D. Liu, E. Hesselmeier, V. Vorobyov, A. Denisenko, *et al.*, “Fabrication and nanophotonic waveguide integration of silicon carbide colour centres with preserved spin-optical coherence,” *Nature Materials*, vol. 21, no. 1, pp. 67–73, 2022.
- [161] N. Son, P. Carlsson, J. Ul Hassan, E. Janzén, T. Umeda, J. Isoya, A. Gali, M. Bockstedte, N. Morishita, T. Ohshima, *et al.*, “Divacancy in 4h-SiC,” *Physical Review Letters*, vol. 96, no. 5, p. 055501, 2006.
- [162] W. F. Koehl, B. B. Buckley, F. J. Heremans, G. Calusine, and D. D. Awschalom, “Room temperature coherent control of defect spin qubits in silicon carbide,” *Nature*, vol. 479, no. 7371, pp. 84–87, 2011.
- [163] D. J. Christle, P. V. Klimov, C. F. de las Casas, K. Szász, V. Ivády, V. Jokubavicius, J. Ul Hassan, M. Syväjärvi, W. F. Koehl, T. Ohshima, N. T. Son, E. Janzén, A. Gali, and D. D. Awschalom, “Isolated spin qubits in SiC with a high-fidelity infrared spin-to-photon interface,” *Physical Review X*, vol. 7, no. 2, p. 021046, 2017.
- [164] C. P. Anderson, E. O. Glen, C. Zeledon, A. Bourassa, Y. Jin, Y. Zhu, C. Vorwerk, A. L. Crook, H. Abe, J. Ul-Hassan, *et al.*, “Five-second coherence of a single spin with single-shot readout in silicon carbide,” *Science Advances*, vol. 8, no. 5, p. eabm5912, 2022.
- [165] D. J. Christle, A. L. Falk, P. Andrich, P. V. Klimov, J. U. Hassan, N. T. Son, E. Janzén, T. Ohshima, and D. D. Awschalom, “Isolated electron spins in silicon carbide with millisecond coherence times,” *Nature Materials*, vol. 14, no. 2, pp. 160–163, 2015.
- [166] C. P. Anderson, A. Bourassa, K. C. Miao, G. Wolfowicz, P. J. Mintun, A. L. Crook, H. Abe, J. Ul Hassan, N. T. Son, T. Ohshima, and D. D. Awschalom, “Electrical and optical control of single spins integrated in scalable semiconductor devices,” *Science*, vol. 366, pp. 1225–1230, Dec. 2019.

- [167] A. Bourassa, *Control of Spin Qubits in a Classical Electronics Material*. PhD thesis, The University of Chicago, 2021.
- [168] B. Magnusson, N. T. Son, A. Cs r , A. G llstr m, T. Ohshima, A. Gali, and I. G. Ivanov, “Excitation properties of the divacancy in 4H-SiC,” *Physical Review B*, vol. 98, no. 19, p. 195202, 2018.
- [169] A. L. Falk, B. B. Buckley, G. Calusine, W. F. Koehl, V. V. Dobrovitski, A. Politi, C. A. Zorman, P. X.-L. Feng, and D. D. Awschalom, “Polytype control of spin qubits in silicon carbide,” *Nature Communications*, vol. 4, no. 1, p. 1819, 2013.
- [170] J. Davidsson, V. Iv dy, R. Armiento, T. Ohshima, N. Son, A. Gali, and I. A. Abrikosov, “Identification of divacancy and silicon vacancy qubits in 6H-SiC,” *Applied Physics Letters*, vol. 114, no. 11, p. 112107, 2019.
- [171] H. Singh, A. N. Anisimov, P. G. Baranov, and D. Suter, “Identification of different silicon vacancy centers in 6H-SiC,” *arXiv preprint arXiv:2212.10256*, 2022.
- [172] T. Bosma, G. J. Lof, C. M. Gilardoni, O. V. Zwier, F. Hendriks, B. Magnusson, A. Ellison, A. G llstr m, I. G. Ivanov, N. Son, *et al.*, “Identification and tunable optical coherent control of transition-metal spins in silicon carbide,” *npj Quantum Information*, vol. 4, no. 1, pp. 1–7, 2018.
- [173] L. Spindlberger, A. Cs r , G. Thiering, S. Putz, R. Karhu, J. U. Hassan, N. Son, T. Fromherz, A. Gali, and M. Trupke, “Optical properties of vanadium in 4H silicon carbide for quantum technology,” *Physical Review Applied*, vol. 12, no. 1, p. 014015, 2019.
- [174] M. Bickermann, D. Hofmann, T. L. Straubinger, R. Weingartner, and A. Winnacker, “On the preparation of vanadium-doped semi-insulating SiC bulk crystals,” in *Materials Science Forum*, vol. 389, pp. 139–142, Transtec Publications; 1999, 2002.
- [175] J. Schneider, H. M ller, K. Maier, W. Wilkening, F. Fuchs, A. D rnen, S. Leibenzeder, and R. Stein, “Infrared spectra and electron spin resonance of vanadium deep level impurities in silicon carbide,” *Applied Physics Letters*, vol. 56, no. 12, pp. 1184–1186, 1990.
- [176] M. Rejhon, M. Brynza, R. Grill, E. Belas, and J. Kunc, “Investigation of deep levels in semi-insulating vanadium-doped 4H-SiC by photocurrent spectroscopy,” *Physics Letters A*, vol. 405, p. 127433, 2021.
- [177] J. Elzerman, R. Hanson, L. Willems van Beveren, B. Witkamp, L. Vandersypen, and L. P. Kouwenhoven, “Single-shot read-out of an individual electron spin in a quantum dot,” *Nature*, vol. 430, no. 6998, pp. 431–435, 2004.



- 
- [178] M. Pfender, N. Aslam, P. Simon, D. Antonov, G. Thiering, S. Burk, F. Fávoro de Oliveira, A. Denisenko, H. Fedder, J. Meijer, *et al.*, “Protecting a diamond quantum memory by charge state control,” *Nano Letters*, vol. 17, no. 10, pp. 5931–5937, 2017.
- [179] A. Barbiero, J. Huwer, J. Skiba-Szymanska, D. J. Ellis, R. M. Stevenson, T. Muñozàller, G. Shooter, L. E. Goff, D. A. Ritchie, and A. J. Shields, “High-performance single-photon sources at telecom wavelength based on broadband hybrid circular Bragg gratings,” *ACS Photonics*, vol. 9, no. 9, pp. 3060–3066, 2022.
- [180] M. Kunzer, H. Müller, and U. Kaufmann, “Magnetic circular dichroism and site-selective optically detected magnetic resonance of the deep amphoteric vanadium impurity in 6H-SiC,” *Physical Review B*, vol. 48, no. 15, p. 10846, 1993.
- [181] J. Reinke, H. Wehrich, S. Greulich-Weber, and J.-M. Spaeth, “Magnetic circular dichroism of a vanadium impurity in 6H-silicon carbide,” *Semiconductor Science and Technology*, vol. 8, no. 10, p. 1862, 1993.
- [182] G. Wolfowicz, F. J. Heremans, C. P. Anderson, S. Kanai, H. Seo, A. Gali, G. Galli, and D. D. Awschalom, “Quantum guidelines for solid-state spin defects,” *Nature Reviews Materials*, vol. 6, no. 10, pp. 906–925, 2021.
- [183] M. Felle, J. Huwer, R. Stevenson, J. Skiba-Szymanska, M. Ward, I. Farrer, R. Penty, D. Ritchie, and A. Shields, “Interference with a quantum dot single-photon source and a laser at telecom wavelength,” *Applied Physics Letters*, vol. 107, no. 13, p. 131106, 2015.
- [184] J. Hendriks, C. M. Gilardoni, C. Adambukulam, A. Laucht, and C. H. van der Wal, “Coherent spin dynamics of hyperfine-coupled vanadium impurities in silicon carbide,” *arXiv preprint arXiv:2210.09942*, 2022.
- [185] T. Astner, P. Koller, C. M. Gilardoni, J. Hendriks, N. Son, I. Ivanov, J. Hassan, C. van der Wal, and M. Trupke, “Vanadium in Silicon Carbide: Telecom-ready spin centres with long relaxation lifetimes and hyperfine-resolved optical transitions,” *arXiv preprint arXiv:2206.06240*, 2022.
- [186] J. L. O’Brien, A. Furusawa, and J. Vučković, “Photonic quantum technologies,” *Nature Photonics*, vol. 3, pp. 687–695, Dec. 2009.
- [187] B. L. Higgins, D. W. Berry, S. D. Bartlett, H. M. Wiseman, and G. J. Pryde, “Entanglement-free Heisenberg-limited phase estimation,” *Nature*, vol. 450, no. 7168, pp. 393–396, 2007.
- [188] D. W. Berry and H. M. Wiseman, “Optimal states and almost optimal adaptive measurements for quantum interferometry,” *Physical Review Letters*, vol. 85, no. 24, p. 5098, 2000.

## BIBLIOGRAPHY

---

- [189] A. Ly, M. Marsman, J. Verhagen, R. P. Grasman, and E.-J. Wagenmakers, “A tutorial on Fisher information,” *Journal of Mathematical Psychology*, vol. 80, pp. 40–55, 2017.
- [190] H. Jeffreys, “An invariant form for the prior probability in estimation problems,” *Proceedings of the Royal Society of London. Series A. Mathematical and Physical Sciences*, vol. 186, no. 1007, pp. 453–461, 1946.
- [191] C. W. Helstrom, “Quantum detection and estimation theory,” *Journal of Statistical Physics*, vol. 1, pp. 231–252, 1969.
- [192] F. Albarelli, M. Barbieri, M. G. Genoni, and I. Gianani, “A perspective on multiparameter quantum metrology: From theoretical tools to applications in quantum imaging,” *Physics Letters A*, vol. 384, no. 12, p. 126311, 2020.
- [193] R. Demkowicz-Dobrzański, W. Górecki, and M. Guţă, “Multi-parameter estimation beyond quantum Fisher information,” *Journal of Physics A: Mathematical and Theoretical*, vol. 53, no. 36, p. 363001, 2020.
- [194] J. L. Beckey, M. Cerezo, A. Sone, and P. J. Coles, “Variational quantum algorithm for estimating the quantum fisher information,” *Physical Review Research*, vol. 4, no. 1, p. 013083, 2022.
- [195] W. Zhong, Z. Sun, J. Ma, X. Wang, and F. Nori, “Fisher information under decoherence in Bloch representation,” *Physical Review A*, vol. 87, no. 2, p. 022337, 2013.
- [196] J. Dittmann, “Explicit formulae for the Bures metric,” *Journal of Physics A: Mathematical and General*, vol. 32, no. 14, p. 2663, 1999.
- [197] R. Nishii, “Optimality of experimental designs,” *Discrete Mathematics*, vol. 116, no. 1-3, pp. 209–225, 1993.
- [198] M. Amaya, N. Linde, and E. Laloy, “Adaptive sequential Monte Carlo for posterior inference and model selection among complex geological priors,” *Geophysical Journal International*, vol. 226, no. 2, pp. 1220–1238, 2021.
- [199] L. Lang, W.-s. Chen, B. R. Bakshi, P. K. Goel, and S. Ungarala, “Bayesian estimation via sequential Monte Carlo sampling-Constrained dynamic systems,” *Automatica*, vol. 43, no. 9, pp. 1615–1622, 2007.
- [200] P. Del Moral, A. Doucet, and A. Jasra, “An adaptive sequential Monte Carlo method for approximate Bayesian computation,” *Statistics and Computing*, vol. 22, pp. 1009–1020, 2012.
- [201] C. E. Granade, C. Ferrie, N. Wiebe, and D. G. Cory, “Robust online Hamiltonian learning,” *New Journal of Physics*, vol. 14, no. 10, p. 103013, 2012.

- 
- [202] J. Liu and M. West, “Combined parameter and state estimation in simulation-based filtering,” *Sequential Monte Carlo Methods in Practice*, pp. 197–223, 2001.
- [203] A. Y. Kitaev, “Quantum measurements and the Abelian Stabilizer Problem,” *Electron. Colloquium Comput. Complex.*, vol. TR96, 1995.
- [204] A. Cooper, W. K. C. Sun, J.-C. Jaskula, and P. Cappellaro, “Environment-assisted quantum-enhanced sensing with electronic spins in diamond,” *Physical Review Applied*, vol. 12, no. 4, p. 044047, 2019.
- [205] R. Said, D. Berry, and J. Twamley, “Nanoscale magnetometry using a single-spin system in diamond,” *Physical Review B*, vol. 83, no. 12, p. 125410, 2011.
- [206] C. Bonato, M. S. Blok, H. T. Dinani, D. W. Berry, M. L. Markham, D. J. Twitchen, and R. Hanson, “Optimized quantum sensing with a single electron spin using real-time adaptive measurements,” *Nature Nanotechnology*, vol. 11, no. 3, p. 247, 2016.
- [207] P. Cappellaro, “Spin-bath narrowing with adaptive parameter estimation,” *Physical Review A*, vol. 85, no. 3, p. 030301, 2012.
- [208] A. Hentschel and B. C. Sanders, “Efficient algorithm for optimizing adaptive quantum metrology processes,” *Physical Review Letters*, vol. 107, no. 23, p. 233601, 2011.
- [209] R. Santagati, A. A. Gentile, S. Knauer, S. Schmitt, S. Paesani, C. Granade, N. Wiebe, C. Osterkamp, L. P. McGuinness, J. Wang, *et al.*, “Hamiltonian learning for the estimation of magnetic fields with nanoscale quantum sensors,” in *Quantum Information and Measurement*, pp. F4A–3, Optica Publishing Group, 2019.
- [210] R. Santagati, A. A. Gentile, S. Knauer, S. Schmitt, S. Paesani, C. Granade, N. Wiebe, C. Osterkamp, L. P. McGuinness, J. Wang, *et al.*, “Quantum sensing of magnetic fields using quantum hamiltonian learning,” in *Frontiers in Optics*, pp. FTu8D–3, Optical Society of America, 2020.
- [211] R. Santagati, A. A. Gentile, S. Knauer, S. Schmitt, S. Paesani, C. Granade, N. Wiebe, C. Osterkamp, L. P. McGuinness, J. Wang, *et al.*, “Magnetic-field learning using a single electronic spin in diamond with one-photon readout at room temperature,” *Physical Review X*, vol. 9, no. 2, p. 021019, 2019.
- [212] T. Joas, S. Schmitt, R. Santagati, A. A. Gentile, C. Bonato, A. Laing, L. P. McGuinness, and F. Jelezko, “Online adaptive quantum characterization of a nuclear spin,” *npj Quantum Information*, vol. 7, no. 1, pp. 1–8, 2021.
- [213] H. T. Dinani, D. W. Berry, R. Gonzalez, J. R. Maze, and C. Bonato, “Bayesian estimation for quantum sensing in the absence of single-shot detection,” *Physical Review B*, vol. 99, p. 125413, Mar 2019.

## BIBLIOGRAPHY

---

- [214] M. D. Shulman, S. P. Harvey, J. M. Nichol, S. D. Bartlett, A. C. Doherty, V. Umansky, and A. Yacoby, “Suppressing qubit dephasing using real-time Hamiltonian estimation,” *Nature Communications*, vol. 5, no. 1, p. 5156, 2014.
- [215] S. Mavadia, V. Frey, J. Sastrawan, S. Dona, and M. J. Biercuk, “Prediction and real-time compensation of qubit decoherence via machine learning,” *Nature Communications*, vol. 8, no. 1, p. 14106, 2017.
- [216] E. Scerri, E. M. Gauger, and C. Bonato, “Extending qubit coherence by adaptive quantum environment learning,” *New Journal of Physics*, vol. 22, no. 3, p. 035002, 2020.
- [217] A. D. Elliott, “Confocal microscopy: principles and modern practices,” *Current Protocols in Cytometry*, vol. 92, no. 1, p. e68, 2020.
- [218] E. Hecht, “Optics (4th edition ed.),” *Addison-Wesley, San Francisco*, vol. 2, p. 3, 2002.
- [219] M. Marvin, “Microscopy apparatus,” Dec. 19 1961.  
US Patent 3,013,467.
- [220] O. Patange, “On an instrument for the coherent investigation of nitrogen-vacancy centres in diamond,” Master’s thesis, University of Waterloo, 2013.
- [221] B. Yang, X. Chen, Y. Wang, S. Feng, V. Pessino, N. Stuurman, N. H. Cho, K. W. Cheng, S. J. Lord, L. Xu, *et al.*, “Epi-illumination SPIM for volumetric imaging with high spatial-temporal resolution,” *Nature Methods*, vol. 16, no. 6, pp. 501–504, 2019.
- [222] M. J. Booth, “Microscope Resolution Estimation and Normalised Coordinates,” *Zenodo*, Dec 2020.
- [223] E. A. Donley, T. P. Heavner, F. Levi, M. Tataw, and S. R. Jefferts, “Double-pass acousto-optic modulator system,” *Review of Scientific Instruments*, vol. 76, no. 6, p. 063112, 2005.
- [224] J. E. H. Young and S.-K. Yao, “Design considerations for acousto-optic devices,” *Proceedings of the IEEE*, vol. 69, no. 1, pp. 54–64, 1981.
- [225] D. Misonou, K. Sasaki, S. Ishizu, Y. Monnai, K. M. Itoh, and E. Abe, “Construction and operation of a tabletop system for nanoscale magnetometry with single nitrogen-vacancy centers in diamond,” *AIP Advances*, vol. 10, no. 2, p. 025206, 2020.
- [226] L. Jiang, J. Hodges, J. Maze, P. Maurer, J. Taylor, D. Cory, P. Hemmer, R. L. Walsworth, A. Yacoby, A. S. Zibrov, *et al.*, “Repetitive readout of a single electronic spin via quantum logic with nuclear spin ancillae,” *Science*, vol. 326, no. 5950, pp. 267–272, 2009.

- [227] M. Steiner, P. Neumann, J. Beck, F. Jelezko, and J. Wrachtrup, “Universal enhancement of the optical readout fidelity of single electron spins at nitrogen-vacancy centers in diamond,” *Physical Review B*, vol. 81, no. 3, p. 035205, 2010.
- [228] C. J. Terblanche, E. C. Reynhardt, and J. A. Van Wyk, “<sup>13</sup>C Spin–Lattice Relaxation in Natural Diamond: Zeeman Relaxation at 4.7 T and 300 K Due to Fixed Paramagnetic Nitrogen Defects,” *Solid state nuclear magnetic resonance*, vol. 20, no. 1-2, pp. 1–22, 2001.
- [229] M. G. Dutt, L. Childress, L. Jiang, E. Togan, J. Maze, F. Jelezko, A. Zibrov, P. Hemmer, and M. Lukin, “Quantum register based on individual electronic and nuclear spin qubits in diamond,” *Science*, vol. 316, no. 5829, pp. 1312–1316, 2007.
- [230] I. Lovchinsky, A. Sushkov, E. Urbach, N. P. de Leon, S. Choi, K. De Greve, R. Evans, R. Gertner, E. Bersin, C. Müller, *et al.*, “Nuclear magnetic resonance detection and spectroscopy of single proteins using quantum logic,” *Science*, vol. 351, no. 6275, pp. 836–841, 2016.
- [231] N. Aslam, M. Pfender, P. Neumann, R. Reuter, A. Zappe, F. Fávoro de Oliveira, A. Denisenko, H. Sumiya, S. Onoda, J. Isoya, *et al.*, “Nanoscale nuclear magnetic resonance with chemical resolution,” *Science*, vol. 357, no. 6346, pp. 67–71, 2017.
- [232] G. Waldherr, J. Beck, P. Neumann, R. Said, M. Nitsche, M. Markham, D. Twitchen, J. Twamley, F. Jelezko, and J. Wrachtrup, “High-dynamic-range magnetometry with a single nuclear spin in diamond,” *Nature nanotechnology*, vol. 7, no. 2, pp. 105–108, 2012.
- [233] A. Dréau, P. Spinicelli, J. Maze, J.-F. Roch, and V. Jacques, “Single-shot readout of multiple nuclear spin qubits in diamond under ambient conditions,” *Physical review letters*, vol. 110, no. 6, p. 060502, 2013.
- [234] Y.-C. Chen, B. Griffiths, L. Weng, S. S. Nicley, S. N. Ishmael, Y. Lekhai, S. Johnson, C. J. Stephen, B. L. Green, G. W. Morley, *et al.*, “Laser writing of individual nitrogen-vacancy defects in diamond with near-unity yield,” *Optica*, vol. 6, no. 5, pp. 662–667, 2019.
- [235] A. Gruber, A. Dräbenstedt, C. Tietz, L. Fleury, J. Wrachtrup, and C. Von Borczyskowski, “Scanning confocal optical microscopy and magnetic resonance on single defect centers,” *Science*, vol. 276, no. 5321, pp. 2012–2014, 1997.
- [236] S. Karaveli, O. Gaathon, A. Wolcott, R. Sakakibara, O. A. Shemesh, D. S. Peterka, E. S. Boyden, J. S. Owen, R. Yuste, and D. Englund, “Modulation of nitrogen vacancy charge state and fluorescence in nanodiamonds using electrochemical potential,” *Proceedings of the National Academy of Sciences*, vol. 113, no. 15, pp. 3938–3943, 2016.

- [237] R. Fukuda, P. Balasubramanian, I. Higashimata, G. Koike, T. Okada, R. Kagami, T. Teraji, S. Onoda, M. Haruyama, K. Yamada, *et al.*, “Lithographically engineered shallow nitrogen-vacancy centers in diamond for external nuclear spin sensing,” *New Journal of Physics*, vol. 20, no. 8, p. 083029, 2018.
- [238] J. D. Beitner, *Investigating approaches to enhance sensing capabilities of nitrogen-vacancy centres in nanodiamond*.  
PhD thesis, University of Cambridge, 2017.
- [239] R. H. Brown and R. Q. Twiss, “Correlation between photons in two coherent beams of light,” *Nature*, vol. 177, no. 4497, pp. 27–29, 1956.
- [240] A. Beveratos, R. Brouri, J.-P. Poizat, and P. Grangier, “Bunching and antibunching from single NV color centers in diamond,” in *Quantum Communication, Computing, and Measurement 3*, pp. 261–267, Springer, 2002.
- [241] L. Stewart, Y. Zhai, J. Dawes, M. Steel, J. Rabeau, and M. Withford, “Single photon emission from diamond nanocrystals in an opal photonic crystal,” *Optics Express*, vol. 17, no. 20, pp. 18044–18053, 2009.
- [242] M. Berthel, O. Mollet, G. Dantelle, T. Gacoin, S. Huant, and A. Drezet, “Photophysics of single nitrogen-vacancy centers in diamond nanocrystals,” *Physical Review B*, vol. 91, no. 3, p. 035308, 2015.
- [243] A. Cuche, A. Drezet, Y. Sonnefraud, O. Faklaris, F. Treussart, J.-F. Roch, and S. Huant, “Near-field optical microscopy with a nanodiamond-based single-photon tip,” *Optics Express*, vol. 17, no. 22, pp. 19969–19980, 2009.
- [244] J.-F. Wang, F.-F. Yan, Q. Li, Z.-H. Liu, H. Liu, G.-P. Guo, L.-P. Guo, X. Zhou, J.-M. Cui, J. Wang, *et al.*, “Coherent control of nitrogen-vacancy center spins in silicon carbide at room temperature,” *Physical Review Letters*, vol. 124, no. 22, p. 223601, 2020.
- [245] T. Plakhotnik and D. Gruber, “Luminescence of nitrogen-vacancy centers in nanodiamonds at temperatures between 300 and 700 K: perspectives on nanothermometry,” *Physical Chemistry Chemical Physics*, vol. 12, no. 33, pp. 9751–9756, 2010.
- [246] F. Jelezko, T. Gaebel, I. Popa, A. Gruber, and J. Wrachtrup, “Observation of coherent oscillations in a single electron spin,” *Physical Review Letters*, vol. 92, no. 7, p. 076401, 2004.
- [247] V. K. Sewani, H. H. Vallabhapurapu, Y. Yang, H. R. Firdaus, C. Adambukulam, B. C. Johnson, J. J. Pla, and A. Laucht, “Coherent control of NV- centers in diamond in a quantum teaching lab,” *American Journal of Physics*, vol. 88, no. 12, pp. 1156–1169, 2020.

- [248] M. Tusun, X. Rong, and J. Du, “Physics of quantum coherence in spin systems,” *Chinese Physics B*, vol. 28, no. 2, p. 024204, 2019.
- [249] V. Jacques, P. Neumann, J. Beck, M. Markham, D. Twitchen, J. Meijer, F. Kaiser, G. Balasubramanian, F. Jelezko, and J. Wrachtrup, “Dynamic polarization of single nuclear spins by optical pumping of nitrogen-vacancy color centers in diamond at room temperature,” *Physical Review Letters*, vol. 102, no. 5, p. 057403, 2009.
- [250] V. Ivády, K. Szász, A. L. Falk, P. V. Klimov, D. J. Christle, E. Janzén, I. A. Abrikosov, D. D. Awschalom, and A. Gali, “Theoretical model of dynamic spin polarization of nuclei coupled to paramagnetic point defects in diamond and silicon carbide,” *Physical Review B*, vol. 92, no. 11, p. 115206, 2015.
- [251] R. Fischer, A. Jarmola, P. Kehayias, and D. Budker, “Optical polarization of nuclear ensembles in diamond,” *Physical Review B*, vol. 87, no. 12, p. 125207, 2013.
- [252] F. Poggiali, P. Cappellaro, and N. Fabbri, “Measurement of the excited-state transverse hyperfine coupling in NV centers via dynamic nuclear polarization,” *Physical Review B*, vol. 95, no. 19, p. 195308, 2017.
- [253] G. Lindblad, “On the generators of quantum dynamical semigroups,” *Communications in Mathematical Physics*, vol. 48, no. 2, pp. 119–130, 1976.
- [254] L. Busaite, R. Lazda, A. Berzins, M. Auzinsh, R. Ferber, and F. Gahbauer, “Dynamic  $^{14}\text{N}$  nuclear spin polarization in nitrogen-vacancy centers in diamond,” *Physical Review B*, vol. 102, no. 22, p. 224101, 2020.
- [255] D. Budker, D. Kimball, D. F. Kimball, and D. P. DeMille, *Atomic physics: an exploration through problems and solutions*. Oxford University Press, USA, 2004.
- [256] R. Epstein, F. Mendoza, Y. Kato, and D. Awschalom, “Anisotropic interactions of a single spin and dark-spin spectroscopy in diamond,” *Nature Physics*, vol. 1, no. 2, pp. 94–98, 2005.
- [257] N. D. Lai, D. Zheng, F. Jelezko, F. Treussart, and J.-F. Roch, “Influence of a static magnetic field on the photoluminescence of an ensemble of nitrogen-vacancy color centers in a diamond single-crystal,” *Applied Physics Letters*, vol. 95, no. 13, p. 133101, 2009.
- [258] P. Maletinsky, S. Hong, M. S. Grinolds, B. Hausmann, M. D. Lukin, R. L. Walsworth, M. Loncar, and A. Yacoby, “A robust scanning diamond sensor for nanoscale imaging with single nitrogen-vacancy centres,” *Nature Nanotechnology*, vol. 7, no. 5, pp. 320–324, 2012.

## BIBLIOGRAPHY

---

- [259] L. Rondin, J.-P. Tetienne, P. Spinicelli, C. Dal Savio, K. Karrai, G. Dantelle, A. Thiaville, S. Rohart, J.-F. Roch, and V. Jacques, “Nanoscale magnetic field mapping with a single spin scanning probe magnetometer,” *Applied Physics Letters*, vol. 100, no. 15, p. 153118, 2012.
- [260] A. Magnets, “What are permanent magnets temperature coefficients  $\alpha$  and  $\beta$ ?,” May 2022.
- [261] G. Thiering and A. Gali, “Theory of the optical spin-polarization loop of the nitrogen-vacancy center in diamond,” *Physical Review B*, vol. 98, no. 8, p. 085207, 2018.
- [262] I. P. Radko, M. Boll, N. M. Israelsen, N. Raatz, J. Meijer, F. Jelezko, U. L. Andersen, and A. Huck, “Determining the internal quantum efficiency of shallow-implanted nitrogen-vacancy defects in bulk diamond,” *Optics Express*, vol. 24, no. 24, pp. 27715–27725, 2016.
- [263] V. Acosta, A. Jarmola, E. Bauch, and D. Budker, “Optical properties of the nitrogen-vacancy singlet levels in diamond,” *Physical Review B*, vol. 82, no. 20, p. 201202, 2010.
- [264] G. Wolfowicz, C. P. Anderson, B. Diler, O. G. Poluektov, F. J. Heremans, and D. D. Awschalom, “Vanadium spin qubits as telecom quantum emitters in silicon carbide,” *Science Advances*, vol. 6, no. 18, p. eaaz1192, 2020.
- [265] C. E. Bradley, J. Randall, M. H. Abobeih, R. C. Berrevoets, M. J. Degen, M. A. Bakker, M. Markham, D. J. Twitchen, and T. H. Taminiau, “A ten-qubit solid-state spin register with quantum memory up to one minute,” *Physical Review X*, vol. 9, no. 3, p. 031045, 2019.
- [266] M. Zhong, M. P. Hedges, R. L. Ahlefeldt, J. G. Bartholomew, S. E. Beavan, S. M. Wittig, J. J. Longdell, and M. J. Sellars, “Optically addressable nuclear spins in a solid with a six-hour coherence time,” *Nature*, vol. 517, no. 7533, pp. 177–180, 2015.
- [267] F. Arute, K. Arya, R. Babbush, D. Bacon, J. C. Bardin, R. Barends, R. Biswas, S. Boixo, F. G. Brandao, D. A. Buell, *et al.*, “Quantum supremacy using a programmable superconducting processor,” *Nature*, vol. 574, no. 7779, pp. 505–510, 2019.
- [268] Y. Wu, W.-S. Bao, S. Cao, F. Chen, M.-C. Chen, X. Chen, T.-H. Chung, H. Deng, Y. Du, D. Fan, *et al.*, “Strong quantum computational advantage using a superconducting quantum processor,” *Physical Review Letters*, vol. 127, no. 18, p. 180501, 2021.
- [269] A. Crippa, R. Ezzouch, A. Aprá, A. Amisse, R. Laviéville, L. Hutin, B. Bertrand, M. Vinet, M. Urdampilleta, T. Meunier, *et al.*, “Gate-reflectometry dispersive readout and coherent control of a spin qubit in silicon,” *Nature Communications*, vol. 10, no. 1, pp. 1–6, 2019.



- [270] M. Vinet, “The path to scalable quantum computing with silicon spin qubits,” *Nature Nanotechnology*, vol. 16, no. 12, pp. 1296–1298, 2021.
- [271] L. T. Hall, C. D. Hill, J. H. Cole, B. Städler, F. Caruso, P. Mulvaney, J. Wrachtrup, and L. C. Hollenberg, “Monitoring ion-channel function in real time through quantum decoherence,” *Proceedings of the National Academy of Sciences*, vol. 107, no. 44, pp. 18777–18782, 2010.
- [272] R. Schoelkopf, A. Clerk, S. Girvin, K. Lehnert, and M. Devoret, “Qubits as spectrometers of quantum noise,” in *Quantum Noise in Mesoscopic Physics*, pp. 175–203, Springer, 2003.
- [273] D. Schmid-Lorch, T. Häberle, F. Reinhard, A. Zappe, M. Slota, L. Bogani, A. Finkler, and J. Wrachtrup, “Relaxometry and Dephasing Imaging of Superparamagnetic Magnetite Nanoparticles Using a Single Qubit,” *Nanoletters*, vol. 15, p. 4942, 2015.
- [274] A. Finco, A. Haykal, R. Tanos, F. Fabre, S. Chouaieb, W. Akhtar, I. Robert-Philip, W. Legrand, F. Ajejas, K. Bouzehouane, *et al.*, “Imaging non-collinear antiferromagnetic textures via single spin relaxometry,” *Nature Communications*, vol. 12, no. 1, pp. 1–6, 2021.
- [275] L. Nie, A. Nusantara, V. Damle, R. Sharmin, E. Evans, S. Hemelaar, K. Van der Laan, R. Li, F. Perona Martinez, T. Vedelaar, *et al.*, “Quantum monitoring of cellular metabolic activities in single mitochondria,” *Science Advances*, vol. 7, no. 21, p. eabf0573, 2021.
- [276] M. Caouette-Mansour, A. Solyom, B. Ruffolo, R. D. McMichael, J. Sankey, and L. Childress, “Robust Spin Relaxometry with Fast Adaptive Bayesian Estimation,” *Phys. Rev. Appl.*, vol. 17, p. 064031, Jun 2022.
- [277] L. T. Hall, J. H. Cole, and L. C. L. Hollenberg, “Analytic solutions to the central-spin problem for nitrogen-vacancy centers in diamond,” *Physical Review B*, vol. 90, no. 7, p. 075201, 2014.
- [278] C. J. Stephen, B. L. Green, Y. N. D. Lekhai, L. Weng, P. Hill, S. Johnson, A. C. Frangeskou, P. L. Diggie, Y. C. Chen, M. J. Strain, E. Gu, M. E. Newton, J. M. Smith, P. S. Salter, and G. W. Morley, “Deep three-dimensional solid-state qubit arrays with long-lived spin coherence,” *Physical Review Applied*, vol. 12, no. 6, p. 064005, 2019.
- [279] V. Dobrovitski, A. Feiguin, D. Awschalom, and R. Hanson, “Decoherence dynamics of a single spin versus spin ensemble,” *Physical Review B*, vol. 77, no. 24, p. 245212, 2008.
- [280] E. Bauch, S. Singh, J. Lee, C. A. Hart, J. M. Schloss, M. J. Turner, J. F. Barry, L. M. Pham, N. Bar-Gill, S. F. Yelin, and R. L. Walsworth, “Decoherence of ensembles of nitrogen-vacancy centers in diamond,” *Physical Review B*, vol. 102, p. 134210, Oct 2020.

## BIBLIOGRAPHY

---

- [281] E. Bauch, S. Singh, J. Lee, C. A. Hart, J. M. Schloss, M. J. Turner, J. F. Barry, L. M. Pham, N. Bar-Gill, S. F. Yelin, *et al.*, “Decoherence of ensembles of nitrogen-vacancy centers in diamond,” *Physical Review B*, vol. 102, no. 13, p. 134210, 2020.
- [282] B. L. Dwyer, L. V. Rodgers, E. K. Urbach, D. Bluvstein, S. Sangtawesin, H. Zhou, Y. Nassab, M. Fitzpatrick, Z. Yuan, K. De Greve, E. L. Peterson, H. Knowles, T. Sumarac, J.-P. Chou, A. Gali, V. Dobrovitski, M. D. Lukin, and N. P. de Leon, “Probing Spin Dynamics on Diamond Surfaces Using a Single Quantum Sensor,” *PRX Quantum*, vol. 3, p. 040328, Dec 2022.
- [283] M. J. Arshad, C. Bekker, B. Haylock, K. Skrzypczak, D. White, B. Griffiths, J. Gore, G. W. Morley, P. Salter, J. Smith, *et al.*, “Online adaptive estimation of decoherence timescales for a single qubit,” *arXiv preprint arXiv:2210.06103*, 2022.
- [284] Y.-H. Zhang and W. Yang, “Improving spin-based noise sensing by adaptive measurements,” *New Journal of Physics*, vol. 20, no. 9, p. 093011, 2018.
- [285] S. L. Braunstein and C. M. Caves, “Statistical distance and the geometry of quantum states,” *Physical Review Letters*, vol. 72, no. 22, p. 3439, 1994.
- [286] L. Robledo, L. Childress, H. Bernien, B. Hensen, P. F. Alkemade, and R. Hanson, “High-fidelity projective read-out of a solid-state spin quantum register,” *Nature*, vol. 477, no. 7366, pp. 574–578, 2011.
- [287] I. Zohar, B. Haylock, Y. Romach, M. J. Arshad, N. Halay, N. Drucker, R. Stöhr, A. Denisenko, Y. Cohen, C. Bonato, *et al.*, “Real-time frequency estimation of a qubit without single-shot-readout,” *Quantum Science and Technology*, vol. 8, no. 3, p. 035017, 2023.
- [288] R. Cleve, A. Ekert, C. Macchiavello, and M. Mosca, “Quantum algorithms revisited,” *Proceedings of the Royal Society of London. Series A: Mathematical, Physical and Engineering Sciences*, vol. 454, no. 1969, pp. 339–354, 1998.
- [289] A. Y. Kitaev, A. Shen, and M. N. Vyalyi, *Classical and quantum computation*. No. 47, American Mathematical Soc., 2002.
- [290] S. Danilin, A. V. Lebedev, A. Vepsäläinen, G. B. Lesovik, G. Blatter, and G. Paraoanu, “Quantum-enhanced magnetometry by phase estimation algorithms with a single artificial atom,” *npj Quantum Information*, vol. 4, no. 1, p. 29, 2018.
- [291] B. Higgins, D. Berry, S. Bartlett, M. Mitchell, H. Wiseman, and G. Pryde, “Demonstrating Heisenberg-limited unambiguous phase estimation without adaptive measurements,” *New Journal of Physics*, vol. 11, no. 7, p. 073023, 2009.

- [292] C. Bonato and D. W. Berry, “Adaptive tracking of a time-varying field with a quantum sensor,” *Physical Review A*, vol. 95, no. 5, p. 052348, 2017.
- [293] A. J. Hayes and D. W. Berry, “Swarm optimization for adaptive phase measurements with low visibility,” *Physical Review A*, vol. 89, no. 1, p. 013838, 2014.
- [294] N. Wiebe and C. Granade, “Efficient Bayesian phase estimation,” *Physical Review Letters*, vol. 117, no. 1, p. 010503, 2016.
- [295] N. Nusran, M. U. Momeen, and M. G. Dutt, “High-dynamic-range magnetometry with a single electronic spin in diamond,” *Nature Nanotechnology*, vol. 7, no. 2, p. 109, 2012.
- [296] P. Neumann, J. Beck, M. Steiner, F. Rempp, H. Fedder, P. R. Hemmer, J. Wrachtrup, and F. Jelezko, “Single-shot readout of a single nuclear spin,” *Science*, vol. 329, no. 5991, pp. 542–544, 2010.
- [297] P. C. Humphreys, N. Kalb, J. P. J. Morits, R. N. Schouten, R. F. L. Vermeulen, D. J. Twitchen, M. Markham, and R. Hanson, “Deterministic delivery of remote entanglement on a quantum network,” *Nature*, vol. 558, pp. 268–273, June 2018.
- [298] A. Sipahigil, R. E. Evans, D. D. Sukachev, M. J. Burek, J. Borregaard, M. K. Bhaskar, C. T. Nguyen, J. L. Pacheco, H. A. Atikian, C. Meuwly, R. M. Camacho, F. Jelezko, E. Bielejec, H. Park, M. Lonfçar, and M. D. Lukin, “An integrated diamond nanophotonics platform for quantum-optical networks,” *Science*, vol. 354, pp. 847–850, Nov. 2016.
- [299] P.-J. Stas, Y. Q. Huan, B. Machielse, E. N. Knall, A. Suleymanzade, B. Pingault, M. Sutula, S. W. Ding, C. M. Knaut, D. R. Assumpcao, Y.-C. Wei, M. K. Bhaskar, R. Riedinger, D. D. Sukachev, H. Park, M. Lonfçar, D. S. Levonian, and M. D. Lukin, “Robust multi-qubit quantum network node with integrated error detection,” *Science*, vol. 378, pp. 557–560, Nov. 2022.
- [300] G. Grosso, H. Moon, B. Lienhard, S. Ali, D. K. Efetov, M. M. Furchi, P. Jarillo-Herrero, M. J. Ford, I. Aharonovich, and D. Englund, “Tunable and high-purity room temperature single-photon emission from atomic defects in hexagonal boron nitride,” *Nature Communications*, vol. 8, p. 705, Sept. 2017.
- [301] A. Gottscholl, M. Kianinia, V. Soltamov, S. Orlinskii, G. Mamin, C. Bradac, C. Kasper, K. Krambrock, A. Sperlich, M. Toth, I. Aharonovich, and V. Dyakonov, “Initialization and read-out of intrinsic spin defects in a van der Waals crystal at room temperature,” *Nature Materials*, vol. 19, pp. 540–545, May 2020.
- [302] M. Raha, S. Chen, C. M. Phenicie, S. Ourari, A. M. Dibos, and J. D. Thompson, “Optical quantum nondemolition measurement of a single rare earth ion qubit,” *Nature Communications*, vol. 11, no. 1, p. 1605, 2020.

## BIBLIOGRAPHY

---

- [303] A. Ruskuc, C.-J. Wu, J. Rochman, J. Choi, and A. Faraon, “Nuclear spin-wave quantum register for a solid-state qubit,” *Nature*, vol. 602, pp. 408–413, Feb. 2022.
- [304] J. V. Rakonjac, D. Lago-Rivera, A. Seri, M. Mazzera, S. Grandi, and H. de Riedmatten, “Entanglement between a Telecom Photon and an On-Demand Multimode Solid-State Quantum Memory,” *Phys. Rev. Lett.*, vol. 127, p. 210502, Nov 2021.
- [305] P. Tamarat, T. Gaebel, J. R. Rabeau, M. Khan, A. D. Greentree, H. Wilson, L. C. L. Hollenberg, S. Prawer, P. Hemmer, F. Jelezko, and J. Wrachtrup, “Stark Shift Control of Single Optical Centers in Diamond,” *Phys. Rev. Lett.*, vol. 97, p. 083002, Aug 2006.
- [306] L. C. Bassett, F. J. Heremans, C. G. Yale, B. B. Buckley, and D. D. Awschalom, “Electrical Tuning of Single Nitrogen-Vacancy Center Optical Transitions Enhanced by Photoinduced Fields,” *Phys. Rev. Lett.*, vol. 107, p. 266403, Dec 2011.
- [307] J. H. Weber, B. Kambs, J. Kettler, S. Kern, J. Maisch, H. Vural, M. Jetter, S. L. Portalupi, C. Becher, and P. Michler, “Two-photon interference in the telecom C-band after frequency conversion of photons from remote quantum emitters,” *Nature Nanotechnology*, vol. 14, pp. 23–26, Jan. 2019.
- [308] F. Yan, *Low temperature photoluminescence study on defect centers in silicon carbide*. PhD thesis, University of Pittsburgh, 2009.
- [309] S.-K. Kim, E. Y. Jung, and M.-H. Lee, “Defect-Induced Luminescence Quenching of 4H-SiC Single Crystal Grown by PVT Method through a Control of Incorporated Impurity Concentration,” *Compounds*, vol. 2, no. 1, pp. 68–79, 2022.
- [310] C. Hemmingsson, N. Son, A. Ellison, J. Zhang, and E. Janzén, “Negative-U centers in 4H silicon carbide,” *Physical Review B*, vol. 58, no. 16, p. R10119, 1998.
- [311] N. T. Son, X. T. Trinh, L. S. Løvlie, B. G. Svensson, K. Kawahara, J. Suda, T. Kimoto, T. Umeda, J. Isoya, T. Makino, *et al.*, “Negative-U system of carbon vacancy in 4H-SiC,” *Physical Review Letters*, vol. 109, no. 18, p. 187603, 2012.
- [312] X. T. Trinh, K. Szász, T. Hornos, K. Kawahara, J. Suda, T. Kimoto, A. Gali, E. Janzén, and N. T. Son, “Negative-U carbon vacancy in 4H-SiC: Assessment of charge correction schemes and identification of the negative carbon vacancy at the quasicubic site,” *Physical Review B*, vol. 88, no. 23, p. 235209, 2013.
- [313] J. Sumakeris, J. Jenny, and A. Powell, “Bulk crystal growth, epitaxy, and defect reduction in silicon carbide materials for microwave and power devices,” *MRS Bulletin*, vol. 30, no. 4, pp. 280–286, 2005.

- [314] N. Achtziger and W. Witthuhn, “Band gap states of Ti, V, and Cr in 4H–silicon carbide,” *Applied Physics Letters*, vol. 71, no. 1, pp. 110–112, 1997.
- [315] N. Achtziger and W. Witthuhn, “Band-gap states of Ti, V, and Cr in 4H-SiC: Identification and characterization by elemental transmutation of radioactive isotopes,” *Physical Review B*, vol. 57, no. 19, p. 12181, 1998.
- [316] A. Evwaraye, S. Smith, and W. Mitchel, “Optical admittance studies of vanadium donor level in high-resistivity p-type 6H-SiC,” *Journal of applied physics*, vol. 79, no. 1, pp. 253–258, 1996.
- [317] J. Baur, M. Kunzer, and J. Schneider, “Transition metals in SiC polytypes, as studied by magnetic resonance techniques,” *physica status solidi (a)*, vol. 162, no. 1, pp. 153–172, 1997.
- [318] W. Mitchel, R. Perrin, J. Goldstein, A. Saxler, M. Roth, S. Smith, J. Solomon, and A. Evwaraye, “Fermi level control and deep levels in semi-insulating 4H–SiC,” *Journal of applied physics*, vol. 86, no. 9, pp. 5040–5044, 1999.
- [319] J. M. Langer and H. Heinrich, “Deep-Level Impurities: A Possible Guide to Prediction of Band-Edge Discontinuities in Semiconductor Heterojunctions,” *Phys. Rev. Lett.*, vol. 55, pp. 1414–1417, Sep 1985.
- [320] L. Spindlberger, A. Csóré, G. Thiering, S. Putz, R. Karhu, J. U. Hassan, N. Son, T. Fromherz, A. Gali, and M. Trupke, “Optical properties of vanadium in 4H silicon carbide for quantum technology,” *Physical Review Applied*, vol. 12, no. 1, p. 014015, 2019.
- [321] B. Tissot and G. Burkard, “Spin Structure and Resonant Driving of Spin-1/2 Defects in SiC,” *Physical Review B*, vol. 103, no. 6, p. 064106, 2021.
- [322] B. Tissot, M. Trupke, P. Koller, T. Astner, and G. Burkard, “Nuclear spin quantum memory in silicon carbide,” *Phys. Rev. Research*, vol. 4, p. 033107, Aug 2022.
- [323] B. Tissot and G. Burkard, “Hyperfine Structure of Transition Metal Defects in SiC,” *Physical Review B*, vol. 104, no. 6, p. 064102, 2021.
- [324] V. Heine and C. H. Henry, “Theory of the isotope shift for zero-phonon optical transitions at traps in semiconductors,” *Physical Review B*, vol. 11, pp. 3795–3803, May 1975.
- [325] M. Cardona and M. L. W. Thewalt, “Isotope effects on the optical spectra of semiconductors,” *Rev. Mod. Phys.*, vol. 77, pp. 1173–1224, Nov 2005.
- [326] P. Udvarhelyi, V. O. Shkolnikov, A. Gali, G. Burkard, and A. Pályi, “Spin-Strain Interaction in Nitrogen-Vacancy Centers in Diamond,” *Physical Review B*, vol. 98, no. 7, p. 075201, 2018.

- [327] S. B. van Dam, M. Walsh, M. J. Degen, E. Bersin, S. L. Mouradian, A. Galiullin, M. Ruf, M. IJspeert, T. H. Taminiau, R. Hanson, and D. R. Englund, “Optical coherence of diamond nitrogen-vacancy centers formed by ion implantation and annealing,” *Physical Review B*, vol. 99, p. 161203, Apr. 2019.
- [328] L. J. Rogers, K. D. Jahnke, T. Teraji, L. Marseglia, C. Müller, B. Naydenov, H. Schauffert, C. Kranz, J. Isoya, L. P. McGuinness, *et al.*, “Multiple intrinsically identical single-photon emitters in the solid state,” *Nature Communications*, vol. 5, no. 1, p. 4739, 2014.
- [329] R. E. Evans, A. Sipahigil, D. D. Sukachev, A. S. Zibrov, and M. D. Lukin, “Narrow-Linewidth Homogeneous Optical Emitters in Diamond Nanostructures via Silicon Ion Implantation,” *Phys. Rev. Applied*, vol. 5, p. 044010, Apr 2016.
- [330] R. Nagy, D. B. R. Dasari, C. Babin, D. Liu, V. Vorobyov, M. Niethammer, M. Widmann, T. Linkewitz, I. Gediz, R. Stöhr, H. B. Weber, T. Ohshima, M. Ghezellou, N. T. Son, J. Ul-Hassan, F. Kaiser, and J. Wrachtrup, “Narrow inhomogeneous distribution of spin-active emitters in silicon carbide,” *Applied Physics Letters*, vol. 118, no. 14, p. 144003, 2021.
- [331] A. Gritsch, L. Weiss, J. Früh, S. Rinner, and A. Reiserer, “Narrow optical transitions in erbium-implanted silicon waveguides,” *Physical Review X*, vol. 12, no. 4, p. 041009, 2022.
- [332] L. Bergeron, C. Chartrand, A. T. K. Kurkjian, K. J. Morse, H. Riemann, N. V. Abrosimov, P. Becker, H.-J. Pohl, M. L. W. Thewalt, and S. Simmons, “Silicon-Integrated Telecommunications Photon-Spin Interface,” *PRX Quantum*, vol. 1, p. 020301, Oct 2020.
- [333] E. R. MacQuarrie, C. Chartrand, D. B. Higginbottom, K. J. Morse, V. A. Karasyuk, S. Roorda, and S. Simmons, “Generating T centres in photonic silicon-on-insulator material by ion implantation,” *New Journal of Physics*, vol. 23, p. 103008, oct 2021.
- [334] C. Chartrand, L. Bergeron, K. J. Morse, H. Riemann, N. V. Abrosimov, P. Becker, H.-J. Pohl, S. Simmons, and M. L. W. Thewalt, “Highly enriched  $^{28}\text{Si}$  reveals remarkable optical linewidths and fine structure for well-known damage centers,” *Physical Review B*, vol. 98, p. 195201, Nov 2018.
- [335] A. Durand, Y. Baron, W. Redjem, T. Herzig, A. Benali, S. Pezzagna, J. Meijer, A. Y. Kuznetsov, J.-M. Gérard, I. Robert-Philip, M. Abbarchi, V. Jacques, G. Cassabois, and A. Dréau, “Broad Diversity of Near-Infrared Single-Photon Emitters in Silicon,” *Phys. Rev. Lett.*, vol. 126, p. 083602, Feb 2021.

- [336] A. Tiranov, A. Ortu, S. Welinski, A. Ferrier, P. Goldner, N. Gisin, and M. Afzelius, “Spectroscopic study of hyperfine properties in  $^{171}\text{Yb}^{3+}:\text{Y}_2\text{SiO}_5$ ,” *Physical Review B*, vol. 98, p. 195110, Nov 2018.
- [337] R. Ahlefeldt, N. Manson, and M. Sellars, “Optical lifetime and linewidth studies of the  $^7\text{F}_0 \rightarrow ^5\text{D}_0$  transition in  $\text{EuCl}_3 \cdot 6\text{H}_2\text{O}$ : A potential material for quantum memory applications,” *Journal of luminescence*, vol. 133, pp. 152–156, 2013.
- [338] R. L. Ahlefeldt, M. R. Hush, and M. J. Sellars, “Ultrannarrow Optical Inhomogeneous Linewidth in a Stoichiometric Rare-Earth Crystal,” *Phys. Rev. Lett.*, vol. 117, p. 250504, Dec 2016.
- [339] S. Chen, M. Raha, C. M. Phenicie, S. Ourari, and J. D. Thompson, “Parallel single-shot measurement and coherent control of solid-state spins below the diffraction limit,” *Science*, vol. 370, no. 6516, pp. 592–595, 2020.
- [340] T. Rendler, J. Neburkova, O. Zemek, J. Kotek, A. Zappe, Z. Chu, P. Cigler, and J. Wrachtrup, “Optical imaging of localized chemical events using programmable diamond quantum nanosensors,” *Nature Communications*, vol. 8, no. 1, pp. 1–9, 2017.
- [341] L. Nie, A. C. Nusantara, V. G. Damle, M. V. Baranov, M. Chipaux, C. Reyes-San-Martin, T. Hamoh, C. P. Epperla, M. Guricova, P. Cigler, *et al.*, “Quantum sensing of free radicals in primary human dendritic cells,” *Nano Letters*, vol. 22, no. 4, pp. 1818–1825, 2021.
- [342] T. Staudacher, F. Shi, S. Pezzagna, J. Meijer, J. Du, C. A. Meriles, F. Reinhard, and J. Wrachtrup, “Nuclear magnetic resonance spectroscopy on a (5-nanometer) 3 sample volume,” *Science*, vol. 339, no. 6119, pp. 561–563, 2013.
- [343] Y. Schälte and J. Hasenauer, “Efficient exact inference for dynamical systems with noisy measurements using sequential approximate Bayesian computation,” *Bioinformatics*, vol. 36, no. Supplement\_1, pp. i551–i559, 2020.
- [344] F. Belliardo, V. Cimini, E. Polino, F. Hoch, B. Piccirillo, N. Spagnolo, V. Giovannetti, and F. Sciarrino, “Optimizing quantum-enhanced Bayesian multiparameter estimation in noisy apparatus,” *arXiv preprint arXiv:2211.04747*, 2022.
- [345] L. J. Fiderer, J. Schuff, and D. Braun, “Neural-network heuristics for adaptive bayesian quantum estimation,” *PRX Quantum*, vol. 2, no. 2, p. 020303, 2021.
- [346] A. Hentschel and B. C. Sanders, “Machine learning for precise quantum measurement,” *Physical Review Letters*, vol. 104, no. 6, p. 063603, 2010.
- [347] V. Cimini, M. Valeri, E. Polino, S. Piacentini, F. Ceccarelli, G. Corrielli, N. Spagnolo, R. Oselame, and F. Sciarrino, “Deep reinforcement learning for quantum multiparameter estimation,” *Advanced Photonics*, vol. 5, no. 1, p. 016005, 2023.

- [348] S. Nolan, A. Smerzi, and L. Pezzè, “A machine learning approach to Bayesian parameter estimation,” *npj Quantum Information*, vol. 7, no. 1, p. 169, 2021.
- [349] K. Jung, M. Abobeih, J. Yun, G. Kim, H. Oh, A. Henry, T. H. Taminiau, and D. Kim, “Deep learning enhanced individual nuclear-spin detection,” *npj Quantum Information*, vol. 7, no. 1, p. 41, 2021.
- [350] C. Bekker, M. J. Arshad, P. Cilibrizzi, C. Nikolatos, P. Lomax, G. S. Wood, R. Cheung, W. Knolle, N. Ross, B. Gerardot, *et al.*, “Scalable fabrication of hemispherical solid immersion lenses in silicon carbide through grayscale hard-mask lithography,” *Applied Physics Letters*, vol. 122, no. 17, 2023.
- [351] N. T. Son, C. P. Anderson, A. Bourassa, K. C. Miao, C. Babin, M. Widmann, M. Niethammer, J. Ul Hassan, N. Morioka, I. G. Ivanov, *et al.*, “Developing silicon carbide for quantum spintronics,” *Applied Physics Letters*, vol. 116, no. 19, p. 190501, 2020.
- [352] B. Merkel, A. Ulanowski, and A. Reiserer, “Coherent and Purcell-enhanced emission from erbium dopants in a cryogenic high-Q resonator,” *Physical Review X*, vol. 10, no. 4, p. 041025, 2020.
- [353] J. Hagemeyer, C. Bonato, T.-A. Truong, H. Kim, G. J. Beirne, M. Bakker, M. P. Van Exter, Y. Luo, P. Petroff, and D. Bouwmeester, “H1 photonic crystal cavities for hybrid quantum information protocols,” *Optics Express*, vol. 20, no. 22, pp. 24714–24726, 2012.
- [354] D. Lukin, *Silicon Carbide on Insulator Quantum Photonics with Color Centers*. PhD thesis, 2022.
- [355] C. Wang, Z. Fang, A. Yi, B. Yang, Z. Wang, L. Zhou, C. Shen, Y. Zhu, Y. Zhou, R. Bao, *et al.*, “High-Q microresonators on 4H-silicon-carbide-on-insulator platform for nonlinear photonics,” *Light: Science & Applications*, vol. 10, no. 1, p. 139, 2021.
- [356] D. Lukin, C. Dory, M. Radulaski, S. Sun, S. D. Mishra, M. Guidry, D. Vercruyssen, and J. Vučković, “4H-SiC-on-insulator platform for quantum photonics,” in *CLEO: Science and Innovations*, pp. SM2F–6, Optica Publishing Group, 2019.
- [357] D. M. Lukin, C. Dory, M. A. Guidry, K. Y. Yang, S. D. Mishra, R. Trivedi, M. Radulaski, S. Sun, D. Vercruyssen, G. H. Ahn, *et al.*, “4H-silicon-carbide-on-insulator for integrated quantum and nonlinear photonics,” *Nature Photonics*, vol. 14, no. 5, pp. 330–334, 2020.
- [358] A. Y. Piggott, J. Lu, K. G. Lagoudakis, J. Petykiewicz, T. M. Babinec, and J. Vučković, “Inverse design and demonstration of a compact and broadband on-chip wavelength demultiplexer,” *Nature Photonics*, vol. 9, no. 6, pp. 374–377, 2015.



- [359] A. Y. Piggott, J. Petykiewicz, L. Su, and J. Vučković, “Fabrication-constrained nanophotonic inverse design,” *Scientific Reports*, vol. 7, no. 1, p. 1786, 2017.
- [360] A. Bourassa, C. P. Anderson, K. C. Miao, M. Onizhuk, H. Ma, A. L. Crook, H. Abe, J. Ul-Hassan, T. Ohshima, N. T. Son, *et al.*, “Entanglement and control of single nuclear spins in isotopically engineered silicon carbide,” *Nature Materials*, vol. 19, no. 12, pp. 1319–1325, 2020.
- [361] D. M. Lukin, M. A. Guidry, J. Yang, M. Ghezellou, S. D. Mishra, H. Abe, T. Ohshima, J. Ul-Hassan, and J. Vučković, “Optical superradiance of a pair of color centers in an integrated silicon-carbide-on-insulator microresonator,” *arXiv preprint arXiv:2202.04845*, 2022.